AD_____

Award Number: W81XWH-08-2-0030

TITLE: Helmet Sensor - Transfer Function and Model Development

PRINCIPAL INVESTIGATOR:
McEntire, B. Joseph, MS
Chancey, V. Carol, PhD
Walilko, Timothy, PhD
Rule, Gregory T, P.E.
Weiss, Gregory
Bass, Cameron, PhD
Jay Shridharani, MS

CONTRACTING ORGANIZATION:

T. R.U.E. Research Foundation
San Antonio, TX 78217

REPORT DATE: September 2010

TYPE OF REPORT: Final Addendum

PREPARED FOR: U.S. Army Medical Research and Materiel Command
Fort Detrick, Maryland 21702-5012

DISTRIBUTION STATEMENT:

- ✓ Approved for public release; distribution unlimited

REPORT DOCUMENTATION PAGE

Form Approved
OMB No. 0704-0188

1. REPORT DATE *(DD-MM-YYYY)*	2. REPORT TYPE	3. DATES COVERED *(From - To)*
01-09-2010	Final Addendum	15 MAY 2008 - 31 Aug 2010

4. TITLE AND SUBTITLE
Helmet Sensor – Transfer Function and Model Development

5a. CONTRACT NUMBER

5b. GRANT NUMBER
W81XWH-08-2-0030

5c. PROGRAM ELEMENT NUMBER

6. AUTHOR(S)
McEntire, B. Joseph, Chancey, V. Carol, Walilko, Timothy, Rule, Gregory, Weiss, Gregory, Bass, Cameron, Shridharani, Jay

5d. PROJECT NUMBER

5e. TASK NUMBER

5f. WORK UNIT NUMBER

7. PERFORMING ORGANIZATION NAME(S) AND ADDRESS(ES)
T. R.U.E. Research Foundation
San Antonio, TX 78217

8. PERFORMING ORGANIZATION REPORT NUMBER

9. SPONSORING / MONITORING AGENCY NAME(S) AND ADDRESS(ES)
US Army Medical Research and Materiel Command
Fort Detrick MD 21702-5012

10. SPONSOR/MONITOR'S ACRONYM(S)

11. SPONSOR/MONITOR'S REPORT NUMBER(S)

12. DISTRIBUTION / AVAILABILITY STATEMENT
Approved for public release, distribution unlimited.

13. SUPPLEMENTARY NOTES

14. ABSTRACT
The Vice Chief of Staff of the Army (VCSA) directed that Soldier combat helmets be fitted with electronic sensor technologies to sense and record helmet response to dynamic events. These events could be exposure to blast events (IEDs), ballistic impacts, and/or blunt impacts. The sensors record orthogonal accelerations and blast overpressure levels. However, since helmets are not rigidly coupled to the head, and are not rigid bodies and often experience local deformations during impact, the measured helmet response will be different from the head response. The objective of this effort is the characterize the differences between helmet and head responses by conducting controlled physical tests; and then use these results to develop appropriate transfer functions (numerical equations or models) that approximate head exposures based on the observed helmet response. The physical testing included ballistic impact and blast overpressure tests. This report provides a description of the tests performed and an assessment of the quality of the data collected for the purpose of validating the transfer function and model.

15. SUBJECT TERMS
Helmet Sensor, Helmet Response, Transfer Function, Blast, Shock Tube, Ballistic Impact, Head Response, Head Injury

16. SECURITY CLASSIFICATION OF:			17. LIMITATION OF ABSTRACT	18. NUMBER OF PAGES	19a. NAME OF RESPONSIBLE PERSON
a. REPORT	b. ABSTRACT	c. THIS PAGE			USAMRMC
U	U	U	UU	239	19b. TELEPHONE NUMBER *(include area code)*

Table of Contents

1. Introduction

The Vice Chief of Staff of the Army (VCSA) directed that Soldier combat helmets be fitted with electronic sensor technologies to sense and record helmet response to dynamic events. These events could be exposure to blast events (IEDs), ballistic impacts, and/or blunt impacts. The sensors record orthogonal accelerations and blast overpressure levels. Collected sensor data could be useful to researchers and materiel developers by increasing the knowledge and understanding of the kinematic and dynamic parameters of operational threats, which would help define appropriate performance requirements for protective equipment.

However, since helmets are not rigidly coupled to the head, and are not rigid bodies and often experience local deformations during impact, the measured helmet response will be different from the head response. The objective of this effort is the characterize the differences between helmet and head responses by conducting controlled physical tests; and then use these results to develop appropriate transfer functions (numerical equations or models) that approximate head exposures based on the observed helmet response. The physical testing included ballistic impact and blast overpressure tests. This data was also used to populate a data signal library of various exposures, needed to investigate the potential to identify unique signal characteristics and patterns which could be indicative of the different exposures. Once a reliable transfer function is obtained, substantial increases in understanding of human tolerance to blast events, ballistic impacts, and/or blunt impacts can be made, leading to safer helmet designs for both military and civilian applications.

In phase one, ARA conducted controlled shock tube tests using an 18” shock tube and an instrumented headform outfitted with an Advanced Combat Helmet (ACH) and both versions of the Helmet Mounted Sensor Systems (HMSS). These systems are the focus of the Phase I shock tube testing, and the overall objective of Phase 1 is to confirm whether the current Generation One HMSS can properly detect and quantify blast exposure to an individual. Secondary to this objective was to collect controlled blast exposure data using laboratory grade sensors to enable the development of the helmet to head blast exposure transfer function and a model to enable prediction of the total blast exposure to the human brain in a given blast event.

In Phases two and three, ARA and Duke University developed helmet to head force transfer functions and a model to predict the head response from helmet mounted sensor data. These models are developed and presented in a this report.

In phase four, ARA and Duke University conducted a series of free-field blast tests using a variety of instrumented headforms and cadaver heads. The goal of these tests was to provide data with which to validate the transfer function and response models developed in phases two and three. This report provides a description of the tests performed and an assessment of the quality of the data collected for the purpose of validating the transfer function and model.

2. Body

2.1. Transfer Function and Numerical Models

The principal objective of this study was the development of a transfer function and numerical model which translates the helmet-mounted sensor response data to a head-centered biomechanical response.

Explosive detonation in the open air produces a shockwave followed by a blast wind. Human injury from these blasts has been studied for many years. Unfortunately this work provides limited insight to the current issues because many of these early studies involve ideal planar blast waves in the far field (i.e., ideal Friedlander waves). The previous work is not directly applicable because when a protected individual is in close proximity to a blast, it is difficult to understand the biodynamic effects of the explosive event. In the near field, blast may not present as a point source, and the pressure waves are not ideal Friedlander waves. This deviation from ideal form may complicate the analysis using existing injury criteria. In a blast environment, the assessment of injuries while wearing protective Soldier equipment should include the major mechanisms of injury expected from the blast and subsequent blunt trauma.

For the current methodology, the emphasis is placed on injury criteria to assess nonfatal injuries. The justification for this approach is the desire to increase understanding of injury mechanisms and human tolerance when exposed to nonfatal (i.e., treatable) blasts, and the implications on protective equipment. As there are potentially different protection mechanisms in different body regions, the current methodology focuses on blast trauma to the head. Further, a momentum exchange timescale of 0.1 to 30 ms is assumed for all high rate blast and blunt impacts. Available test devices and established injury assessment criteria are discussed for their relevance to assess near-field blast injury. Protective helmets typically cite peak acceleration measured in test headforms for assessment of blunt impact performance. The motorcycle helmet industry adopted standards that provide a minimum level of head protection during accidents. Early motorcycle helmet standards established a peak head form acceleration limit of 400G as the pass-fail criteria. The 400G threshold is considered to be the limit for serious head and brain injury. Interpretation of this requirement is that any helmet tests producing head form accelerations greater than 400G fails.

This acceleration threshold was based on cadaver head impact research results conducted by Wayne State University. The result of this research was a head acceleration tolerance curve (Figure 2.1-1), which suggested an acceleration and time dependency relationship. Basically, the greater the acceleration level experienced by the head, the shorter the time duration that can be tolerated before injury. The FMVSS 218 incorporates time dependency into their standard. The US Army has established more rigorous standards based on reconstructions of concussive accidents: 175G peak headform acceleration for aviation helmets and 150G as the mean headform acceleration for combat helmets.

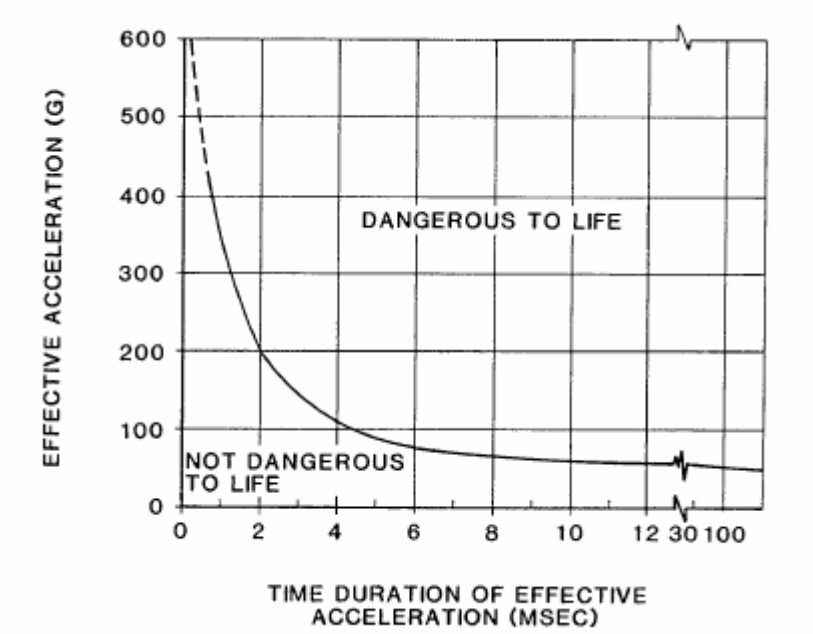

Figure 2.1-1. Wayne State tolerance curve for the human brain in forehead impacts against plane, unyielding surfaces.

As shown in blast epidemiology data, head injuries are very significant, often from tertiary blast. These injuries may be caused by direct blast impingement on the head or by blunt trauma from impingement of the protective gear. One injury criterion commonly used with the Hybrid III dummy head/neck complex is the Head Impact Criterion (HIC) for concussive head injury based on the Wayne State Concussive Tolerance Curve. HIC includes the effect of acceleration time history $a(t)$ and the duration of the acceleration. For low rate impacts, a HIC value of 1000 is often specified as the level for onset of severe head injury. The maximum time duration of HIC is limited to a specific value, usually 0.015 s. HIC is evaluated using a head tri-axial accelerometer at the head center of gravity. This standard is often used to assess head injury using Hybrid III dummies in frontal impacts. However, HIC is based on human cadaver and animal impact data with durations that are usually five milliseconds or greater, with only limited data available for shorter durations. The acceleration effects of near field blasts are often shorter than five milliseconds, raising questions about the applicability of the usual injury criteria to high rate blast head trauma. However, relatively heavier equipment such as an EOD suit give different HIC values when evaluated with Hybrid II and Hybrid III dummies.

Under this effort, the first iteration of developing the helmet/head transfer function focused on simplified input parameters from the test data, including peak helmet acceleration data in all three directions, and peak helmet angular rate data. However, initial evaluation of the collected helmet sensor data indicated that its quality (from both models) was insufficient in the areas of signal quality and frequency to build a transfer function. Additionally, though the research team found that the signals collected, if the data was of sufficient quality, may be able to be used to differentiate among spurious and meaningful loading information; differentiate among different types of insults to the head; and develop transformation functions to convert the signal traces into

clinically meaningful information, these relationships were not linear and thus not conducive to a simple linear transfer function.

The signal data was evaluated to determine if discrimination of impact direction can be determined along with the error ranges. However, due to the helmet response during the ballistic testing, it was apparent that the signals could not be used to assess ballistic impacts without significant accounting for the material properties of the helmet and surrogate head. The resonant frequency response significantly interfered with the acceleration signals. The traces were analyzed based on the shock tube tests, and validated against the free field blast tests, to determine their utility input excitation function to a model in order to approximate the human biomechanical response to the external loadings.

For both the lumped sum parameter transfer function and the helmet to head finite element model (FEM), the signal data from the laboratory sensors was not sufficient to provide a validated prediction against the free field data. The complex, nonlinear nature of the helmet response, compounded by the dynamic resonance of the helmet and the FOCUS headform confounded the signal inputs. However, based on the collected data, the initial development of both models is complete, and the team has identified the requirements to complete the development of an engineering level (lumped sum parameter) helmet to head transfer function that would effectively predict human biomechanical response, and an integrated helmet to head FEM that would provide injury predictions.

The predicted human biomechanical response along with validated injury criteria for primary blast can provide an assessment of possible injury. With this information, soldiers will be able to receive the appropriate treatment and have a reduced risk of repeated injuries or long term consequences.

2.1.1. Data for transfer function development

In developing the helmet to head transfer functions, only the laboratory sensor data was used to train the models. This decision was based on two facts: (1) the Generation 1 Helmet Mounted Sensors (HMS) are already considered obsolete and will be replaced by the Generation 2 sensors within the next 12-24 months; and (2) the laboratory sensors have enhanced frequency response relative to the commercially available helmet sensors and are capable of measuring the event at a very high sample rate. Further discussion of the HMS is in Section 2.2.

The data collected from the shock tube tests in Phase 1 was used for this transfer function and validated against the free field blast data from Phase 4. The ballistic impact data was not used in building the transfer function for reasons that will be described in Section 2.3.2.4.

The laboratory sensors used consisted of pressure transducers in the shock tube, on the helmet, and on the head to insure repeatability of the input conditions. The dynamic response of the helmet was measured using two 4-axis accelerometer arrays located at locations close to the HMSS. Each array had 3 linear orthogonal accelerometers and one angular rate sensor oriented in the direction of the blast wave. Headform response was measured using another 4-axis accelerometer array placed at the CG of the FOCUS and the approximate CG of the PMHS.

The acceleration data was analyzed to determine the peak resultant acceleration for the simple linear model, and the time histories were used in the lumped parameter and finite element models. The goal of the simple linear model was to provide a predictor of the peak head acceleration, while the lumped parameter and finite element models should predict the acceleration time history. The transfer function must be able to predict the center of gravity acceleration and global movement of the human head based on the sensor traces collected on the helmet.

From the data for all orientations, blast conditions, and both headforms (Figure 2.1.1-1), there is a weak trend. Much of the variance appears to be PMHS response of the head in the frontal condition that is not reflected in FOCUS response.

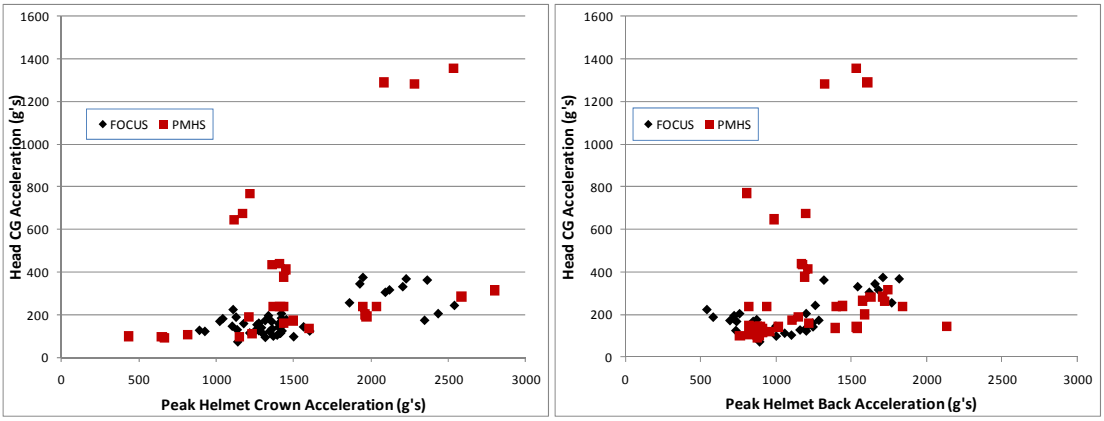

(a) **(b)**

Figure 2.1.1-1. Peak Head vs helmet acceleration measured at the (a) crown and (b) back of the helmet.

2.1.2. Simple Transfer Function

Statistical significance and trends were evaluated using a general linear model (GLM). This method allowed for the analysis of variance in test datasets, and assessment of variation of both categorical and continuous variables. This model also supported identification of unbalanced experimental design, and of general interactions between variables. Variables are shown in **Error! Reference source not found.***2.1.2 – 1*, and the model form is

$$\text{Acceleration} = \text{Constant} + \boldsymbol{\beta}_1 \times \text{Variable}_1 + \boldsymbol{\beta}_2 \times \text{Variable}_2 + \ldots + \text{Higher Order Terms} \quad (1)$$

Table 2.1.2 – 1
Variables for the General Linear Model.

Categorical Variables	
Surrogate	FOCUS Dummy, Cadaver
Orientation	Front, Side, Rear
Continuous Variable	
Helmet Acceleration (Rear and crown)	Peak resultant and time histories
Response Variable	
Head Acceleration	Peak resultant and time histories

The GLM was normalized such that negative coefficients lower the response compared to the average – generally a positive outcome. For example, if an orientation showed statistically significant lower headform acceleration, the coefficient generated by the general linear model for that parameter would be negative. Note that the model coefficients for each categorical variable sum to zero since the effect of the mean is included in the constant term for the model. In addition, linear models were developed to predict the relationship between helmet acceleration and headform acceleration.

2.1.2.1. Development Methodology

The model was developed using shock tube data due to the large number of tests conducted, and has statistically significant coefficients. It is known that shock tubes can simulate the blast overpressure waves generated in explosive blasts, and a shock tube is significantly less expensive to operate. The ultimate goal was to determine if helmet acceleration could be used to predict the headform acceleration. In addition, the general linear model was used to determine the other variables of interest.

The ballistic impacts were not used in the linear transfer function development due to the large variability. Ballistic impacts are very localized in their energy transmission, so the headform reacts primarily due to backface deformation in the helmets directly hitting the headform. This deformation is dependent on the projectile used, the velocity of the projectile, the angle of impact, and the location on the helmet impacted. However, the laboratory grade sensors mounted to the outside surface of the helmet will read a significant response for any impact. Therefore, it is very difficult to generate an accurate model with the limited number of ballistic impacts conducted in this test series. In addition, the HMSS-B only recorded data for 5 of 18 ballistic impacts.

2.1.2.2. Shock tube data

In total, ARA completed 100 shock tube tests with the FOCUS headform, which includes preparatory tests and several repeat tests. ARA completed the required tests at 15 psi incident pressure and 1 msec duration, 15 psi and 3 msec, and 30 psi and 1 msec. All data from laboratory sensors and the HMSS were downloaded and collected following each shock test. All data from the laboratory sensors was processed and uploaded to the ftp server.

At Duke, the helmets were tested in multiple configurations to determine the effects of dummy versus cadaver, helmet orientation, and input conditions –similar to the ARA shock tube tests. For the three test conditions, Duke completed 52 cadaver tests and 58 FOCUS tests. A thorough discussion of the shock tube tests, test matrices, and data is in Section 2.3.1.

2.1.2.2.1. FOCUS Headform Response

Linear regression models (Figure 2.1.2.2.1 - 1) were developed to correlate the response of the headform to an incident overpressure. The incident overpressure was measured at 3 locations evenly distributed around the circumference of the shock tube ¼" from the end of the tube. The peak pressures at each location were averaged and used to predict the peak resultant acceleration for the headform. As expected, the model shows an increase in the head CG acceleration for increasing incident overpressure. The model depends on the incident overpressure as seen by the high correlation coefficients and on the location of the impact since the points fall on different lines. It appears the headform responds similarly for front and rear impacts for the FOCUS tests.

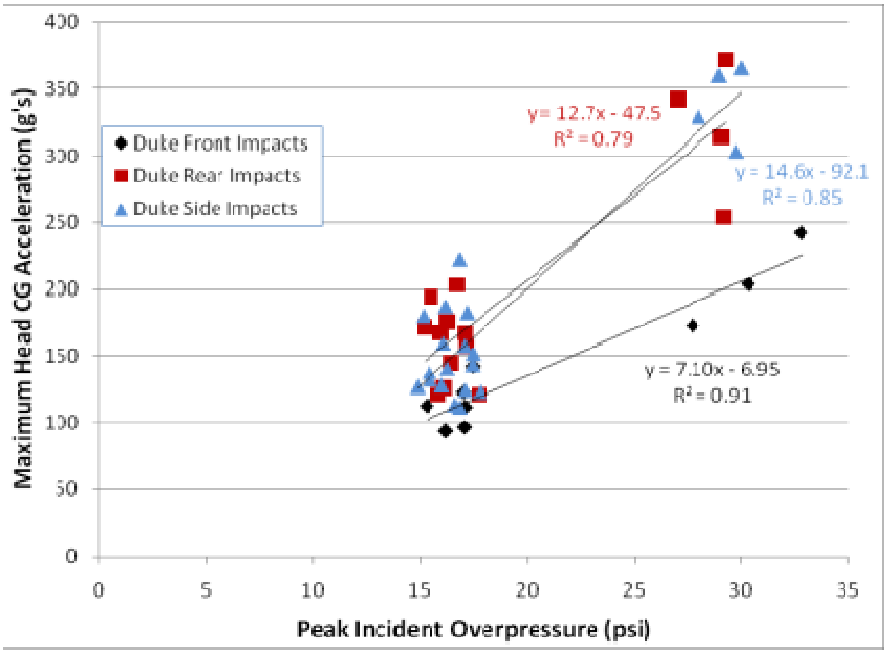

Figure 2.1.2.2.1 – 1. Dynamic response of the FOCUS head CG for varying blast levels.

2.1.2.2.2. PMHS Headform Response

The same analysis is shown for the PMHS headform in Figure 2.1.2.2.2 - 1. Similar to the results seen with the FOCUS headform, an increase in pressure results in an increase in head CG acceleration. For the PMHS, the side and rear impacts appear to have similar responses. In contrast, the linear coefficient for response for the front impact is substantially larger than for the side or rear orientations. The substantial difference between the frontal response for the PMHS and the FOCUS headform is likely the differences in response of the surrogates themselves under direct shock application. Side and rear orientation helmet coverage has approximately 50% larger projected area, so helmet transmission is similar between the two headforms. It is also

possible the front response is different due to instrumentation techniques, although this has not been confirmed.

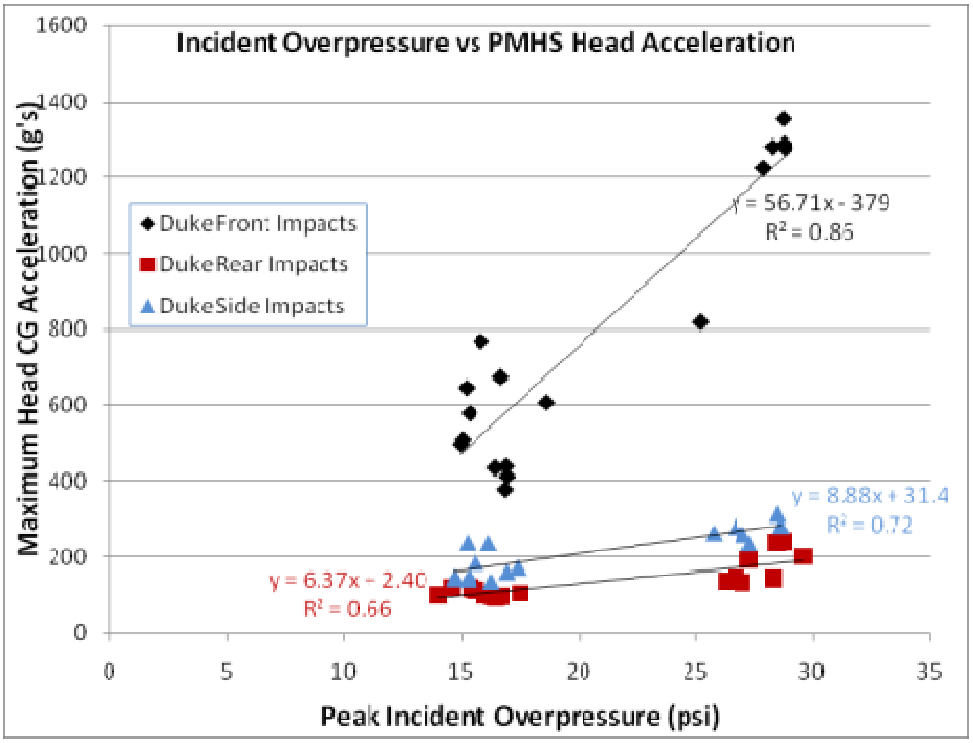

Figure 2.1.2.2.2 – 1. Dynamic response of the PMHS head CG for varying blast levels.

2.1.2.2.3. Laboratory Sensor Response to Incident Overpressure

Biofidelity of mounted helmet response may be assessed using helmet response when fitted on a PMHS and FOCUS. For each blast condition, the response of the helmet (Figure 2.1.2.2.3 - 1) using the laboratory sensors is similar between the FOCUS and the PMHS except for side impacts for the 15psi @ 1ms tests. This suggests two things: (1) the FOCUS may be an acceptable platform for evaluating helmet response alone and (2) the loose coupling between the helmet and the head causes the helmet response to be independent of the surrogate used.

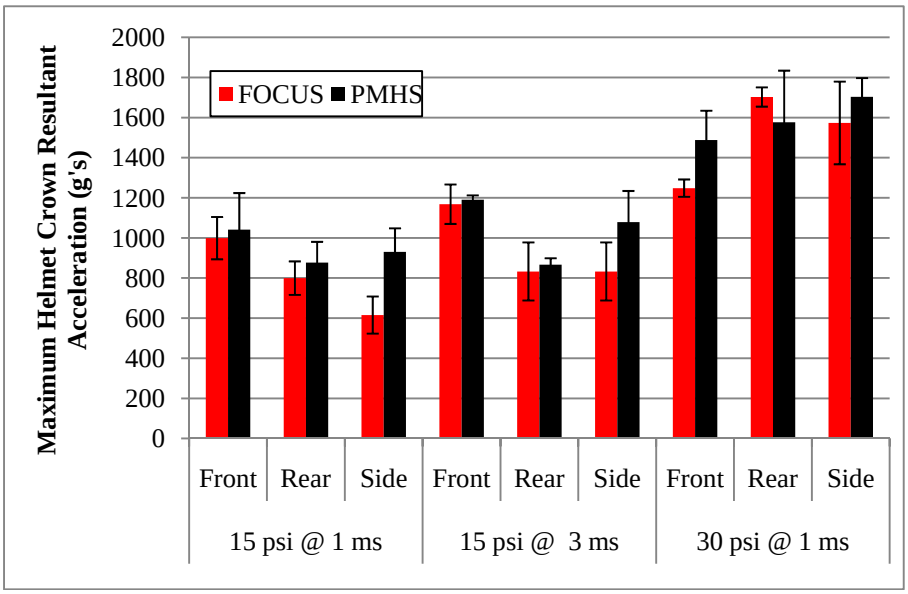

Figure 2.1.2.2.3 - 1. Maximum helmet crown acceleration for the various blast and headform configurations.

2.1.2.2.4. Head versus helmet laboratory sensor response

The ultimate goal of this study is to assess the potential for the development of transfer functions relating the helmet response to a soldier's head response. The first stage of a transfer function is the development of a simple model relating helmet response to head response. For this assessment, the laboratory sensors are used to validate the helmet sensors since they have enhanced frequency response relative to the commercially available helmet sensors and are capable of measuring the event at a very high sample rate. From the data for all orientations, blast conditions, and both headforms (Figure 2.1.2.2.4 – 1), there is a weak trend. Much of the variance appears to be PMHS response in the frontal condition that is not reflected in FOCUS response. The general linear model will be discussed below.

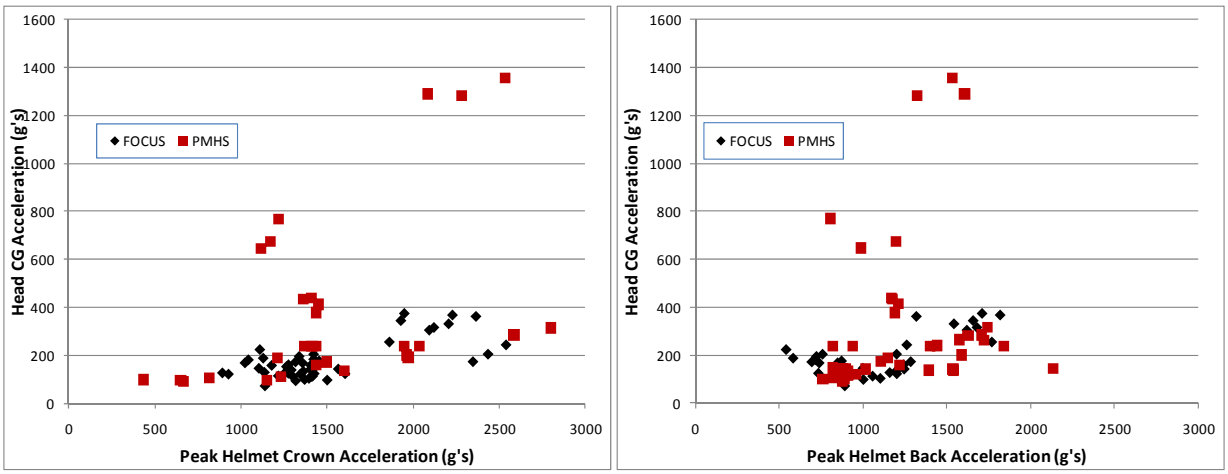

(a) (b)

Figure 2.1.2.2.4 – 1. Head versus helmet acceleration measured at the (a) crown and (b) helmet back.

2.1.2.2.5. PMHS Helmet/Head Laboratory Sensor Response

The PMHS is used as an anatomical surrogate providing the closest laboratory system to that expected to be seen in the field by a soldier. Thus, it is the standard to which the FOCUS headform will be judged. All orientation impacts on the PMHS headform using the accelerometer array with laboratory sensors located at the crown of the helmet is shown in Figure 2.1.2.2.5 – 1. As expected, an increase in helmet acceleration is correlated with an increase in helmet acceleration. Note that the rear and side impact results appear to follow similar trends, however the front tests appear have a different trend. This is likely due to the area of protection the helmet provides in these orientations. The front of the helmet has less area of coverage since it must allow the solider visibility. Owing to this effect, the blast wave is less attenuated and the head sees a larger direct acceleration in the frontal direction.

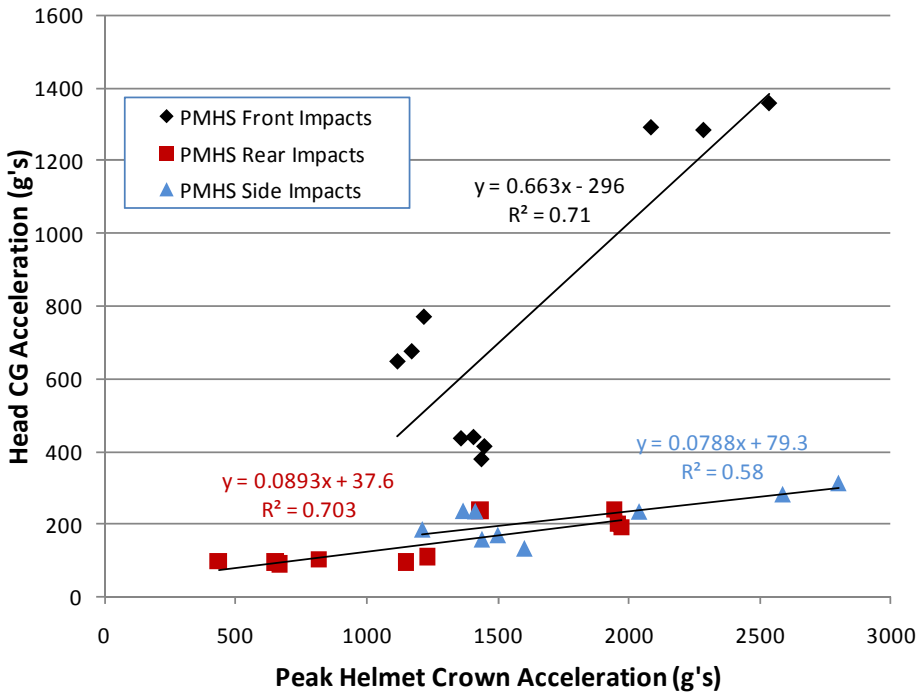

Figure 2.1.2.2.5 – 1. PMHS head acceleration versus helmet crown acceleration.

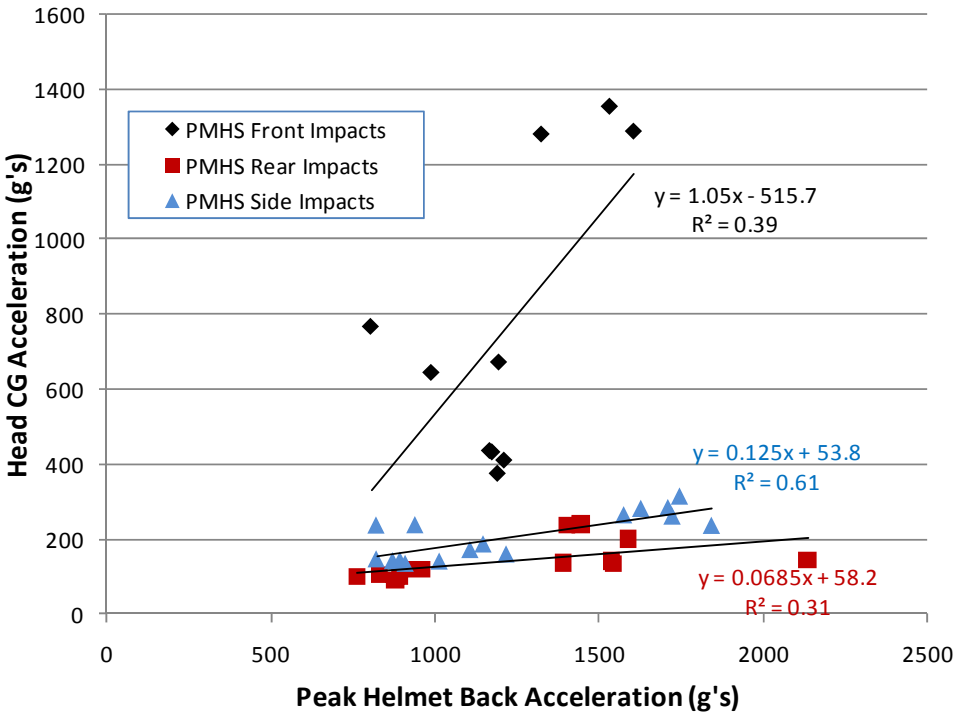

Figure 2.1.2.2.5 – 2. PMHS head acceleration versus helmet rear acceleration.

2.1.2.2.6. FOCUS Head/Helmet Laboratory Sensor Response

The FOCUS headform was used to determine if a mechanical surrogate could be used to replacement for a human cadaver. The FOCUS has good experimental spread (Figure 2.1.2.2.6 – 1), within the 5% uncertainty of the accelerometers. It appears each orientation has a linear relationship between the peak helmet acceleration and the peak acceleration seen at the headform center of gravity. Also, the 15psi 1ms tests are not statistically significantly different from the 15psi 3ms tests ($p = 0.3151$, $\alpha = 0.05$). Similar to the PMHS, the rear and side tests statistically have the same response ($p = 0.364$, $\alpha = 0.05$). However, front impacts have a statistically different response from side and rear impacts ($p < 0.01$, $\alpha = 0.05$).

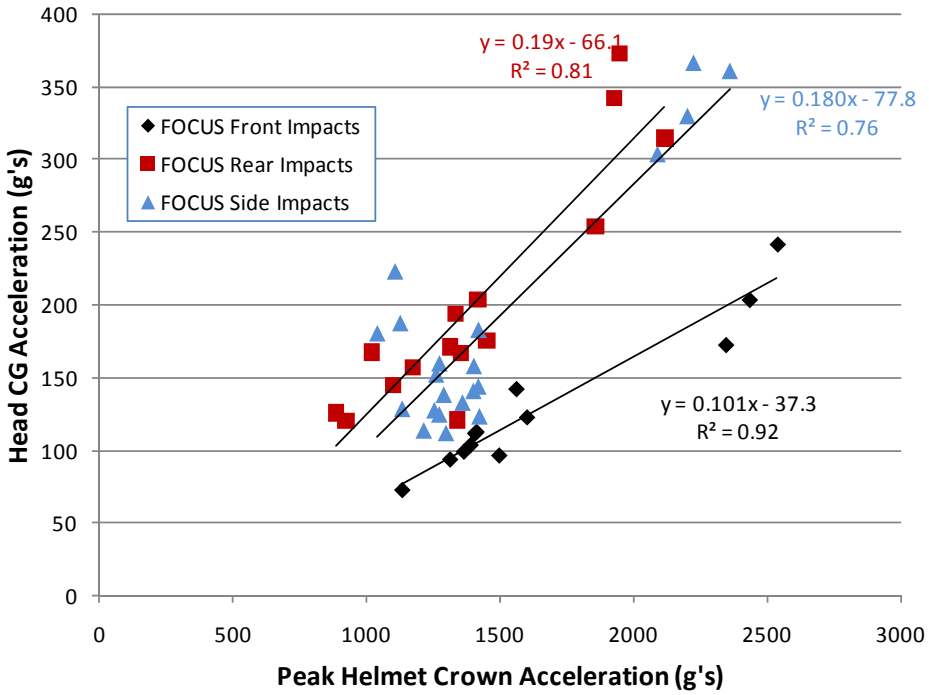

Figure 2.1.2.2.6 – 1. FOCUS head acceleration versus helmet crown acceleration

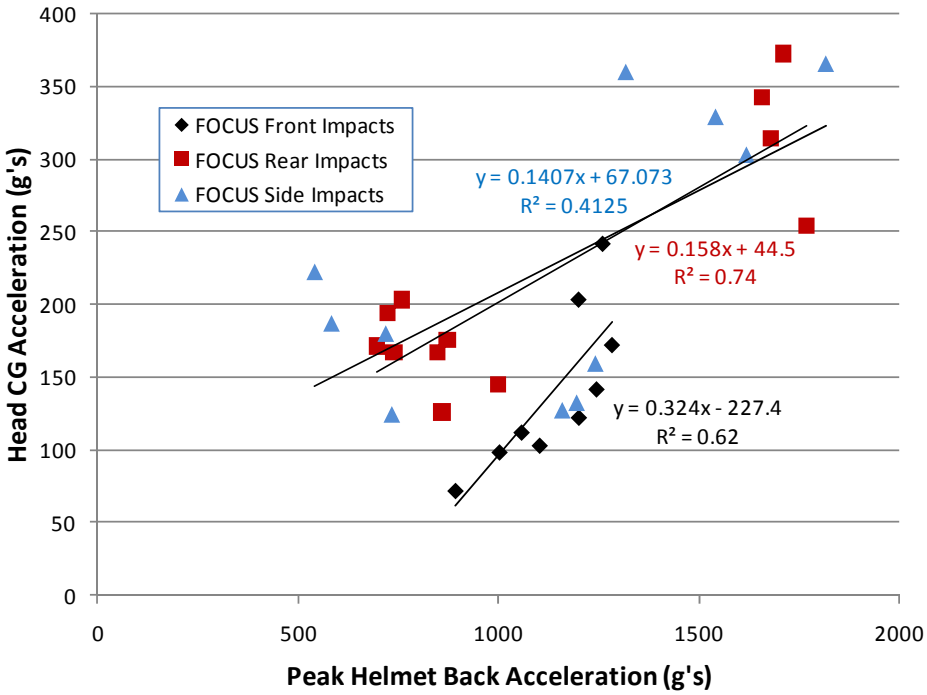

Figure 2.1.2.2.6 – 2. FOCUS head acceleration versus helmet back acceleration

2.1.2.3. General Linear Model for Helmet to Head Response

General linear model results allow the investigation of the relative effect of test variables. For the current linear model, each model coefficient for categorical variables may be directly compared, and the model coefficient for the peak helmet acceleration has been normalized by the mean acceleration to compare it with the categorical variables. Lower coefficients in this model imply lower peak acceleration values. The general linear model statistical results of Phase 1 and the effects of the surrogate and orientation are shown in Figure 2.1.2.3 – 1, and the model coefficients are reported in Table 2.1.2.3 – 1. All the coefficients shown were statistically significantly different save the coefficients for the constant and the rear orientation and the total R^2 of the model was 43%. Note that the coefficient for the helmet acceleration peak has been multiplied by the mean helmet peak resultant acceleration (1620 g) to allow comparison with the categorical variables in Figure 2.1.2.3 – 1. As an example, to use the linear model to predict response for a cadaver specimen in the frontal orientation, one would select cadaver by multiplying the GLM coefficient by 1 and select the frontal orientation by multiplying the frontal GLM coefficient by 1, multiply the measured crown acceleration by the GLM coefficient for the crown acceleration, multiply all other coefficients by zero (not present) and sum to produce the predicted head acceleration.

The relative importance of each of the GLM coefficients may be assessed by comparing the coefficients. As anticipated, the helmet acceleration from the laboratory crown sensor was the strongest correlate with the head acceleration. The average response in frontal orientation is about 150-200g greater than that for the side or rear orientations, and the cadaver response is

greater than dummy response. The difference in headform response may be attributed to the effect of the frontal response seen in Figure 2.1.2.3 – 1.

Table 2.1.2.3 – 1
General Linear Model Coefficients

Variable		**GLM Coeff.**	**p**
Constant		-5.8±76 g	0.94
Crown Res. Accel		0.198±0.048 (319±78 g)	<0.001
Surrogate	Cadaver	85±23 g	<0.001
	Dummy	-85±23 g	<0.001
Orientation	Front	124±34 g	<0.001
	Rear	-53±32 g	0.105
	Side	-72±33 g	<0.001

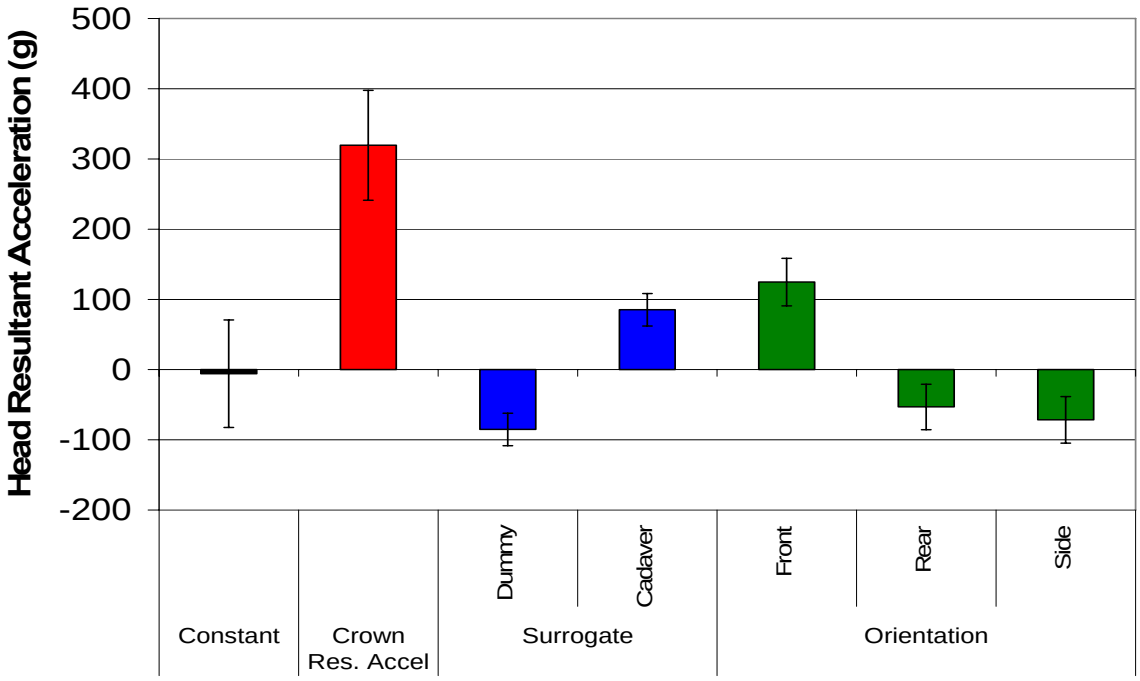

Figure 2.1.2.3 – 1. General Linear Model coefficients versus head resultant acceleration response.

2.1.2.4. Validation Results

The above models were validated using freefield data generated using C-4 at similar overpressure and duration levels to the 15psi @ 3ms and 30psi @ 1ms. These tests were conducted for the FOCUS and PMHS oriented in the front condition. The model predictions are shown in Figure 2.1.2.4 – 1 in which Linear Model 1 is based on the crown accelerometer array and Linear Model 2 is based on the rear accelerometer array.

The results show a severe under prediction of the headform acceleration based on the helmet acceleration. It is unlikely a linear model would be sufficient to model the momentum transfer of a nonlinear shock wave through a helmet, through viscoelastic pads, and into the head. However, this model does account for a portion of the headform acceleration.

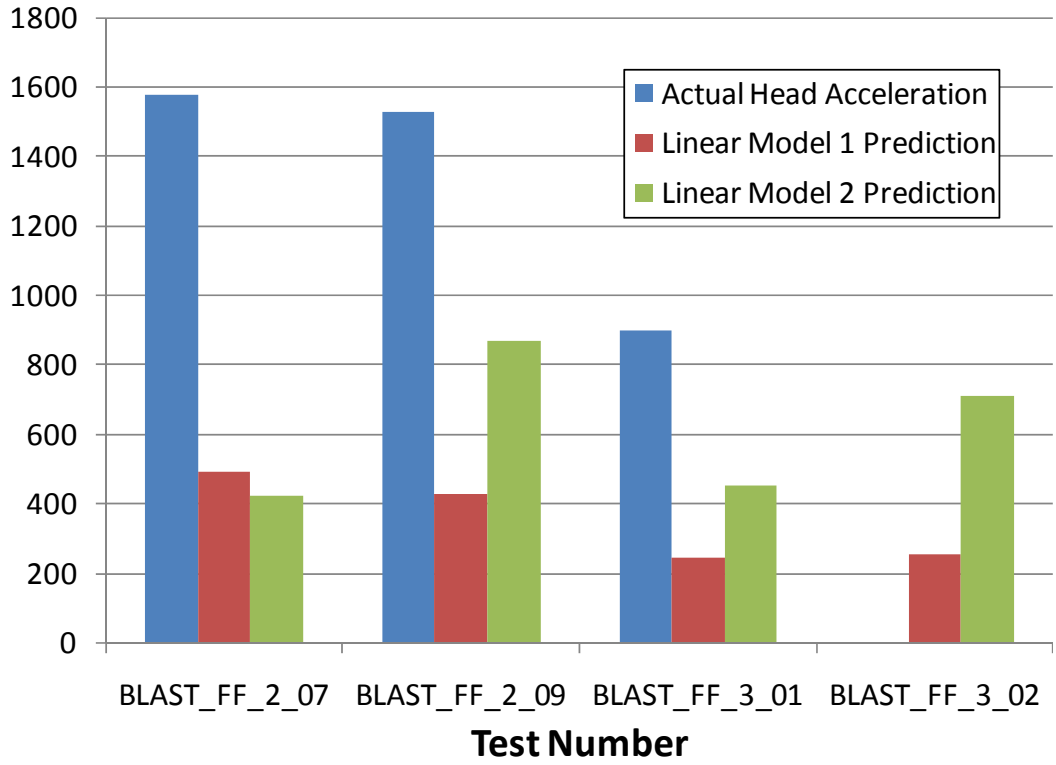

Figure 2.1.2.4 – 1. Prediction from the linear models on the validation data.

2.1.3. Lumped Sum Parameter Model

2.1.3.1. Description of the Model

The lumped-parameter model is a simple physics-based model that estimates the motion of a human head wearing an advanced combat helmet (ACH). The helmet motion, caused by blast wave or impact, is characterized by an accelerometer package mounted to the helmet and is the input to the model. Helmet movement causes head movement through the padding stresses, which are a function of strain, strain rate, and temperature. The model predictions of head movement are compared to data acquired from shock tube tests, where simulated blast waves impacted a helmeted headform.

The helmet-head model is written as a script in Matlab. It reads the Nicolet time domain files (*.wft) recorded by the data acquisition system. In some cases the sensor calibrations were revised after the data was recorded. These corrected data files were converted to comma-separated variables (*.csv) text files. The script contains the names and path of the input files. A separate version of the script was saved for each test.

2.1.3.2. Assumptions

The lumped-parameter model treats the helmet shell as a rigid body whose motion is measured by a tri-axial accelerometer cube mounted to the helmet. Acceleration is integrated to yield velocity change, and double-integrated to provide position change. Actual helmet motion results from forces caused by the blast or impact, and the reactionary padding and strap forces. Some of these forces are unknown (the reactionary padding and strap forces) since helmet motion is measured through the accelerometers and the helmet mass is not a part of the model.

The lumped-parameter model assumes the helmet translates without rotation. During the shock tube tests, used to refine and evaluate the model, one angular rate sensor was mounted on the helmet. But the data quality was poor, precluding its use as a model input. High-speed videos taken during the tests showed no significant rotation during the period when significant head accelerations, which usually lasted less than 10 ms.

Head acceleration is calculated from pad forces, and does not consider neck response forces, air pressures acting directly on the head, or strap forces. Omitting neck and strap forces permits the helmet and head to become separated vertically in the model. The model is only valid for the initial impact between helmet and head. Additional assumptions used in the model development are shown in Table 2.1.3.2-1 along with the technical basis and anticipated effects.

Table 2.1.3.2-1.
Helmet/Head Lumped-Parameter Model Assumptions.

Assumption	Basis	Effect
Rigid helmet and head	No measurement method.	Unknown, but expected to be small, except for ballistic impact.
No rotation of helmet or head	Available sensors are insufficient; high-speed video shows validity.	Small for initial impact. May be import for blunt impact.
No air pressure	Difficult or impossible to measure in a field-able unit.	Depends on the orientation, but may be important.
No neck response	Neck load cell could be used, but not in a field-able unit.	In some cases reaction is seen in the Z direction, which is stiffer than the lateral directions.
No strap forces	Difficult or impossible to measure in a field-able unit.	Small, except when the head is tilted away from blast.
Frictionless pads	No measurement method	Unknown
All pads are initially free of strain, with no gap to the head	Initial strains would vary for different head sizes and shapes.	Unknown

2.1.3.3. Advanced Combat Helmet (ACH)

The model considered ACH helmets with Team Wendy padding in the standard configuration, as shown in Figure 2.1.3.3-1. The standard padding configuration contains seven pads: two trapezoidal pads at the front and rear, four oblong pads placed on each side of the trapezoidal pads, and one crown pad. The helmet geometry controls the orientation of each pad. Pads are assumed to be frictionless, so that padding forces act normal to the surface.

The padding area and orientations were measured and included in the model. The pad areas are shown in Table 2.1.3.3-1. The foam pads were cut open and found to have a dual density: a lower density on the side in contact with the head and a higher density on the side in contact with the helmet. The pads are enclosed in plastic that prevents moisture intrusion and are then covered with fabric to provide comfort to the wearer and holds the pads to the Velcro tabs inside the helmet. The plastic enclosure also prevents air from escaping the padding and thus may increase the padding stiffness.

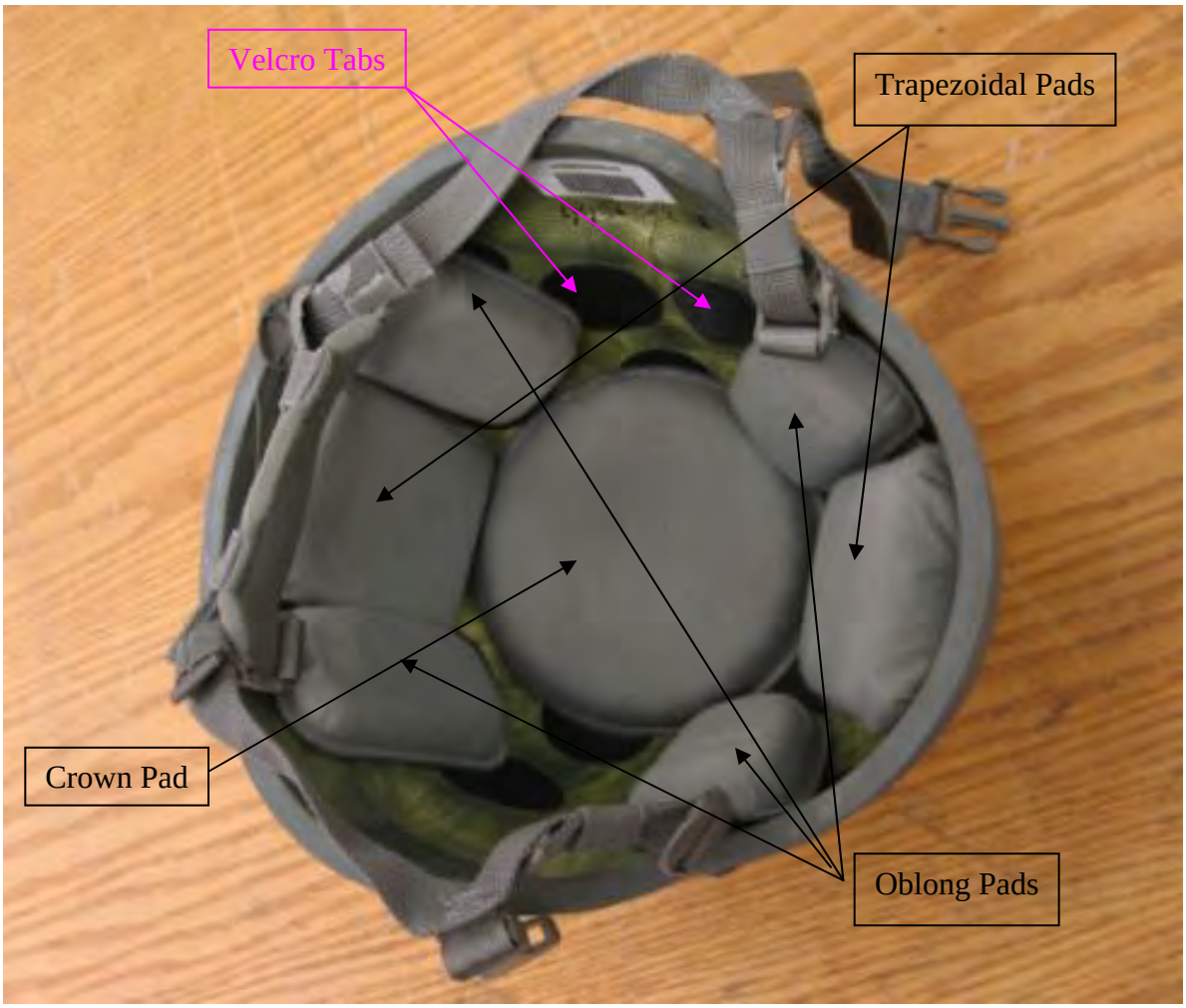

Figure 2.1.3.3-1. ACH helmet with padding.

Table 2.1.3.3-1.
Padding size and weight.

Pad Type	Area, $inch^2$	Thickness, inch	Mass lbm	Density lbm/ft^3
Crown	19.6	3/4	0.0345	4.05
Trapezoidal	10.1	3/4	0.0175	3.98
oblong	6.3	3/4	0.0110	4.00
			Average	4.01

2.1.3.4. Padding Response

The dynamic response of the foam padding was taken from an SAE Technical Paper authored by C. C. Chou et. al. [18]. Chou provides equations to calculate stress in polyurethane foams as a function of strain, strain rate, temperature, and initial density. Chou measured stress vs. strain at four rates, three temperatures, and three densities; and then formulated polynomial equations to interpolate between the measurements. The basic stress-strain response of foam with a single density is shown in Figure 2.1.3.4-1. Chou characterizes the response with a 7th order polynomial for the quasi-static compression. Since the helmet-padding foam had two different densities, the shape of the stress-strain curve would be substantially different. The model used the 7th order polynomial provided by Chou, with a low foam density representative of the softer material. This is a reasonable approach for strains less than about 40%, but is inaccurate at higher strains.

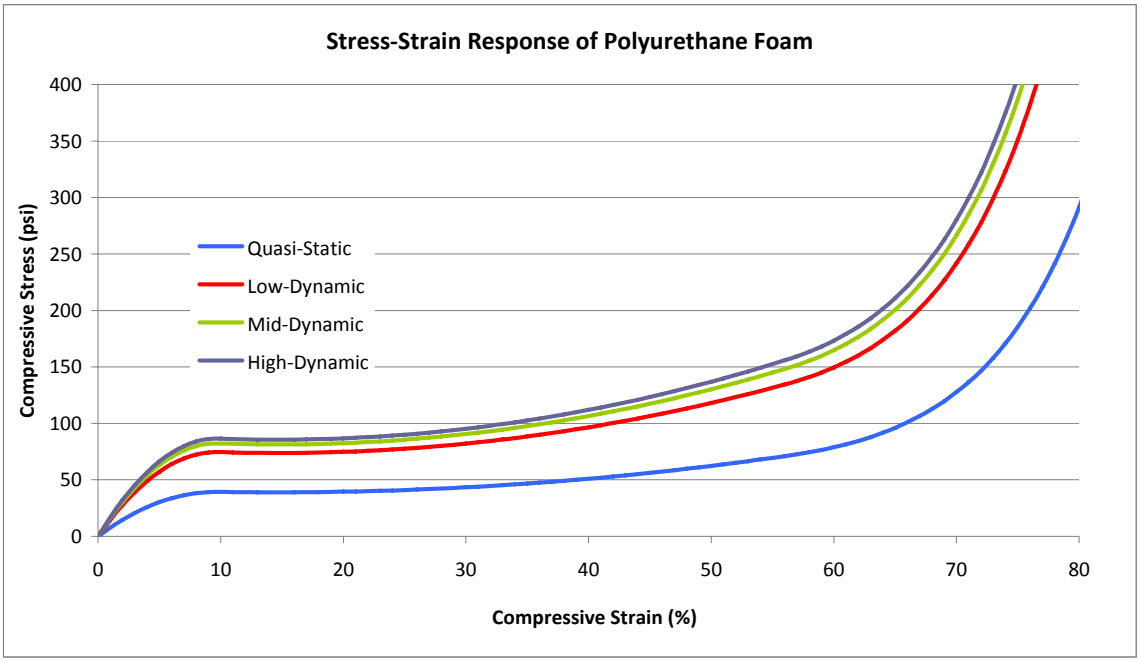

Figure 2.1.3.4-1. Stress-Strain response of polyurethane foam (taken from Chou et. al.).

The dynamic stress is calculated by multiplying the 7th order polynomial for quasi-static strain by a rate/temperature function, and a density function:

$$\sigma = H \cdot G \cdot f$$

where:

H = rate/temperature function,
G = density function, and
f = quasi-static stress-strain function.

The rate function was generated by fitting a 3rd order polynomial to stress measured at four different rates, shown in Figure 2.1.3.4-1. The 3rd order polynomial fits the four measured data points exactly, and works well for interpolating between them. Early versions of the lumped parameter model showed that the strain rates were much higher than those measured by Chou (whose maximum rate was 110%/sec), and the extrapolated rate function became huge. Therefore, an alternative rate function was sought that would be flatter at high rates, reflecting the trend of the measured data shown in Figure 2.1.3.4-2, instead of the polynomial that became very large at high strain rates. A logarithmic curve, also shown in Figure 2.1.3.4-2, was used instead in the model. Although this extrapolation is more in line with the trend of the data, this is still a huge extrapolation, as strain rates were on the order of 10,000%/sec and higher.

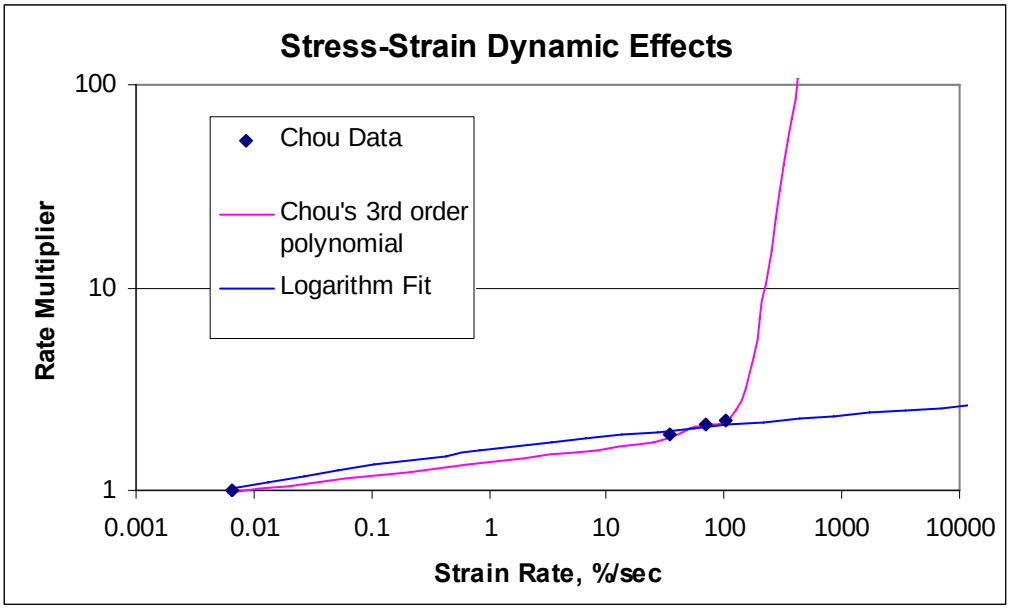

Figure 2.1.3.4-2. Dynamic effects of stress-strain in foam padding.

None of Chou's experimental data was for negative strain rates, and the logarithmic function cannot be calculated for a negative strain rate. At these high strain rates it was assumed that negative strain rates would cause the head to become separated from the pad, and no force would be present.

The model assumes all pads are initially at zero strain, and just in contact with the head. The precise geometry of the head surrogate in the helmet may cause some pads to be initially

strained, or there may be a gap between the head and the pad. These uncertainties are not accounted for in the model, and they would vary with individual head sizes/shapes.

The padding density used in the model was adjusted to match the predicted head response to the measured data in shock tube tests with rear impact and tilted 30˚ into the blast. Higher padding densities caused higher head accelerations with shorter durations. A density of 3.0 lbm/ft^3 was chosen to approximate the lower-density portion of the foam. For comparison, the average foam density shown in Table 5 was 4.0 lbm/ft^3.

2.1.3.5. Shock Tube Test Data

Shock tube tests were performed in April – June, 2010 at Applied Research Associates' Rocky Mountain Division in Littleton, Colorado. The shock tube is made from 18-in diameter pipe and the driver gas was air. Aluminum membranes between the driver and the shock tube establish a shock pressure, and the length of the driver section can be adjusted to control the duration of the pressure pulse. Tests were done with incident peak pressures of 15 and 30 psi, and durations of 1 and 3 ms. These tests were described previously in a separate report. The shock tube is shown in Figure 2.1.3.5-1. During shock tube testing the helmets also included two helmet-mounted sensor systems (HMSS). The HMSS were recorded but their data was not used in this model.

Figure 2.1.3.5-1. 18-inch diameter shock tube.

2.1.3.6. Results

Results were consistent for tests of the same orientation, pressure and duration, so only one condition is illustrated.

2.1.3.6.1. Rear Impact, Tilted 30˚ Toward the Blast.

This orientation is presented first because the blast has the least amount of area acting directly upon the head, and the straps will have little to no effect during the time period of

interest. Predicted head accelerations are compared to the measured accelerations. Measured accelerations were low-pass filtered at 1650 Hz, as they are for HIC calculations.

Figure 2.1.3.6.1-1 compares head accelerations and velocities predicted by the model to the measured accelerations and velocities. Figure 2.1.3.6.1-2 shows the padding strains, forces, and strain rates. The pad forces drop to zero at about 5ms, where the strain rates go negative. Comparison of accelerations in Figure 2.1.3.6.1-1 shows higher-frequency components in the measured accelerations than are present in the model estimates. To evaluate accelerations averaged over the impact period, a similar comparison of velocities shown in lower plot of Figure 2.1.3.6.1-1. The predicted velocity in the Z direction is somewhat higher than what was measured. After the initial impact the Z velocity drops toward zero, probably due to neck response. In the X direction the correlation is not as good. The X velocity is significantly underestimated by model, compared to the measured velocity. The Y axis is an axis of symmetry, so response in this direction was expected to be small.

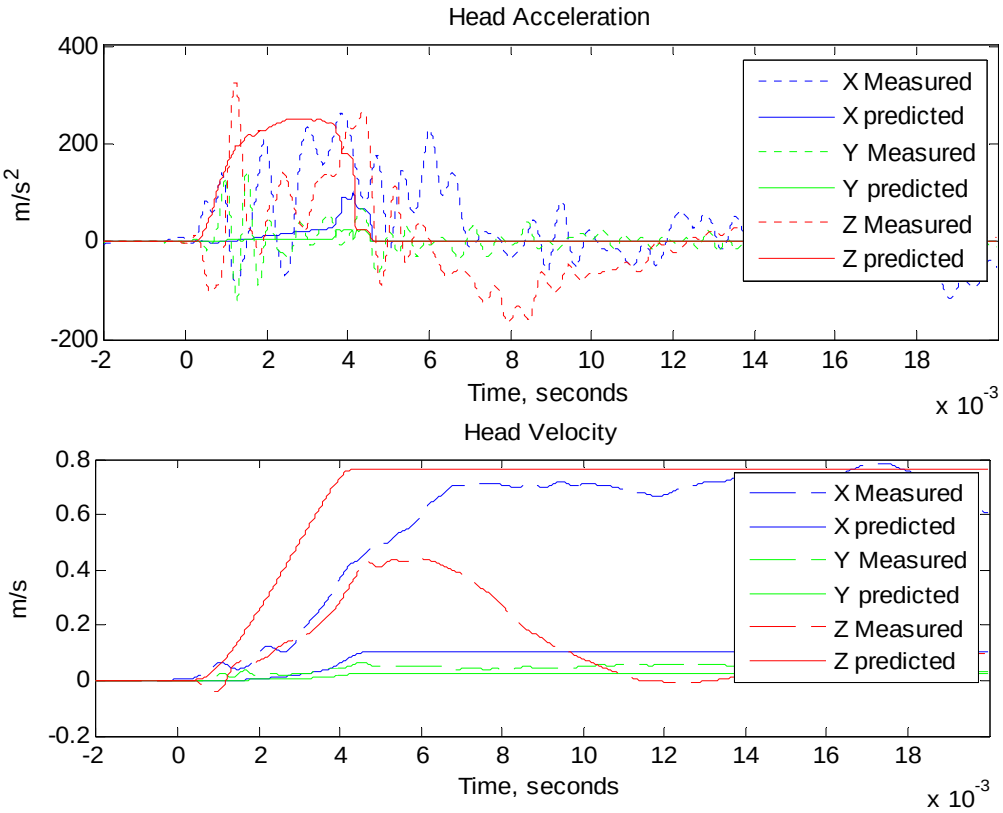

Figure 2.1.3.6.1-1. Head accelerations and velocities predicted by the model compared to measured head accelerations. From Test 24: Rear orientation, tilted 30˚ toward the blast 15 psi incident pressure, 1 ms duration.

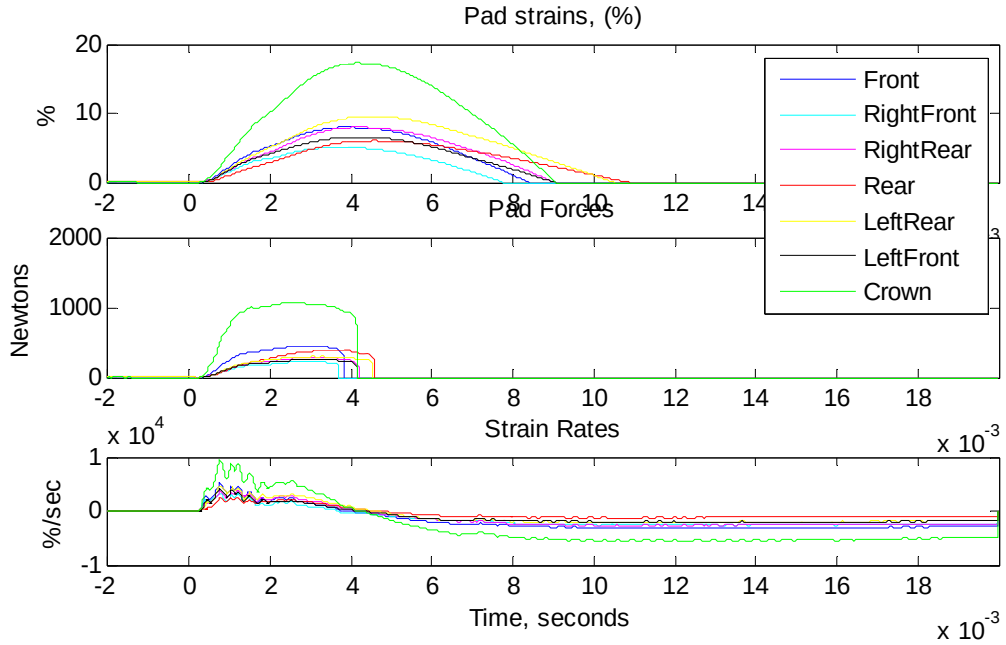

Figure 2.1.3.6.1-2. Model prediction of helmet pad strains and forces for Test 24.

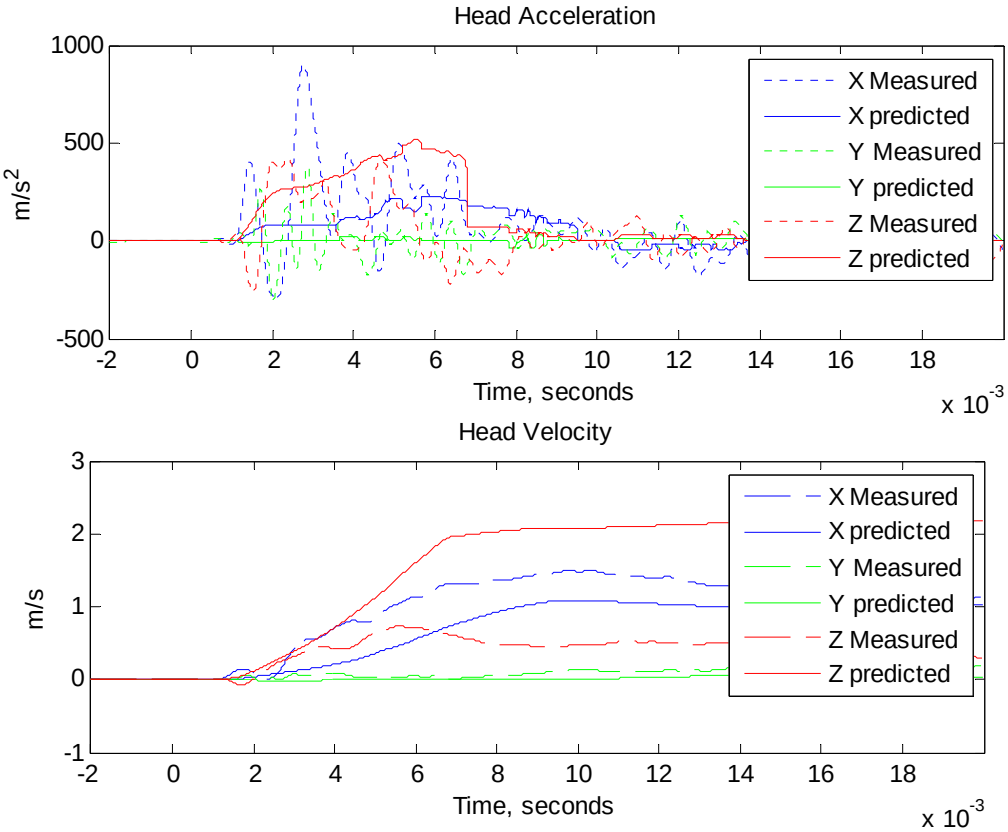

Figure 2.1.3.6.1-3. Head accelerations and velocities from Test 58: Rear orientation, tilted 30˚ toward the blast 15 psi incident pressure, 3 ms duration.

The results for 15 psi incident pressure and 3 ms duration are shown in Figures 2.1.3.6.1-3 and 2.1.3.6.1-4, and the results for 30 psi incident pressure and 1 ms duration are shown in Figures 2.1.3.6.1-5 and 2.1.3.6.1-6. At 15 psi, 3 ms, the model overestimates velocity in the Z direction and slightly underestimates velocity in the X direction. At 30 psi, 1 ms, the model underestimates velocity in both the X and Z directions.

The reasons for the differences between the measured and predicted velocities are unknown. Inaccuracies in the padding dynamic response is partly to blame, as the higher density foam would have become engaged at the strain levels predicted in the 15 psi, 3 ms, and 30 psi, 1 ms tests. The results would be higher stresses resulting in higher velocities, particularly in the X direction where strains were highest.

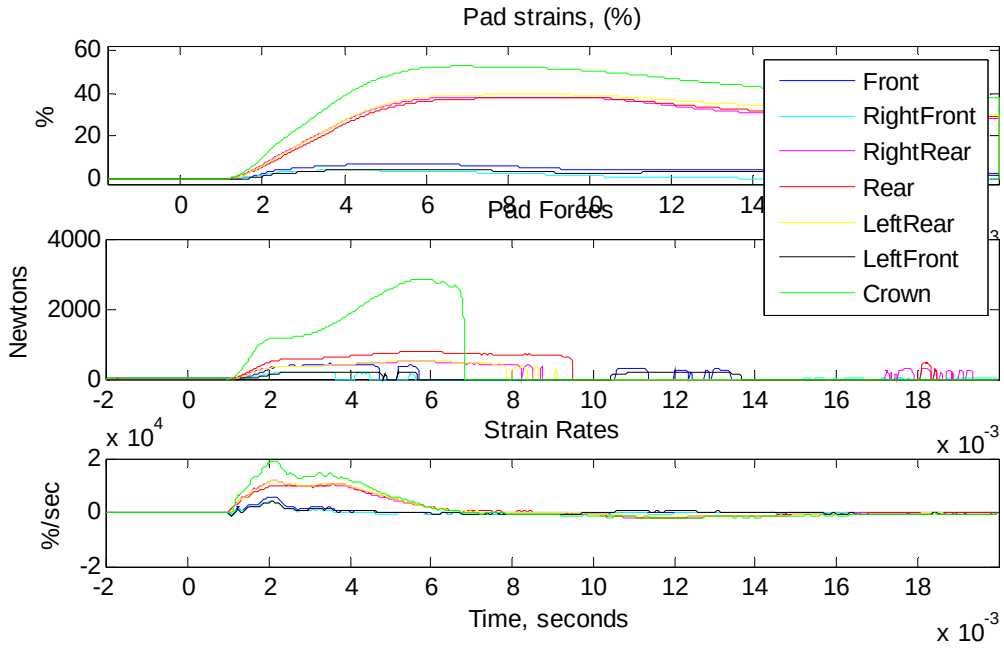

Figure 2.1.3.6.1-4. Helmet padding strains and forces from Test 58.

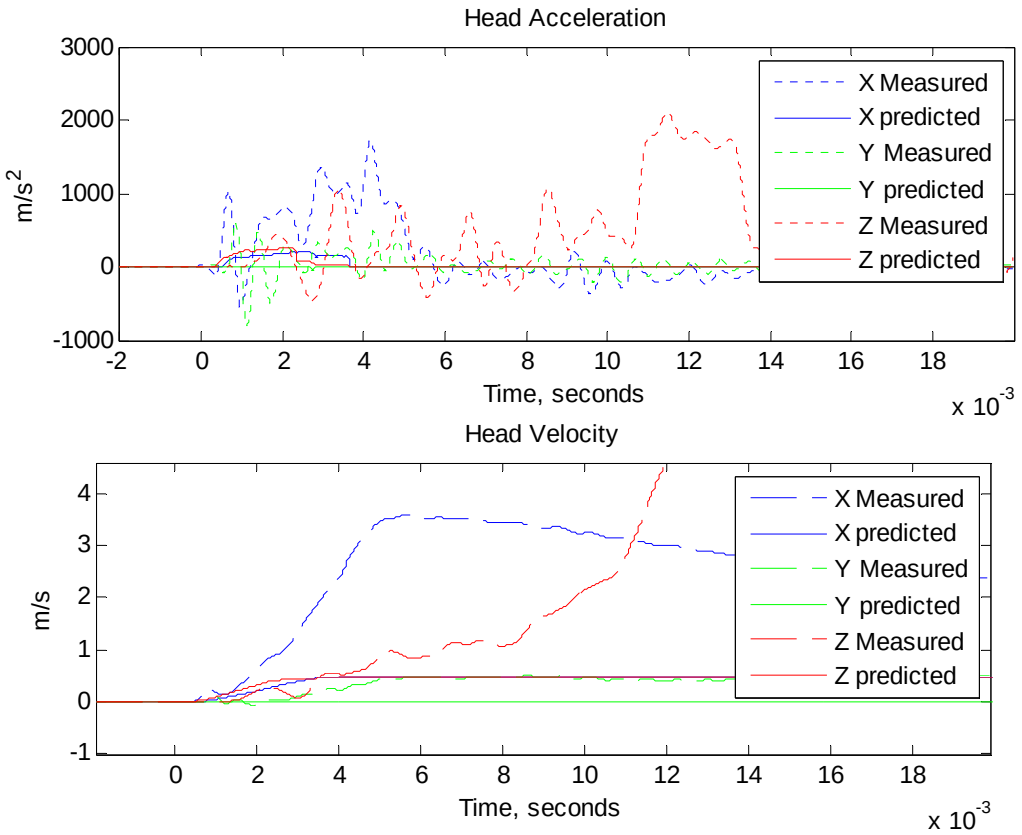

Figure 2.1.3.6.1-5. Head accelerations and velocities from Test 90: 30 psi incident, 1 ms duration, tilted 30˚ toward the blast.

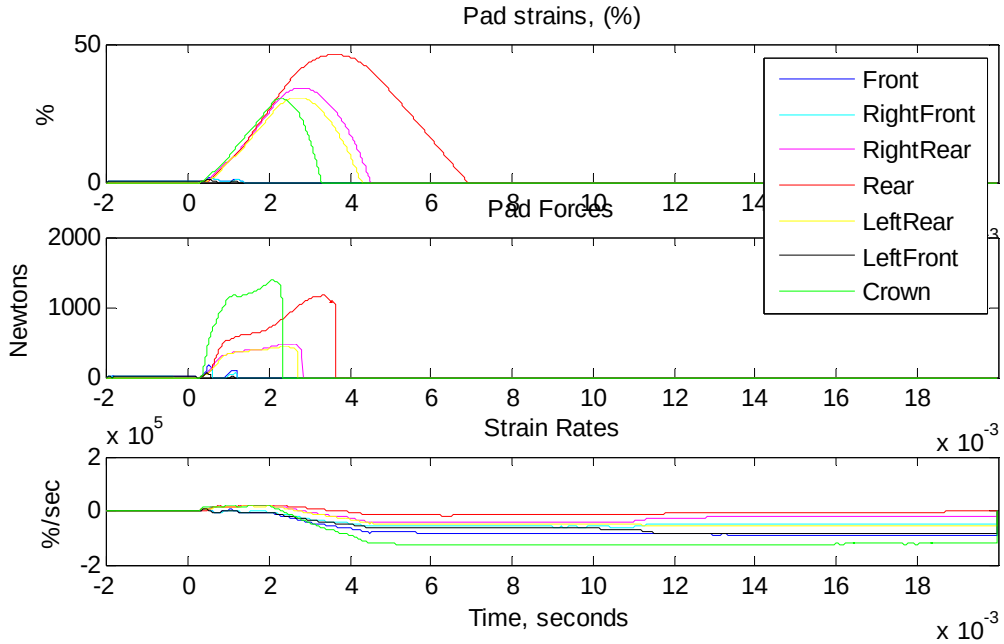

Figure 2.1.3.6.1-6. Helmet padding strains and forces from Test 90

2.1.3.6.2. Rear Impact, Level with the Blast.

In the rear-level orientation the model predicted head velocities far below those measured in tests at 15 psi and 1 ms as shown in Figure 2.1.3.6.2-1. Figure 2.1.3.6.2-2 shows the corresponding padding strains were small and of short duration. However, at 15 psi and 3 ms, the model did a much better job, slightly underestimating velocity in the X direction while making an excellent prediction of velocity in the Z direction (Figure 2.1.3.6.2-3). The resulting padding forces, shown in Figure 2.1.3.6.2-4, had a longer duration. For 30 psi and 1 ms, the predicted X velocity did not match with the measured velocity. Padding strains of 50% indicate the denser foam would become engaged. These are shown in Figures 2.1.3.6.2-5 and 2.1.3.6.2-6.

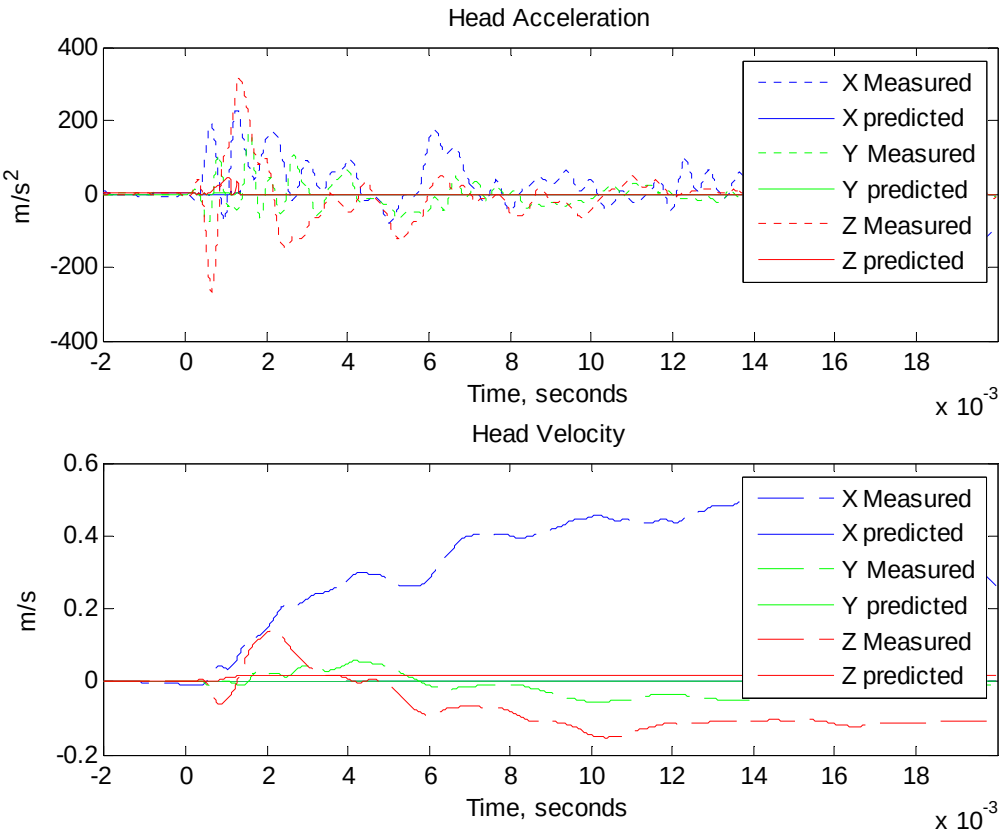

Figure 2.1.3.6.2-1. Head accelerations and velocities predicted by the model compared to measured head accelerations. From Test 21: Rear - level, 15 psi incident pressure, 1 ms duration.

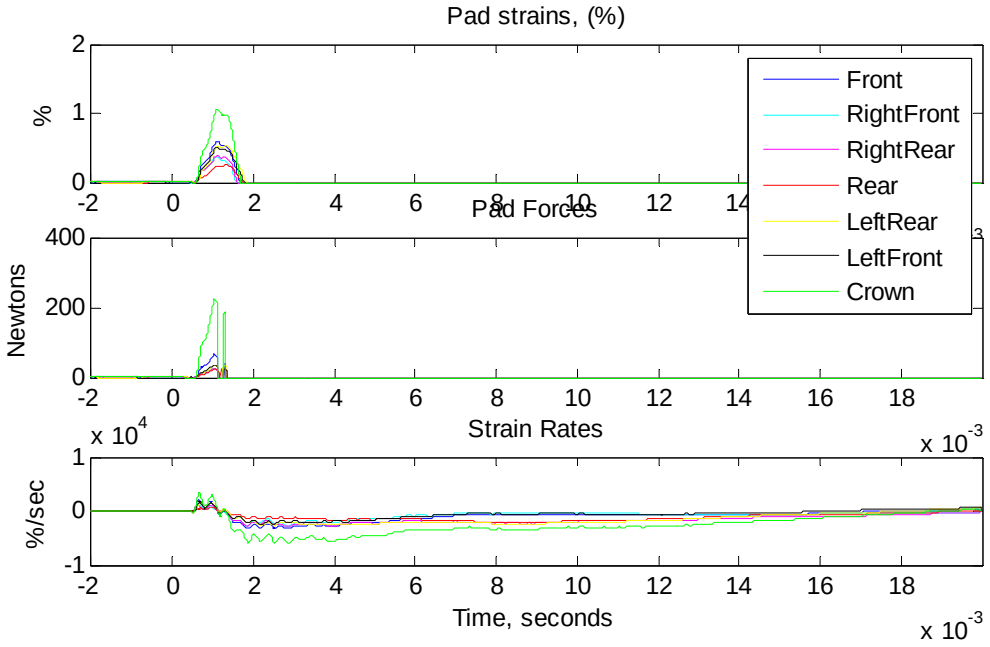

Figure 2.1.3.6.2-2. Helmet padding strains and forces from Test 21.

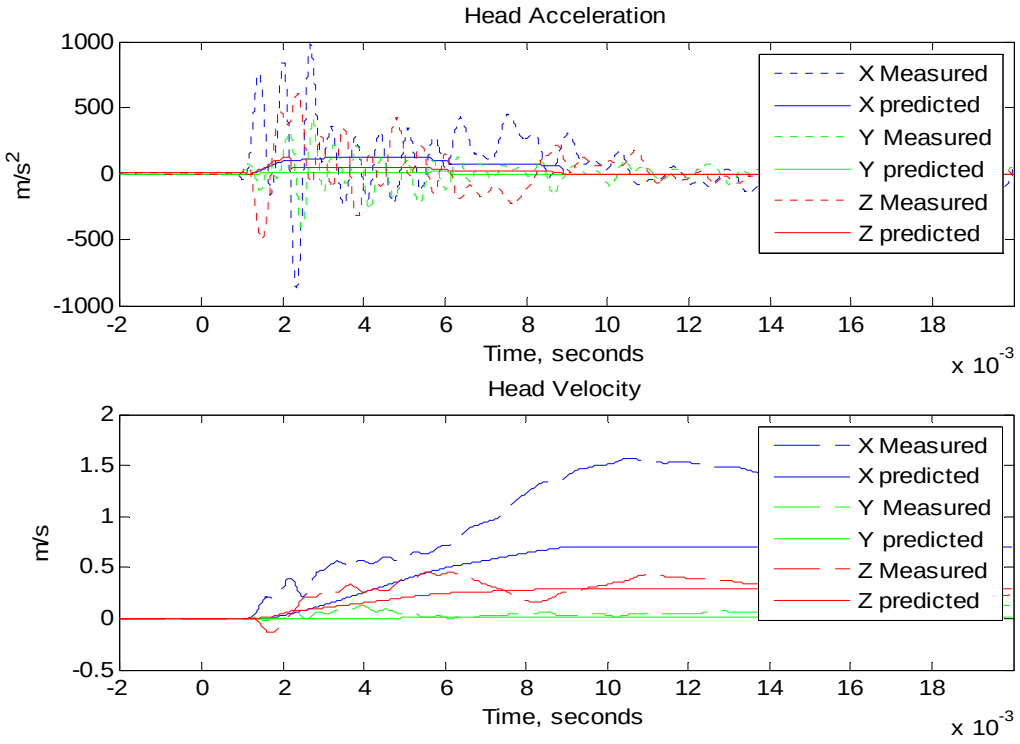

Figure 2.1.3.6.2-3. Head accelerations and velocities predicted by the model compared to measured head accelerations. From Test 51: Rear - level, 15 psi incident pressure, 3 ms duration.

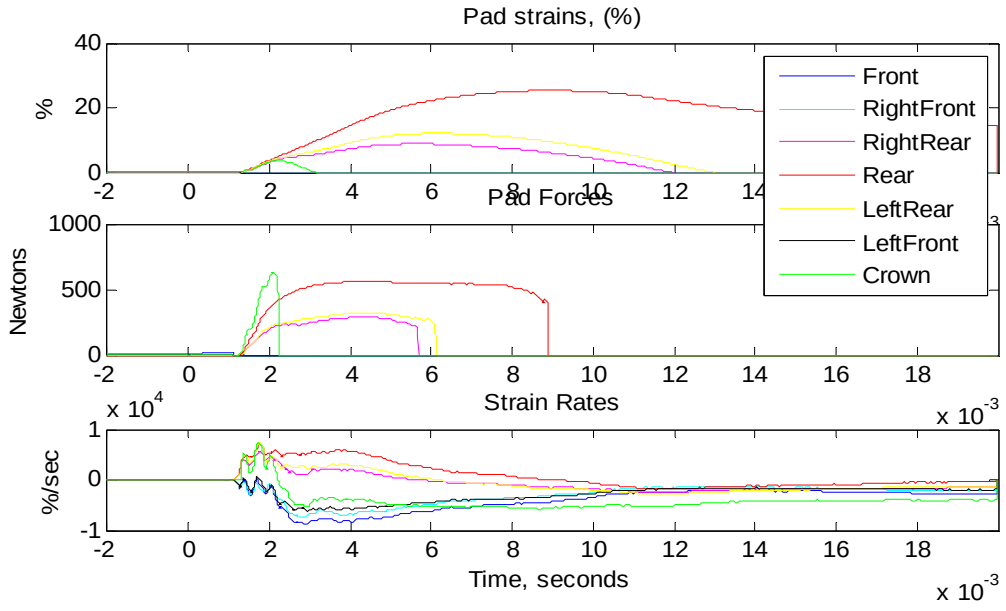

Figure 2.1.3.6.2-4. Helmet padding strains and forces from Test 51

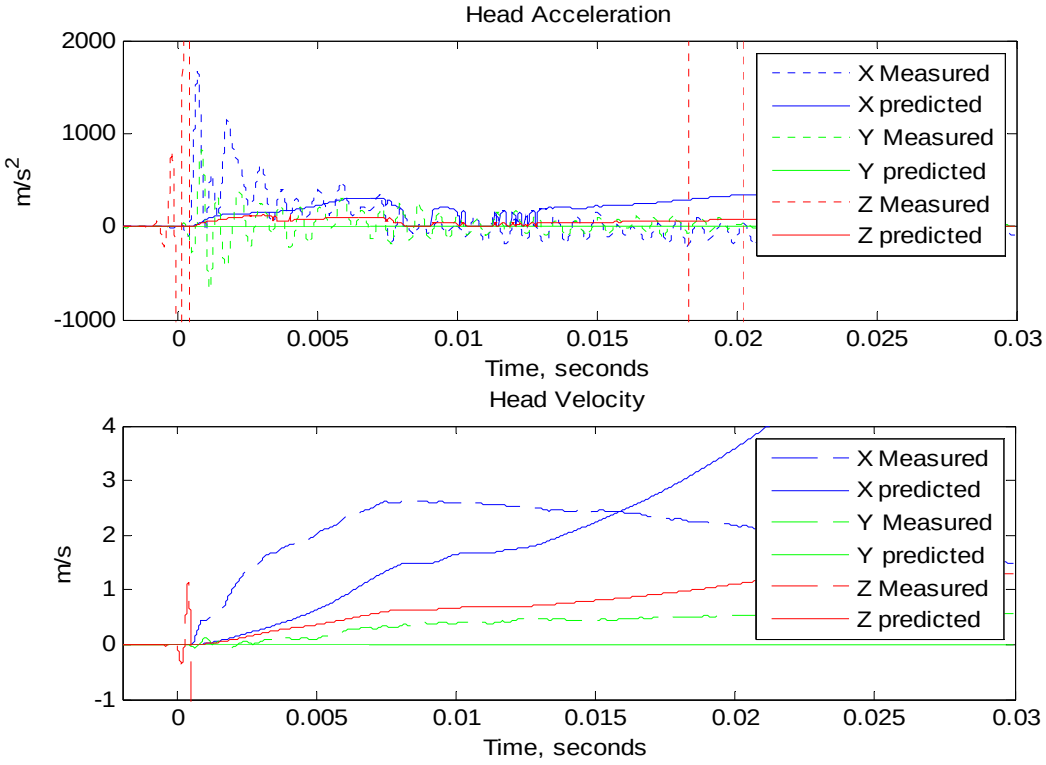

Figure 2.1.3.6.2-5. Head accelerations and velocities predicted by the model compared to measured head accelerations. From Test 95: Rear-level, 30 psi incident pressure, 1 ms duration. The Z-axis head acceleration sensor failed during the test.

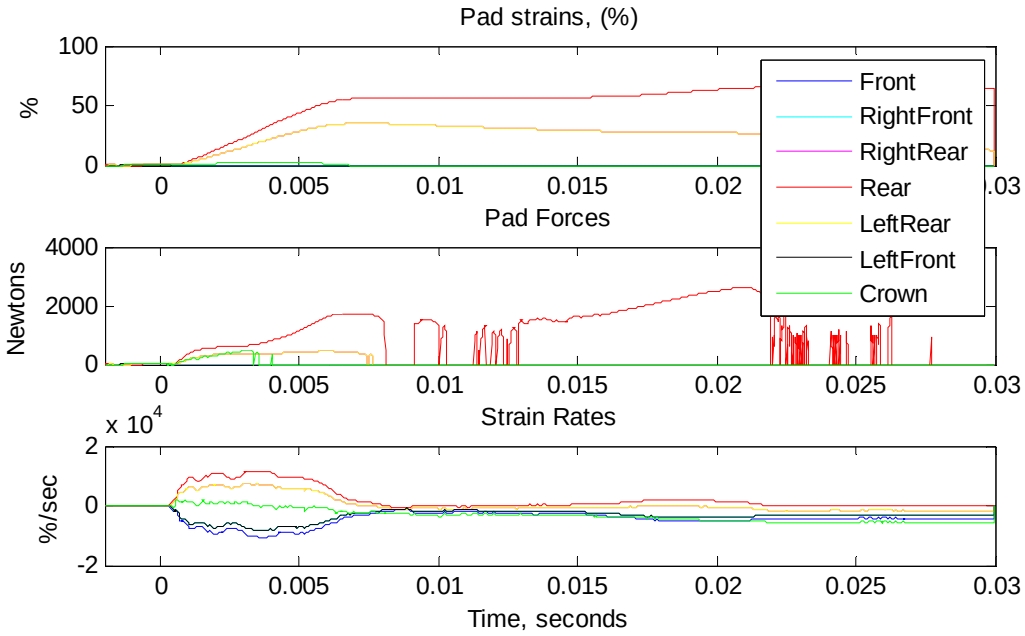

Figure 2.1.3.6.2-6. Helmet padding strains and forces from Test 95.

2.1.3.6.3. Rear Impact, Tilted 30˚ Away from the Blast.

When the head is tilted away from the blast, the first motion of the helmet is to pull away from the head. In this case the lumped parameter model does not do a good job of predicting acceleration or velocity. One example is shown in Figures 2.1.3.6.3-1 and 2.1.3.6.3-2, for a test at 15 psi incident pressure, 3 ms duration. Additional time-history traces are provided in the Appendix.

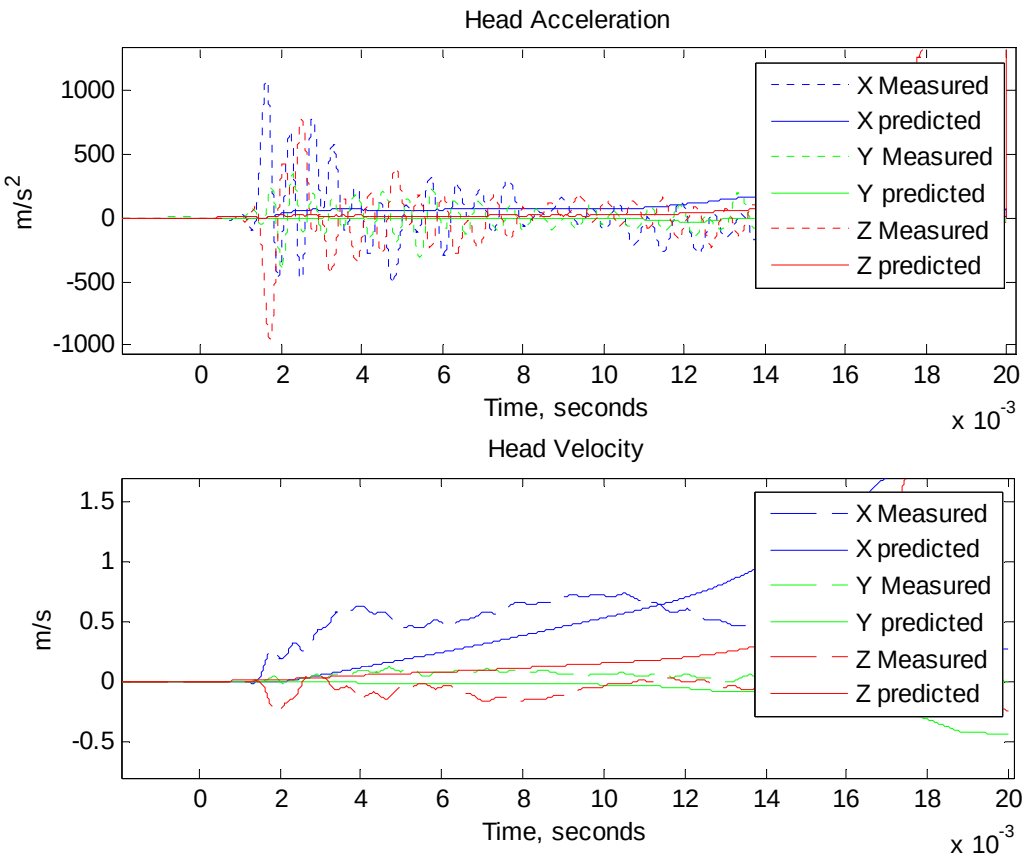

Figure 2.1.3.6.3-1.Head accelerations and velocities predicted by the model compared to measured head accelerations. From Test 54: Rear orientation, tilted 30˚ away from the blast, 15 psi incident pressure, 3 ms duration.

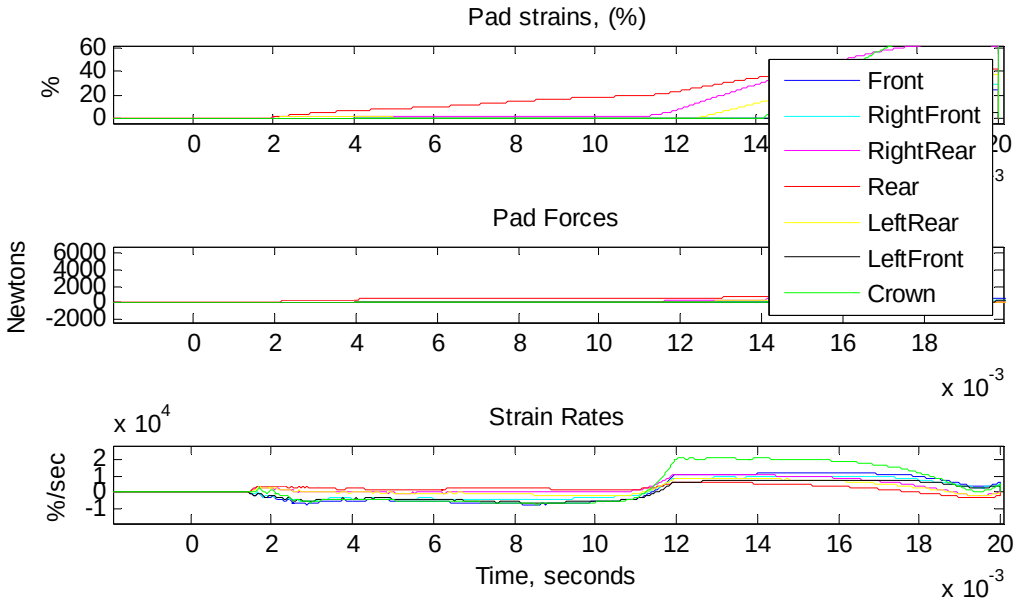

Figure 2.1.3.6.3-2. Helmet padding strains and forces from Test 54.

2.1.3.6.4. Frontal Impacts

The front, level orientation results are shown in Figures 2.1.3.6.4-1 and 2.1.3.6.4-2 for 15-psi incident, 3-ms duration. The model underestimates the head motion in the X direction. In the Z direction the model predicts a positive head velocity (down) while the measurements indicate the movement is up.

At 15-psi, 1-ms, the results are shown in Figures 2.1.3.6.4-3 and 2.1.3.6.4-4. The model accurately predicts the velocity in the X direction, but predicts a higher velocity in the Z directions than indicated by measured acceleration.

At 30 psi, 1 ms, the results are shown in Figures 2.1.3.6.4-5 and 2.1.3.6.4-6. The model underpredicts the head velocity in both the X and Z directions. The head Z axis accelerometer failed during the test at 3.2 ms, causing the measured velocity to drop sharply.

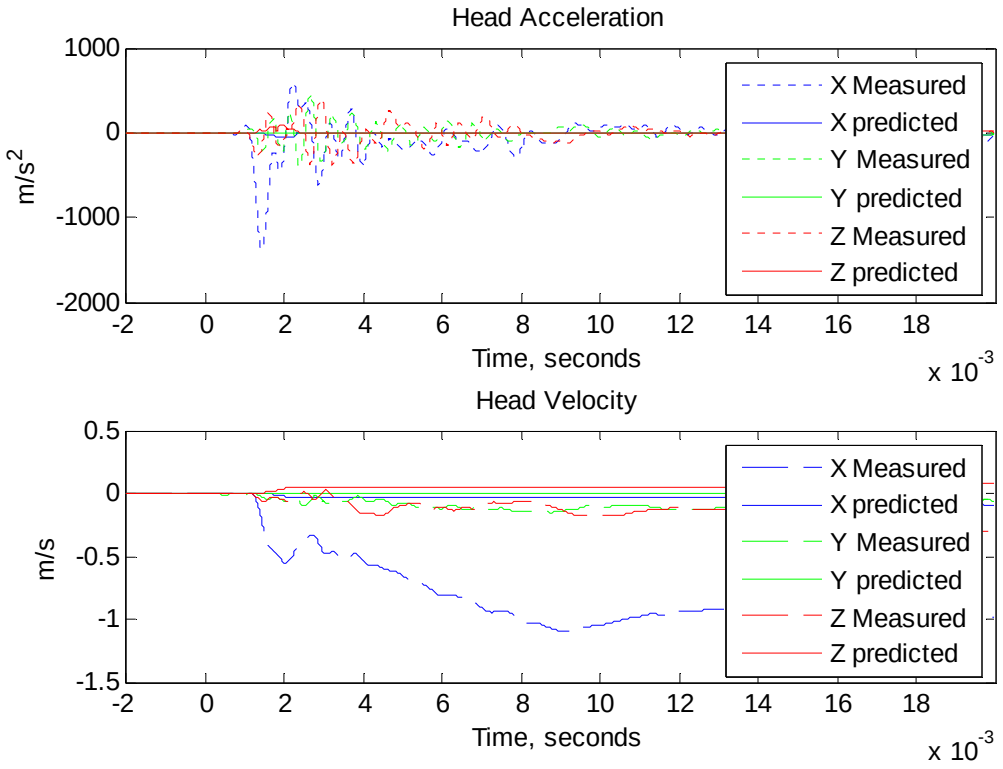

Figure 2.1.3.6.4-1. Head accelerations and velocities predicted by the model compared to measured head accelerations. From Test 40: Front orientation, level, 15 psi incident pressure, 3 ms duration.

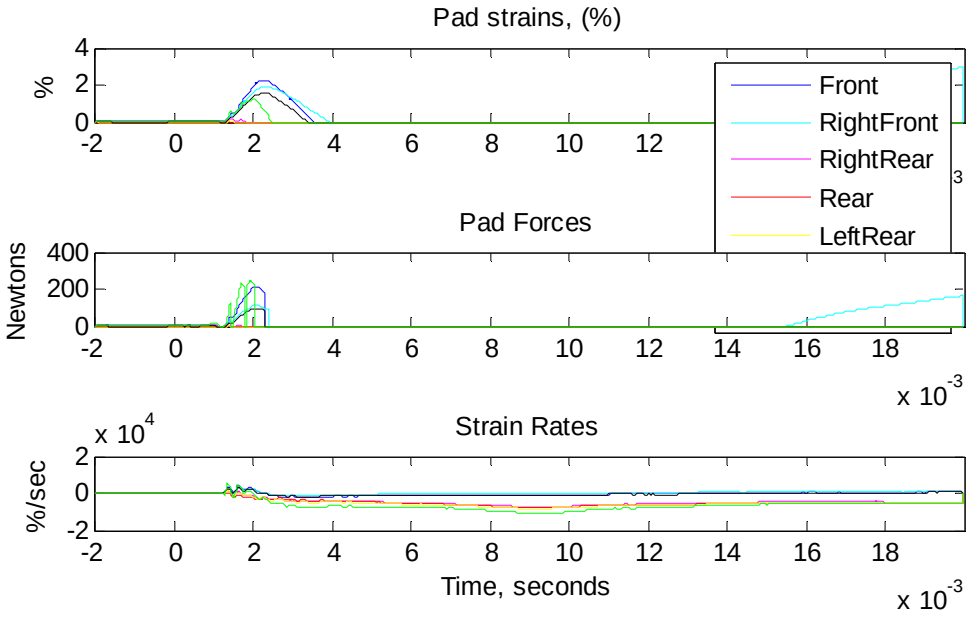

Figure 2.1.3.6.4-2. Helmet padding strains and forces from Test 40.

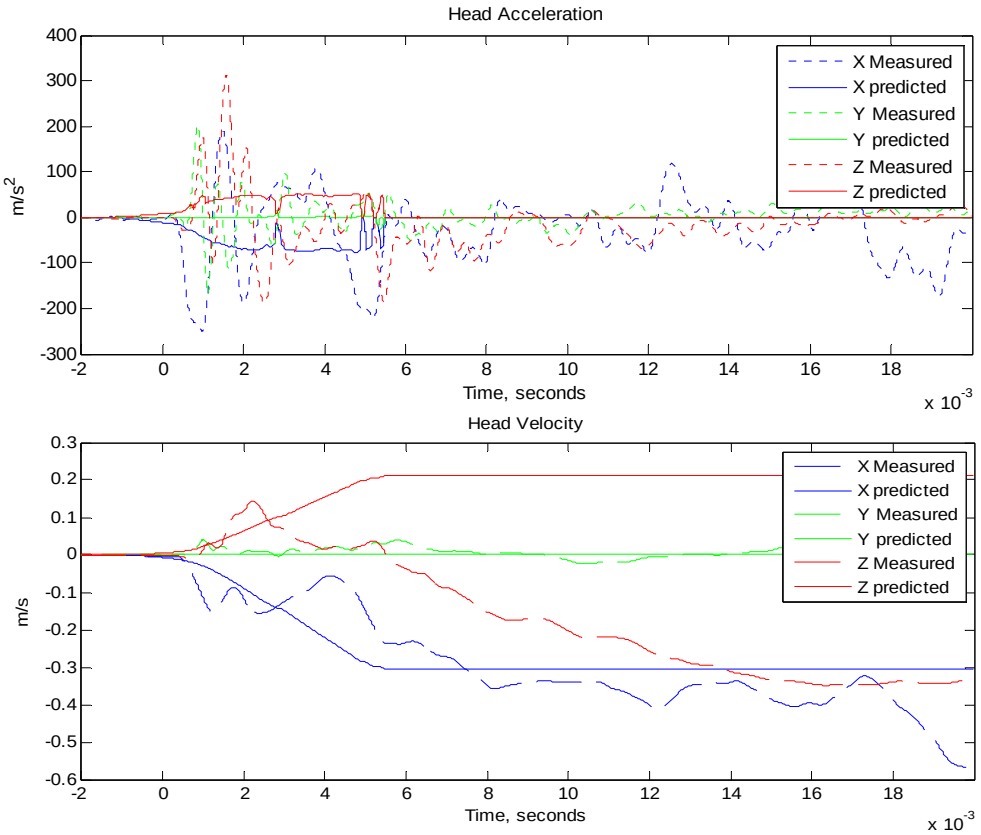

Figure 2.1.3.6.4-3. Head accelerations and velocities predicted by the model compared to measured head accelerations. From Test 5: Front orientation, level, 15 psi incident pressure, 1 ms duration.

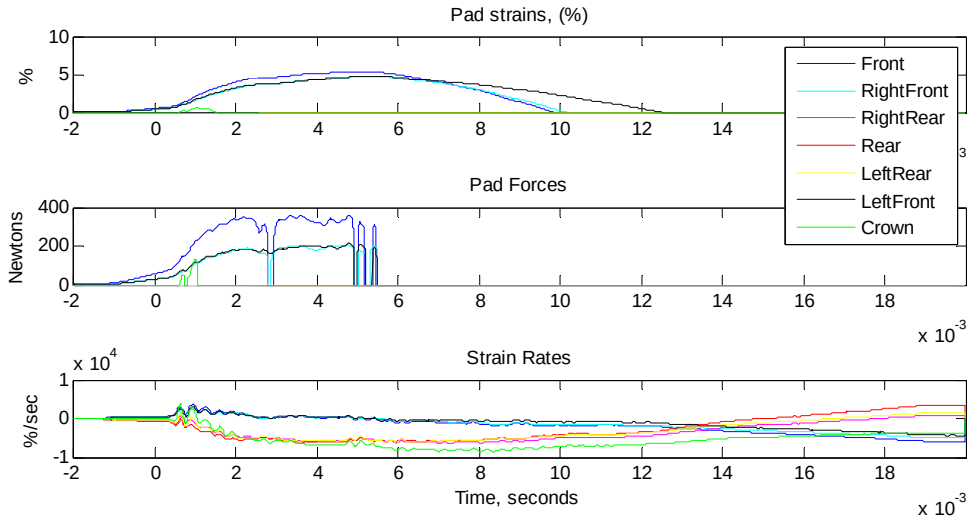

Figure 2.1.3.6.4-4. Helmet padding strains and forces from Test 5.

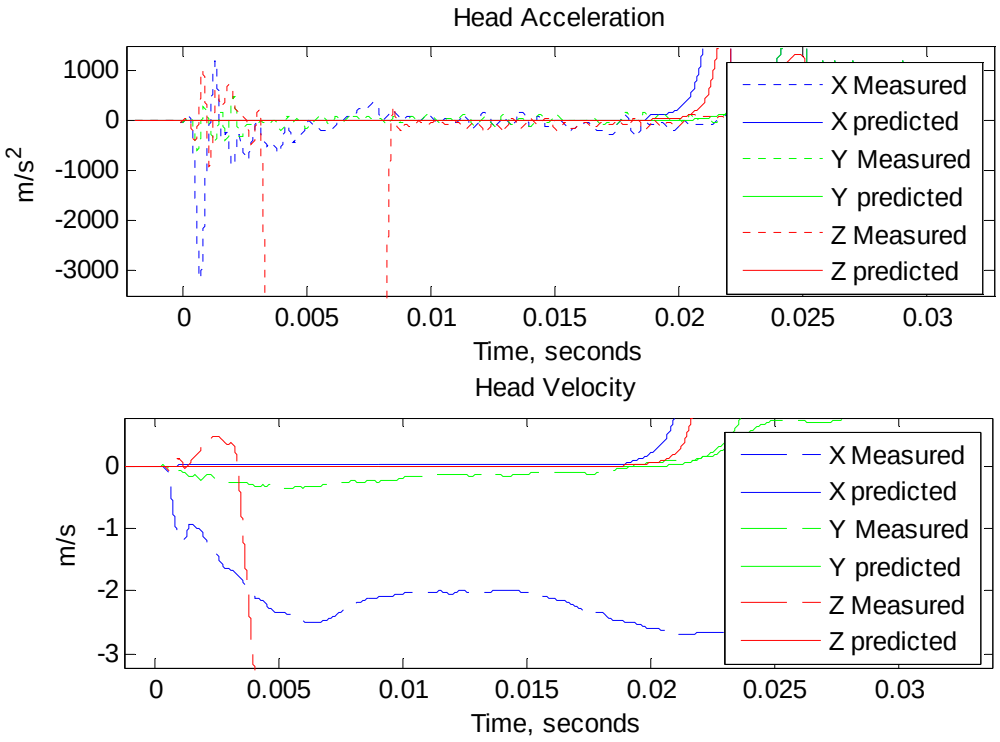

Figure 2.1.3.6.4-5. Head accelerations and velocities from Test 84: Front orientation, level, 30 psi incident pressure, 1 ms duration. The rapid drop in Z measured acceleration and velocity is due to a data glitch.

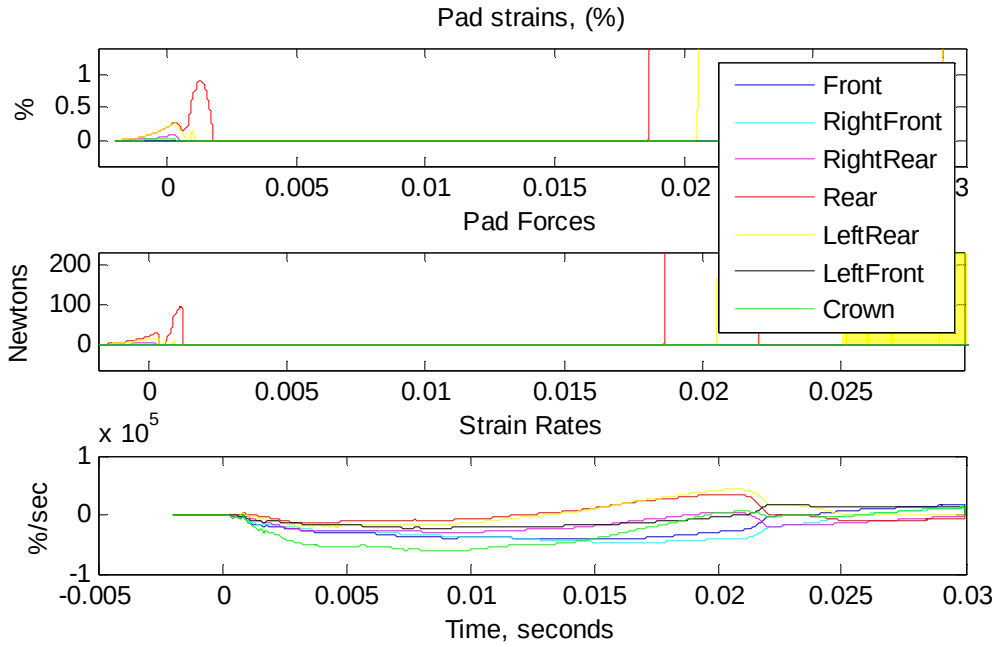

Figure 2.1.3.6.4-6. Helmet padding strains and forces from Test 84.

2.1.3.7. Performance of the Model

The Head accelerations predicted by the lumped-parameter model lack higher-frequency components found in the measured data. The predicted head acceleration is usually a single impact, with the padding forces acting in sync. For this reason velocities are also compared, providing a time-averaged value of acceleration. Padding strains, strain rates, and forces are shown over the period of impact, which is less than 10 ms in most cases.

For each configuration the model performance was qualitatively evaluated based on the velocity in the on-axis (X for front and rear orientations, Y for side orientations) lateral direction and the z direction. This evaluation was done visually, based on the plotted velocity, with a criterion of 50% error between the model prediction and the measured velocity. The results are summarized in Tables 2.1.3.7-1 and 2.1.3.7-2. In the on-axis lateral direction, the model prediction was acceptable in 5 out of 17 test conditions, and in the z direction the model prediction was acceptable in 7 out of 15 test conditions. In tests where the headform was tilted away from the blast, the model predicted the helmet to be quickly lifted from the head, and the model's performance was poor. These tests are not included in Tables 2.1.3.7-1 and 2.1.3.7-2.

Table 2.1.3.7-1.
Qualitative Evaluation of Model Performance: On-Axis Direction

	15 psi, 1 ms	15 psi, 3 ms	30 psi, 1 ms
Rear Tilted 30˚ toward	Under estimates	**Acceptable**	Over estimates
Rear Level	Under estimates	Under estimates	Under estimates
Front Tilted 30˚ toward	Over estimates	**Acceptable**	**Acceptable**
Front Level	Under estimates	Under estimates	Under estimates
Left Side Tilted 30˚ toward	Under estimates	**Acceptable**	Insufficient data
Left Side Level	**Acceptable**	Under estimates	**Acceptable**

Table 2.1.3.7-2.
Qualitative Evaluation of Model Performance: Z-axis direction

	15 psi, 1 ms	15 psi, 3 ms	30 psi, 1 ms
Rear Tilted 30˚ toward	Over estimates	**Acceptable**	**Acceptable**
Rear Level	Under estimates	**Acceptable**	Insufficient data
Front Tilted 30˚ toward	**Acceptable**	Over estimates	Over estimates
Front Level	**Acceptable**	**Acceptable**	Under estimates
Left Side Tilted 30˚ toward	Under estimates	Over estimates	Insufficient data
Left Side Level	Under estimates	**Acceptable**	Insufficient data

2.1.3.8. Recommendations for Model Improvement

The lumped parameter model uses padding forces to predict head movement. To accurately predict these forces we need a better characterization of padding forces as a function of strain and strain rate. The dual-density foam used in the padding would have very different stress-strain properties than the single density foam characterized by Chou. The strain rate-dependent effects need to be characterized at the high rates that were encountered here, up to 20,000 %/sec. This is not as daunting as it seems: impact testing at 4 m/s on helmet pads would be sufficient.

Neck response could be brought incorporated into the model, using data from the neck load cell. Neck forces could not be measured in a field-able unit, but this would facilitate improvements in model fidelity. During the shock tube tests, recorded forces and moments from

the lower neck load cell were recorded. The upper neck load cell measures forces directly to/from between the head and neck, and would be a better choice.

The model could be adjusted and evaluated at slower strain rates, such as from blunt impact tests. None of these recommendations would significantly complicate the model, and would improve its performance.

2.1.3.9. Validation Results

To validate the performance of the lumped-parameter model, blast testing was done at 15 psi, 3 ms duration and 30 psi incident pressure, 1 ms duration. Figures 2.1.3.9-1 and 2.1.3.9-2 compare head velocities and accelerations during a blast test consisting of 1.625 lbs of C-4 explosive at 6 feet, with an incident pressure of 30 psi and 1 ms duration. Figures 2.1.3.9-3 and 2.1.3.9-4 compare head velocities and accelerations during a blast tests consisting of 14 lbs of C-4 at 20 ft to get an incident pressure of 15 psi with 3 ms duration. Both are frontal, level impacts.

The model predictions and the measured head responses have similar profiles between the two tests. But the model predictions in the X direction are significantly lower than the measured responses, and the model predictions in the Z direction are significantly higher than the measured responses.

In the X direction, some of the differences can be attributed to the blast acting directly upon the head.

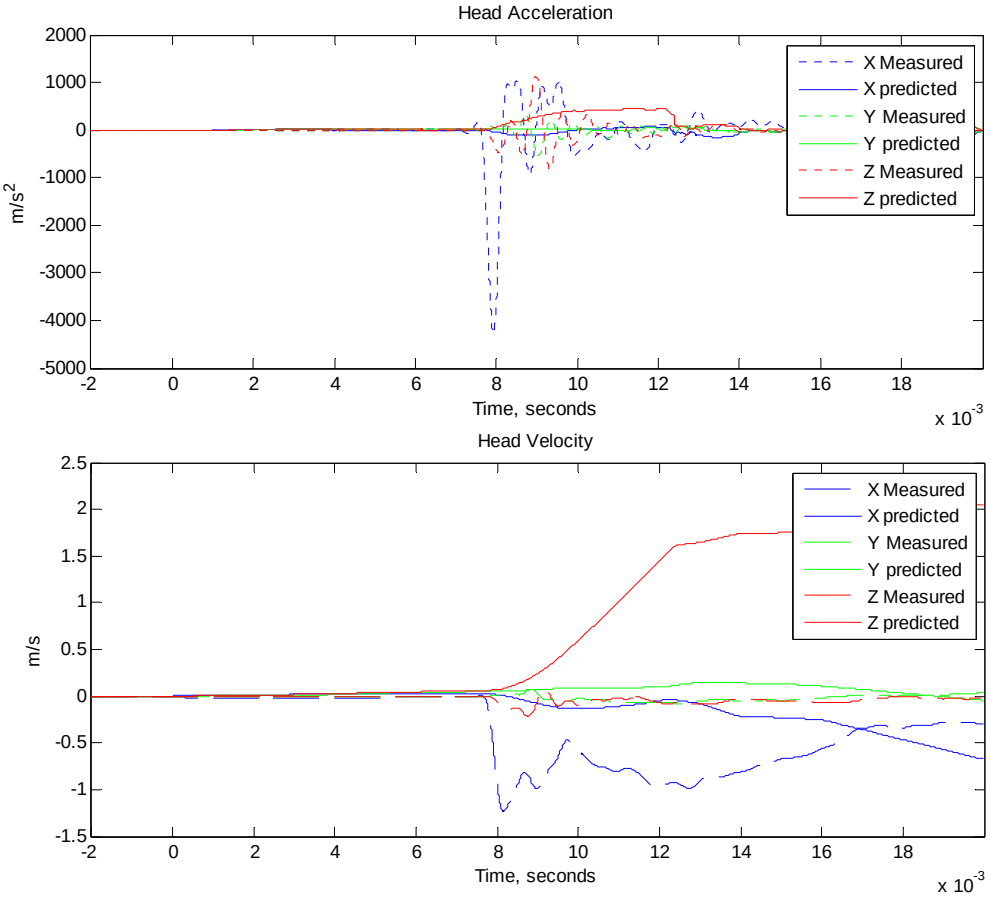

Figure 2.1.3.9-1. From blast test 3.1, with 15 psi incident pressure and 3 ms duration.

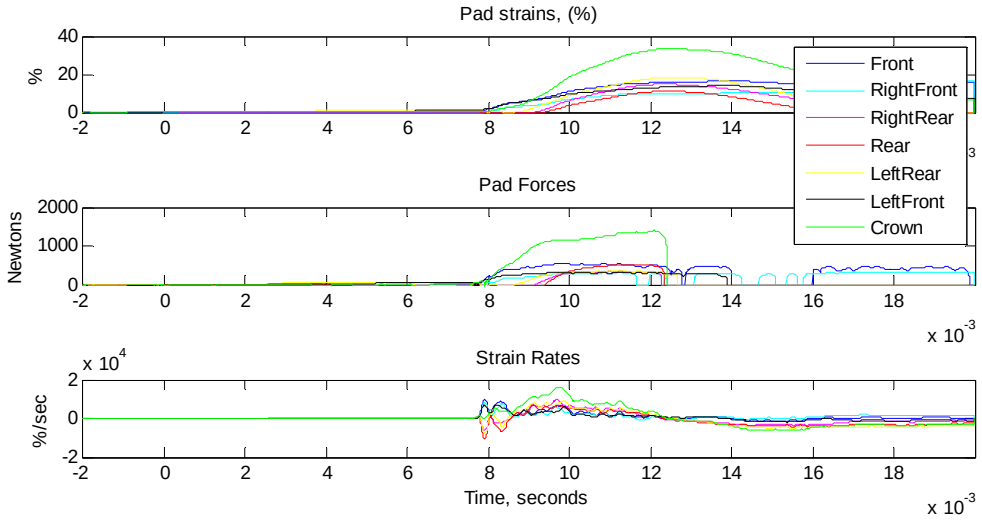

Figure 2.1.3.9-2. Padding forces from blast test 3.1.

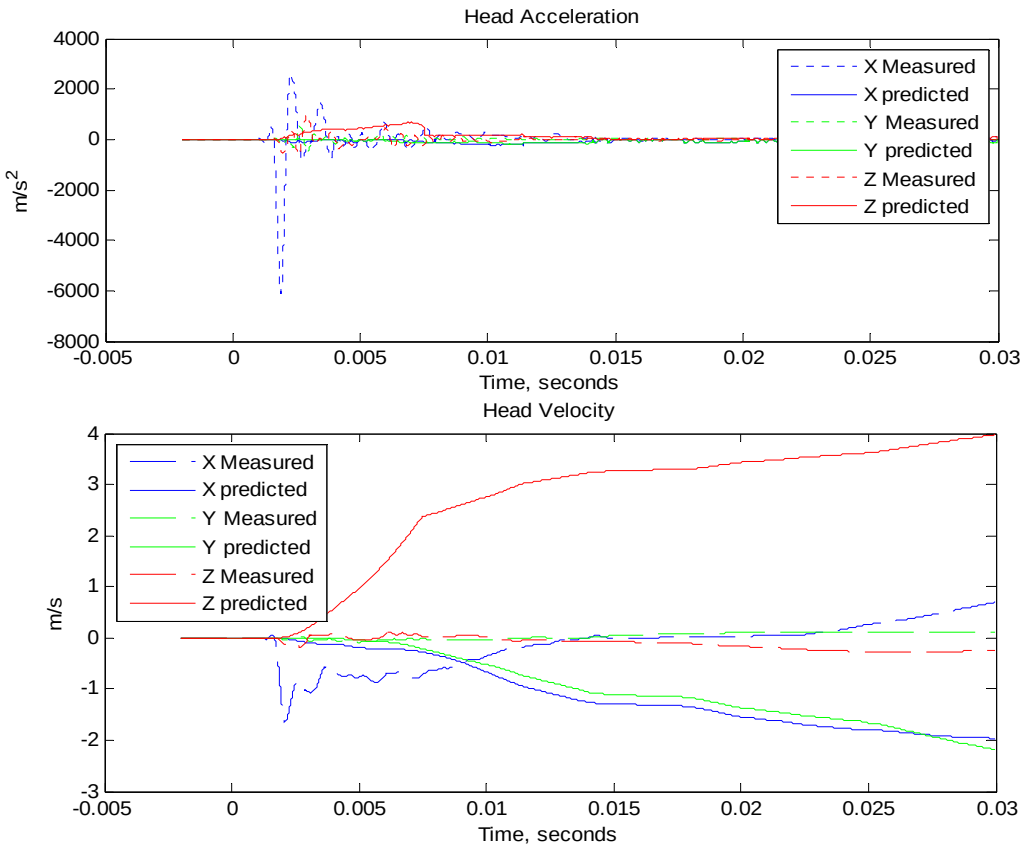

Figure 2.1.3.9-3. From blast test 2.7, with 30 psi incident pressure and 1 ms duration.

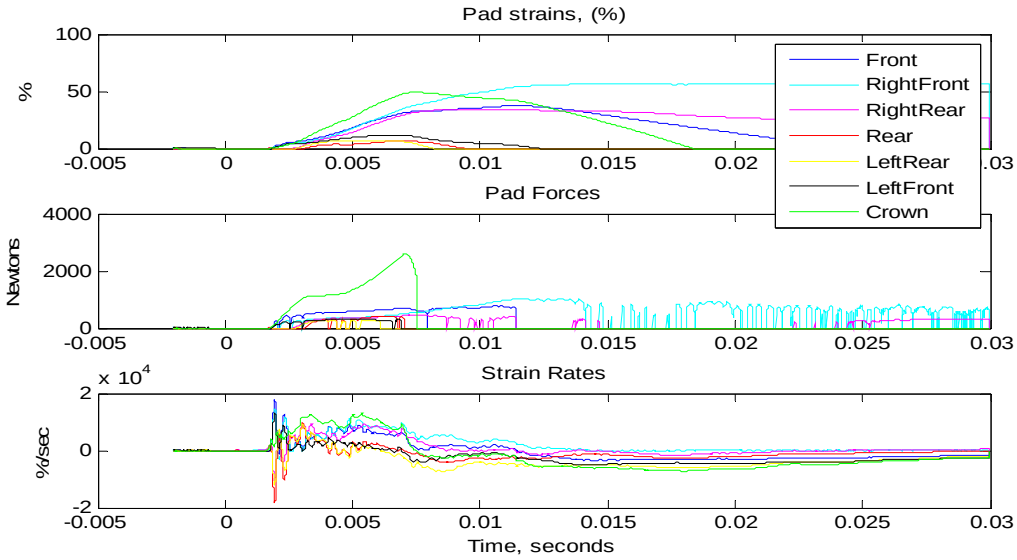

Figure 2.1.3.9-4. Padding forces from blast test 2.7

2.1.3.10. Analysis and Discussion

The lumped-parameter model uses measured helmet acceleration as the input that creates padding strains, stresses, and head movement. Overall, the performance of the lumped-parameter model was disappointing. With an improved pad response, the model performance could be enhanced significantly. Other elements, such as initial pad strains, are more difficult to correct and may require adjustment for the individual wearing the helmet. To convert accelerations into padding strains and strain rates, they must be integrated to velocities to get strain rates, and again integrated to position to get strains. This double integration is simple in theory, but in practice it is inherently unstable. Accelerometers are designed to respond to acceleration in a single direction, but they also respond to several other factors including: (1) acceleration in the transverse directions, (2) zero shift due to acceleration, (3) base strain sensitivity, and (4) sensitivity to mounting torque. Due to these and other factors, the integrations are reliable for only a few milliseconds.

Double integration of acceleration is an established technology in navigation systems for aircraft and submarines. But at the high accelerations and frequencies we are measuring, equivalent sensing platforms are not available.

The measured accelerations in the Focus head included large, high-frequency components that were not present in the lumped-parameter model predictions. These are believed to be artifacts of the Focus construction. If so, a simple model will never be able to predict them, nor does it need to.

2.1.4. Finite Element Model

2.1.4.1. Introduction to Finite Element Modeling

Anecdotal evidence from the current conflicts in Iraq and Afghanistan suggests that blast-related events are contributing to the increase in mild traumatic brain injury (TBI) symptoms seen in returning soldiers [1]. Despite the use of helmets, cases of TBI have been reported in protected soldiers exposed to primary blast waves [2]. However, it is unknown what mechanisms occur within the brain that cause injury from blast exposure, or whether these mechanisms are similar to those associated with inertial or blunt impact injuries.

Likewise, the role of the helmet and suspension system in attenuating or exacerbating the effects of blast exposure is uncertain. Keown et al. [3] tested helmets with different types of padding in blast conditions and concluded that helmet padding offered significant blast impact attenuation but did not quantify these effects, and suggested that a correlation exists between blast and blunt protection effectiveness. Current US military helmets are certified against standards designed to reduce the risk of injury from ballistic and blunt impacts, not blast exposure. Recent studies have assessed the performance of helmets in blast [4], and these methods may be used to compliment ballistic and blunt impact standards [5].

This study also investigated various options for helmet padding to assess potential differences across blast shock conditions. Optimization of padding is one strategy that can be utilized to improve blast and blunt helmet protection. Flexible polyurethane (PU) foams are commonly used in padding for military helmets, as they provide deformation recovery to meet the current helmet specifications [5]. Expanded polystyrene (EPS) and expanded polypropylene (EPP) foams are considered 'crushable foams' as they recover little to no deformation following the impact. EPS foams are common in 'single-hit' protection applications such as in motorcycle and bike helmets since they have almost no shape recovery following impact [6]. EPP does recover from deformation, but so slowly that its impact response can be considered 'crushable', which makes EPP foams appropriate for 'multi-hit' protection applications such as in hockey and football helmets [6]. It is unknown what factors make foam a good candidate for blast attenuation in helmets.

Finite element (FE) models of the head may provide insight into the mechanisms that cause brain injury. FE models have been widely used to study brain injury from blunt or inertial impact [7]. Recently, FE models of the head and brain have been developed specifically for studying the effects of blast [8, 9]. Blast FE models are more complex than impact FE models because they require a) a large air domain to model incident blast wave subsequent wave reflections, b) fluid-structure interaction (FSI) between a compressible flow model (Eulerian) and a solid model (Lagrangian), and c) a refined FE mesh to capture high-frequency wave propagation (shock). These requirements make blast modeling computationally demanding, and accordingly two dimensional models have been used in the past to research the internal response of the body to blast [10].

The objective of this study was to evaluate head and helmet accelerations for a helmet and suspension system in blast loading using a two dimensional FE model. The response includes both the initial blast wave propagation through the helmet and head and the subsequent interaction between the helmet and head. A general linear model was used to identify key factors in the helmet and padding that may improve personal protection by examining the kinematic response of the head/helmet system.

2.1.4.2. Finite Element Model Methods

2.1.4.2.1. Model Geometry and Discretization

A two dimensional FE model of the human head was previously developed to characterize the internal response of the brain under primary blast exposure with the presence of a helmet. The model geometry based on the high-resolution (0.33 mm/pixel) female dataset (Age: 59, Height: 1.65m) from the Visible Human Project [11]. An axial slice photo was selected at approximately the anterior-most portion of the frontal lobe (Figure 2.1.4.2.1-1A). The scalp was modified to remove the excess posterior skin, and the geometry was scaled to match the head breadth and depth dimensions of the 50th percentile male US Army personnel [12].

A 2 mm thick cerebral spinal fluid (CSF) layer was added between the skull and grey matter that was not easily distinguished or not present in the cadaver axial slice photo. The skull was

divided into three layers: outer table, diploë, and inner table. The diploë was set at 40% of the skull thickness to correspond with empirical measurements [13]. The model was composed of seven parts: CSF, grey matter, white matter, nervous tissue (thalamus, caudate and lentiform nucleus), inner and outer table, diploë, and scalp.

The head model was discretized using hexahedral elements with a maximum edge length of 2 mm. The model is 2 mm thick hexahedral elements and model nodes are constrained to planer deformation. The model consists of 7650 elements (average Jacobian ratio of 0.83) that have an average characteristic length of 1.5 mm. A three dimensional model of the head at this level of mesh refinement would consist of over 600,000 elements. The segmented and discretized head model is shown in Figure 2.1.4.2.1-1B.

The helmet geometry was based on a CT slice of an unused Advanced Combat Helmet (ACH). The slice was located at approximately the same plane as the brain model when the helmet is worn. Padding was attached to the helmet and was allowed to equilibrate with the head model to establish an initial fitted position for each pad type. The assembled model of the head fitted into the helmet is shown in Figure 2.1.4.2.1-1C.

(A) (B) (C)

Figure 2.1.4.2.1-2. Side-by-side comparisons of head slice (A), meshed model (B), and model with fitted helmet (C)

The head and helmet model was positioned in the middle of a 1350 x 950 mm Eulerian domain representing the air surrounding the head/helmet system. The nominal size of the air mesh elements was 2 x 2 mm, with the size of the element gradually increasing away from the head model. The size of this domain was determined in a convergence study, and was sufficiently large enough to minimize the effects of non-reflecting boundaries. The number of elements in the air domain was approximately 140,000.

2.1.4.2.2. Material Properties

Material properties for the head model were chosen with emphasis on higher rate properties. For the purposes of this model, all brain tissues were modeled using the same linear viscoelastic material model. The CSF was modeled using the Mie-Gruneisen equation of state of water. Cavitation was included by limiting the minimum pressure in the CSF to -100 kPa. Skull and

scalp materials were modeled using linear viscoelastic theory. A summary of the head model material properties is found in Table 2.1.4.2.2-1.

Table 2.1.4.2.2-1.
Summary of Material Properties in the Model

Part	Material Parameters (Head)	Ref
Brain	= 1.06 gm/cm^3 G_1 = 50 kPa G_2 = 6.215 kPa G_3 = 2.496 kPa G_4 = 1.228 kPa G_5 = 1.618 kPa G_∞ = 0.27 kPa K = 2190 MPa $_1$ = 100 ms^{-1} $_2$ = 4.35 ms^{-1} $_3$ = 0.2 ms^{-1} $_4$ = 0.0053 ms^{-1} $_5$ = 5.1e-6 ms^{-1}	[14]
Scalp	= 1.13 gm/cm^3 G_1 = 355 kPa G_2 = 399 kPa G_3 = 35.6 kPa G_∞ = 408 kPa K = 2190 MPa $_1$ = 0.005 ms^{-1} $_2$ = 0.05 ms^{-1} $_3$ = 0.5 ms^{-1}	[16]
CSF	= 1.00 gm/cm^3 = 8x10^{-7} P_{cav} = -100 kPa C = 1484 m/s S_1 = 1.979 $\tilde{}$ = 0.110	[20] [19, 21]

Part	Material Parameters (PPE)	Ref
Helmet	= 1.23 gm/cm^3 E_1 = 18.5 GPa E_2 = 18.5 GPa E_3 = 6.0 GPa $_{21}$ = 0.25 G_{12} = 0.77 GPa G_{23} = 2.72 GPa G_{31} = 2.72 GPa $_{31}$ = 0.33 $_{32}$ = 0.33	[15]
Inner & Outer Tables	= 2.00 gm/cm^3 G_1 = 1052 MPa G_2 = 2163 MPa G_∞ = 2169 kPa K = 4700 MPa $_1$ = 0.03 ms^{-1} $_2$ = 275 ms^{-1}	[17, 18] [19]
Diploë	= 1.13 gm/cm^3 G_1 = 454 MPa G_2 = 935 MPa G_∞ = 937 kPa K = 2030 MPa $_1$ = 0.03 ms^{-1} $_2$ = 275 ms^{-1}	[17] [19, 22]

The Kevlar/resin helmet was modeled as an orthotropic elastic material based on van Hoof et al. [15]. Material directions 1 and 2 were tangential to the helmet surface, while material direction 3 was normal to directions 1 and 2 through the thickness of the helmet. This material model did not consider viscoelastic effects or damage, and the helmet straps were not modeled.

Three different types of foam of various densities were modeled for the helmet padding: four densities of flexible PU (56, 72, 88, and 104 gm/L) [18], two densities of EPS (61 and 112 gm/L) [23], and three densities of EPP (35, 77, and 150 gm/L) [22]. As a reference, the density of one flexible PU foam commonly used in the ACH was measured to be 83 gm/L. In general, the PU foams were softer than the EPS and EPP foams, and foam stiffness increased with density. Figure 2.1.4.2.2-1.1.4.2.2-1A compares the stress of each foam (at 20% compression) based on foam density. Mechanical properties were based on high-rate compression foam studies at strain rates to at least 1500 1/s [18, 22, 23]. Stress-strain curves at the various tested strain rates were imported into the model, which tabulated the current stress-state as a function of strain and strain rate during material loading (unloading response was based on the quasi-static stress-strain curve). An example of a set of stress-strain curves that were used in the model (61 gm/L EPS) is shown in Figure 2.1.4.2.2-1B.

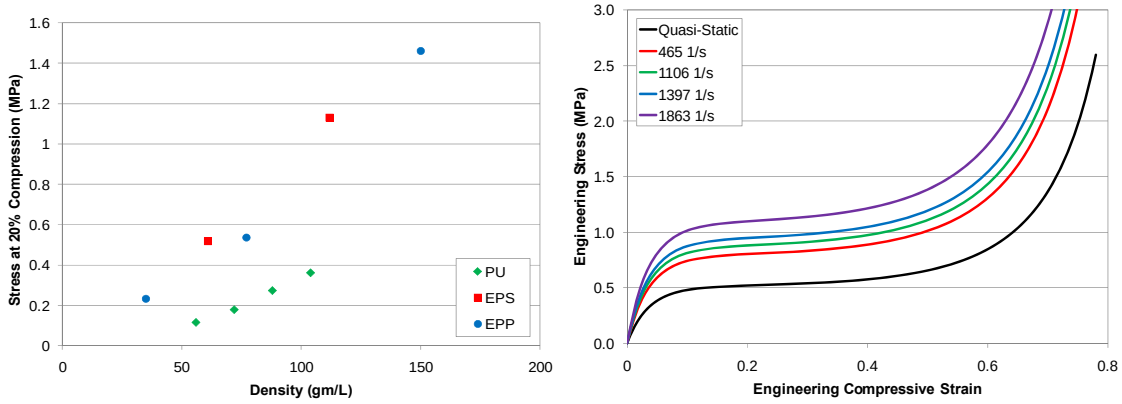

(A) (B)

Figure 2.1.4.2.2-1. Mechanical properties of some foam materials, (A) Comparison of stress (at 20% strain) versus density, and (B) stress-strain curves for 61 gm/L EPS.

2.1.4.3. Blast Modeling and Test Conditions

A planar blast wave was modeled in air using the ideal gas law EOS (= 1.4). It was assumed that all blast loading was outside of the contact surface of the blast, so modeling of the detonation EOS was not considered. The blast wave was introduced into the model by prescribing pressure, temperature, and velocity on a layer of 'ambient' air elements located on one boundary of the air domain. This method allowed for the application of a fully developed blast wave using an efficient domain size.

Eleven different blasts cases were simulated, with blast waves ranging between 50 and 2000 kPa peak incident overpressure and between 2 and 6 ms of positive phase duration (Table 2). Cases 1, 2 and 7 correspond to blast levels associated with ear drum rupture [24], Cases 3, 4, 8, and 9 correspond to levels associated with pulmonary-based fatality [25], and Cases 5, 6 and 11 correspond to the estimated blast levels associated with brain-based primary blast fatality [26].

The head was oriented for frontal blast exposure, with the blast propagating in the anterior/posterior direction. Eleven different helmet configurations were simulated and compared (Table 2.1.4.3-1). This includes the unprotected configuration (Group 1) where the bare head model was directly exposed to the blast, the helmet-only configuration (Group 2) where the head model was equipped with the helmet but no padding (to simulate helmets with only strap-based suspension systems), and the nine padded configurations (Groups 3-11) where a helmet was modeled with different foam padding. Each blast case was simulated for each helmet configuration totaling 121 simulations for the study. All blasts were simulated to 30 ms using LS-DYNA v971 R4.2.1 (Livermore Software Technology Corp., Livermore, CA).

Table 2.1.4.3-1.
Model Test conditions

Helmet Configuration		Blast Conditions						
Group	Padding Type	Case	Injury Condition	Incident Overpressure (kPa)	Duration (ms)	Impulse (kPa-ms)	Equivalent ConWEP Blast	
							Charge (kg)	Distance (m)
1	No Helmet	1	< LD50 Ear	50	2.0	34.14	0.291	2.55
2	Helmet, No Pads	2	> LD50 Ear	100	2.0	55.72	0.501	2.16
3	PU (56 gm/L)	3	Lung Threshold	200	2.0	101.8	1.31	2.16
4	PU (72 gm/L)	4	~ LD50 Lung	500	2.0	157.9	1.56	1.53
5	PU (88 gm/L)	5	~ LD50 Head	1000	2.0	200.7	1.42	1.09
6	PU (104 gm/L)	6	~ LD99 Head	2000	2.0	416.3	13. 5	1.67
7	EPS (61 gm/L)	7	< LD50 Ear	50	6.0	102.4	7.85	7.65
8	EPS (112 gm/L)	8	Lung Threshold	100	6.0	166.9	13.5	6.47
9	EPP (35 gm/L)	9	~ LD50 Lung	200	6.0	305.9	35.4	6.49
10	EPP (77 gm/L)	10	~ LD50 Head	500	6.0	472.6	41.8	4.58
11	EPP (15 gm/L)	11	~ LD99 Head	1000	6.0	605.5	39.0	3.29

2.1.4.4. Data Analysis

All results are presented relative to the unprotected head group. Protection effectiveness for different helmet configurations was based on metrics associated with head or brain injury. These include global kinematic responses (peak head acceleration and Head Injury Criterion) and local tissue responses (peak pressure and peak principle strain). A ratio between a helmeted result and the unprotected result for a given blast condition was used as the performance assessment. The smaller the ratio, the more the helmet has attenuated the blast effects, and a ratio greater than one indicates the helmet has exacerbated these effects.

Head acceleration and Head Injury Criterion (HIC) are based on the rigid body motion of the head, which was calculated as the acceleration of the head model center of gravity (CG). HIC was first introduced by Versace [27] and further modified by the National Highway Transportation Safety Administration (NHTSA) as the head injury assessment in the Federal Motor Vehicle Safety Standards (FMVSS). HIC was calculated using the unfiltered resultant head acceleration since filtering the data at the usual 1650 Hz is not suitable for blast [28].

No evidence exists at this time to confirm the mechanism that is responsible for blast brain injuries. However, it has been hypothesized that the dynamic pressure in the brain or the resulting high rate brain strain caused by an exposure to a primary blast wave is associated with the blast TBI. Both peak pressure and peak principle strain were recorded for each brain element, and mapped onto the model to give region-specific distribution of potential injury. To avoid having a single element to characterize the response, peak values reported for a each

helmet configuration refer to the 5% volume threshold rather than the absolute maximum value measured in the brain. All strains reported in this study are true strains.

Finally, a general linear model (GLM) (= 0.05, $p < 0.05$ was significant) was developed for each metric using the ratios of the padded helmet results to the unprotected results. The model identified blast and foam characteristics that were significant factors for the helmet protection. Independent variables included blast parameters (peak incident overpressure and duration) and foam parameters (foam type and density). The logarithm (base 10) of peak pressure was used to correspond with the spacing of blast pressures chosen for this study. Foam type was a nominal variable where flexible foam = -1, and crushable foam = 1. Blast impulse was not included since it was correlated with overpressure and duration, and foam stiffness was not included because it was correlated with foam type and density (Figure 2.1.4.2.2-1A). A backwards elimination method was used to reduce the GLM to significant variables only.

2.1.4.5. Results

An example of the planar blast wave impinging on the bare head model is shown in Figure 2.1.4.5-1.

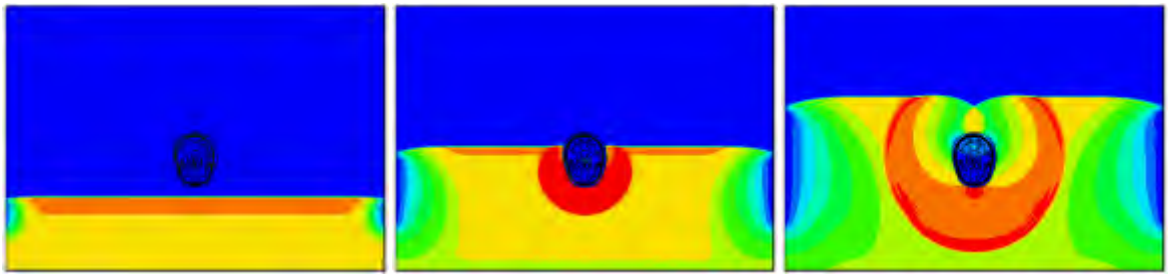

t = 0.6 ms t = 1.0 ms t = 1.4 ms

Figure 2.1.4.5-1. The time-lapsed progression of a blast wave impinging on the unprotected head model

2.1.4.5.1. Global Kinematic Response – Acceleration and HIC

Configurations without helmet were characterized by a high, sharp-rising head acceleration that decayed rapidly (Figure 2.1.4.5.1-1A). Peak head acceleration for the unprotected cases was well correlated with peak incident overpressure ($R^2 = 0.98$). Inclusion of the helmet substantially reduced the initial head acceleration. The initial peak accelerations created by the primary blast wave were relatively low (10% ± 1% of unprotected case) for the helmet-only configuration, until the helmet eventually impacted the head causing higher peak accelerations (55% ± 18% of unprotected case) at the highest blast levels (Figure 2.1.4.5.1-1B).

The peak head acceleration of the helmeted configurations were compared with the unprotected case (Figure 2.1.4.5.1-1B). The two least dense foams (PU 56 gm/L and EPP 35 gm/L) had the lowest peak accelerations for all blast cases (27% ± 14% of unprotected case). At lower blast levels (< 200 kPa) and with denser padding (> 56 gm/L), the head had similar or higher peak acceleration than without the helmet (90% to 190% of unprotected case). These

peak accelerations were caused by the coupling between the helmet, padding, and head, and typically occurred 5-10 ms after the initial blast wave. At higher blast levels (LD50+ Head), peak head acceleration was caused by the initial blast wave rather than during the helmet-head coupling phase post-blast. These peak accelerations were still less than the peak acceleration for the unprotected case (32% ± 11% of unprotected case).

The GLM for peak head acceleration indicated that an increase in foam density increased the peak head acceleration ($p < 0.001$), while the effectiveness of the helmet in reducing peak head acceleration relative to the unprotected case increased with blast pressure ($p < 0.001$). No other factors were statistically significant and the results of the GLM are presented in Table 2.1.4.5.1-1.

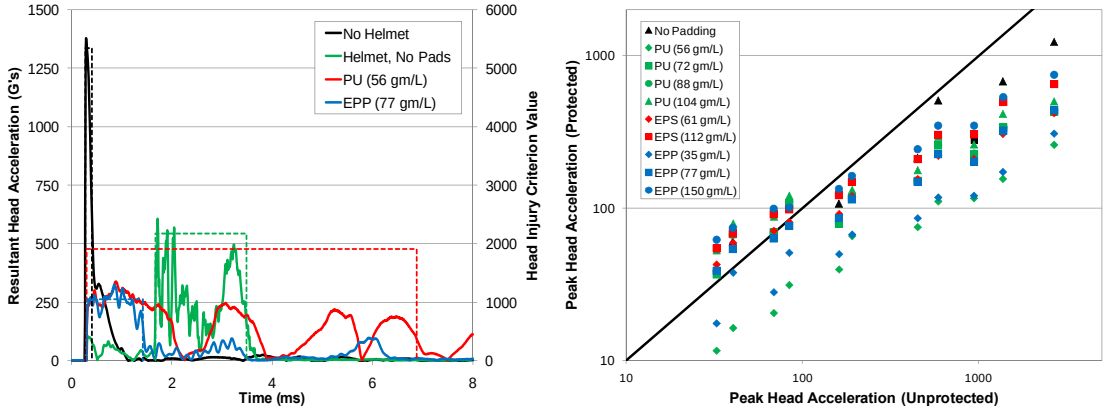

(A) (B)

Figure 2.1.4.5.1-1. (A) Example of head acceleration time-history (solid lines) and HIC window (dotted lines) for various configurations, and (B) comparison of peak head acceleration for different helmet configurations

Owing to the sharp-rising, rapidly decaying head acceleration, the unprotected head cases had very short HIC durations (range: 0.08 - 0.5 ms). Similar to peak head acceleration, HIC values of the helmeted cases (with the exception of PU 56 gm/L and EPP 35 gm/L) were higher than that of the unprotected case at lower blast cases (< 200 kPa) because of the coupled helmet-head response post-blast (Figure 2.1.4.5.1-2A). Accordingly, HIC values for flexible PU foams were usually greater than the typically stiffer crushable EPS and EPP foams at lower blast cases (1244% ± 415% of unprotected case for PU compared to 415% ± 153% for EPS and EPP). At higher blast levels, the difference between foam types was less discernible (52% ± 31% of unprotected case for PU compared to 33% ± 18% for EPS and EPP).

The difference between foam types was attributed to the greater kinetic energy (KE) dissipation of the crushable foams during the impact. For each blast case, the average peak KE of the head for the crushable foam configurations was consistently lower than that of the flexible foam configuration, a difference which increased with blast impulse (Figure 2.1.4.5.1-2B). These results implied that the crushable foams transferred up to 35% less kinetic energy to the head than the flexible foams.

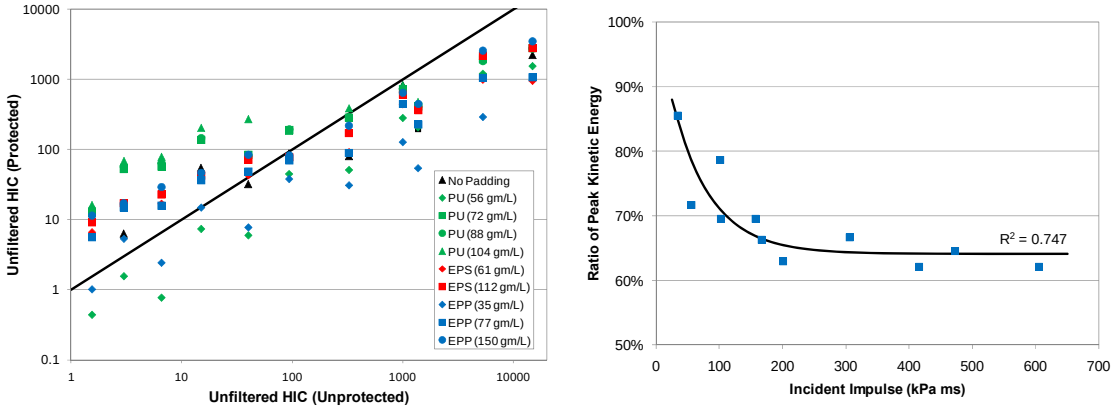

(A) (B)

Figure 2.1.4.5.1-2. (A) Comparison of helmet configurations for unfiltered HIC and (B) comparison of peak kinetic energy of the head for crushable and flexible foams

The GLM for HIC indicated that crushable foams decreased HIC ($p < 0.001$), while the effectiveness of the helmet in reducing HIC relative to the unprotected case increased with blast pressure ($p < 0.001$). No other factors were statistically significant and the results of the GLM are presented in Table 2.1.4.5.1-1.

Table 2.1.4.5.1-1.
General Linear Models for Foam Padded Helmet Configurations

Protected/Unprotected Ratio	**General Linear Model**	**R^2**
Peak Acceleration	$2.03 + 0.0057*\text{Density} - 0.76*\log_{10}P_{Inc}$	0.783
HIC	$14.52 - 1.22*\text{FoamType} - 4.83*\log_{10}P_{Inc}$	0.430

2.1.4.5.2. Acceleration Transfer Function

For the foam that is representative of the ACH (TW) foam (PU, 88 g/L), the helmet to head transfer function for peak resultant acceleration across all conditions simulated is shown in Figure 2.1.4.5.2-1. A power law regression fit of the form:

$$\text{Head Peak Resultant} = (2.89 \pm 0.19) * (\text{Helmet Peak Resultant})^{0.5426}$$

has a correlation coefficient of 0.92 and the fit is not excluded by the Durbin-Watson statistic. The helmet response is larger than the head response, as expected, and does not follow a linear trend. The regression statistics of the power law fit suggest that the model and the helmet/head response are well-behaved for a wide range of blast inputs in the frontal orientation.

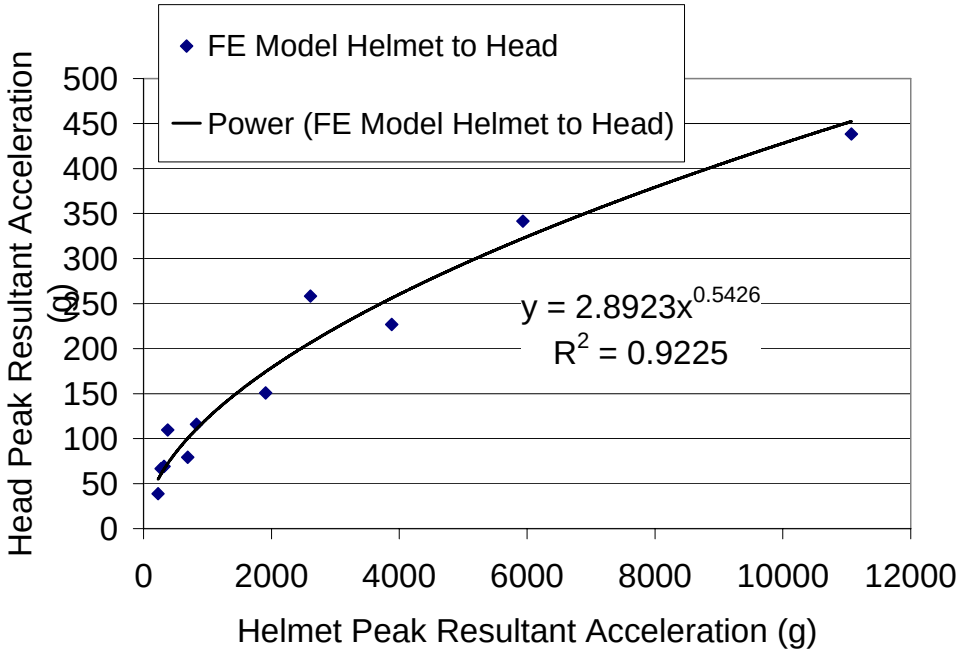

Figure 2.1.4.5.2-1. Helmet to Head Transfer for Peak Resultant Acceleration

2.1.4.6. Discussion of Finite Element Results

The results of this study imply that the computation of ACH-like helmet response to head response is well behaved under the controlled circumstances modeled in this limited study. It is also clear that padding choice has the potential for improving the protective capabilities of military helmets in blast, confirming previous experimental studies [3]. This study also identified certain characteristics of foam materials that may enhance or degrade the protection capabilities of the helmet. These assessments were based on analyzing the global response of the head and the local response of the brain subsequent to blast impingement. However, the helmet protection cannot be truly evaluated until blast brain injury mechanisms are properly identified, and injury metrics are established.

Based on the metrics used in this study, the helmet reduced the effects of blast exposure relative to the unprotected case in all measures investigated in this study. While use of the helmet augmented the response of the head at low blast levels, helmet attenuation increased with increasing blast pressure such that the helmet offered better protection at blast levels that are considered injurious. Lower foam density decreased peak head acceleration and peak brain pressure. Strains induced by the primary blast wave itself were very small, but helmet-head coupling post-blast intensified the relative motion between the skull and the brain leading to greater tissue deformation. Coupling was reduced with crushable foams, which generated lower HIC values and lower brain strain than flexible foams. Furthermore, crushable foams reduced the magnitude of KE of the head by dissipated energy owing to the crushing action during the loading phase of impact.

The metrics used in the current study to assess helmet protection were based on global kinematic and responses that have been associated with head and brain injury in the past. Peak

head acceleration is used in many helmet standards for blunt impact protection, including the ACH. The ACH specifies that helmets must produce less than 150 Gs peak headform acceleration from a 3.0 m/s (10 ft/s) impact [5]. This criterion is easily exceeded for even relatively mild blast levels [4].

The current HIC tolerance specified in FMVSS 208 (Occupant Crash Protection) for blunt head impact of a mid-sized male is 700, which the head acceleration data to be filtered at 1650 Hz (CFC1000). At this filter frequency, a significant portion of high frequency blast data is removed, and the acceleration pulse decreases in magnitude and increases in duration, decreasing the HIC value. Thus, established practice for using HIC for blast biomechanics is to filter data at 40 kHz [28]. It is uncertain if HIC can be adopted or adapted for use in unprotected blast injury, as the HIC durations are far less (< 0.5 ms) than that of the blunt impact durations used to formulate the criterion [27]. However, helmet protection effectively widens the acceleration pulse of the head in blast, causing HIC durations to be within the range that HIC was originally developed. Thus, use of HIC with for a protected head in blast may be applicable.

2.1.4.7. Validation Results

Upon further investigation of the freefield PMHS data, the head CG accelerometers gave a response, but one indicative of broken sensors (Figure 2.1.4.7 – 1). Each accelerometer is attached to the same rigid body, so each should respond to the input at approximately the same time. However, the X and Y responds about 0.5ms late and it oscillates at a much different frequency as the Z-acceleration. The response of X and Y acceleration resembles that of a broken strain gauge. Due to this issue, the finite element model could not be validated with the freefield data.

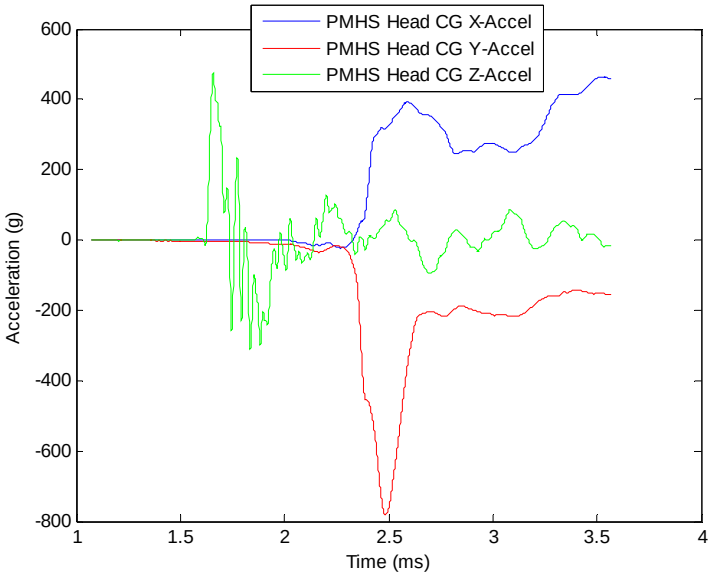

Figure 2.1.4.7 – 1. PMHS head CG response to explosive blast overpressure wave from test 2.07.

2.1.4.8. Analysis and Discussion

Limitations of this study include the assumption of plane strain; the predicted values reported in this study will change if modeling the three dimensional head and helmet. Helmet and head aerodynamics decrease the acceleration of the head and pressures seen in the brain. Helmet straps, although not likely to have substantial effect in the pressure propagation phase, may have an effect during the helmet/head coupling phase. However, as this study was comparative (helmet cases to non-helmet cases), it is likely that the relative results reported in this study would still apply in three dimensions, and that relative response between helmet configurations will be consistent.

2.1.5. Discussion of Results

Simply by reviewing the available shock tube test data, it was apparent that the simple linear method would not be adequate to identify the variety of potential blast scenarios. Both the lumped sum model and the FEM were assessed against the available free field blast test data collected during phase 4 (Section 2.4). Neither performed particularly well, and as they stand, the lumped sum model was somewhat superior and affords a 50% solution. The recommended improvements would benefit both models, however, the final selection will depend on a number of factors:

- Availability of material properties data to inform the FEM appropriately.
- On board computational capability of the HMSS or computer using the model.

FEMs historically use significant computational power to run, and it may not be realistic to require a deployed medic to run a simulation for 5-10 minutes or longer for every blast event recorded on every HMSS he may be responsible for downloading. This is the value of an engineering model like the lumped sum model. The FEM can provide valuable data for informing the lumped sum model, and this simplified model can run instantly on most computers and provide a reasonable estimate of brain response based on the sensor input from the field.

The helmet exhibited a significant resonance response to both shock and ballistic loads during the tests, as did the FOCUS headform. This indicates that the helmet and headform exhibit a multi modal response and additional blast and materials testing are necessary to enable the models to account for this response. An initial, low frequency modal analysis was completed by Duke University to initially characterize this effect.

2.1.5.1. Key Research Accomplishments

- Application of finite element model for helmet/head interactions in blast based on an ACH helmet and various padding types including current ACH padding (Team Wendy).
- Determination of transfer function between helmet and head peak resultant acceleration. Stable nonlinear fit emphasizes potential for developing helmet to head transfer functions.

- Investigation of padding properties demonstrates the potential for the optimization of pad properties for blast protection. This study also identified certain characteristics of foam materials that may enhance or degrade the protection capabilities of the helmet. However, the helmet protection cannot be truly evaluated until blast brain injury mechanisms are properly identified, and injury metrics are established
- A lumped-parameter numerical model was created in Matlab.
- The model was used to model the numerous physical shock tube tests performed by ARA.
- Identified limitations of the numerical model and areas to improve model performance.

2.1.5.2. Modal and Dynamic Analysis of Helmet Systems

2.1.5.2.1. Background

As specimen response to blast has much higher significant frequency content than is usual for automobile impacts, HIC has been evaluated for blast with a $4x10^4$ Hz HIC filter rather than a 1650 Hz filter used in automobile impacts. This will increase the HIC value for blast relative to automobile impacts, likely requiring a modified injury reference value. Further investigations are required to determine the effects of momentum transfer for short duration blasts, but it has been asserted that the low rate HIC value with the high rate filter is conservative for blast with the high rate filter. Historically, closed injuries from blast have been recognized only in gas-containing organs such as the lung and bowel.

It is unknown whether brain injury produced by blast (high rate) may be differentiated from ordinary blunt trauma (low rate), but several pieces of evidence suggest that the mechanisms of injury at high rate may be different than those at low rates. Though novel mechanisms have been proposed for blast brain injuries including high rate thermal and/or radiofrequency (RF) coupling with human tissue, one likely mechanism is a high rate mechanical insult to the brain that triggers neurochemical cascades leading to cellular or axonal degeneration at strain levels much lower than those seen in low-rate events that cause brain injury (automobile crashes, falls, etc.).

A recent test series was constructed to minimize RF and thermal coupling with the test specimen to evaluate the effect of high rate mechanical insults alone. These tests found evidence of brain injury in large animal specimens for short duration blasts that do not result in fatal pulmonary injuries. Diffuse axonal injury from these blasted specimens was compared with the control specimens that resulted in no injuries (Figure 2.1.5.2.1-1).

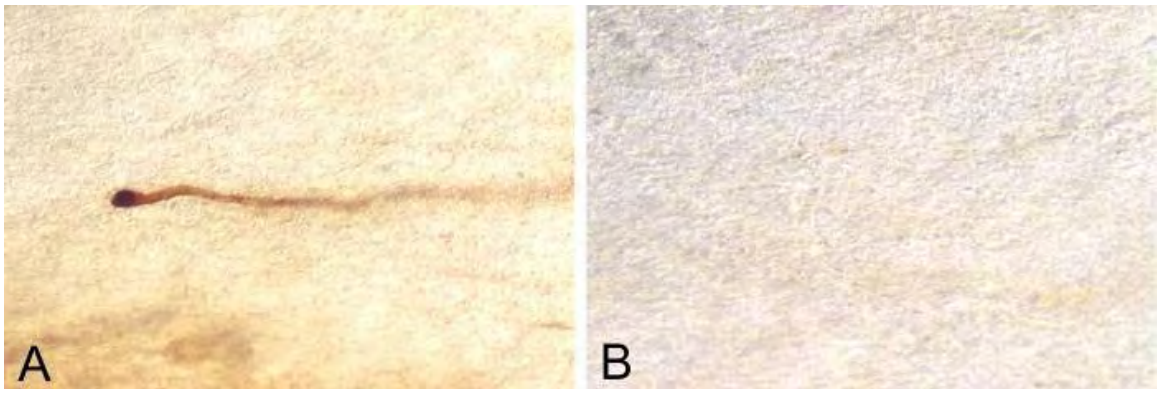

Figure 2.1.5.2.1-1. Blast brain injury. A. Diffuse axonal injury in blasted specimen, B. No injury in control specimen

Mechanical response of the specimen head under these blast conditions were assessed using HIC. For this high frequency weighted HIC calculation, the values obtained during testing for all test conditions are still below the low frequency HIC reference value of 1000 as seen in Figure 2.1.5.2.1-2. These HIC values may represent a high-rate threshold brain injury value. It is important to note that momentum transfer in blast under the conditions tested is generally lower than momentum transfer in injurious automobile crashes with attendant lower brain strain . This may indicate a different injury mechanism in blast than large deformation brain strain usually attributed to automobile crash brain injuries. There have been a number of criticisms of HIC for low rate impacts, including the lack of rotational dynamic inputs. However, better assessment techniques are currently unknown, and the suitability of the application of HIC to high rate blast is unknown.

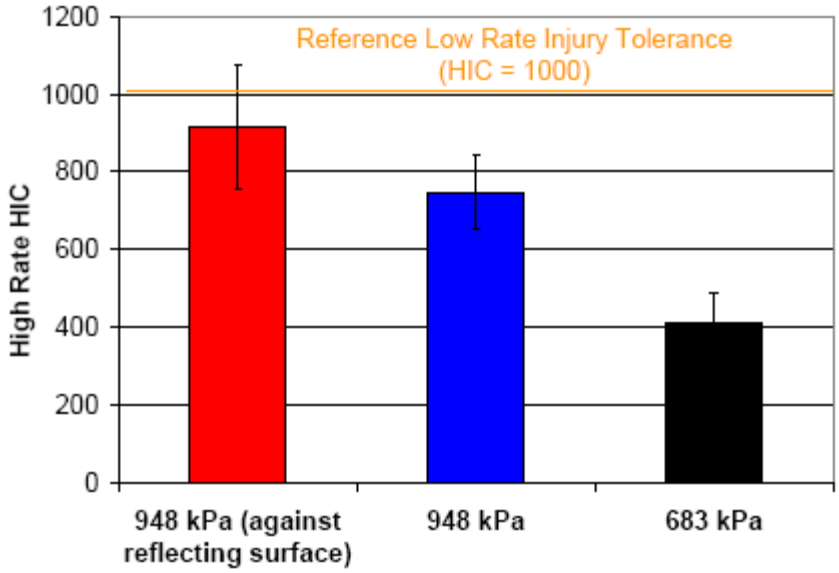

Figure 2.1.5.2.1-2. Average HIC Values for the Varying Test Conditions (Average incident pressure for each condition is reported below the graph).

Neck injuries from blasts are possible because the head and the chest may experience accelerations independent of one another under blast loading. Physical trauma to the neck may be evaluated using neck force transducers that may be incorporated into the Hybrid III dummy. Barring local damage to the neck itself, the dynamic impulse in the neck must be transmitted through the relative motion of the head and the chest. This transmission of force is relatively slow compared to the impact of the blast wave. Therefore, neck injuries in blast are similar in rate to impact neck injuries that have been identified in automobile safety and other contexts. Two existing neck injury criteria are appropriate. For upper neck injuries, an injury standard exists for the Hybrid III dummies promulgated by the U.S. Department of Transportation termed the Nij criteria. An injury reference value of Nij = 1.0 corresponds to a 30% risk of severe neck injury. For lower neck injuries under inertial loading, an injury criterion has been developed based on lower neck force and moment values of cadaveric specimens. Both criteria account for the effects of neck tension/compression loads and flexion/extension moments. While the Hybrid III neck is not especially biofidelic in bending, this may be less important in blast where large motion kinematics is not expected to dominate injury mechanisms.

2.1.5.2.2. Experimental Variables/Sources of Variance

Real-time engineering field data of direct blast exposure may provide medical personnel with an immediate assessment of the risk of brain injury, and lead to faster and more effective medical treatments. However, mounting such instrumentation in a robust, repeatable and unobtrusive fashion is difficult. One approach is to mount instrumentation, including accelerometers, angular rate sensors and pressure sensors to a Soldier's helmet. However, inputs to existing low-rate injury criteria require head-centered engineering data. To attain this data requires an association of the blast response of the helmet with that of the head and brain for existing low-level injury criteria and, presumably, for any future blast injury criteria. This association is complicated by helmet mechanical response and deformation, by helmet position, by padding response and padding conditions, Soldier anthropometry, temperature, presence of moisture and other complications. The most important sources of variance are discussed below.

1. Helmet type: The low and high rate mechanical response of nominally identical helmets from different manufacturers is not necessarily the same. Further, the existing compliance tests, ballistic tests and drop tests, do not completely mechanically constrain the helmet response. This study will focus on a single all Kevlar helmet type from a single vendor though later studies may include helmets from other vendors.
2. Helmet variables will include helmet position (e.g., azimuthal or axial rotation misfits) and helmet size.
3. Human anthropometry: The potential Soldier population includes males and females of various anthropometric dimensions. This population presents large variation in general size and detailed width and length-related detail. Further, the presence of moisture, hair and other factors may influence detailed helmet response. Testing using post mortem human specimens (PMHS) may be used to quantify variance in human anthropometry and interfacial effects including water.

4. Dummy anthropometry: Dummy tests are used for development and compliance testing of helmet systems. There are several available dummies, including the Hybrid-III, FMVSS-218, and Army Thor head and neck systems.
5. Padding type: The padding types currently used are viscoelastic, and the response may be strongly temperature sensitive. Further, the pads may be relocated or not used at all. Available current padding includes MSA and Team Wendy pads. Additional padding systems may include the Skydex pad and other potential padding systems.
6. Loading direction: The response of the helmet may change with direction of loading. The current protocol includes impacts at seven different impact sites on the helmet. However, response variation may occur between impact sites. Further, variation in response may result from rotation and from glancing impacts which may be offset in the coronal, sagittal or transverse planes. Indeed, in scenarios such as IED impact initiating vehicle rolling complex loading patterns are likely.
7. Loading rate: Between blunt impacts and blast or ballistic impacts, the strain rate in the helmet material, and hence the loading rate, may vary from slower than 1 s-1 to faster than 1000 s-1. The type of impact will change the response of the helmet and hence, the response of the sensor system. For low rate blunt impacts, velocities of 14 ft/sec, 10 ft/sec, and 7 ft/sec may be considered typical with ~5 kg headforms. For ballistic impacts, the helmet may see large backface deformation. Depending on range, helmets may accelerate greater than 4000G under nonlethal blast loading.
8. Helmet accessories: The structural response of the helmet will be affected by the addition of mass and structural components onto the helmet shell. Soldiers frequently attach different accoutrements to their helmets depending on the particular mission requirements. These devices could include any combinations of night vision systems, mounting brackets, battery packs, communication systems, and face shields, etc. Additionally, the helmet response could be further affected the use and tension in the chin and nape straps, especially the low rate blunt impact response. Owing to time-duration and response effects, it is unlikely that the use of the chinstrap will affect high rate response. However, it is important to confirm this.
9. External clothing: External clothing worn under or over the helmet, such as the flash balaclava (e.g. nomex hood), watch cap, chemical-biological protective gear, or camouflage covers may alter the transfer function between the helmet and the head.

These variables are also complicated by the different energy sources that apply external loads to the helmets. These energy sources include blast overpressures, ballistic impacts, and blunt impacts. These energy sources result in different loading rates being applied to the helmet which could alter either the helmets mechanical and dynamic response and thereby require a unique transfer function for each energy source.

As a preliminary stage in the development of an analytic transfer function that uses helmet accelerations to predict head center of gravity accelerations, a modal analysis of the helmet mechanical response is necessary to determine the dynamic vibrational response from an impulse input. This may be used to assess local stiffnesses as a function of the input acceleration and boundary conditions, local dampling ratios, and local response to acceleration input. This is

necessary to determine the helmet vibrational response, and to separate this response from the whole helmet motion that may be transferred to the head.

2.1.5.2.3. Modal Analysis Methodology

Modal analysis (eg. Nightingale, 1991) was performed on 5 ACH helmets, including all helmet sizes (S, M, L, XL, XXL), to determine the natural frequency of each helmet. The helmet was struck with an impulse hammer in various locations and the resulting vibration was measured. Accelerometers allowing for the measurement of 6 directional degrees of freedom were placed at the apex of the helmet. The helmet was struck at 5 equally spaced locations in the midsagittal and midcoronal planes. With 10 locations of impact and 5 tests per location, there were 50 total tests per helmet. This will enable a characterization of the vibrational response of the helmet subject to impacts at various locations along the surface of the helmet. The accelerometers capturing the data include a PCB Triaxial Accelerometer to measure x, y, and z accelerations and three DTS-ARS angular rate sensors to measure the rotation about these axes.

Additional testing was performed to further characterize the vibrational response of the large sized helmet. This included mounting the sensors on the inside of the helmet, mounting the sensors at a 2nd location between the midsagittal and midcoronal planes, with and without pads on the inside of the helmet, and with the helmet placed on top of a Hybrid III headform with the chinstrap at two levels of tension. With a total of 10 test conditions, and 50 tests per condition, 500 tests were performed.

The helmet was isolated to minimize the effect of surrounding noise and vibrations in the room by being suspended by a fishing line connected to a horizontal beam. The helmet was assumed to come to a complete rest 120 seconds after the last time it was touched. At this time, the helmet was struck with the impulse hammer and allowed to resonate until the vibration dissipates.

The data analysis consists of normalizing the acceleration response to the applied force input. Then, a fast Fourier Transform was applied to the resulting time domain transfer function to compute the fundamental frequencies and the natural frequency of the helmets. This was performed for each of the 32 tests on each of the 5 helmets.

Test Equipment:
3x DTS-ARS Sensors (Strain Gage)
1x 500g PCB Triaxial Accelerometer (ICP)
1x PCB Impulse Hammer (ICP)
25 lbs Test Fishing Line
Fishing Swivels

Table 2.1.5.2.3-1.
Test Matrix for Modal Analysis Testing

Date	Test	Helmet Size	Pads	Sensor Location	On Hybrid III	Number of Impact Locations	Repeats	Total
7/2/2009	L-NP-AO	Large	No	A, outside	No	10	5	50
7/2/2009	L-NP-AI	Large	No	A, inside	No	10	5	50
7/2/2009	L-P-AO	Large	Yes	A, outside	No	10	5	50
7/8/2009	L-NP-BO	Large	No	B, outside	No	10	5	50
7/8/2009	S-NP-AO	Small	No	A, outside	No	10	5	50
7/8/2009	M-NP-AO	Medium	No	A, outside	No	10	5	50
7/8/2009	XL-NP-AO	X-Large	No	A, outside	No	10	5	50
7/8/2009	XXL-NP-AO	XX-Large	No	A, outside	No	10	5	50
7/9/2009	L-P-AO-H3-L	Large	No	A, outside	Yes	10	5	50
7/9/2009	L-P-AO-H3-T	Large	No	A, outside	Yes	10	5	50
								500

Figure 2.1.5.2.3-1. Test setup and instrumentation for the large helmet setup

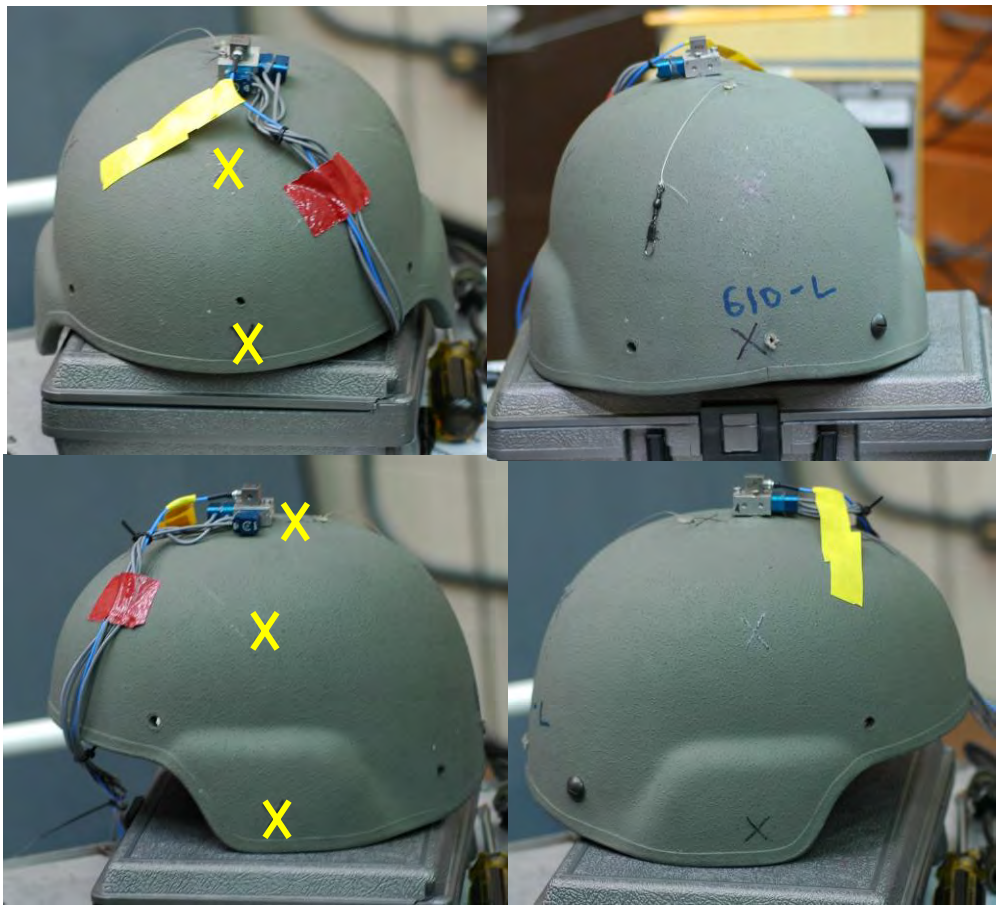

Figure 2.1.5.2.3-2. Impact Locations for the front (top right), back (top left), left (bottom left), and right (bottom right) sides of the large helmet.

2.1.5.2.4. Modal Analysis Results

Data was collected at a sample rate of 100,000 samples per second and filtered at 6000 Hz. This was done to remove high frequency noise from the data. Such a low filter level was chosen because the frequency content of the input force from the impact hammer had a maximum of 2000 Hz. This means that the frequency content of the resulting vibration will not contain frequencies greater than 2000Hz, and anything greater than 2000 Hz is considered to be noise. A typical force impulse can be seen in Figure 2.1.5.2.4-1. The vibrational response of such an input can be seen in Figure 2.1.5.2.4-2. As it can be seen, the input force has a very short duration of 5 ms and a sharp rise in force. This is a good representation of a typical impulse wave which theoretically should be of infinite magnitude and infinitesimally small duration. The resulting vibration starts out at a high magnitude and exponentially decays to zero. This is typical of any damped, linear system in which the vibrations are allowed to naturally dissipate.

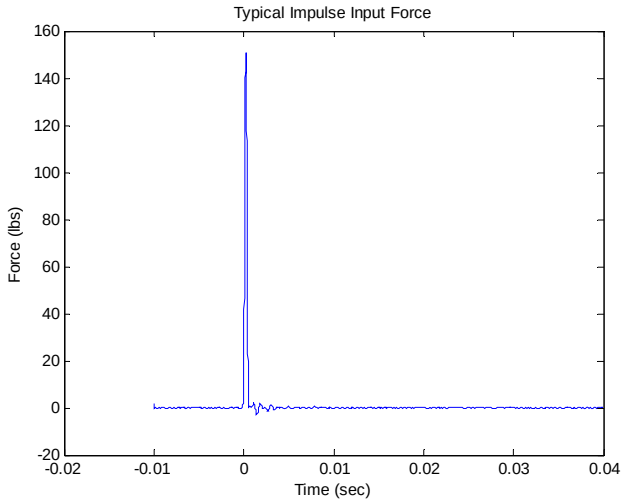

Figure 2.1.5.2.4-1. Typical impulse input force characterized by a very high magnitude and very short duration.

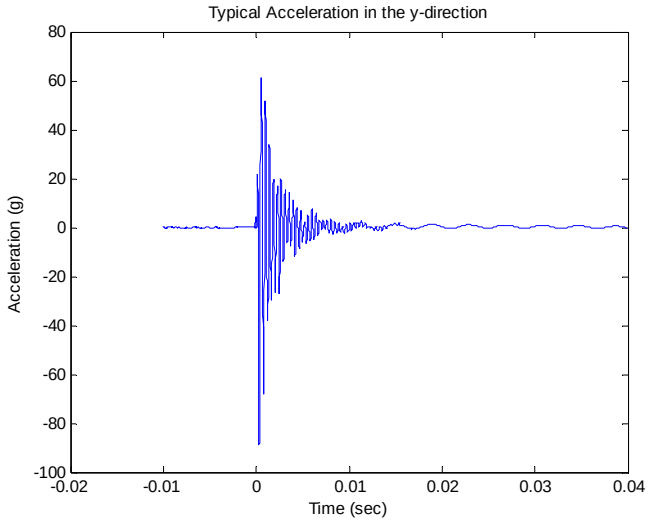

Figure 2.1.5.2.4-2. Typical response to an impulse input force.

It was discovered that impacts at the ear cups of the helmet result in a double impact between helmet and hammer. This is likely due to a higher frequency mode vibrating and striking the impact hammer before it rebounds out of the way. This also occurs for impacts near the brim of the front and back of the helmets. However these front and rear double hits occur much later than those at the ear cups. Due to the double impacts, MC-1, MC-5, MS-1, and MS-5 tests were not included in the analysis. Figure 2.1.5.2.4-3 shows the force input indicating these double impacts.

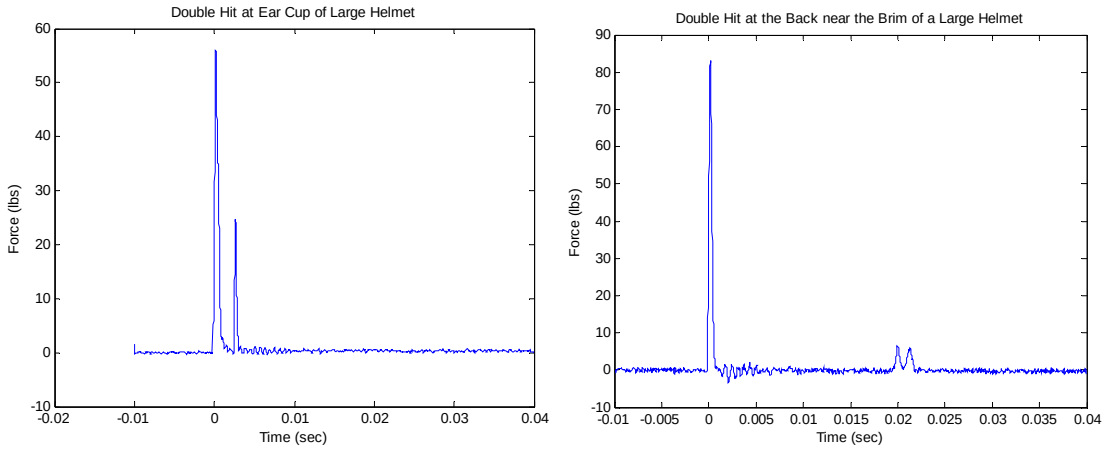

Figure 2.1.5.2.4-3. Double hits at the ear cup and the front of the large sized helmet.

Tables C1 through C10 in Appendix C describe the modal frequencies, magnitudes, and damping ratios for each of the tests conducted. Table C-1 shows the modal parameters for a large helmet without pads and the sensor mounted on the outside surface of the crown of the helmet. From the table, it can be seen that the fundamental frequency varies based on impact location, but it primarily stays 366 Hz with a magnitude of 30dB. However, for the MS-2 location, which is a couple inches up from the front brim of the helmet in the midsagittal plane, the dominant frequency is 787Hz, making this location more susceptible to interference with instrumentation measuring high frequency impacts.

The modal parameters when pads are added under the helmet can be seen in Table C-2. It shows the fundamental frequency drops from 350Hz to 275-330Hz. This is likely the effects of the added mass of the padding combined with the viscoelastic coupling between the pads and the helmet. The natural frequency is inversely proportional to the square root of the nodal mass. By adding mass to the helmet, the natural frequency drops through inertial coupling. The higher frequency modes continue to have similar frequencies and amplitudes.

Mounting the sensor on the inside of the helmet shell has a limited impact on the response, however, mounting the sensor at the second response location does provide evidence of additional response nodes. The transverse speed of sound was measured in the ACH helmet at approximately 1000m/s. For a maximum frequency of 2000Hz, the minimum node spacing was estimated as 50cm. As the helmet is much smaller than this, this calls into question the relevant sound speed for transverse excitations in the helmet.

Table C-5 shows the first vibrational modal frequency for the small helmet is approximately 220Hz with a large amplitude range between 20 and 50dB. Higher frequency modes exist, but at significantly lower amplitude than the lower frequency modes. Also, the small helmet exhibited more low frequency modes than the large helmet.

The medium helmet exhibits similar characteristics with a natural frequency between 170 and 230Hz, but the magnitude is more stable at 25dB. The XL helmet shows a fundamental frequency between 158Hz and 220Hz with a magnitude between 26dB and 32dB. Again, this is

significantly different than the large helmet. The XXL helmet has a natural frequency of 292Hz with a magnitude of approximately 35dB. This is much closer to the response originally seen in the large helmet.

A large helmet was placed on a Hybrid III headform to see if the viscoelastic pads would significantly dampen the vibrations with different chinstrap tension values. The data shows a fundamental frequency around 170Hz at a magnitude of 35dB for a loose chinstrap and the same fundamental frequency with a magnitude of 38dB for a tight chinstrap. So, the difference in chinstrap tension was not reflected in the vibration response at the positions of the response sensors.

2.1.5.2.5. Conclusions

Modal analysis is important in determining the both the energy transfer between the helmet and head and for determining helmet vibrational interference with sensor measurements intended to approximate helmet rigid body motion. If a helmet is excited at its natural frequency, it will act as a mechanical amplifier, and the energy transmitted to the head will be large. With this information, vibrational and damping response may be included in the transfer model to maximize the value of helmet sensor information.

Based on the modal analysis data, there are a large range of frequencies of concern for helmet based measurements with helmets of each size. In particular, the high frequency resonant models will change the sensor response to helmet dynamics and must be included in any transfer function model.

The results show substantial variance in the modal response seen based on impact location, helmet size, and other test configuration parameters. This is consistent with the presence of a nonlinear system, where modal analysis assumes a linear relationship between input and output. This variance can be due to the nodal mass and also the nonlinearity of the system. Due to the complex geometry and the composite structure of the helmet, there were coupled modes which are hard to distinguish. In addition, coupled modes indicate a range of frequencies where the helmet will vibrate at large amplitude.

The data shows the presence of vibrational nodes based on the test in which the sensor was moved from the crown of the helmet to the front of the helmet in between the midsagittal and midcoronal planes. This is likely due to the complex geometry of the helmets.

In conclusion, the modal analysis results will need to be included in any transfer model including impact location and helmet size. This information is an important precursor to the development of transfer models for blunt, ballistic and blast trauma and will need to be incorporated into any future head-based injury criterion using helmet mounted sensor systems.

Further work includes the investigation of the dynamic response of the loose coupling between the head and the helmet. As existing and future injury criteria are head-based, and as there are substantial differences in response between the head and the helmet in blast and blunt

trauma environments, the helmet modal response is essential to the development of an analytical or computational technique for transferring helmet to head dynamic response.

Additionally, the frequency content of the blast wave impacting the helmet includes modes significantly higher in frequency content than the 2000 Hz studied with the impact hammer. Further investigation of the helmet response at their higher frequencies is necessary to identify potential resonant frequencies in that range.

Finally, through the data collected during the shock tube tests in Phase 1, significant differences in the FOCUS Headform and PMHS Head responses were identified. It is apparent that the FOCUS and PMHS head also have resonant frequencies in the range of interest that differ significantly from each other. In order to adapt test data from these headforms into a transfer function, it is further necessary to identify those resonant frequencies to enable filtering them out of the data.

2.1.6. Analysis and Conclusions

At this time, due to the lack of appropriate high rate material response data for the helmet pads, and the need to identify the high frequency resonance modes for the helmets and headforms, neither transfer function model is ready for operational use. However, based on operational requirements for a helmet to head transfer function, both the lumped parameter and the FEM should have significant roles to play.

The nature of the helmet to head interaction is dynamic and nonlinear. These problems are ideal for finite element methods. However, FEMs are rarely simple and fast enough to be an operational tool. By including characterization of the high rate material responses for the helmet pads, and enabling the model to filter out resonance responses of the helmet and headform, the FEM would become a valuable research tool that could inform the engineering model. For example, first principles numerical model simulations have been used to build datasets that generated simpler blast environment methods.

The Lumped parameter model, when properly informed with the same material properties and response frequencies of the FEM, will make an ideal tool for far forward use and enable front line medics and doctors to assess for potential TBI.

The following conclusions are made based on the results of the model development under Phases 2 and 3:

- The helmet reduced the effects of blast exposure relative to the unprotected case in all measures investigated in this study. While use of the helmet augmented the response of the head at low blast levels, helmet attenuation increased with increasing blast pressure such that the helmet offered better protection at blast levels that are considered injurious. Lower foam density decreased peak head acceleration and peak brain pressure.
- Strains induced by the primary blast wave itself were very small, but helmet-head coupling post-blast intensified the relative motion between the skull and the brain leading to greater tissue deformation. Coupling was reduced with crushable foams, which generated lower HIC

values and lower brain strain than flexible foams. Furthermore, crushable foams reduced the magnitude of KE of the head by dissipating energy owing to the crushing action during the loading phase of impact.

- A modal analysis of the high frequency response and determination of the high rate nonlinear material properties of the helmets, pads, and FOCUS headform will be necessary to complete development of the FEM and transfer function.
- The blunt impact criterion specified for the Army current combat helmet (150G peak acceleration) is easily exceeded for even relatively mild blast levels.
- The lumped-parameter numerical model best fit the exposure data from the 15 psi incident pressure, 3 ms duration test condition.

2.2. First Generation Helmet Mounted Sensor Assessment

The objective of this task was to determine how well the output from the HMSS matched the output from the lab sensors. The collected signal data was also evaluated for evidence of baseline shifts and drifts. To meet this objective the performance of two of the first generation helmet mounted sensor systems (HMSS) were compared to the output from an array of laboratory style sensors. The lab sensor arrays were placed in close proximity each of the HMSS and collected similar data to the HMSS. Table 2.2-2 is an overview of the key features of each HMSS compared to the lab sensors. For the purposes of this report the HMSS will be referred to as HMSS-A and HMSS-B.

Table 2.2-2:
Comparison of Key Features

Feature	HMSS A	HMSS B	Lab Sensor
Sensor Location	Inside at Apex	Exterior on Back	Multiple
Pressure	Time history	Peak in Bars	Time History (4 Loc)
Pressure Loc	Interior	Exterior	Exterior
Accel Directions	X,Y,Z	X,Y,Z	X,Y,Z (2 Loc)
Sampling Rate	~20k samples/sec	~10k samples/sec	2,000k samples/sec
Trigger	90g	90g	System Trigger
Pre Trigger	None	None	40 ms
Filtering	Variable (1,650 Hz)		Variable (200,000 Hz)

2.2.1. Description of HMSS A

The HMSS-A helmet mounted sensor system intended to measure helmet accelerations in three directions and overpressures inside the helmet while in an operational military environment. The located of the system is the apex of the helmet on the inside surface. The unit is microcontroller and self triggered when a threshold level of 90g is crossed by any of the

accelerometers. The data is then stored on non-volatile memory for later retrieval. Acceleration and overpressure data logged by HMSS-A are downloadable to a windows based PC running the HMS Download Utility application (Figure 2.2.1-3) via a micro USB cable. The HMSS-A Download Utility outputs the data stored in unit into three files.

The download process is completed in two stages. The first stage is to acquire the list of stored events in the recorded. The second stage is to download the events and then upload them to the PC. When the event data is uploaded to the PC the data is stored in a subfolder called "data". In the data folder, one subfolder is created for each recorder using the recorder's serial number. Two types of files are created in each recorder folder:

1. A file called eventlist.csv contains a list of all events that are stored in the folder for that specific unit.
2. THE second type of file is the event file. This file has a specific naming convention XXXXX-YYYYY.csv where XXXXX represents the serial number of the recorder and the YYYYY is the unique identifier (eventID). The files are text files with comma separated values (CSV).

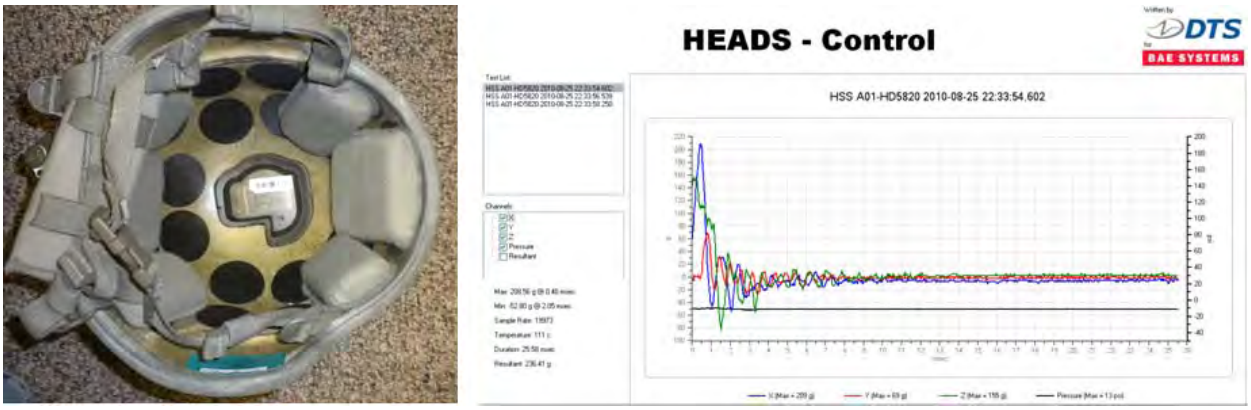

Figure 2.2.1-3: HMSS-A Sensor and Software

2.2.2. Description of HMSS B

The HMSS-B helmet mounted acceleration datalogger is intended to measure helmet accelerations in three directions, peak overpressure and temperature in an operational military environment. HMSS-B is attached to the rear of the helmet sing the existing bolts. The pressure sensor is located on the exterior of the unit recording the peak overpressure measured instead of the pressure time trace. Acceleration and overpressure data logged by the HMS is downloadable to a PC running the HMS Download Utility application via a micro USB cable. The HMS Download Utility PC application displays the downloaded data and saves it to an Excel format spreadsheet file or an ASCII file. The HMS download utility is used to import, view and save files.

From the manual, two types of events are logged: Blast and Non-Blast. To be logged, an event the signal must exceed both the acceleration threshold and either the Blast or Non-Blast

event overpressure threshold. The acceleration threshold, the Blast and Non-Blast overpressure thresholds and the calibration constants are set at the factory and cannot be changed.

Figure 2.2.2-1: HMSS-B Sensor and Software

2.2.3. Comparison Sensors (Laboratory)

A list of laboratory instrumentation is provided in Figure 2.2.4-1. Data was sampled at 2Msamples/second with a 26 msec pre-trigger and 524 msec duration data using a High Techniques meDAQ data acquisition system. The data was downloaded to a PC in WFT format. The pressure sensors listed in Figure 2.2.4-1 were not used in the ballistic testing.

Channel Name	Instrument type	Instrument location	Manufacture & Model
HT1AccX	Accelerometer	Apex of Helmet	Endevco 7270
HT1Accy	Accelerometer	Apex of Helmet	Endevco 7270
HT1AccZ	Accelerometer	Apex of Helmet	Endevco 7270
HTARS	Angular Rate	Apex of Helmet	DTS 50k
HT2AccX	Accelerometer	Above HMSS-B	Endevco 7270
HT2Accy	Accelerometer	Above HMSS-B	Endevco 7270
HT2AccZ	Accelerometer	Above HMSS-B	Endevco 7270
HT Crown	Pressure Sensor	Helmet Crown	Kulite LQ125B
HT Front	Pressure Sensor	Helmet Front	Kulite LQ125B
HT Rear	Pressure Sensor	Helmet Rear	Kulite LQ125B
HT Side	Pressure Sensor	Helmet Left Side	Kulite LQ125B

Figure 2.2.4-1: Laboratory Instrumentation and Location

2.2.4. HMSS Sensor Response and Data Quality

The responses of the HMSS were compared to the laboratory sensors during the shock tube tests and the ballistic tests. During each of the test series the sensors were evaluated for either frontal, lateral or rear impacts. The level of blast and ballistic loading was varied to determine if the sensor could discriminate between the various loads under each condition. The following is a summary of the performance of the sensor compared to the laboratory sensors.

2.2.4.1. Shock Tube Testing

The outputs from the HMSS were compared to the output from the laboratory sensors gathered during a series of shock tube tests. Comparisons were made between pressure reading and the resultant accelerations. For the shock tube evaluation three pressure levels were evaluated as well as three helmet orientations. For each of the head orientations, the head was positioned in three orientations level, head tilted towards the tube and head tilted away from the tube.

The pressure results indicate that there is a poor correlation between the pressure readings captured by the helmet sensors the pressure reading captured by the helmet sensors for the same event as shown in Figure 2.2.4.1-1 and Figure 2.2.4.1-2. The coefficient of determination (R^2) between the HMSS-A and the pressure sensor at the crown was -0.43. This discrepancy is not unexpected since the pressure from the sensor was captured inside the helmet and the lab sensor reading was taken on the exterior surface of the helmet. The reason for the negative R^2 value is the pressure recorded by HMSS had a negative sign. For the comparisons between the pressure measured on the rear of the helmet and HMSS-B located in the same vicinity the R^2 value was 0.16.

For HMSS-B to record the peak pressure the unit must identify that a blast event occurred. Figure 2.2.4.1-3 and Figure 2.2.4.1-4 are a compilation of the accelerations in all of the directions under all conditions. An analysis was completed to determine if the HMSS performed better for a given impact loading condition or direction. The results of this analysis are shown in the Figure 2.2.4.1-6 bar charts. The color core for Figure 2.2.4.1-6 is as follows: Purple bar represents the average acceleration for the lab sensor (HT-1) located at the apex of the helmet; Red represents HMSS-A, yellow represents HT-2; and light blue represents HMSS-B. The error bars are the maximum and minimum value recorded. The standard deviation for each sensor could not be calculated due to the small sample number at each location for each condition.

Table 2.2.4.1-1 shows the accuracy of the unit to identify that a blast event occurred. Figure 2.2.4.1-3 and Figure 2.2.4.1-4 are a compilation of the accelerations in all of the directions under all conditions. An analysis was completed to determine if the HMSS performed better for a given impact loading condition or direction. The results of this analysis are shown in the Figure 2.2.4.1-6 bar charts. The color core for Figure 2.2.4.1-6 is as follows: Purple bar represents the average acceleration for the lab sensor (HT-1) located at the apex of the helmet; Red represents HMSS-A, yellow represents HT-2; and light blue represents HMSS-B. The error bars are the maximum and minimum value recorded. The standard deviation for each sensor could not be calculated due to the small sample number at each location for each condition.

Table 2.2.4.1-1 shows that under certain loading conditions the HMSS-B was not able to identify that the blast occurred and reported no pressure data. The condition that HMSS-B performed poorly was when the blast was delivered to the front of the helmet which is the surface opposite the sensor. In this orientation the HMSS-B predicted correctly the blast occurred in only 40% of the tests. Overall, HMSS-B correctly identified the blast occurred in 70% of the tests. The orientation that sensor performed best was when the blast wave was directed at the rear surface of the helmet.

In addition to recording the pressures, the units captured the resultant acceleration of the helmet. The acceleration results indicate that again there is a poor correlation between the readings captured by the helmet sensors the reading captured by the helmet sensors for the same event. The R^2 between the HMSS-A and the accelerometers sensor at the crown was 0.14. For the comparisons between the resultant acceleration measured on the rear of the helmet and HMSS-B located in the same vicinity the R^2 was improved at a value of 0.62. The same trends in the data for the X, Y and Z directions were similar for both units.

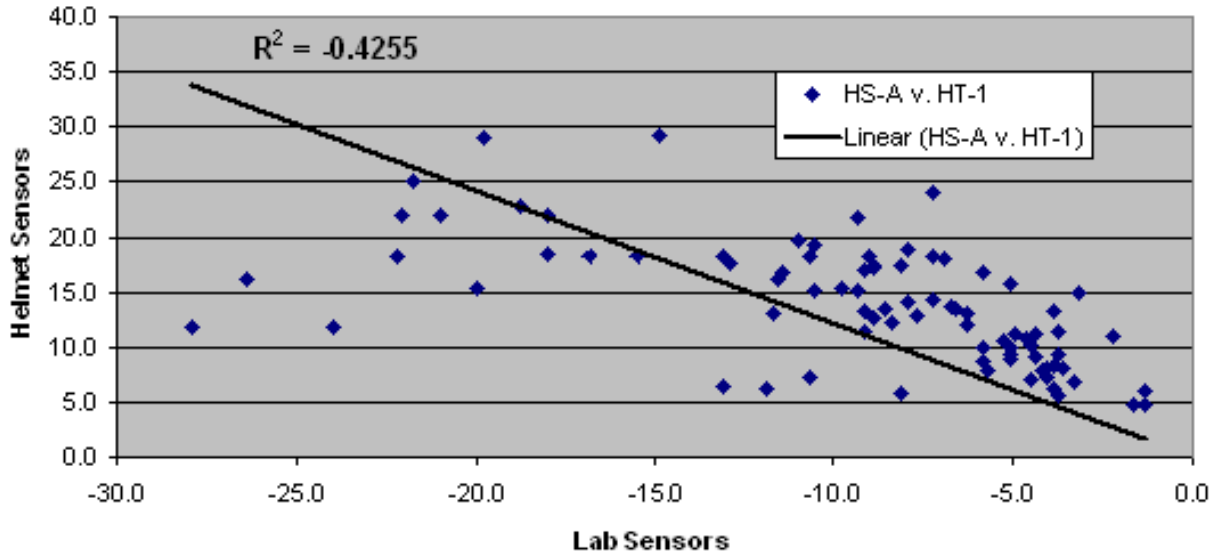

Figure 2.2.4.1-1: Pressures at the Crown of Helmet

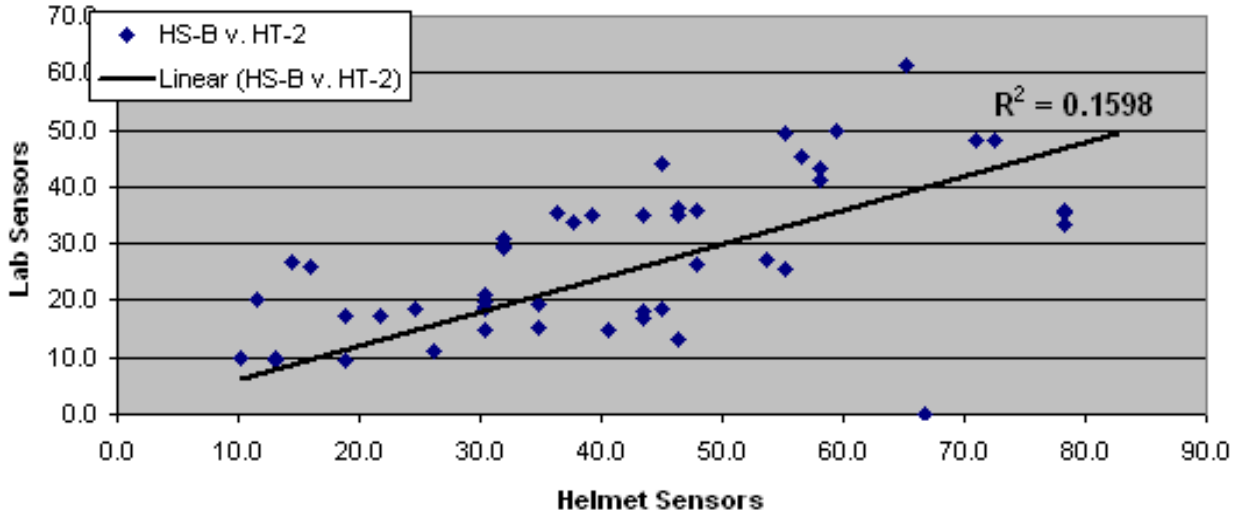

Figure 2.2.4.1-2: Pressures at the Rear of Helmet

Figure 2.2.4.1-3 and Figure 2.2.4.1-4 are a compilation of the accelerations in all of the directions under all conditions. An analysis was completed to determine if the HMSS performed better for a given impact loading condition or direction. The results of this analysis are shown in the Figure 2.2.4.1-6 bar charts. The color core for Figure 2.2.4.1-6 is as follows: Purple bar represents the average acceleration for the lab sensor (HT-1) located at the apex of the helmet; Red represents HMSS-A, yellow represents HT-2; and light blue represents HMSS-B. The error bars are the maximum and minimum value recorded. The standard deviation for each sensor could not be calculated due to the small sample number at each location for each condition.

Table 2.2.4.1-1:
Ability of HMSS-B to Identify Blast Events by Orientation

Orientation	Level	30° Down	30° Up	Overall
Front	36%	41%	42%	40%
Back	100%	60%	100%	87%
Side	50%	100%	100%	82%
Overall	60%	65%	85%	70%

Using Figure 2.2.4.1-6 several observations can be made. The first observation supports the conclusion that the helmet sensors do not agree with the output from the lab sensors. In general the HMSS output is less than the lab sensor in the same region of the helmet. The lower magnitude in signal is most likely due to the difference in sampling rate the frequency response of the sensors themselves. This combination of lower sampling rate and low frequency response affectively filters out the high frequency content of the signal which is captured by the lab sensors and data acquisition system. How important the high frequency content is in terms of injury prediction is unknown but should be captured until that determination can be made.

While the correlation between the lab and HMMS sensors is typically poor there appears to be better agreement when the blast load was directed at the rear of the helmet. One possible explanation is the helmet is more still in this direction and the high frequency content is reduced

Thus far all of the comparisons have been between the lab sensors and the two HMSS. Figure 2.2.4.1-5 and Figure 2.2.4.1-6 shows that there is also poor correlation between lab sensors. The poor correlation between lab sensors suggesting the helmet does not respond as a rigid body. If the shell does not respond as a rigid body during a blast the result suggest one should account for the bending modes if accurate acceleration measurements are to be made.

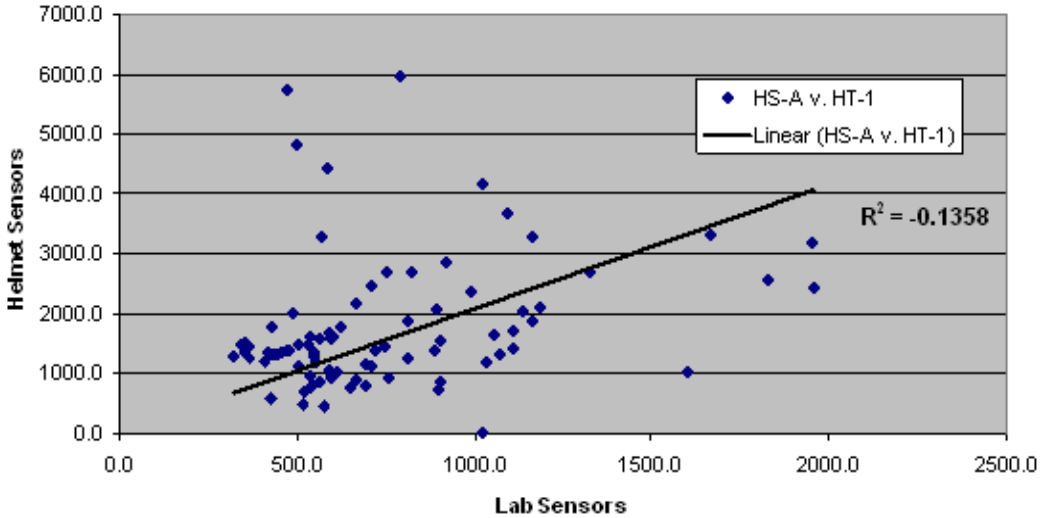

Figure 2.2.4.1-3: Accelerations Measured at the Crown of the Helmet

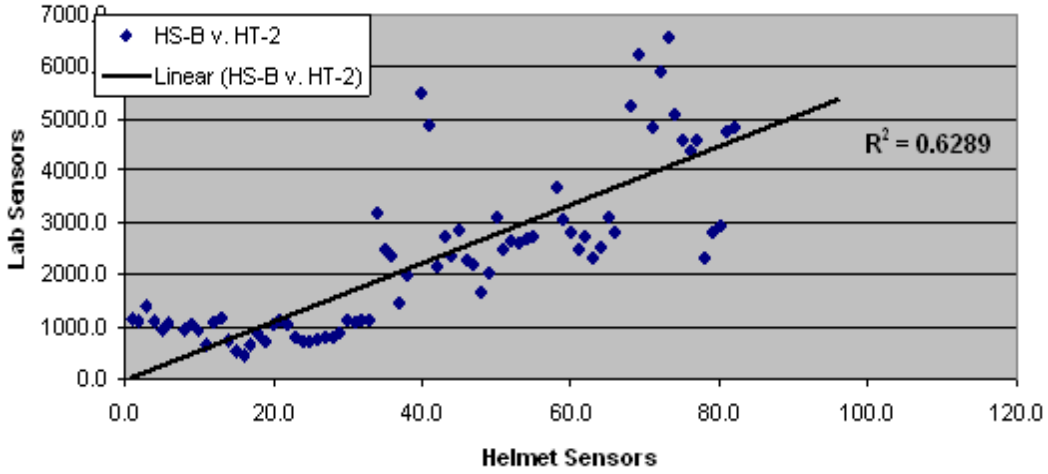

Figure 2.2.4.1-4: Accelerations Measured on the Rear Surface of the Helmet (Shock Tube)

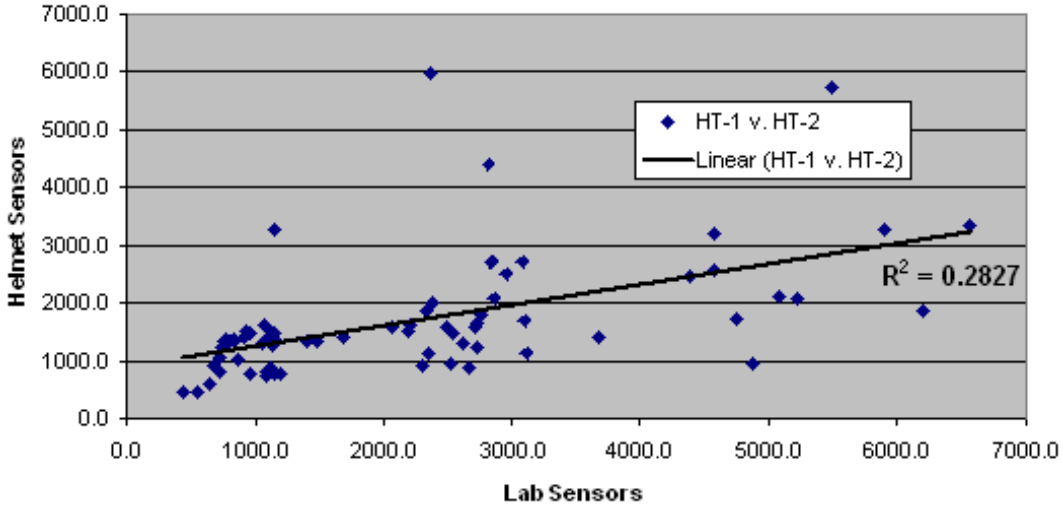

Figure 2.2.4.1-5: Comparison of Outputs between the Lab Sensors (Shock Tube)

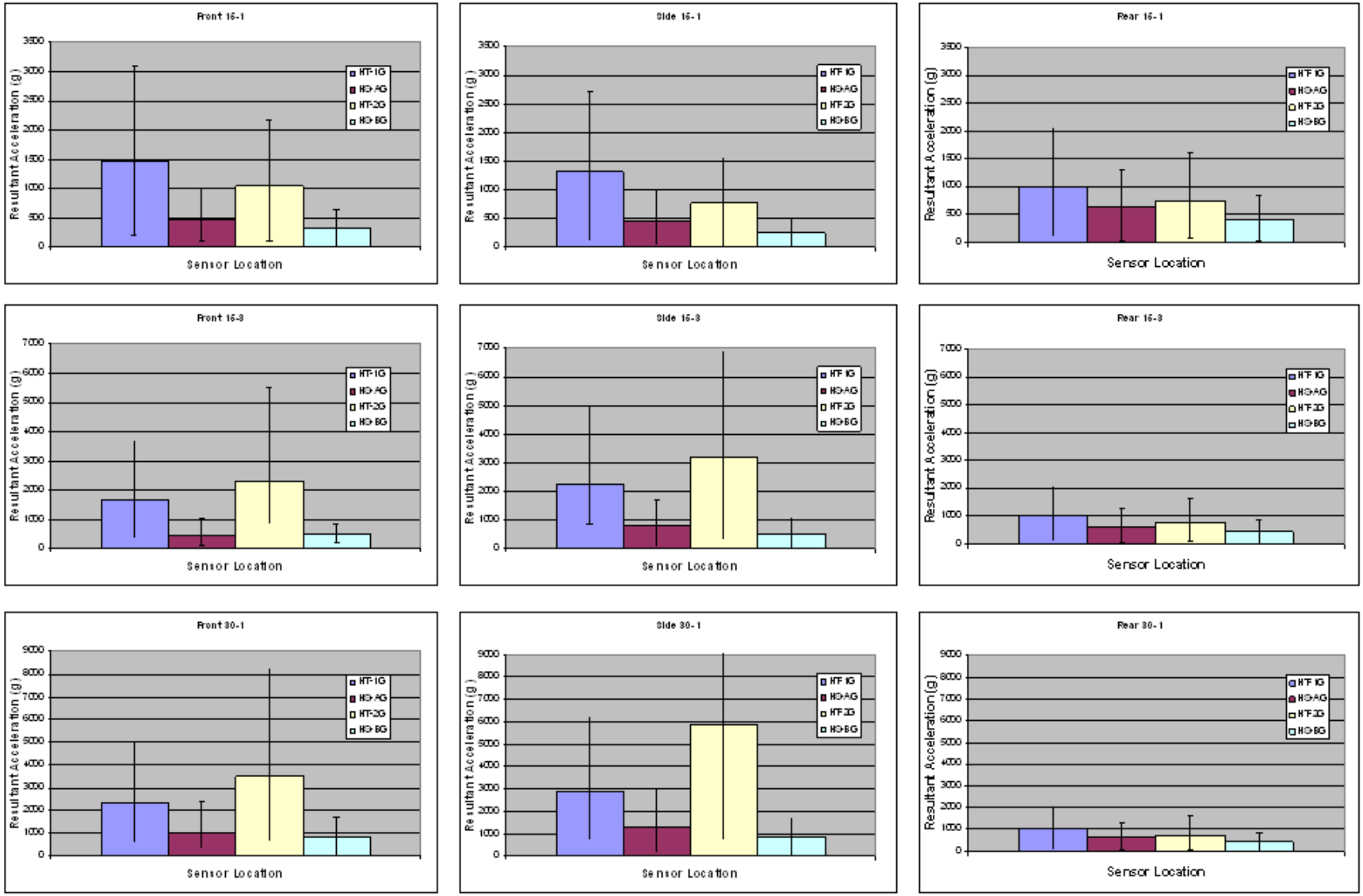

Figure 2.2.4.1-6: Comparison of Acceleration Measurements by Pressure Level and Direction

2.2.4.2. Ballistic Testing

Thus far the discussion has focused on the shock tube results. In addition to shock tube testing, a series of ballistic tests were conducted to evaluate the performance of the two HMSS. The helmet sensor performance for this ballistic test series is shown in Table 2.2.4.2-1. In the ballisitic test series no shots were directed at the rear surface of the helmet so that HMSS-B located on the helmet would not be damaged. Even though no shots were directed at the HMSS-B, the unit did not acquire data on 13 of 18 tests. In each of the failed tests, the unit reported that the battery deactivated before or during the test and no data was found on the unit. In contrast, the HMSS-A sensor produced data on 17 of 18 shots.

Table 2.2.4.2-1:
Helmet Sensor Performance

Round	Velocity	Orientation	HMSS-B	HMSS-A
9mm FMJ	452 m/s	Front	Download successful	Download successful
9mm FMJ	448 m/s	Front	Download successful	Download successful
9mm FMJ	451 m/s	Front	Unit self deactivated	Download successful
225 gr RCC	309 m/s	Front	Unit self deactivated	Download successful
225 gr RCC	316 m/s	Front	Unit self deactivated	Download successful
225 gr RCC	330 m/s	Front	Unit self deactivated	Download successful
225 gr RCC	312 m/s	Lt Side	Download successful	did not recognize post-shot
225 gr RCC	315 m/s	Lt Side	Download successful	Download successful
225 gr RCC	314 m/s	Lt Side	Unit self deactivated	Download successful
9mm FMJ	421 m/s	Rt Side	Unit self deactivated	Download successful
9mm FMJ	428 m/s	Rt Side	Unit self deactivated	Download successful
9mm FMJ	423 m/s	Rt Side	Unit self deactivated	Download successful
225 gr RCC	276 m/s	Rt Side	Unit self deactivated	Download successful
225 gr RCC	280 m/s	Rt Side	Download successful	Download successful
225 gr RCC	292 m/s	Rt Side	Unit self deactivated	Download successful
9mm FMJ	453 m/s	Lt Side	Unit self deactivated	Download successful
9mm FMJ	450 m/s	Lt Side	Unit self deactivated	Download successful
9mm FMJ	452 m/s	Lt Side	Unit self deactivated	Download successful

When activated, both units captured the acceleration of the helmet. Comparison of the HMSS accelerations to the lab sensor results indicate that for ballistic impacts there is a poor correlation between the readings captured by the helmet sensors the reading captured by the helmet sensors for the same ballistic event. The R^2 between the HMSS-A and the accelerometers sensor at the crown was 0.32. The same trends in the data for the X, Y and Z directions were similar. Due to the low data collection rate of HMSS-B under the tested ballistic conditions, a linear regression analysis was not performed for accelerations on this HMSS-B system.

Figure 2.2.4.2-2 is a compilation of the accelerations in all of the directions under all conditions for HMSS-A. An analysis was completed to determine if HMSS-A performed better for a given impact loading condition or direction. The results of this analysis are shown in the Figure 2.2.4.2-3 bar charts. The color core for Figure 2.2.4.2-3 is as follows: Purple bar

represents the average acceleration for the lab sensor (HT-1) located at the apex of the helmet; Red represents HMSS-A, yellow represents HT-2; and light blue represents HMSS-B. The error bars are the maximum and minimum value recorded. The standard deviation for each sensor could not be calculated due to the small sample number at each location for each condition.

Using Figure 2.2.4.2-3 several observations can be made. The first observation supports the conclusion that the helmet sensors do not agree with the output from the lab sensors. In general the HMSS output is less than the lab sensor in the same region of the helmet. The lower magnitude in signal is most likely due to the difference in sampling rate the frequency response of the sensors themselves. This combination of lower sampling rate and low frequency response affectively filters out the high frequency content of the ballistic impact which is captured by the lab sensors and data acquisition system. How important the high frequency content is in terms of injury prediction is unknown but should be captured until that determination can be made. While the correlation between the lab and HMMS sensors is typically poor there appears to be better agreement when the blast load was directed at the rear of the helmet. One possible explanation is the helmet is more still in this direction and the high frequency content is reduced Thus far all of the comparisons have been between the lab sensors and the two HMSS. Figure 2.2.4.2-2 shows that there is also poor correlation between lab sensors. The poor correlation between lab sensors suggesting the helmet does not respond as a rigid body. If the shell does not respond as a rigid body during a ballistic impactthe result suggest one should account for the bending modes if accurate acceleration measurements are to be made.

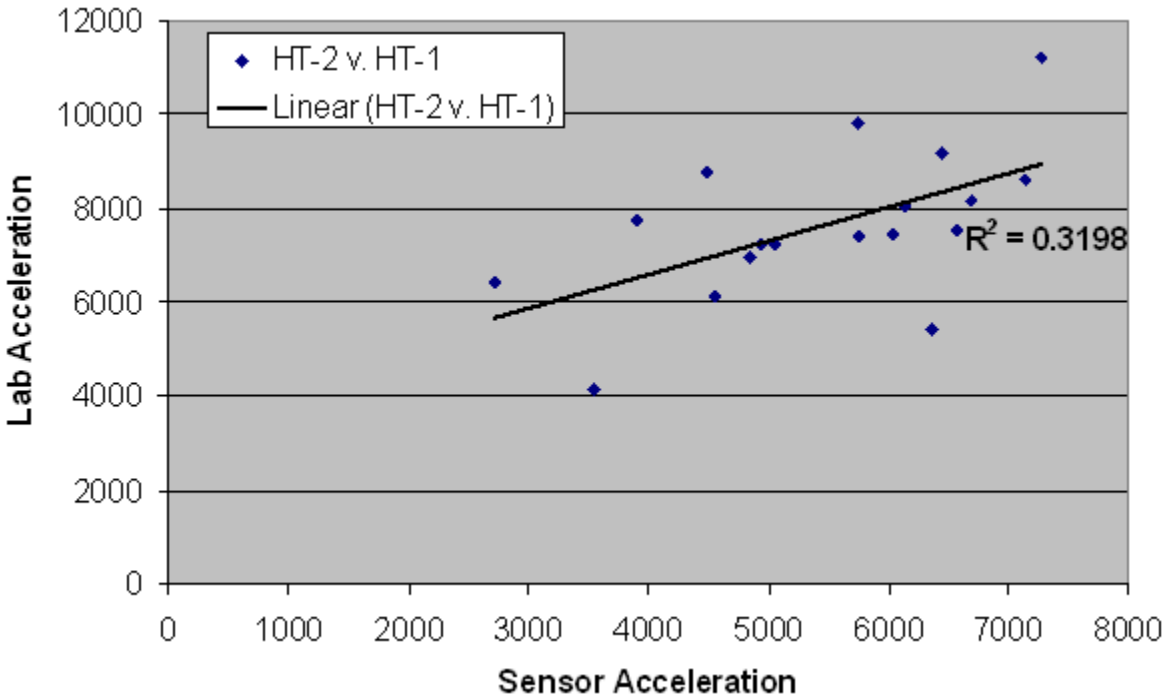

Figure 2.2.4.2-5: Accelerations Measured at the Crown of the Helmet (Ballistic)

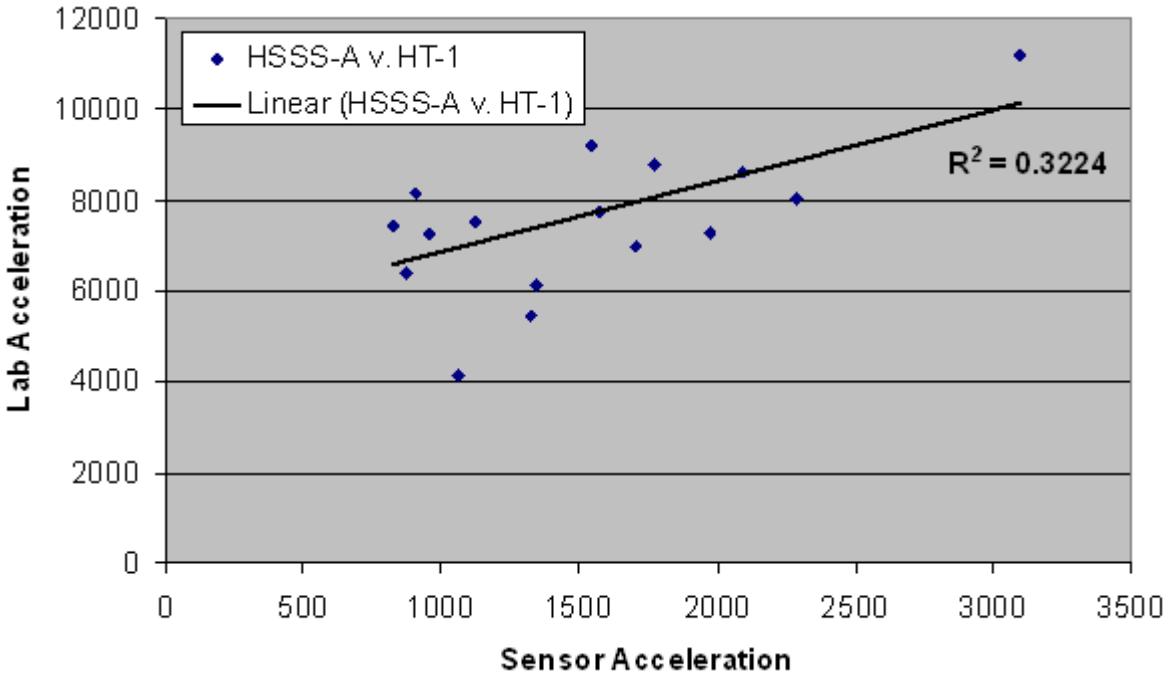

Figure 2.2.4.2-2 Comparison of Lab Accelerations Measured on the Helmet (Ballistic)

In addition to analyzing the the peak values obtained a power spectral density data analysis was completed for the HMSS-A (Figure 2.2.4.2-). This analysis shows a strong resonance at approximately 700 Hz. Owing to its amplitude and location, this is likely structural resonance in the helmet sensor itself. This observation supports a previous observation that the bending modes of the helmet must be accounted for when analyzing the helmet sensor data. Additional research is required to quantify the effect this resonance has on the transfer functions developed.

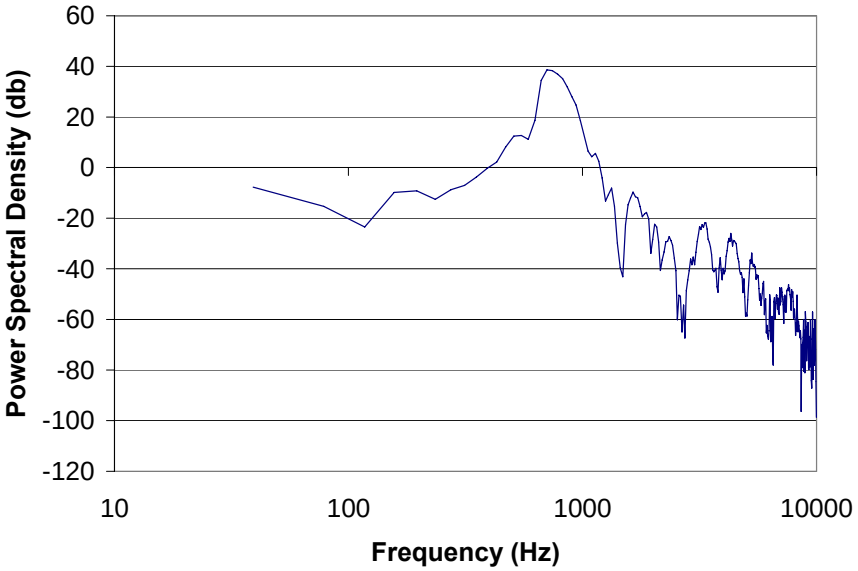

Figure 2.2.4.2-4. Power Spectral Density – HMSS-A (Tes t 9mm_Side)

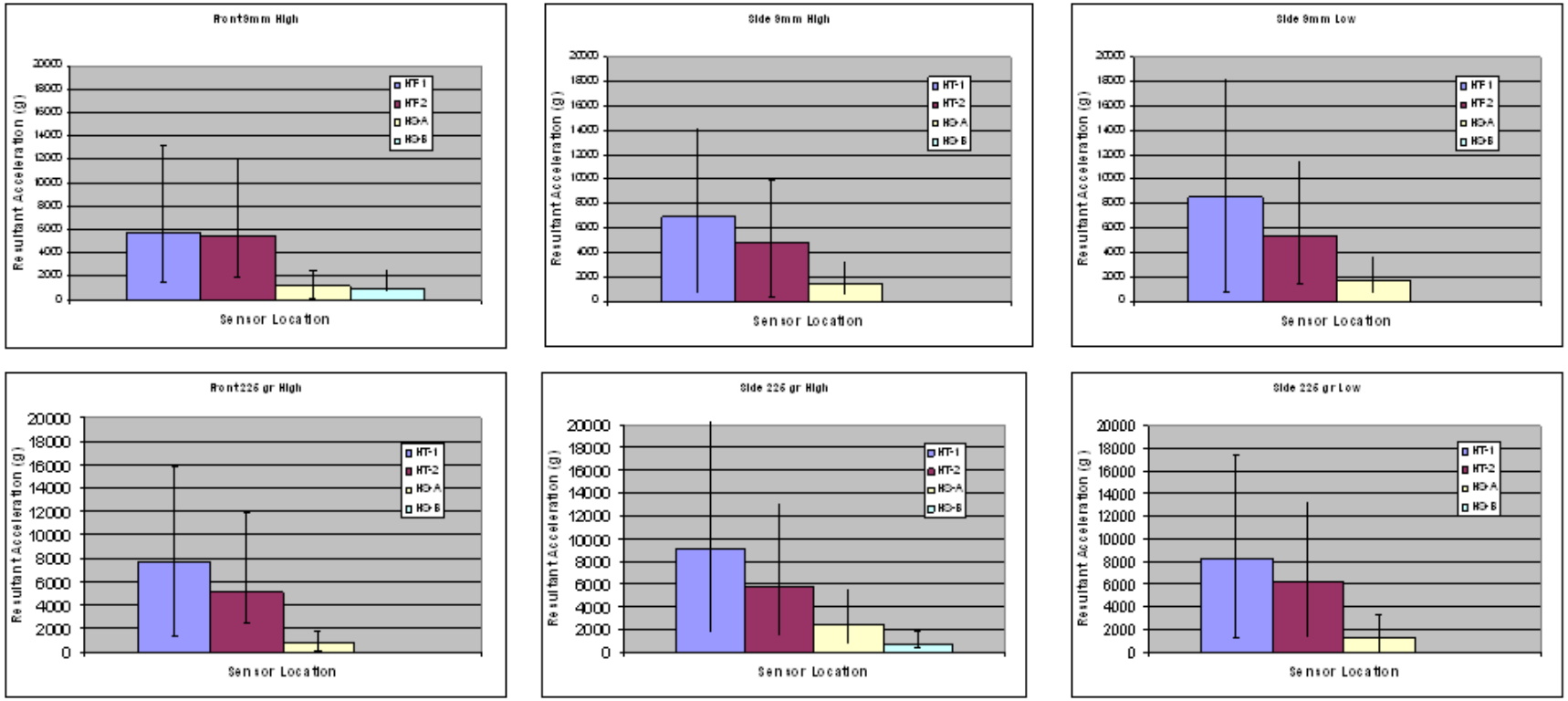

Figure 2.2.4.2-3 Peak Resultant Acceleration – HMSS-A

2.2.4.3. Application of HMSS Results

While the magnitude of the HMSS output poorly represented the magnitude of the lab sensor output, the outputs from the sensors were sufficiently consistent to suggest they could be used to estimate relative differences in the input conditions. Once a data library of a multitude of input conditions is developed, information from the HMSS may be used to estimate the relative magnitude and direction of the threat based on a future library of responses. The following a summary of potential ways the acceleration data could be used to make inference to the environment the helmet was exposed.

2.2.4.3.1. Relative Magnitude of the Blast

Using the acceleration traces, a relative approximation of magnitude of the blast can be made. As such, we tested the HMSS under 3 different blast loads in each configuration. We would expect under each condition to see a greater magnitude response with larger pressures and longer positive phase duration of the blast wave. In Figure 2.2.4.1-6, the bar charts of the acceleration resultants for the HMSS A and B are shown for each series of tests. For HMSS-A the 3-msec shock to the front of the helmet (480 g) appeared similar to the 1-msec shock in the same direction (470g). However, the 30-psi shock caused a significantly higher acceleration traces (1050g) by doubling the magnitude of the resultant helmet acceleration. The differences between all three conditions were much more apparent when examining the traces from HMSS-B (315, 501 & 859g, respectively). The same trends in the data are observed for the side and rear shots although the difference in magnitude changes from direction to direction. These observations suggest that a HMSS could provide a basis for assessing the magnitude of a blast exposure if a well populated database of exposures existed. For this table to be applicable, the direction of the blast or ballistic loading would need to be known in advance. Therefore the magnitude of the blast exposure can only be estimated if the direction of loading is known but there is insufficient connection between the HMSS results and the environmental parameters to quantify the magnitude without the generation of a database of responses.

2.2.4.3.2. Direction of Blast Loading

The following paragraphs provide a potential methodology for estimating the direction of the blast wave using the output from the HMSS. This procedure was found not to be appropriate for quantifying the magnitude of the exposure or the resulting velocity of the head and/or helmet. Therefore the numbers on the y axis for the following figures are provided only to gauge of the relative magnitudes of the x, y and z traces not an estimate of the magnitude of the kinematic motion of the head/helmet system. The following procedure worked best with HMSS-A unit and performed poorly with HMSS-B. The following description is the procedure for determining the direction of impact using only the HMSS-A unit.

The relative magnitude of the traces recorded in the x, y and z directions were observed to have a relationship to the primary axis of the blast. In general, for front or rear shocks the largest magnitude response should come from the X-axis accelerometer with little response from the Y-axis. For a lateral blow the Y-axis would be the primary axis with little contribution from the x-axis. The magnitude of the Z-axis acceleration on either axis could vary as a result of pressure

from the shock moving under or over the helmet when the head is tilted in or away from the shock.

Figure 2.2.4.3.2-1 is the application of this observation. When comparing a series of blast to the front of the helemt, observed was for both the lab and HMSS-A sensors the Y-axis response (in black) was relatively flat in comparison to the X (yellow) and Z traces (green), regardless of the tilt. The same trend between the x and y accelerations were observed when the direction of blast loading is to the side of the helmet (Figure 2.2.4.3.2-2).

The yaw of the blast was estimated by using the Z-axis trace. When the headform is tilted away from the shock, indicating that the blastwave is directed up into the helmet, the Z-axis trace started negative and trended to a postive peak. When the head was tilted into the blast, the Z-axis trace starts out positive but with a negative slope, the trace peaks without going negative, then returns to a large positive peak. When the helmet is level with the blast, the Z-axis trace starts out positive with a negative slope and trends to a negate peak. Below, Figure 2.2.4.3.2-3 shows the response for the 15-psi, 1-msec shots.

While using the magnitude of the acceleration trace the axis of the impact could be used to estimate if the impact was in the front/back axis or a lateral blow, the acceleration trace could not determine if the impact was to the front or back of the helmet. To determine the direction of the blast the integral of the acceleration trace was required. As shown in Figure 2.2.4.3.2-4, the integral of the primary axis indicates the direction of the strike by its sign. In rear hits, the trend in the X-axis integral is positive, indicating movement of the helmet in the positive direction. Using the +/- directions for X and Y as identified in Figure 2.2.4.3.2-5 if the integral of the X-axis trace is positive and the integral of the Y-axis trace is negative, that would indicate a hit to the headform's left-rear quadrant.

This exercise demonstrates that the yaw and direction of a blast was reasonably well estimated using the acceleration trace from the HMSS-A for the conditions tested. The proceedure was not appropriate for quantifing the acceleration or velocity of the helmet resulting from the exposure.

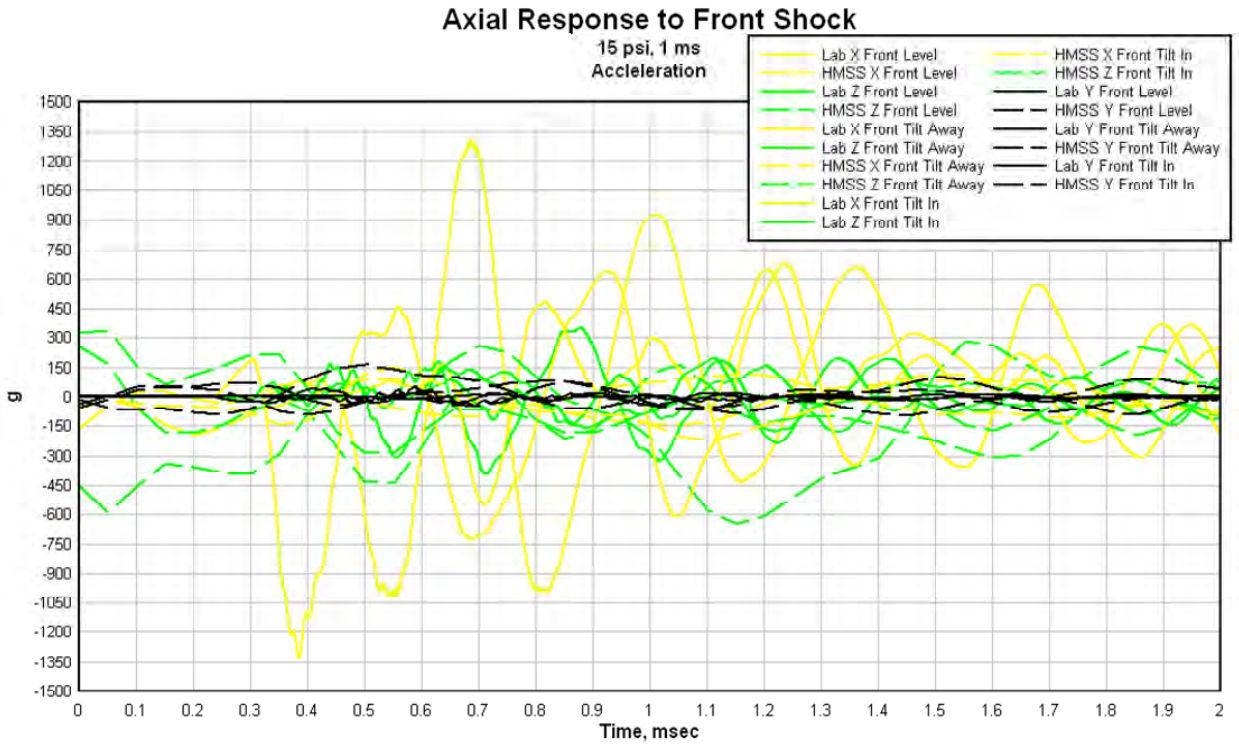

Figure 2.2.4.3.2-1. Front shocks from the Lab and HMSS.

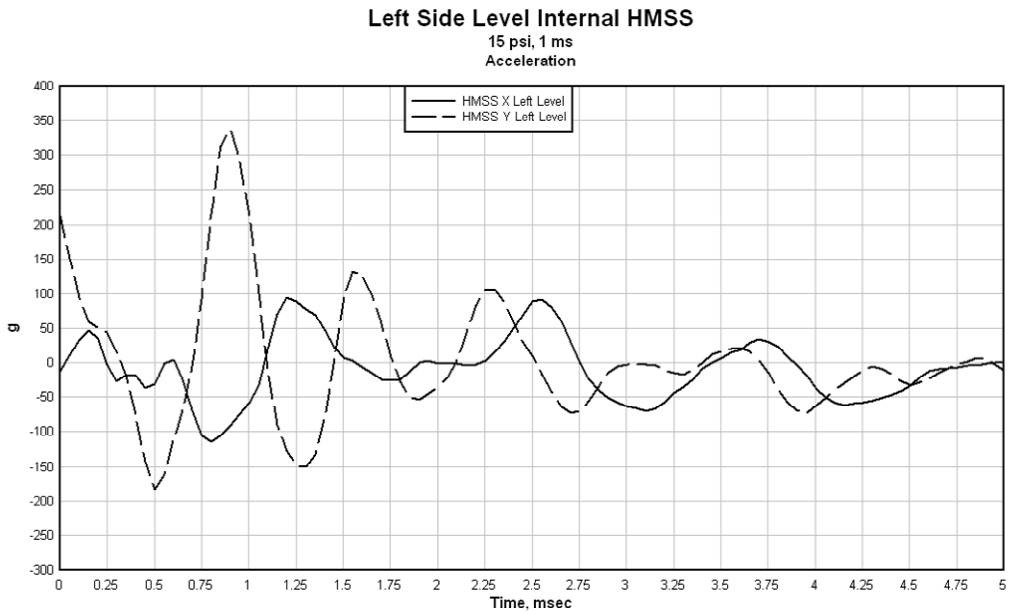

Figure 2.2.4.3.2-2. X and Y-axis response to Front and Rear Level shots.

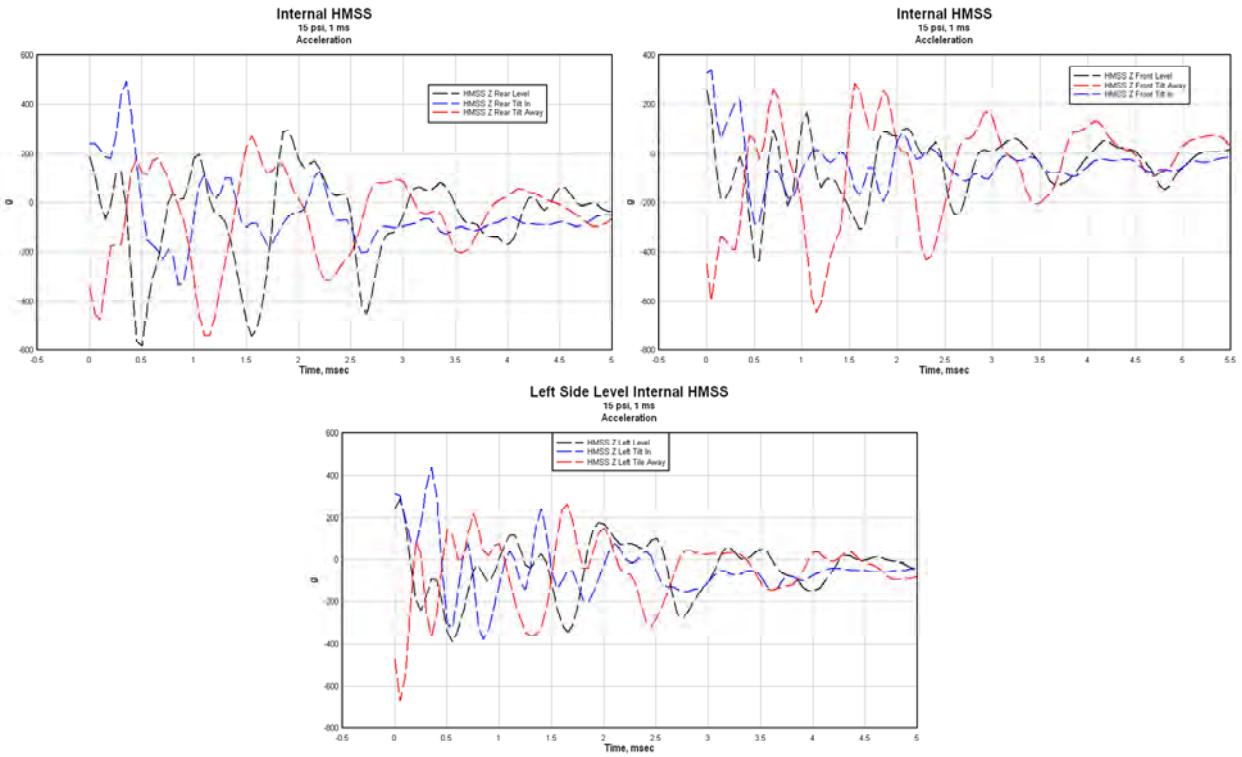

Figure 2.2.4.3.2-3: Z-axis response for front, side and rear hits at various tilts.

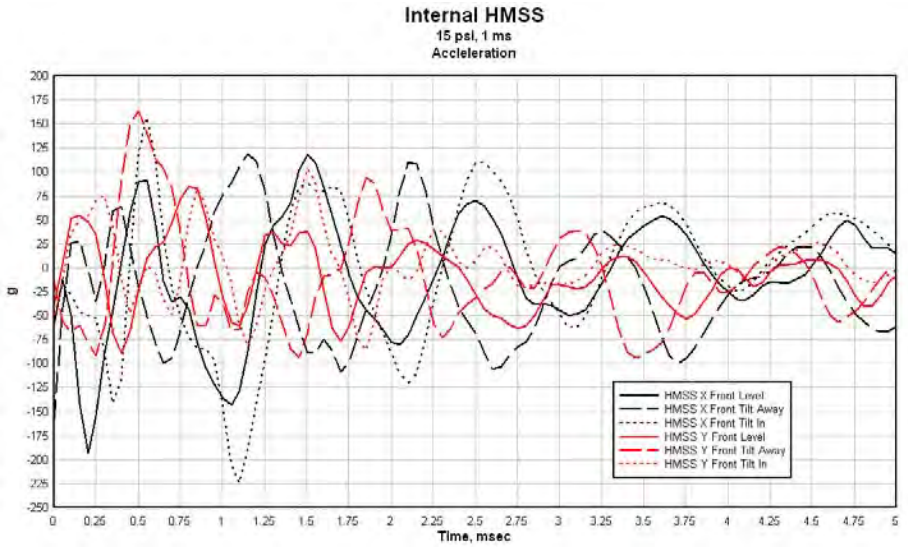

Figure 2.2.4.3.2-4. X and Y-axis response to Front shots with forward and backward tilts.

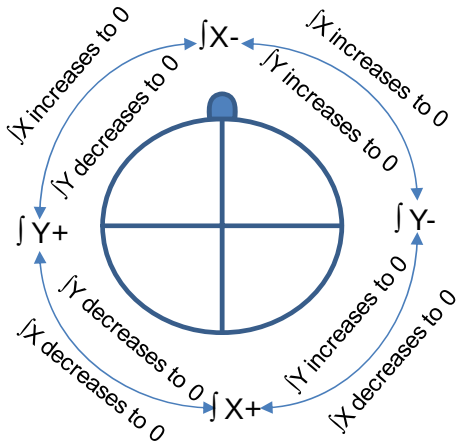

Figure 2.2.4.3.2-5. Integrating the primary axis trace provides the direction of the impact along that axis.

2.2.4.3.3. Ballistic Impacts

Trends in the data collected from the HMSS units during the ballistic tests were not as apparent as during the blast tests. The previous analysis and inspection of the high speed video confirm the expected finds which are ballistic impacts to the helmet are highly localized event and global measurements such as acceleration are not appropriate measures of the severity of the impact. The recommendation from this study is that helmets be examined forensically when estimating the impact direction and location and the electronic HMSS data not be used in that determination.

2.2.5. Summary and Lessons Learned

1. Neither HMSS-A or HMSS-B performed well in predicting the response of the helmet as measured by the lab sensors for either the blast or ballistic conditions tested
2. HMSS-A reasonably estimated the direction of the blast wave after manipulating the collected acceleration-time traces. HMSS-B was found not to reliably predict the direction
3. The relative magnitude of the blast wave could be estimated by both HMSS-A and B but this data would only be useful if a library of blast exposures was available for comparison.
4. The electronic data collected from HMSS-A or HMSS-B was determined to be unreliable for ballistic tests due to the highly local deformations of the helmet shell. A forensic analysis of the helmet itself is therefore recommended to determine the direction and severity of the ballistic impact
5. The helmet shell does appear to respond as a rigid body for either the ballistic impacts or under blast conditions. While the lab sensors and data acquisition system appear to have

sufficient bandwidth to capture the bending modes of the helmet for both blast and ballistic threats, additional research is required to determine how the bending modes of the shell affect the measurements recorded on the surface of the helmet.

2.3. Laboratory Physical Testing

Phase 1 of this effort was to conduct a series of controlled environment tests using instrumented helmets, PMHS heads, and the Facial and Ocular Countermeasure Safety (FOCUS) headform. This data was collected to provide a basis with which to determine the functionality of the Generation I helmet mounted sensor systems (HMSS) and establish a dataset using laboratory grade sensors that was subsequently used to build the helmet to head transfer functions. The tests included both shock tube testing to assess response to blast overpressure, and ballistic testing to confirm the HMSS ability to capture both blast and ballistic impacts to the helmet.

2.3.1. Shock tube testing

Shock tube testing was conducted at ARA and Duke University facilities. The ARA testing was done using a modified 18" shock tube that enabled direct control of the blast wave positive pressure phase duration. Testing at ARA was done using the FOCUS headform only. The Duke University testing was completed on an 12" shock tube. Testing at Duke included both FOCUS and PMHS head tests.

2.3.1.1. Instrumentation

Instrumentation in the headform and on the helmet is listed by sensor type, location, maximum recordable value, units, and channel ID for all shock tube and ballistic tests in Table 2.3.1.1-1. All instrumentation except the HMSSs was sampled at 2 MHz with an anti-aliasing hardware filter at 200 kHz with a 26-msec pre-trigger and 524-msec total duration. The resulting sampled data was post processed with an 8-pole low-pass Butterworth filter at 40 kHz. Data was recorded in the Nicolet Time Domain (wft) binary format. The data provided to USAARL was decimated to 1 MSamples/s and truncated to reduce the file size. The uploaded data was in a columnar ASCII format. The data from the HMSS A and B were downloaded separately after each shock and is not included in the channel list below.

2.3.1.1.1. FOCUS Headform

An instrumented Hybrid III headform known as the Facial and Ocular Countermeasure Safety (FOCUS) and a Hybrid III neck was used (Figure 2.3.1.1.1-2). The instrumentation included a triaxial accelerometer cube and angular rate sensor located at the center of gravity (CG), various pressure sensors . threaded into the bridge of the nose, at each ear, and at the crown, and a load cell in the neck. All accelerometers and angular rate sensors were set up on a left-handed axis to match the directionality of the HMSSs as depicted in Figure 2.3.1.1.1-1**Error! Reference source not found.**.

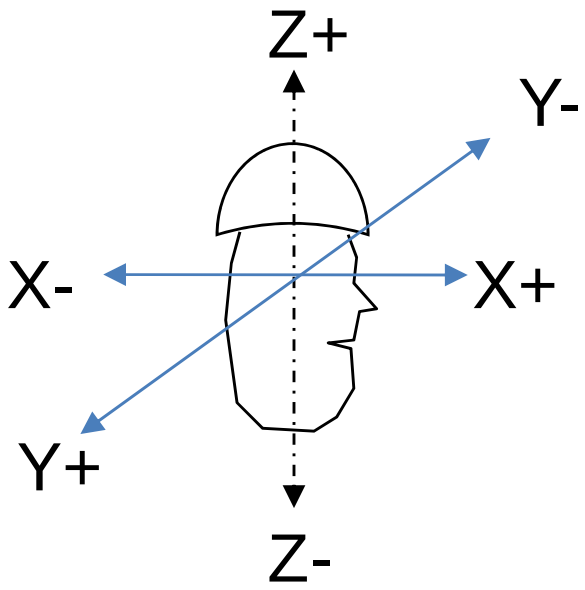

Figure 2.3.1.1.1-1. Headform diagram showing axial directions.

Figure 2.3.1.1.1-2. Facial and Ocular Countermeasure Safety (FOCUS)

2.3.1.1.2. PMHS Heads

The PMHS accelerometer array was aligned with the midsagittal plane and rigidly fixed to a bite plate in the upper maxilla with two screws. This bite plate was then rigidly fixed to the upper maxilla with two screws (Figure 2.3.1.1.2-1). The location of the sensor accelerometer package is approximately 35 mm anterior to the cg and 15 mm inferior to the cg. For peak rotational accelerations of up to 2,000 deg/sec, typical centripetal accelerations are on the order of 5-10 g, so the rotational contribution to the acceleration translated to the head cg will be negligible. The specimen had no evidence of osteopenia or osteoporosis and was approximately 50% male anthropometry. Specimen anthropometry is shown in

Table **2.3.1.1.2-**1**Error! Reference source not found.**.

Table 2.3.1.1-1.
Instrumentation List.

				Tests Included					
Sensor Type	Max Value	Units	Model Number	Duke FOCUS	Duke PMHS	Duke Tube	ARA FOCUS	ARA Tube	Helmet
Pressure Transducer	3450 (500)	kPa (psi)	Endevco 8530B	Left Eye		Interior	Nose	Interior	front
				Right Eye		Exterior	Right Ear	Exterior	Left
				Fore head		Adjacent to Head	Left Ear	Adjacent to Head	Crown
				Right Ear					Back
	345 (50)	kPa (psi)	Endevco 8530C	Crown			Crown		
	860 (125)	kPa (psi)	Kulite LQ125		Crown				
					Back				
					Left				
					Right				
	860 (125)	kPa (psi)	Kulite LQ125B		Front				
Intracranial Pressure	670 (87)	kPa (psi)	Millar 524		Side				
					Crown				
					Front				
Accelerometer	6000	g	Endevco 7270A	CG X	CG X		CG X		HT1 - Crown X
				CG Y	CG Y		CG Y		HT1 - Crown Y
				CG Z	CG Z		CG Z		HT1 - Crown Z
									HT2 - Back X
									HT2 - Back Y
									HT2 - Back Z
Angular Rate Sensor	50,000	deg/ sec	DTS ARS-50K	CG Y	CG Y		CG Y		HT1 - Crown Y
Force, A/P Shear	670 (87)	kPa (psi)	Millar 524	Lower Neck	Lower Neck		Lower Neck		
Force, M/L Shear				Lower Neck	Lower Neck		Lower Neck		
Flex/Ext Momoment				Lower Neck	Lower Neck		Lower Neck		

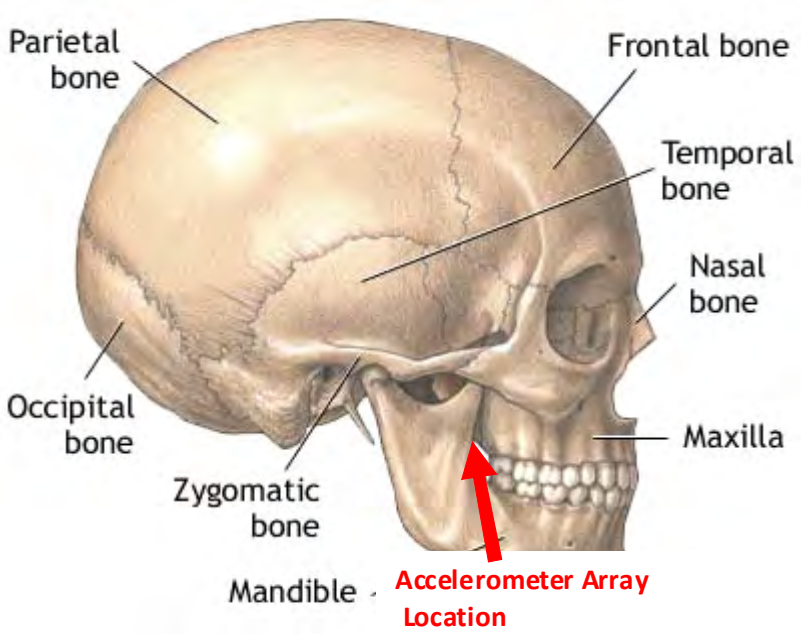

Figure 2.3.1.1.2-1. PMHS 6-axis accelerometer package location (http://nlm.nih.gov)

Table 2.3.1.1.2-1.
Anthropometric Information of the PMHS

PMHS ID	Gender (M/F)	Age (yrs)	Stature (mm)	Weight (kg)
TRUE1	M	75	1650	77.1

2.3.1.1.3. Helmets

To measure the helmet response to the blast, two triaxial accelerometer cubes were mounted on the helmet exterior (shown in Figure 2.3.1.1.3-1). The first cube, HT1, was located at the crown of the helmet, and its xyz coordinate system was aligned within 5 degrees of the FOCUS coordinate system, with the x-axis going toward the wearer's nose (+) and back (-), the y going left (-) or right (+), and the z-axis going up(+) or down(-),. This cube also included an angular rate sensor identical to the one installed at the headform CG. The second cube, HT2, is tilted back 65 degrees from the FOCUS coordinate system. The crown and back locations were chosen for their proximity to the commercial helmet sensors located at the inside surface of the crown of the helmet (HMSS A) and the outside surface of the back of the helmet (HMSS B). . . Finally, four pressure sensors were installed on the helmet at the front, left side, crown immediately in front of HT1 and the back just above Sensor System B.

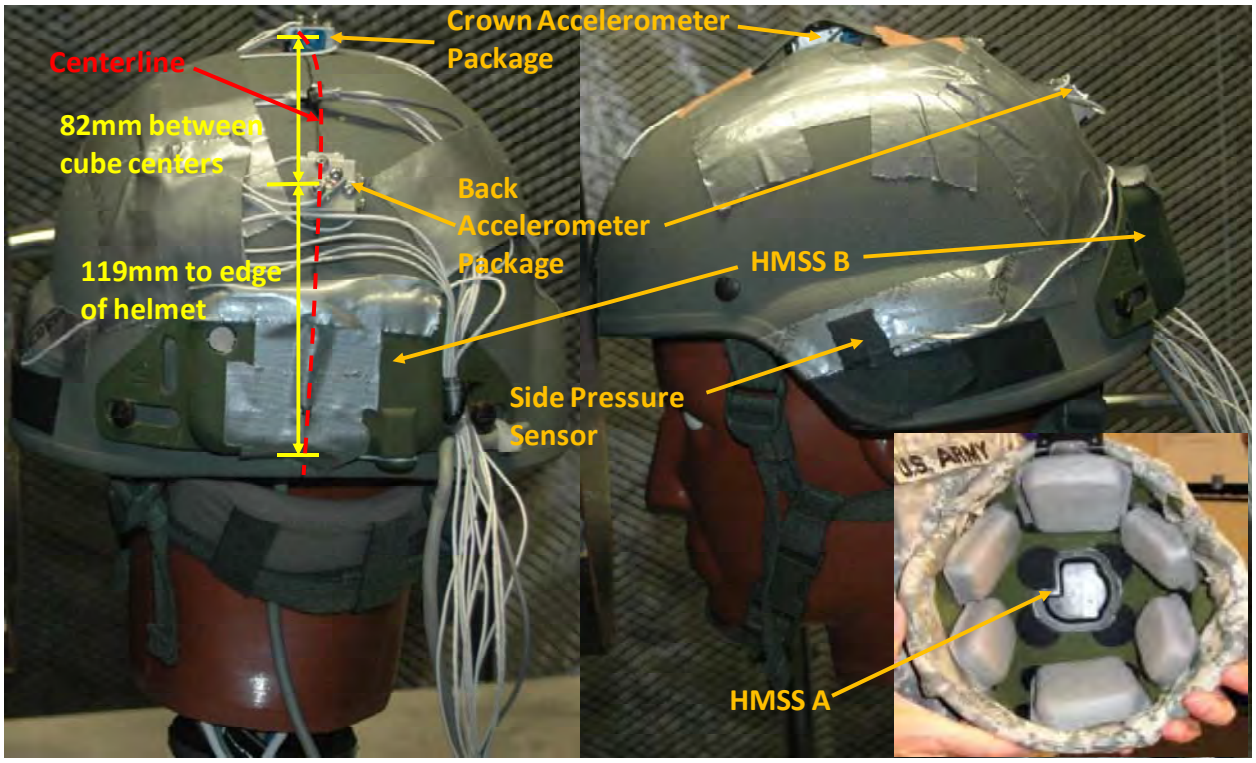

Figure 2.3.1.1.3-6. FOCUS Headform with instrumented helmet; Inset: ACH Helmet showing HMSS A.

The instrumented ACH helmets were fitted onto the head and neck of the FOCUS dummy and the PMHS heads. The head and helmet were positioned at the end of the shock tube with the top of the crown aligned with the top of the shock tube (Figure 2.3.1.1.3-2) for the Duke tests, and the CG of the headform aligned with the center of the shock tube for the ARA tests (Figure 2.3.1.1.3-3). Helmets were tested with the front, side, and rear of the helmet facing the shock tube. The vertical orientation of the FOCUS center of gravity to the shock tube remained constant, and the helmet/head system was positioned so that the closest point on the helmet was located in the plane of the shock tube entrance.

Helmets were tested using a seven pad configuration, including crown, front, back, and four lateral pads (Team Wendy) with a size large helmet manufactured by Rabintek. The pad configuration with the crown pad remove can be seen in the inset picture in Figure 2.3.1.1.2-13.

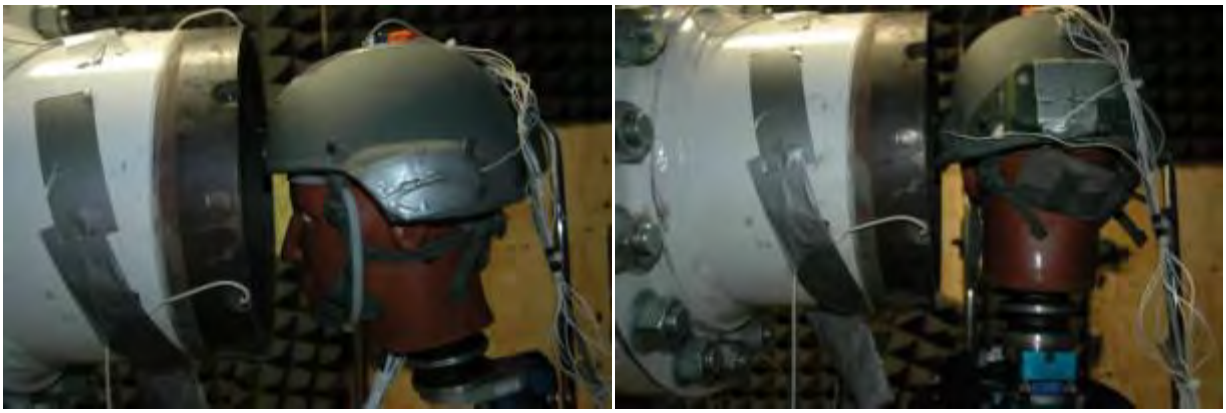

(a) (b)

Figure 2.3.1.1.3-2. FOCUS head and neck with helmet positioned at end of Duke shock tube for (a) front and (b) side impacts.

(a) (b)

Figure 2.3.1.1.3-3. FOCUS head and neck with helmet positioned (a) in cone for long duration blasts and (b) at the end of the ARA shock tube.

2.3.1.1.4. ARA Shock Tube Instrumentation

The ARA shock tube is made from 18-inch steel pipe, with a driven length of 15 feet and an inside diameter of 17 inches (Figure 2.3.1.1.4-1). An expansion cone was attached to the end of the tube in which the specimen was placed for long duration shock waves. Three pressure gauges were used to characterize the shock wave leaving the shock tube. The first pressure gauge was hard-mounted through the top of the shock tube, 5 inches prior to the exit flange. The second pressure gauge was also located at the top, but at 2 inches outside the exit flange. The third pressure gauge was a piezoelectric “pencil gauge” located adjacent to the headform. The latter pressure sensor can be seen in the photograph in Figure 2.3.1.1.3-3.

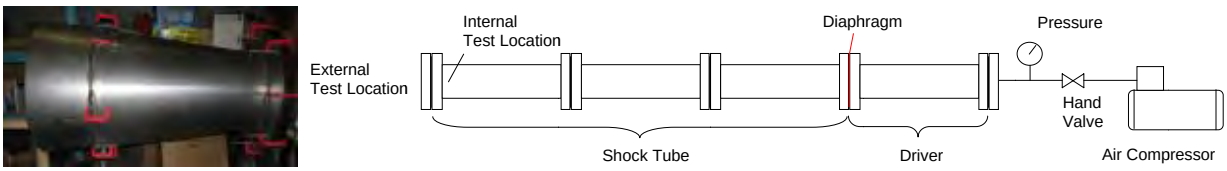

Figure 2.3.1.1.4-1. ARA Shock tube schematic.

2.3.1.1.5. Duke Shock Tube Instrumentation

ARA and Duke shock tube instrumentation set ups were similar. Duke shock tube studies used Duke's 12" shock tube to simulate free field blasts (Figure 2.3.1.1.5-7). Varying driver length, driver gas composition, and membrane thickness allowed for repeatable simulation of blasts of 1-3 ms in positive phase duration and 103-206 kPa (15-30 psi) in peak overpressure. Three pressure transducers were placed at the end of the tube to measure incident pressure. The shock tube configuration at both Duke and ARA can produce Friedlander-type overpressure/duration time histories as shown in Figure 2.3.1.1.5-2.

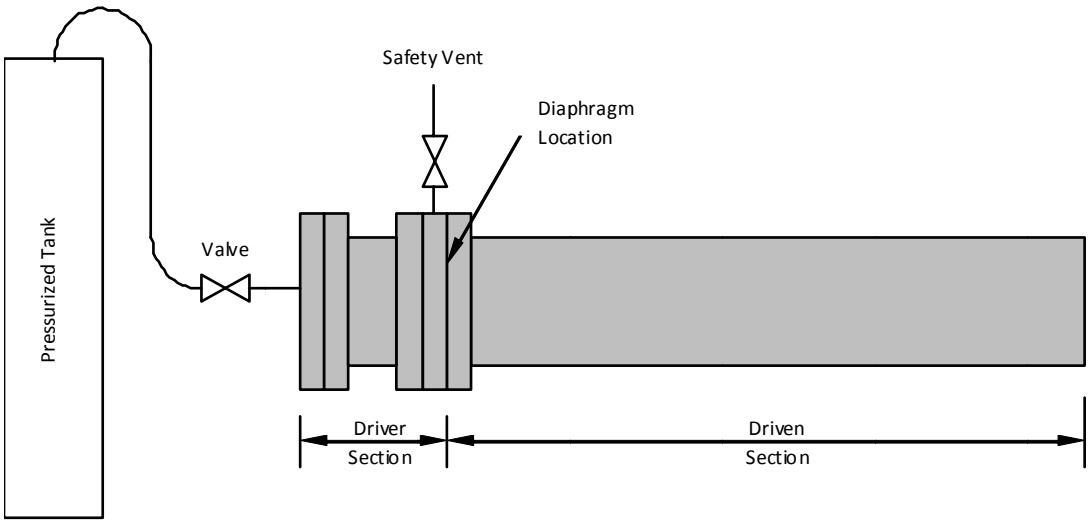

Figure 2.3.1.1.5-7. Duke Shock tube schematic.

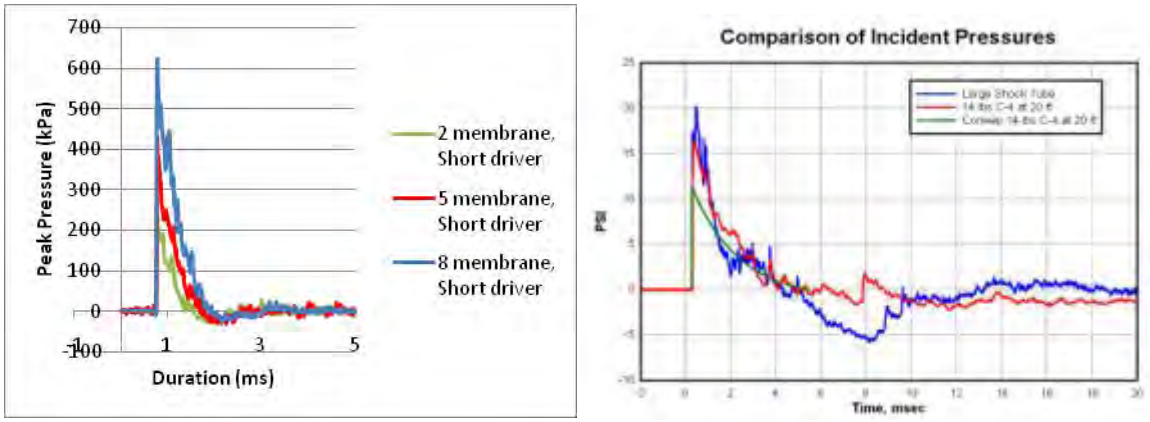

(a) (b)

Figure 2.3.1.1.5-2. Typical overpressure/duration shock tube profiles for the (a) Duke tube and (b) ARA tube.

2.3.1.2. Simulated Threat

Recently, an injury criterion for lethality due to primary blast has been developed using experimental specimens with heads exposed to blasts (Rafaels, 2010). The test conditions selected here are above and below the 50% risk of mild brain meningeal bleeding using the length scaling dependence of Bowen et al (Bowen, 1968) (Table 2.3.1.2-1). These conditions are also similar to overpressure levels for the onset of lung injury from Bass et al (2008).

Table 2.3.1.2-1.
Shock tube test conditions.

Condition Name	Peak Overpressure kPa (psi)	Positive Phase Duration (ms)
Duke		
15 psi@1 ms	108±6 (15.7±0.9)	0.96
15 psi@3 ms	115±5 (16.7±0.7)	3
30 ms@1 ms	196±10 (28.4±1.5)	1.16
ARA		
15 psi@1 ms	101±13 (14.7±2.0)	0.99±0.18
15 psi@3 ms	102±13 (14.8±1.9)	3.20±0.39
30 ms@1 ms	172±18 (25.0±2.7)	0.76±0.37

2.3.1.3. Shock Tube Test Matrix

ARA completed 100 shock tube tests with the FOCUS headform (Table 2.3.1.3-3), completing the required tests at 15 psi incident pressure and 1 msec duration, 15 psi and 3 msec, and 30 psi and 1 msec. Duke completed 58 tests with the FOCUS headform and 52 tests with the PMHS heads. All data from laboratory sensors and the Sensor Systems A and B were downloaded and collected following each shock test. All data from the laboratory sensors was

processed and uploaded to the ftp server. Figure 2.3.1.3-1 shows the orientations used in the shock tube tests.

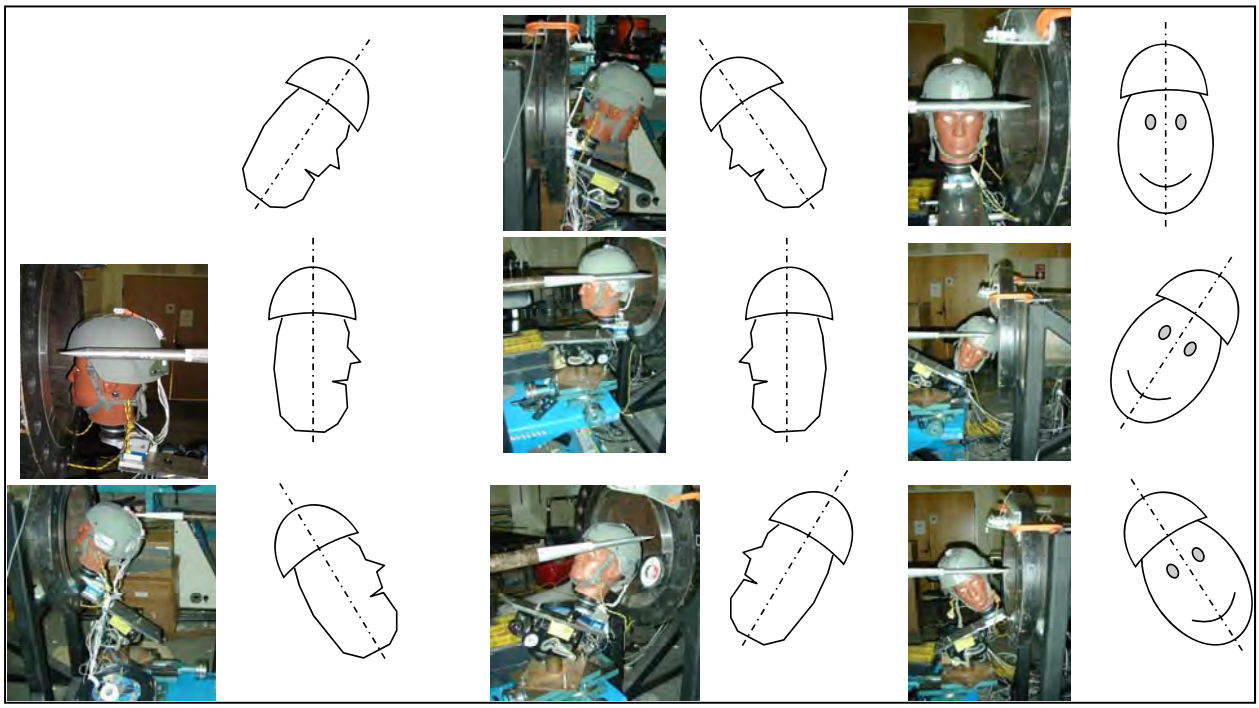

Figure 2.3.1.3-8. Orientations used in the shock tube tests. All pictures shown are without the expansion cone to facilitate visibility of the headform.

At Duke, the helmets were tested in multiple configurations to determine the effects of dummy vs. cadaver, helmet orientation, and input conditions as shown in Table 2.3.1.3-3. For the three test conditions, Duke completed 52 cadaver tests and 50 FOCUS tests. Duke also completed 8 additional FOCUS tests with the crown of the headform oriented to the shock tube opening for a total of 58 FOCUS tests.

Table 2.3.1.3-3.
Matrices of completed tests with 18” shock tube.

Headform Orientation	Peak Incident	Positive Phase	PMHS Shots	FOCUS Shots	
				12" Tube	18" Tube
	15 psi	1 ms	9	3	8
	15 psi	3 ms	3	7	6
Front, Level	30 psi	1 ms	6	3	3
	15 psi	1 ms			5
	15 psi	3 ms			4
Front, Tilt In	30 psi	1 ms			3
	15 psi	1 ms			4
	15 psi	3 ms			3
Front, Tilt Away	30 psi	1 ms			0
	15 psi	1 ms	8	3	4
	15 psi	3 ms	6	4	4
Side, Level	30 psi	1 ms	3	14	3
	15 psi	1 ms			3
	15 psi	3 ms			3
Side, Tilt In	30 psi	1 ms			5
	15 psi	1 ms			3
	15 psi	3 ms			3
Side, Tilt Away	30 psi	1 ms			5
	15 psi	1 ms	6	6	3
	15 psi	3 ms	8	4	4
Rear, Level	30 psi	1 ms	3	6	3
	15 psi	1 ms			3
	15 psi	3 ms			3
Rear, Tilt In	30 psi	1 ms			4
	15 psi	1 ms			3
	15 psi	3 ms			3
Rear, Tilt Away	30 psi	1 ms			5
TOTAL			52	50	100

2.3.1.4. Shot Tube Test Results

The data collected during this phase was used to assess the operational capability of HMSS A and B (Section 2.2) and to build the helmet to head transfer function (Section 2.1). Additionally, the data collected during these tests enabled the team to extract the differences between the FOCUS headform response and a PMHS head response to blast loads. The charts in Figures 2.3.1.4-1, 2, and 3 show the results from the front level shock tube tests.

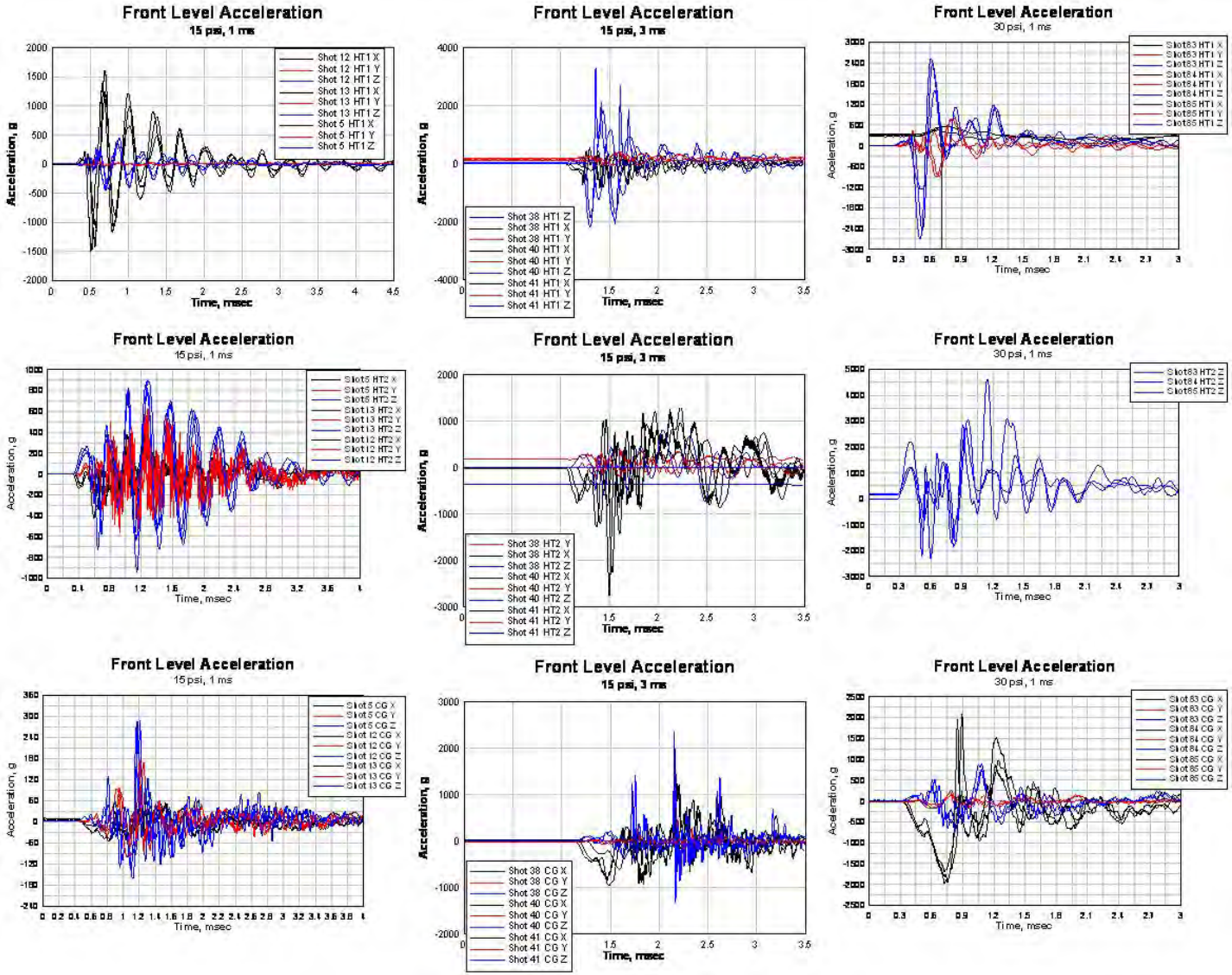

Figure 2.3.1.4-1: Acceleration time histories for front level shock tube tests. From left to right, 15 psi-1 ms, 15 psi-3 ms, 30 psi-1 ms. From top to bottom, helmet crown, helmet rear, FOCUS center of gravity.

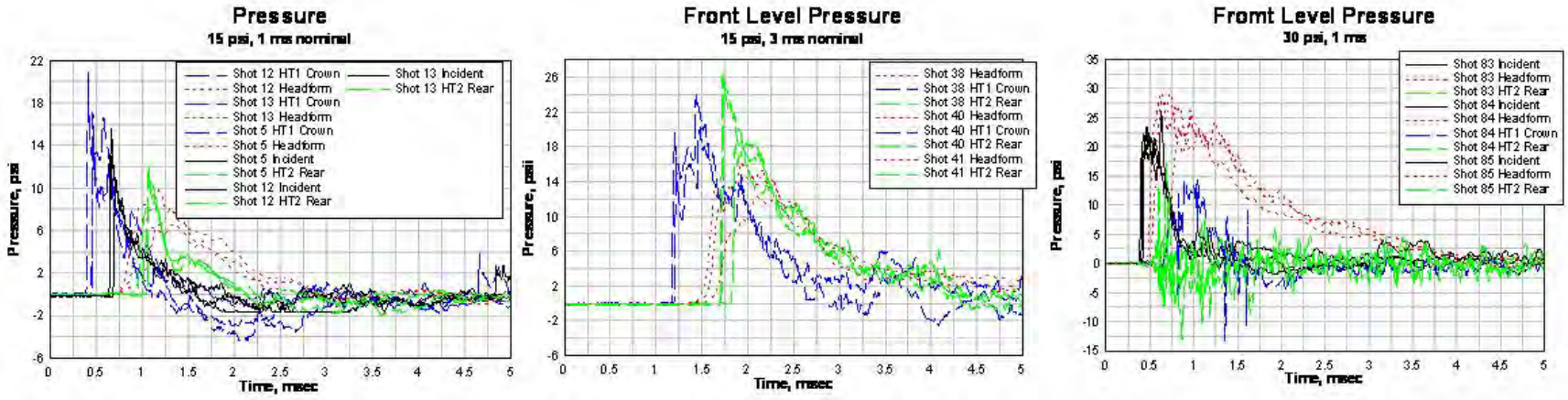

Figure 2.3.1.4-2: Pressure time histories for front level shock tube tests. From left to right, 15 psi-1 ms, 15 psi-3 ms, 30 psi-1 ms.

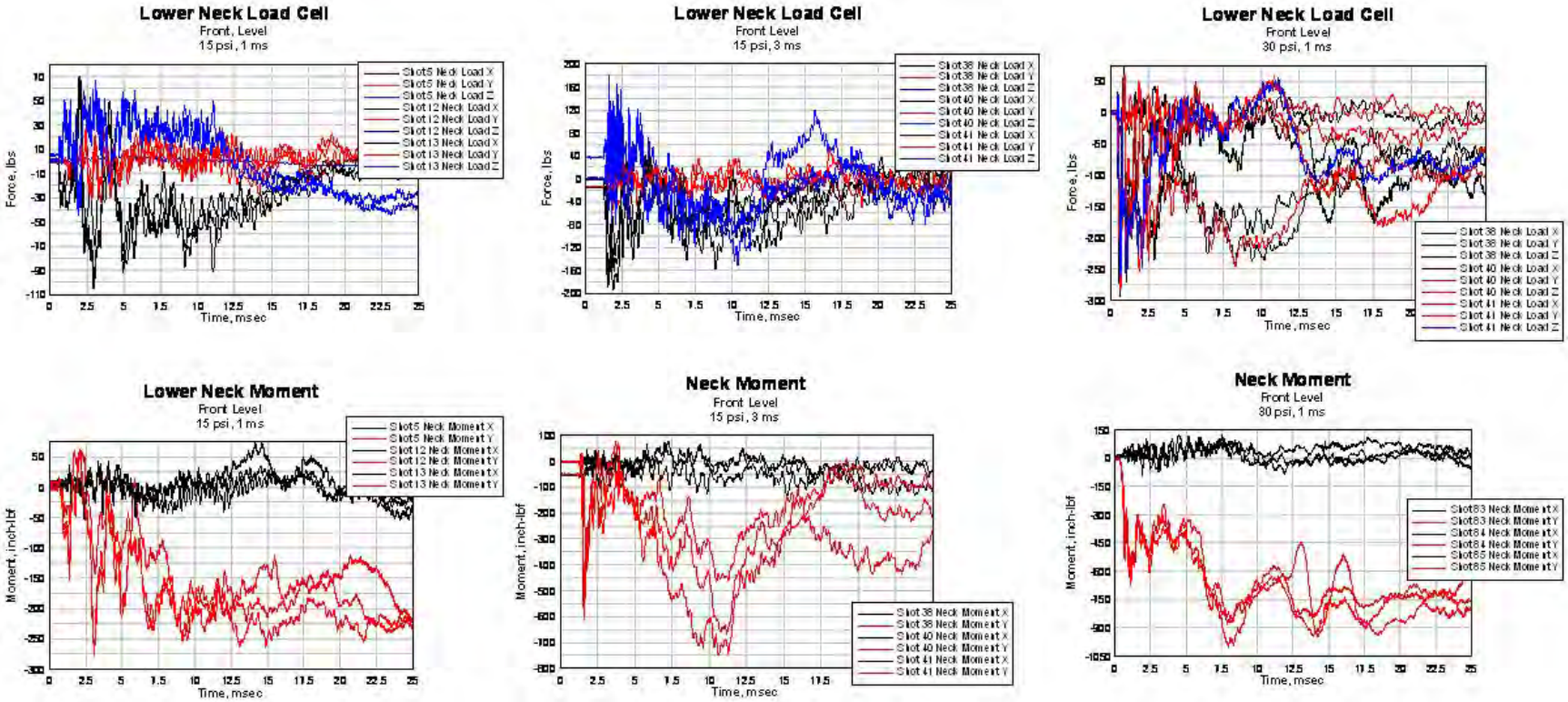

Figure 2.3.1.4-3: Lower neck load cell time histories for front level shock tube tests. From left to right, 15 psi-1 ms, 15 psi-3 ms, 30 psi-1 ms. From top to bottom, neck force, neck moment.

2.3.1.5. Analysis

2.3.1.5.1. Tube characterization (18 inch versus 12 inch)

As shown in Figure 2.3.1.5.1-1, the helmet crown acceleration traces were consistently higher with the 18” shock tube than with the 12” shock tube. This provides data to support the hypothesis that the diameter of the shock tube has a significant effect on the test results. Further characterization would be merited to improve the correlation. It is likely that the volume of air in the shock front striking the head and helmet is larger in the 18” shock tube, thus presenting the target with more momentum ultimately resulting in a larger movement in the helmet and headform accelerometers.

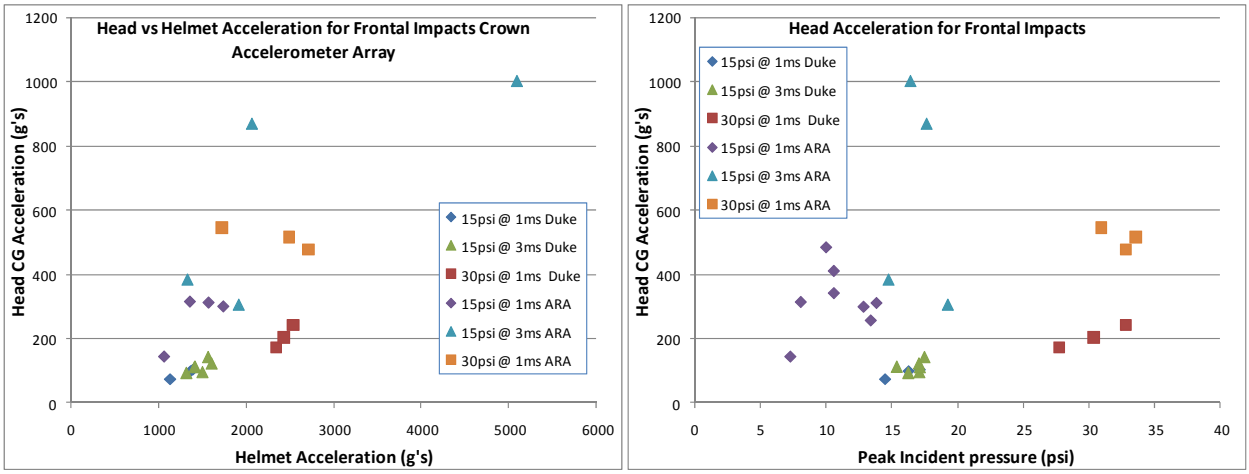

Figure 2.3.1.5.1-1: Duke 12” shock tube and ARA 18” shock tube comparisons as a function of helmet crown acceleration (left) and peak incident pressure (right)

2.3.1.5.2. PMHS versus FOCUS response

The Duke shock tube data provided an opportunity to assess the differences in a cadaver head versus the FOCUS headform. As shown in Figure 2.3.1.5.2-1, the two head surrogates exhibit significantly different responses. Furthermore, these responses very differently depending on the orientation. This can be from a variety of potential factors. The FOCUS skull material differs significantly from the PMHS head and the FOCUS material my provide additional dampening of the forces that is not present in the PMHS heads, resulting in larger detected acceleration traces at the headform center of gravity.

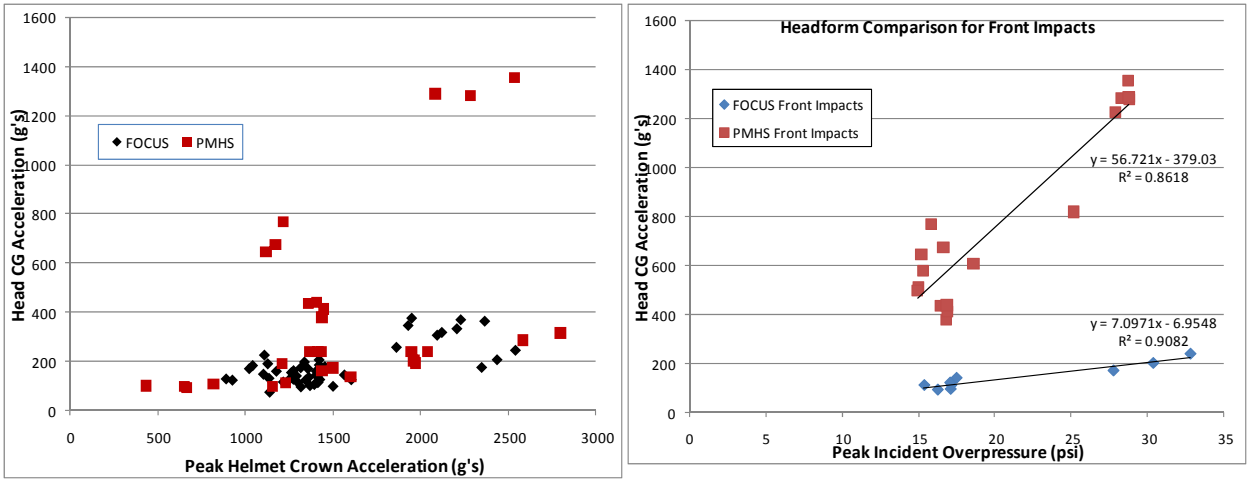

Figure 2.3.1.5.2-1: PMHS and FOCUS shock tube tests with the Duke 12" shock tube comparisons as a function of helmet crown acceleration (left) and peak incident pressure (right)

2.3.1.5.3. Orientation Effects

The test matrix enabled an analysis of the effects of head orientation to the blast. This weighed heavily on the helmet head transfer function. Furthermore, it was evident that the PMHS and FOCUS headform also responded very differently depending on the direction of the blast wave. Lastly, there were obvious differences in the sensor response between the crown and rear mounted laboratory sensors on the helmet.

In Figure 2.3.1.5.3-1, the effects of orientation on translating the incident overpressure to head acceleration can be seen. Generally, the center of gravity (CG) acceleration increases with increasing overpressure. However, the different shapes in the charts show the effect of the direction of the blast and the colors shows the effect of tilting the head toward or away from the blast. Though the scatter in the data makes it difficult to draw firm conclusions, but Figure 2.3.1.5.3-2 shows an apparent trend in the slopes.

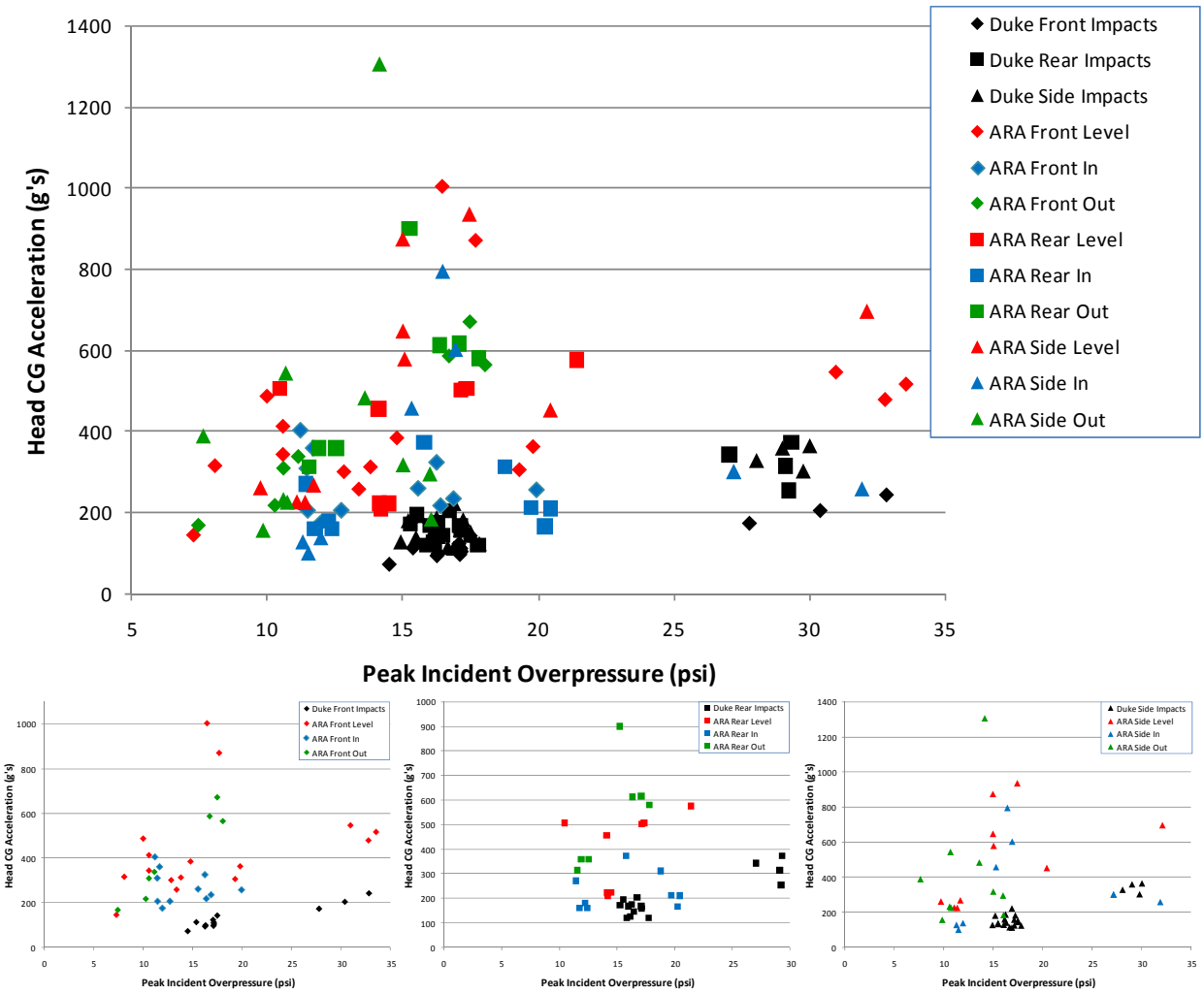

Figure 2.3.1.5.3-1: FOCUS shock tube tests showing CG peak resultant acceleration as a function of peak incident overpressure for the various orientations.

	Slope	R2
FL Duke	7.5356	0.9111
FL ARA	8.3401	0.1028
F In	-5.0312	0.0425
F Out	45.895	0.9416
RL Duke	12.694	0.7877
RL ARA	20.024	0.1764
R In	2.4587	0.0166
R Out	54.726	0.4711
SL Duke	14.643	0.8539
SL ARA	20.818	0.2582
S In	2.1014	0.0049
S Out	17.317	0.0221

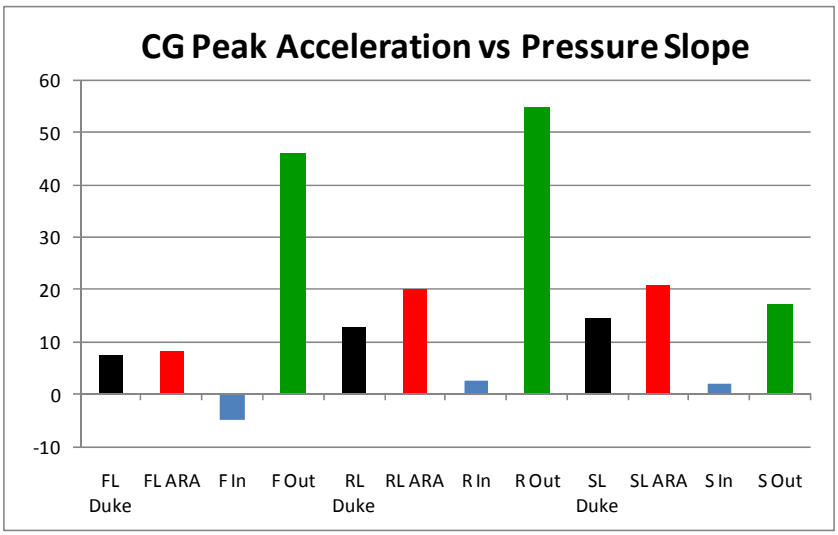

Figure 2.3.1.5.3-2: Comparison of slopes from CG peak resultant acceleration as a function of peak incident overpressure for the various orientations.

The peak resultant acceleration for the rear and crown mounted sensors also varied somewhat from each other. The rear mounted sensor traces tended to respond with a somewhat lower magnitude that the crown, although the difference was almost insignificant, as can be seen in Figure 2.3.1.5.3-3. Figures 2.3.1.5.3-4 and 5 break out these same charts into each orientation for a less cluttered view. The slopes for the crown and rear resultant peaks are compared in Figure 2.3.1.5.3-6.

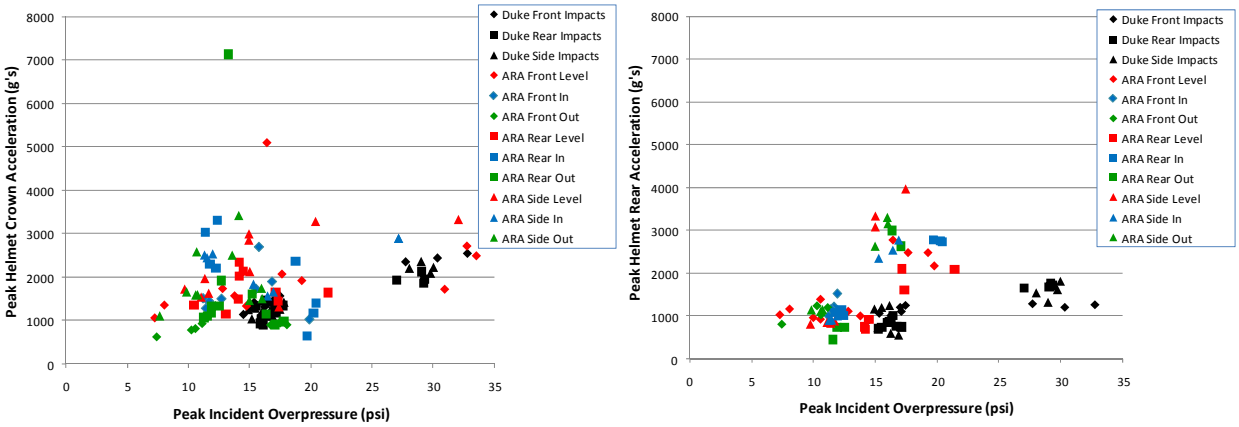

Figure 2.3.1.5.3-3: FOCUS shock tube tests showing peak resultant acceleration for the crown (left) and rear (right) mounted sensors as a function of peak incident overpressure for the various orientations.

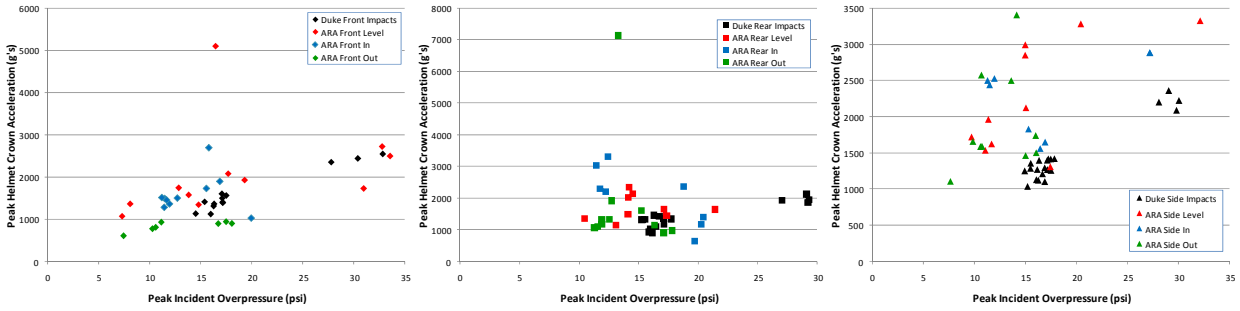

Figure 2.3.1.5.3-4: FOCUS shock tube tests showing peak resultant acceleration for the crown mounted sensor as a function of peak incident overpressure for the various orientations.

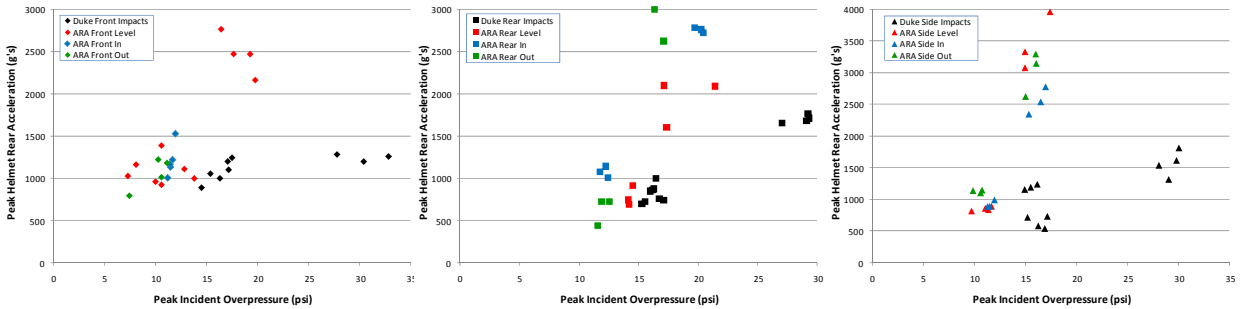

Figure 2.3.1.5.3-5: FOCUS shock tube tests showing peak resultant acceleration for the rear mounted sensor as a function of peak incident overpressure for the various orientations.

	REAR SENSOR		CROWN SENSOR	
	Slope	R2	Slope	R2
FL Duke	12.672	0.4643	75.907	0.9509
FL ARA	134.75	0.6856	34.063	0.0847
F In	661.52	0.9338	23.345	0.024
F Out	102	0.7411	21.281	0.6124
RL Duke	70.776	0.9644	60.874	0.8004
RL ARA	202.6	0.7652	9.3706	0.0055
R In	208.71	0.9892	-172.69	0.6331
R Out	448.02	0.9487	-87.356	0.0135
SL Duke	50.345	0.6035	73.577	0.9214
SL ARA	494.91	0.9391	77.702	0.4438
S In	344.54	0.9928	33.866	0.1723
S Out	356.3	0.98	59.129	0.0609

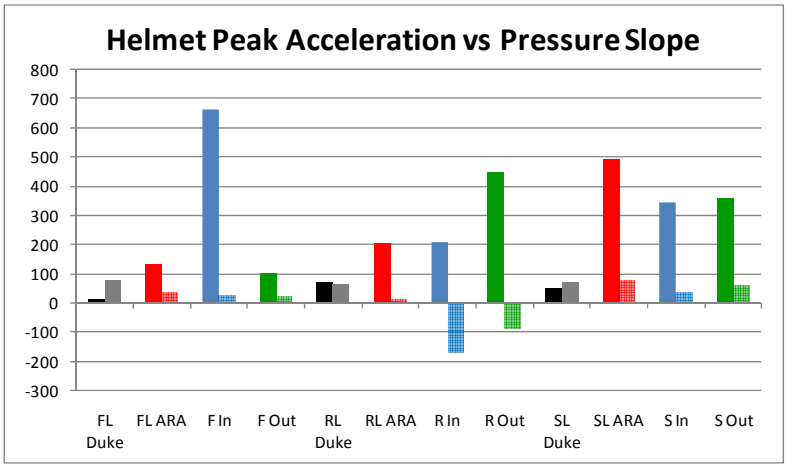

Figure 2.3.1.5.3-6: Comparison of slopes from crown and rear peak resultant acceleration as a function of peak incident overpressure for the various orientations. Left bars are the rear sensors, and the right, faded bars are the crown sensors.

Lastly, we looked at the head CG peak resultant acceleration as it varied with both the crown and rear mounted peak resultants. Figure 2.3.1.5.3-7 shows that the CG sensor traces appeared to respond with a somewhat lower magnitude acceleration in relation to the rear mounted accelerometers versus the crown sensors, although the difference was highly variable due to the data scatter. Figures 2.3.1.5.3-8 and 9 break out these same charts into each orientation for a less cluttered view. The slopes for the crown and rear resultant peaks are compared in Figure 2.3.1.5.3-10.

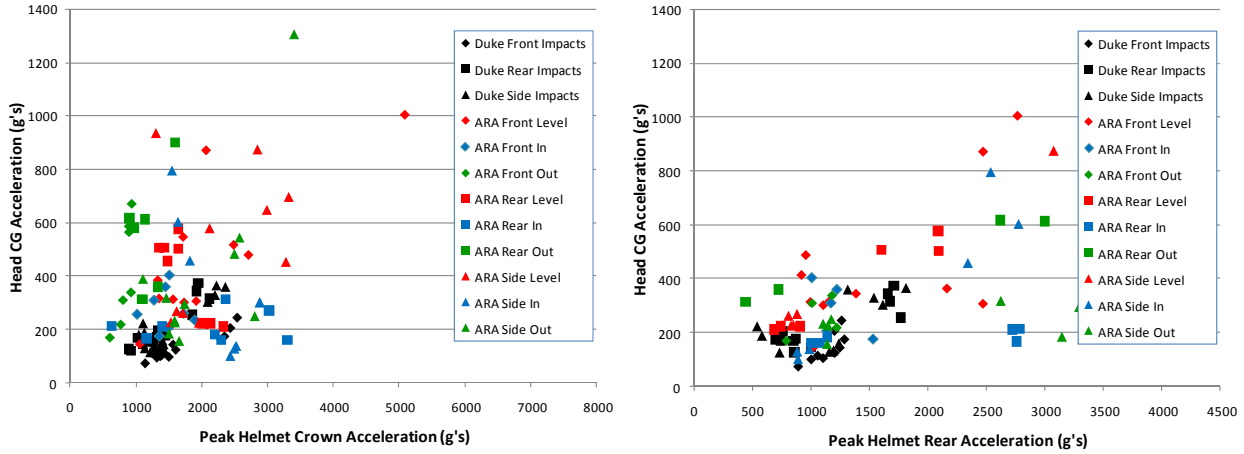

Figure 2.3.1.5.3-7: FOCUS shock tube tests showing peak resultant acceleration for the FOCUS CG as a function of the peak resultant acceleration for the crown (left) and rear (right) mounted sensors for the various orientations.

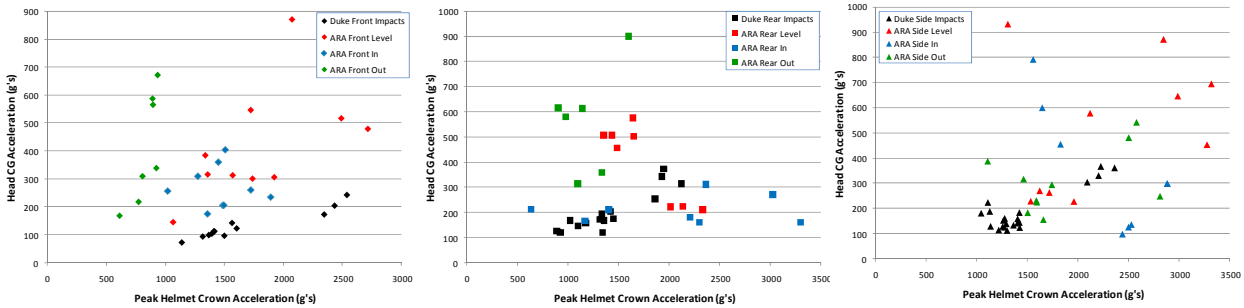

Figure 2.3.1.5.3-8: FOCUS shock tube tests showing peak resultant acceleration for FOCUS CG as a function of the peak resultant acceleration of the crown mounted sensor for the various orientations.

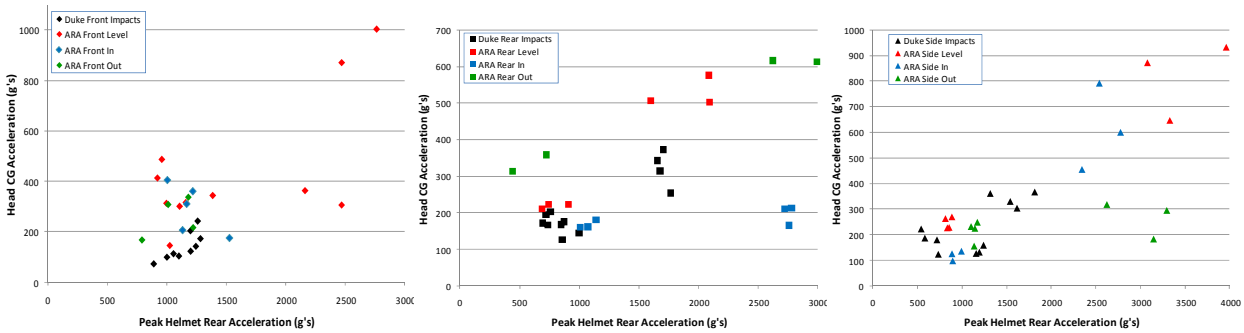

Figure 2.3.1.5.3-9: FOCUS shock tube tests showing peak resultant acceleration for FOCUS CG as a function of the peak resultant acceleration of the rear mounted sensor for the various orientations.

	REAR SENSOR		CROWN SENSOR	
	Slope	R2	Slope	R2
FL Duke	0.3236	0.6165	0.1008	0.9219
FL ARA	0.2392	0.4407	0.1854	0.6266
F In	-0.3595	0.4942	-0.0157	0.0026
F Out	0.216	0.2852	1.3627	0.6275
RL Duke	0.1578	0.7413	0.19	0.8171
RL ARA	0.2518	0.9309	-0.381	0.7943
R In	0.0173	0.4371	0.0081	0.0179
R Out	0.1228	0.9856	0.2361	0.0749
SL Duke	0.1407	0.4125	0.1804	0.7617
SL ARA	0.2163	0.9327	0.11666	0.1102
S In	0.3046	0.8839	-0.3667	0.6162
S Out	0.0219	0.1538	0.3332	0.5347

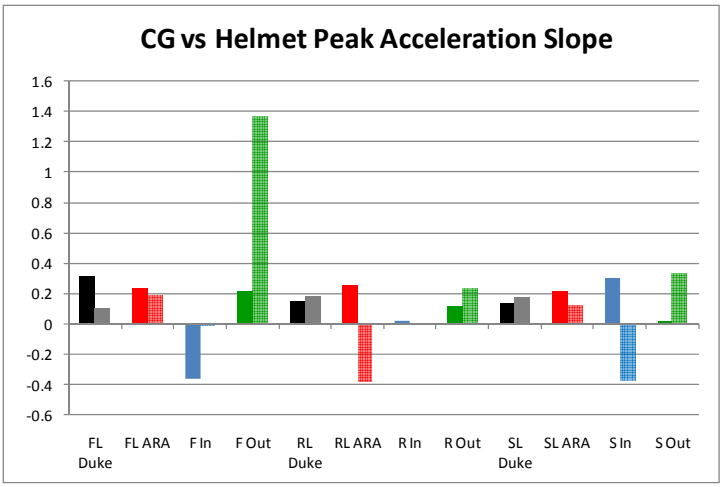

Figure 2.3.1.5.3-10: Comparison of slopes from CG peak resultant acceleration as a function of crown and rear peak resultant acceleration for the various orientations. Left bars are the rear sensors, and the right, faded bars are the crown sensors.

2.3.1.6. Shock tube summary

Overall, a total of 210 shock tube tests were conducted on the FOCUS headform and PMHS heads equipped with and instrumented ACH using 18" and 12" shock tubes. The tests results provided a thorough dataset enabling an assessment of the Generation I HMSS for their ability to detect and characterize a primary blast event. Furthermore, the collected data enabled initial development of a helmet to head lumped sum parameter model. Though the data was insufficient to fully characterize the complex nature of the helmet to head interactions across the spectrum of potential blast exposures, the data was able to provide a basic model and enable identification of sensitive parameters that must be characterized to complete the model development, as discussed in Section 2.1.3,

2.3.2. Ballistic impact testing

The helmet system was evaluated under ballistic impact conditions using a 9mm projectile traveling at two different velocities. The impact velocity of the projectile was be recorded using chronographs positioned between the Gaz Gun and the instrumented helmet. The helmet systems were be evaluated for detection of frontal and side impacts. Nine ballistic impacts are scheduled for this test series. No rear or crown tests will be conducted due to the instrumentation attached to the helmet surface. Results from the helmet sensors will be compared to the results obtained from linear accelerometers and contact pressure gauges attached to the PMHS. To ensure statistically significant results, each location will be impacted three times (once per helmet) for each projectile type tested. To allow for potential alterations in helmet properties by subsequent ballistic impacts, the side hits will be completed prior to the front hits on each helmet. The helmet sensor (both laboratory and Generation One HMSS) data and PMHS data will be used in the development of the transfer function and numerical modeling to predict head response as a function of helmet response and shared with others in order to create a comprehensive data signal library.

2.3.2.1. Test Conditions

In the ballistic test series, the response of the head was measured during impacts from a 9mm FMJ (Full Metal Jacket) and 225 grain RCC (Right Circular Cylinder). The positioning of the headforms is shown in Figure 2.3.2.1-9 using Biokinetic's BLS Headform. Two impact velocities for each projectile were selected so that none of the projectile impacts caused a penetration through the helmet shell. The impact velocities for the 9 mm FMJ munitions were 427±2 m/s and 457±5 m/s which bound the typical velocity for the evaluation of helmets in NIJ 0101.06 Standard for Ballistic Helmets. The velocities for the 225 grain RCC were 284±2 m/s and 311±4 m/s, below the V_o the ACH helmet shell. The projectiles were propelled by a smooth bore gas-actuated pneumatic launcher (Figure 2.3.2.1-10). The launcher was charged with high-pressure helium and used multi-stage valves driven by compressed air to open and close valves as a rapid rate. All of the test surrogates were evaluated upright and in three orientations; front, side, and rear.

Figure 2.3.2.1-9. Representative Impact Locations on the ACH Helmet

Figure 2.3.2.1-10. Duke University Gaz Gun located at PRTC

Prior results indicate the accuracy of the pneumatic launcher is 0.22% for the 9mm projectile, well within allowable experimental error. The accuracy for the 225 gr. FSP is comparable to the 9mm FMJ. This suggests the launcher is an appropriate mechanism for accelerating the projectiles for the evaluation of the helmet sensor systems.

Instrumentation for the ballistic impact tests was selected with three primary objectives: measurement of 1) external skull contact force, 2) global accelerations, and 3) neck forces and moments. The instrumentation attached to the head provides the means of collecting the data required for comparison to the selected mechanical headforms and biological specimens. These measurements will also be compared to the observations from the necropsies, conducted after the test, to determine which are appropriate for evaluating helmet performance in a blast environment.

For the PMHS, the specimen was instrumented with accelerometers and fast-rising contact pressure sensors. The unit of output for the five contact pressure sensors (Figure 2.3.2.1-11) was kilopascals (kPa). In a previous study by Bass et al. it was observed that there was a 50% risk of skull fracture at a level of 50,200 kPa for the PMHS specimens tested. In the Bass study the PMHS wore an ultra high molecular weight polyethylene (HMWPE) helmet. In the current test program all tests were conducted with an ACH helmet at sub-fracture levels so that multiple impacts can be performed on the same specimen.

The acceleration of the surrogate head was recorded for each test. The acceleration cube was located on the surface of the headform. The origin of the cube was located on the head so that one of the axis of the cube was in line with cg of the surrogate head. Figure 2.3.2.1-12 is representative acceleration and angular rate data from the TSWG ballistic tests.

In addition to contact pressures and accelerations, neck loads and moments were recorded for each test by the lower neck load cell. Figure 2.3.2.1-13 is representative neck load data from the TSWG ballistic tests. All the data shown in Figures 2.3.2.1-3, 4 & 5 are from the same frontal impact test but on different time scales.

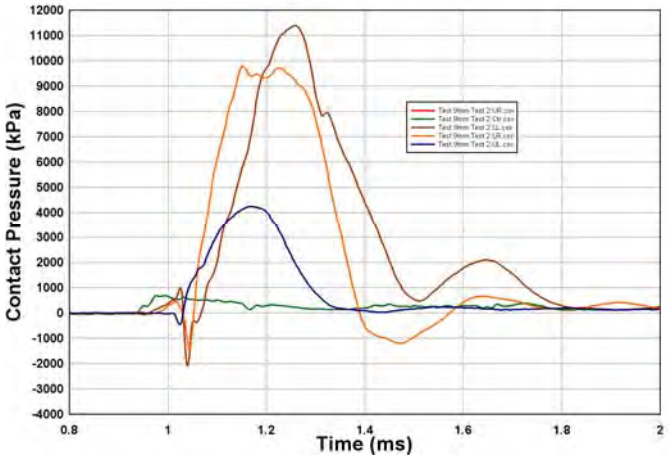

Figure 2.3.2.1-11. Representative Output from the PMHS Contact Pressure Gauges

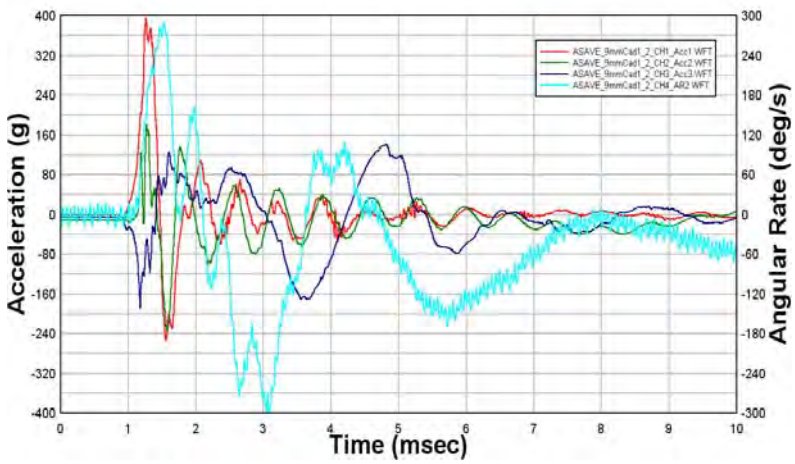

Figure 2.3.2.1-12. Representative Acceleration and Angular Rate Data

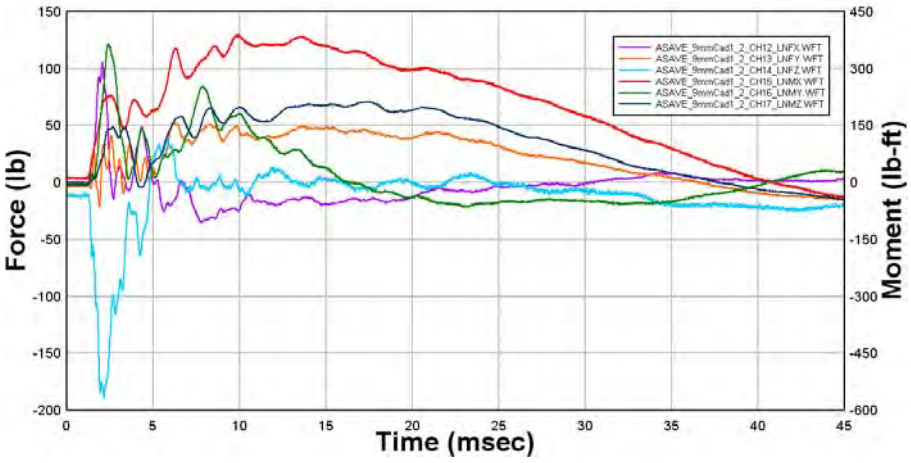

Figure 2.3.2.1-13. Representative Neck Loads and Moment Data

2.3.2.2. Technical Approach for Helmet sensor evaluations

In this test series the helmet sensor systems was evaluated using only the PMHS. The helmet systems were evaluated for detection of frontal, and side impacts. No rear tests were conducted due to the instrumentation attached to the rear and crown surfaces of the ACH. Seven ACH size large helmets with Team Wendy pads were used in this study.

The projectiles used in this test series were the 9mm FMJ and the 255 grain RCC. The target velocities for the 9mm projectile were 427±2 m/s and 457±5 m/s which bound the typical velocity for the evaluation of helmets in NIJ 0101.06 Standard for Ballistic Helmets. The velocities for the 225 grain RCC were 284±2 m/s and 311±4 m/s, below the V_0 of the ACH. The velocities of the projectiles were calculated by determining the time between the breaking of make screens as determined by an oscilloscope connected to the screens.

For the front PMHS positioning, the center of the gas gun barrel was aimed at a point approximately 6 cm above the rim and on the mid-sagittal plane. On the side tests, the center of the barrel was centered on the coronal plane of the PMHS 1 cm above the ear cup. The PMHS was tilted so all impacts have zero obliquity to the helmet surface (Figure 2.3.2.1-1). Three instrumented helmets were used in the ballistic evaluation. The test matrix for the helmet sensor evaluations is shown in Table 2.3.2.2-1 and each helmet was generally struck three times as shown for a total of nine hits. The high velocity tests were used to determine whether the system can detect and differentiate between impact orientations. The low velocity tests were used to determine if the system can detect differences in the projectile velocity at the side location. Data from all of the tests is being compared against blast and blunt impact data collected in the other test series in the program to determine if the systems can differentiate between the various types of impacts.

Table 2.3.2.2-4.
Test Matrix for the Ballistic Evaluation

PMHS	9mm RN		255 grain RCC		Total
	Low	High	Low	High	
	426 m/s	456 m/s	284 m/s	311 m/s	
Front	--	3	--	3	6
Side	3	3	3	3	12
Total	3	6	3	6	18

For the helmet sensor ballistic evaluation only instrumented PMHS was used. Instrumentation was attached to the surface of the PMHS skull and placed internally on the upper maxilla for comparison to the helmet sensor data. Internally, the PMHS accelerometer array was aligned with the midsagittal plane and rigidly fixed to a bite plate in the upper maxilla with two screws. The location of the sensor accelerometer package was approximately 35 mm anterior to the cg and 15 mm inferior to the cg. On the surface of the skull, an array of 5 pressure sensors was placed directly below the impact site. A sixth gauge recorded the strain in the bone to correct for skull deformation. To support the PMHS head and helmet system, the lower neck was potted and rigidly attached to a Hybrid III lower neck six-axis load cell. The head and neck system was not allowed to freely translate after the impact. Data was sampled at 1 MHz with an

anti-aliasing hardware filter at 200 kHz. The resulting sampled data was post processed with an 8-pole low-pass Butterworth filter at 40 kHz to match the shock tube and blunt impact data. The list of the PMHS instrumentation used in the study is listed in Table 2.3.2.2-2. Two cadaveric specimens (149 and 150) were used in this study. CT scans taken post-test will be used to derive anthropometric data. CT scans taken post test were used to derived specimen anthropometric data, shown in Table 2.3.2.2-3

Table 2.3.2.2-5.
Cadaver Ballistic Instrumentation List

Region	No. of Sensors	Axis	Measurement	Sensor Type
Skull	2	x	Acceleration	Endevco 7270
	2	y	Acceleration	Endevco 7270
	2	z	Acceleration	Endevco 7270
	6	NA	Contact Pressure	Dynasen PVF-10-25EK
Lower Neck	2	Shear	Force	Denton
	1	Axial	Force	Denton
	3	Moment	Force	Denton
Total	18			

Table 2.3.2.2-3
PMHS Anthropometry

PMHS	Sex	Age	Weight (kg)	Height (cm)	Head Breadth (mm)	Head Length (mm)	Head Height (mm)
Ballistic #1	M	62	45	170	147.61	186.02	98.63
Ballistic #2	M	75	77.1	165	140.05	183.94	103.41
Blast	M	60	79.4	175	135.23	187.73	92.81

In addition to the helmet sensor systems, to record the response of the helmet to the ballistic impacts laboratory-grade transducers were attached to the helmet. The crown and back locations (Figure 2.3.2.2-1) were chosen for their proximity to the commercial helmet sensors located at the inside surface of the crown of the helmet and the outside surface of the back of the helmet. At each location, a package of three linear accelerometers was rigidly attached to the helmet. In addition to the accelerometer packages, on the crown an angular rate sensor whose sensitivity is in the direction of impact was added. The laboratory helmet instrumentation was sampled at 1 MHz with an anti-aliasing hardware filter at 200 kHz and post processed with an 8-pole low-pass Butterworth filter at 40 kHz to match the shock tube and blunt impact data. The commercial helmet sensors were downloaded using the software native to that system.

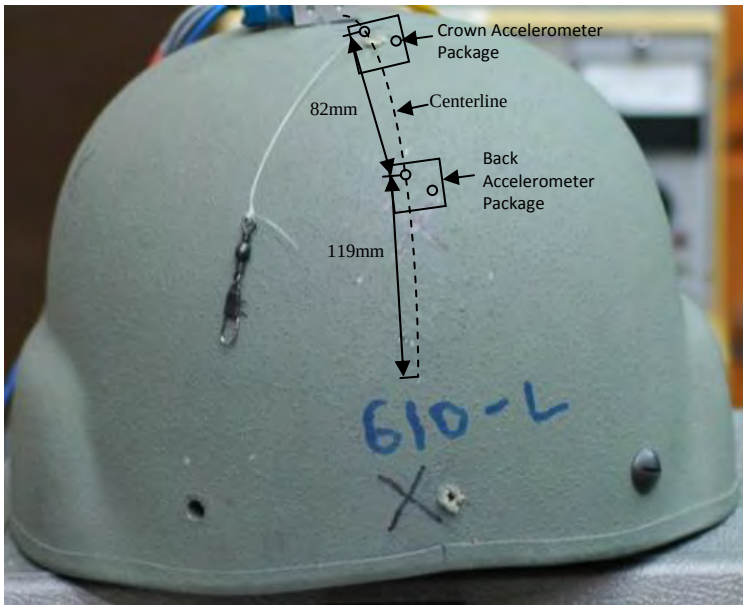

Figure 2.3.2.2-1. Location of the laboratory instrumentation on the helmet.

2.3.2.3. Results

The input test parameters from the ballistic tests are shown in Table 2.3.2.3-1. Velocities for the individual test conditions were generally well grouped as shown in Figure 2.3.2.3-1 with small standard deviations. The high and low groups were statistically significantly different (Student's t-test, $p > 0.05$, $\alpha = 0.05$). Test 50cal_HSS_1.6 produced a depressed fracture from backface deformation (Figure 2.3.2.3-2), but there was no penetration of the helmet. Subsequent tests were performed on the contralateral side of the cadaver from test 50cal_HSS_1.6 and an additional cadaver.

Table 2.3.2.3-1.
Ballistic Test Parameters

Test	Round	Round mass (g)	Tested Velocity (m/s)	Orientation
9mm_HSS_1.1	9 mm FMJ	8.03	452	Front
9mm_HSS_1.2	9 mm FMJ	8.03	448	Front
9mm_HSS_1.3	9 mm FMJ	8.11	451	Front
50cal_HSS_1.1	225 gr RCC	14.64	309	Front
50cal_HSS_1.2	225 gr RCC	14.62	316	Front
50cal_HSS_1.3	225 gr RCC	14.59	330	Front
50cal_HSS_1.4	225 gr RCC	14.60	312	Left
50cal_HSS_1.5	225 gr RCC	14.60	315	Left
50cal_HSS_1.6	225 gr RCC	14.59	314	Left
9mm_HSS_1.4	9 mm FMJ	8.07	421	Right
9mm_HSS_1.5	9 mm FMJ	8.06	428	Right
9mm_HSS_1.6	9 mm FMJ	8.12	423	Right
50cal_HSS_1.7	225 gr RCC	14.58	276	Right
50cal_HSS_1.8	225 gr RCC	14.6	280	Right
50cal_HSS_1.9	225 gr RCC	14.6	292	Right
9mm_HSS_1.7	9 mm FMJ	8.10	453	Left
9mm_HSS_1.8	9 mm FMJ	8.13	450	Left
9mm_HSS_1.9	9 mm FMJ	8.07	452	Left

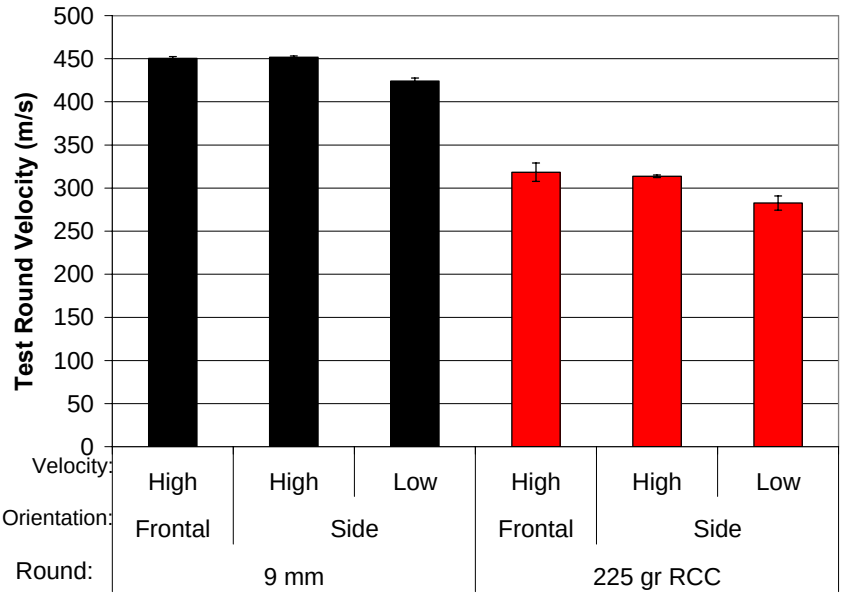

Figure 2.3.2.3-1. Helmet test – Incoming round velocity averages.

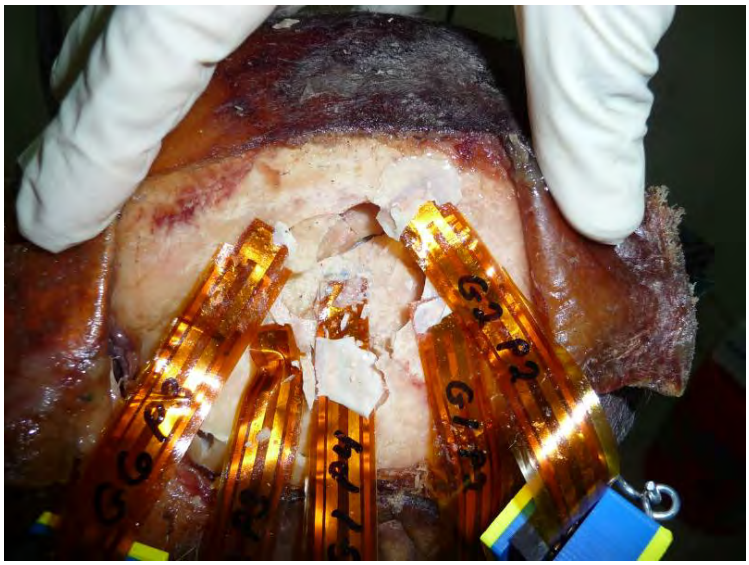

Figure 2.3.2.3-2. Depressed fracture from backface deformation (Test 50cal_HSS_1.6).

2.3.2.3.1. Physical Performance

A post-test view of a helmet is shown in Figure 2.3.2.3.1-1 and 2. Though there is not extensive structural damage to the helmet, the test rounds used in this series generally result in backface deformation sufficient to contact the head. In addition, under the impact site, there is generally permanent deformation, though this deformation was less than the available rattlespace for the ACH.

Figure 2.3.2.3.1-1. View of test helmet in side orientation, showing previously tested side of helmet and Med-Eng sensor.

Figure 2.3.2.3.1-2. View of test helmet in side orientation, showing rear of helmet and Med-Eng sensor.

2.3.2.3.2. Sensors

Data was obtained from laboratory sensors on the exterior crown and the exterior rear of the helmet. In addition, data was obtained at approximately the head center of gravity of the cadaveric specimen. Tables of laboratory crown, rear, and head resultant accelerations and timings are shown in Table 2.3.2.3.1-1, Table 2.3.2.3.1-2 and Table 2.3.2.3.1-3 respectively.

The helmet acceleration resultant peaks for the rear laboratory and crown laboratory sensors are shown in Figure 2.3.2.3.2-1. The average acceleration levels are above 4000 g for each test condition. The rear acceleration peaks are generally smaller than the crown peaks, in contrast to the expectation, based on low amplitude vibrational studies, that the crown resonance peaks have smaller amplitude than the peripheral (rear) locations. There are two likely explanations for this. The first is that the ACH does not behave as a vibrational shell under ballistic loading. There are large local deformations under the incoming projectile which will affect nearby sensors (crown) more than more distant sensors (rear). The second factor is that the Med-Eng sensor on the rear of the helmet likely acts as a relatively massive structural bridge, stiffening the rear structure and decreasing vibrational response in the rear of the helmet. The differences between the peak resultant acceleration between the laboratory sensor locations is statistically significant (Student's t test, $p<0.05$, $\alpha=0.05$), except for the frontal locations.

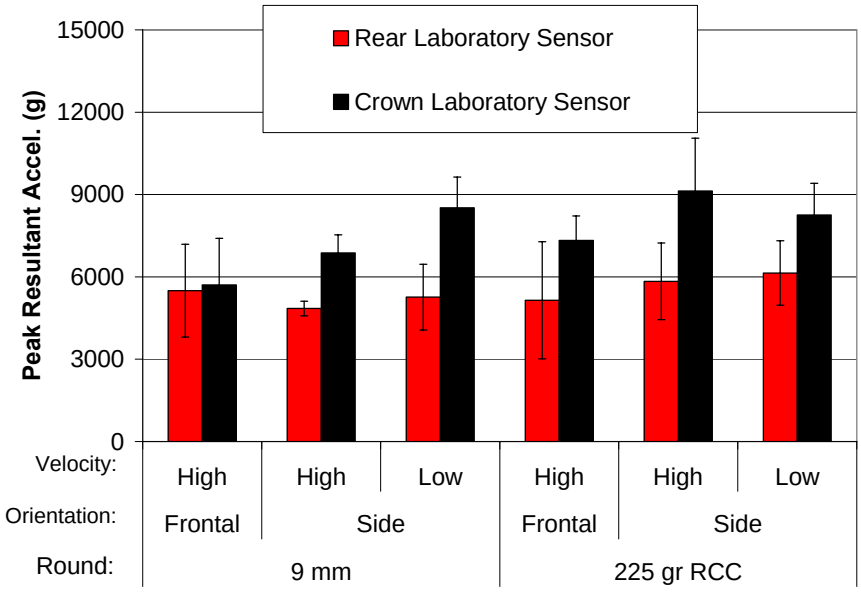

Figure 2.3.2.3.2-2. Helmet Laboratory Sensor Peak Acceleration Resultant, Averaged By Test Conditions

Table 2.3.2.3.1-1.
Crown Laboratory Sensor Acceleration Resultant Data.

	X axis				Y axis				Z axis				Resultant	
Test	**max (g)**	**max time (ms)**	**min (g)**	**min time (ms)**	**max (g)**	**max time (ms)**	**min (g)**	**min time (ms)**	**max (g)**	**max time (ms)**	**min (g)**	**min time (ms)**	**max (g)**	**max time (ms)**
9mm_HSS_1.1	4101	1.16	-1796	1.48	1254	1.03	-636	1.36	792	1.38	-871	1.03	4158	1.16
9mm_HSS_1.2	4967	1.10	-4524	1.28	4454	0.93	-3903	0.99	2649	0.98	-3045	1.15	5437	1.10
9mm_HSS_1.3	7022	1.12	-5877	1.32	3051	0.93	-1352	1.49	3150	1.44	-3358	0.97	7523	1.12
50cal_HSS_1.1	6545	1.49	-7401	1.58	4619	1.30	-1886	1.45	3684	1.78	-3079	1.35	7432	1.58
50cal_HSS_1.2	4668	0.32	-5835	0.35	2733	0.31	-2233	0.35	1608	0.37	-1844	0.35	6399	0.35
50cal_HSS_1.3	5014	1.43	-5974	1.57	5331	1.26	-3196	1.31	7960	1.29	-4399	1.32	8166	1.30
50cal_HSS_1.4	7019	1.67	-2032	1.89	1031	1.48	-992	1.31	3743	1.29	-5328	1.54	7407	1.67
50cal_HSS_1.5	10974	1.65	-4817	1.85	1044	1.53	-2248	1.34	7252	1.44	-6894	1.55	11208	1.66
50cal_HSS_1.6	7524	1.67	-4147	1.92	2252	1.62	-1571	1.46	8321	1.31	-3952	1.68	8784	1.31
9mm_HSS_1.4	6890	0.91	-5237	1.24	1113	1.41	-1123	0.90	5416	0.92	-4377	0.73	8037	0.90
9mm_HSS_1.5	9470	1.25	-6188	1.46	2203	1.05	-5083	0.98	5742	1.18	-8917	0.94	9798	1.25
9mm_HSS_1.6	4917	1.24	-4357	1.46	2368	1.13	-2222	1.04	6988	1.28	-7055	0.95	7718	1.28
50cal_HSS_1.7	3439	1.73	-3611	1.93	1306	1.59	-1063	1.54	9107	1.65	-8925	1.58	9196	1.58
50cal_HSS_1.8	5710	1.69	-4357	1.60	1846	1.61	-2271	1.47	6362	1.68	-7880	1.42	8606	1.68
50cal_HSS_1.9	6541	1.83	-5093	1.46	1517	1.76	-1620	1.63	3344	1.79	-6507	1.45	6969	1.82
9mm_HSS_1.7	5776	1.28	-3902	1.42	754	1.32	-592	2.09	4613	0.93	-3287	1.51	6122	1.28
9mm_HSS_1.8	6273	1.31	-4062	1.54	3062	1.01	-2378	1.29	6215	1.06	-6109	1.20	7248	1.35
9mm_HSS_1.9	6079	1.20	-2714	1.10	1608	1.29	-1578	1.00	5844	1.05	-5484	1.17	7260	1.19

Table 2.3.2.3.1-2.
Rear Laboratory Sensor Acceleration Resultant Data

	X axis				Y axis				Z axis				Resultant	
Test	max (g)	max time (ms)	min (g)	min time (ms)	max (g)	max time (ms)	min (g)	min time (ms)	max (g)	max time (ms)	min (g)	min time (ms)	max (g)	max time (ms)
9mm_HSS_1.1	1137	1.04	-1322	1.11	709	1.17	-607	1.11	3544	1.29	-2625	0.97	3549	1.29
9mm_HSS_1.2	5333	0.95	-4004	1.11	2859	1.40	-2776	1.34	3793	1.25	-3860	0.96	6368	0.96
9mm_HSS_1.3	5763	0.96	-1485	1.01	4692	1.09	-3047	1.16	2882	1.13	-3515	0.97	6573	0.96
50cal_HSS_1.1	5292	1.32	-3948	1.45	2235	1.75	-1898	1.36	4640	1.60	-3295	1.33	6040	1.33
50cal_HSS_1.2	2227	0.29	-2068	0.37	1320	0.35	-1195	0.36	2109	0.39	-1722	0.33	2714	0.29
50cal_HSS_1.3	6069	1.28	-4776	1.32	5685	1.34	-4195	1.38	1904	1.59	-3309	1.30	6691	1.28
50cal_HSS_1.4	1837	1.48	-3496	1.34	4182	1.30	-3862	1.57	4548	1.53	-2581	1.45	5754	1.55
50cal_HSS_1.5	2720	1.60	-4575	1.37	4394	1.33	-2221	1.72	6995	1.58	-4310	1.47	7278	1.58
50cal_HSS_1.6	1854	1.43	-3016	1.38	4249	1.33	-2656	1.57	1623	1.39	-2322	1.50	4486	1.34
9mm_HSS_1.4	5656	0.83	-4208	0.72	2007	1.12	-3295	0.65	3231	0.72	-3305	0.65	6139	0.83
9mm_HSS_1.5	4859	1.14	-4823	1.00	2782	1.37	-5088	0.96	2457	1.02	-1473	0.97	5751	0.95
9mm_HSS_1.6	1480	1.17	-2078	1.05	3104	1.22	-3342	0.98	2705	1.38	-2265	1.58	3898	1.21
50cal_HSS_1.7	5793	1.65	-4760	1.54	4125	1.73	-5105	1.48	3525	1.55	-2746	1.49	6441	1.55
50cal_HSS_1.8	4409	1.60	-4841	1.49	4375	1.86	-4260	1.44	5214	1.50	-3693	2.02	7141	1.49
50cal_HSS_1.9	1449	1.68	-2993	1.52	3352	1.74	-4483	1.47	1820	1.72	-2598	1.49	4846	1.48
9mm_HSS_1.7	1160	1.17	-1671	1.00	2018	0.95	-3250	1.45	3779	1.19	-2476	0.95	4550	1.44
9mm_HSS_1.8	1532	1.32	-1621	1.42	4162	0.95	-4346	1.18	3552	1.43	-2295	1.11	5049	1.42
9mm_HSS_1.9	1880	1.13	-2001	0.97	3770	0.93	-2728	1.21	4110	1.21	-2238	1.08	4943	1.21

Table 2.3.2.3.1-3.
Head Laboratory Sensor Acceleration Resultant Data

	X axis				Y axis				Z axis				Resultant	
Test	**max (g)**	**max time (ms)**	**min (g)**	**min time (ms)**	**max (g)**	**max time (ms)**	**min (g)**	**min time (ms)**	**max (g)**	**max time (ms)**	**min (g)**	**min time (ms)**	**max (g)**	**max time (ms)**
9mm_HSS_1.1	681	4.13	-389	2.55	932	4.01	-513	2.25	510	4.11	-292	3.28	972	4.01
9mm_HSS_1.2	1075	4.33	-673	2.77	1307	4.20	-892	2.53	929	4.35	-570	2.78	1453	4.20
9mm_HSS_1.3	1116	4.34	-337	2.84	979	4.16	-572	2.26	928	4.32	-413	2.45	1264	4.34
50cal_HSS_1.1	1267	4.83	-449	3.10	1020	4.70	-874	2.80	1059	4.85	-444	3.00	1364	4.70
50cal_HSS_1.2	914	1.04	-328	0.69	653	1.00	-581	0.75	527	1.04	-239	0.51	1045	1.04
50cal_HSS_1.3	346	5.10	-272	3.05	447	4.89	-460	3.99	178	5.09	-104	3.04	513	4.88
50cal_HSS_1.4	142	4.18	-121	3.47	182	4.93	-150	4.11	99	4.16	-130	3.37	216	4.17
50cal_HSS_1.5	207	5.68	-157	4.58	284	5.41	-157	4.25	172	5.65	-189	3.50	286	5.41
50cal_HSS_1.6	87	5.94	-72	4.76	139	5.70	-82	1.91	92	2.57	-104	3.38	142	5.70
9mm_HSS_1.4	17	4.09	-15	9.71	27	3.70	-20	2.49	33	4.20	-24	6.49	36	4.20
9mm_HSS_1.5	22	1.97	-19	1.65	31	1.59	-41	2.57	24	2.16	-12	2.35	45	2.56
9mm_HSS_1.6	13	1.77	-15	1.66	26	1.61	-13	2.05	20	8.29	-10	11.20	27	1.61
50cal_HSS_1.7	11	2.31	-13	2.67	24	2.19	-19	2.58	16	8.76	-9	2.00	26	2.20
50cal_HSS_1.8	29	3.45	-41	2.65	48	2.16	-84	2.97	68	2.57	-21	2.29	88	2.97
50cal_HSS_1.9	142	2.57	-94	3.42	135	4.14	-143	2.50	91	3.46	-49	2.70	189	2.51
9mm_HSS_1.7	23	1.96	-20	2.70	26	1.94	-30	2.68	17	12.45	-16	3.11	37	2.69
9mm_HSS_1.8	34	1.98	-32	2.65	43	1.89	-45	2.69	32	2.23	-19	2.71	57	2.68
9mm_HSS_1.9	37	1.93	-27	2.63	52	1.88	-34	2.72	26	2.13	-23	1.93	63	1.90

Unfiltered crown accelerometer spectral data (Figure 2.3.2.3.1-3) shows a peak at lower frequency and amplitude than for the helmet sensor data, likely because of increased coupling to the helmet for the laboratory sensors. This peak is representative of helmet vibrational modes studied in an earlier investigation of helmet characteristics (See Section 2.1.5.3). There is a sharp falloff in frequencies above 10 kHz save two relatively narrowband resonances that will likely have little consequence for head coupled motions.

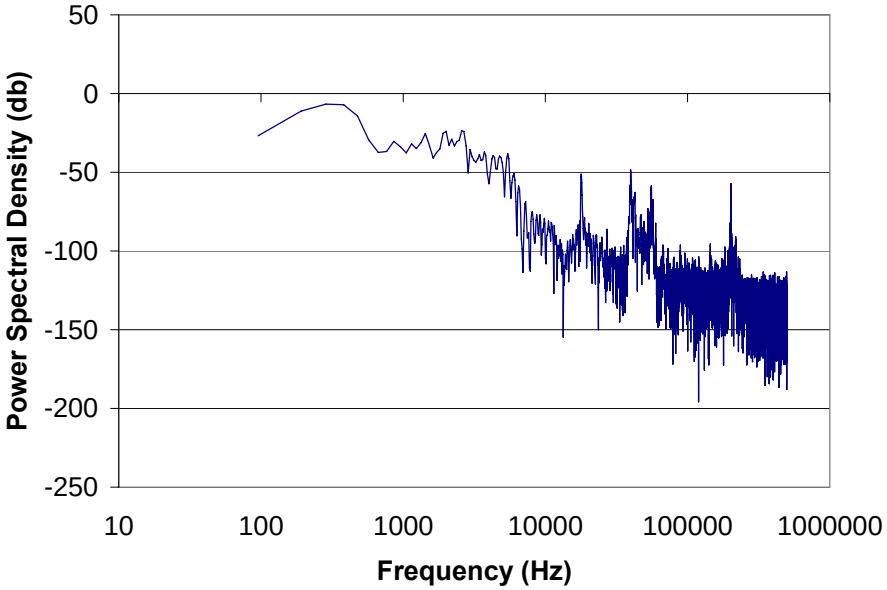

Figure 2.3.2.3.1-3. Power Spectral Density – Crown Laboratory Sensor (Test 9mm_HSS_1.07)

In contrast to the large helmet accelerations, the head acceleration peaks show strong evidence of lack of contact for the side test conditions as shown in Figure 2.3.2.3.1-4 The frontal conditions see head accelerations that average over 1000 g, while the side conditions see peak resultant accelerations less than 50 g for the 9 mm round and less than 250 g for the 225 gr. RCC round. This suggests that the development of a transfer function for ballistic impact to the helmet may be complicated by the general inability to sense backface head contact using the helmet sensors alone.

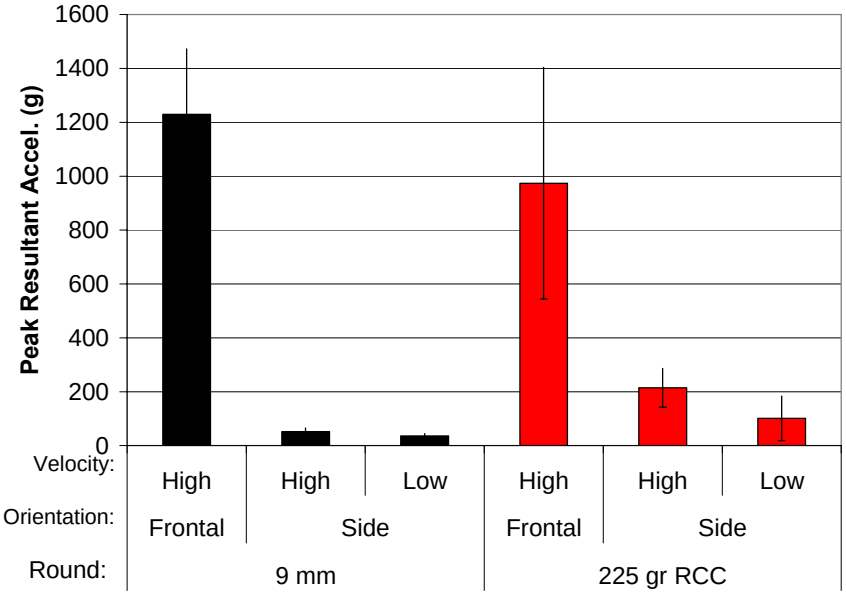

Figure 2.3.2.3.1-4. Head Peak Acceleration Resultant, Averaged By Test Conditions

2.3.2.4. Ballistics Transfer Function

The nonlinear relationship between the helmet response and the head response, especially in the domain between no backface contact and substantial backface contact makes the development of a transfer function between helmet and head difficult for ballistic impacts. Further, differences in fidelity between the helmet sensors tested and the laboratory grade sensors also used in this study suggest that limitations in the generation of sensors tested in this study may limit the potential transfer functions for this type of helmet excitation. Comparing the ratio of head peak resultant and BAE helmet sensor peak resultant (Figure 2.3.2.4-14) with a similar ratio using the average crown and rear laboratory sensor resultant acceleration (Figure 2.3.2.4-2) suggests that such a simple transfer function is unlikely to provide biofidelic results for the tested generation of sensors. Analysis of helmet response in the context of transfer function development with numerical models is ongoing and will be the subject of later reports.

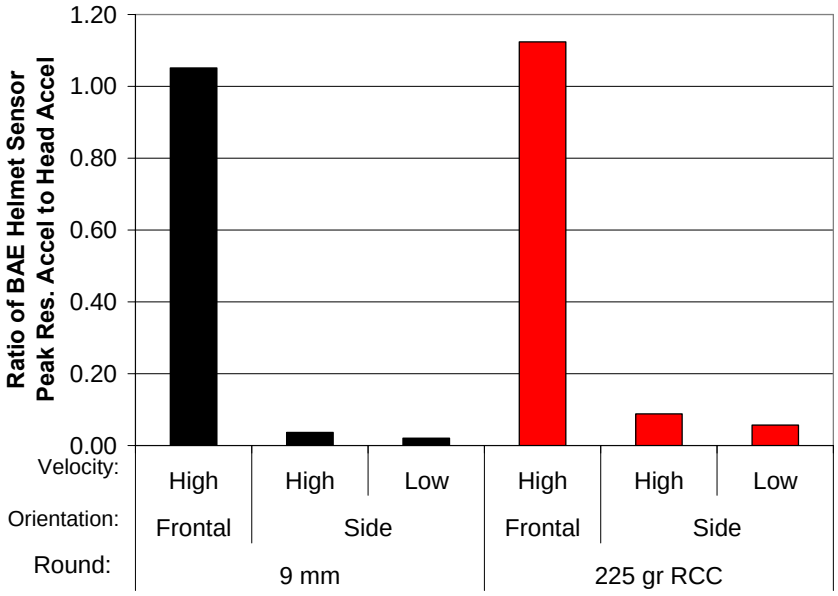

Figure 2.3.2.4-14. Ratio of BAE Helmet Sensor Peak Resultant Acceleration to Head Acceleration, Averaged by Condition

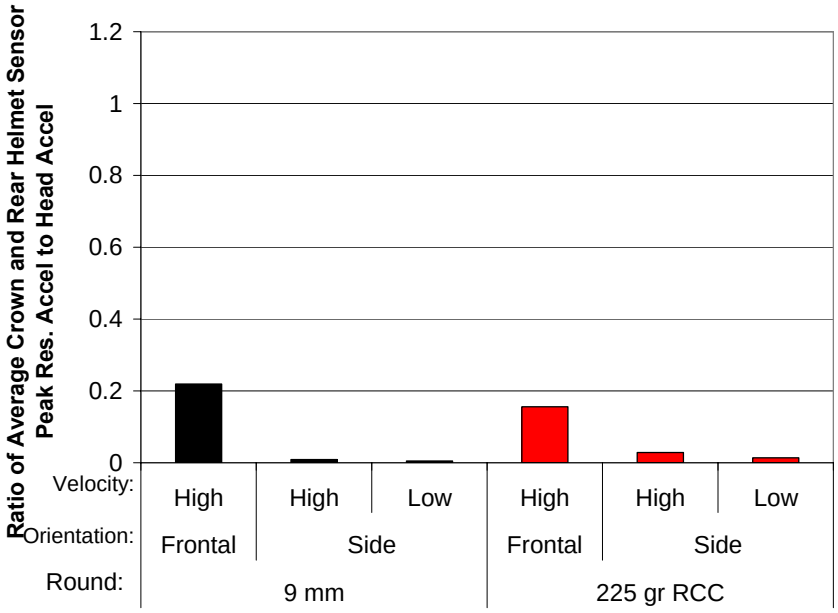

Figure 2.3.2.4-2. Ratio of Average Crown and Rear Helmet Laboratory Sensor Peak Resultant Acceleration to Head Acceleration, Averaged by Condition

2.3.2.5. Conclusions

The obtained ballistic results reveal substantial variability given consistent test conditions. These results are suggestive that a transfer function development may not be supported, at least for the ballistic impact events. Improvements may be realized once advanced signal filtering techniques are applied during continued data reduction efforts and the ongoing effort to develop a transfer function.

Several performance capabilities and limitations of the two HMSS systems have been identified. In fact, the external sensor mounted on the helmet rear failed to remain active and record data. This could have been the result of decayed battery life within the system. The laboratory sensor data will likely prove to be the most useful in the transfer function development. Additional analysis of the data may reveal further limitations of the Gen I Helmet Sensor instrumentation. The laboratory instrumentation data will prove to be extremely valuable to future helmet sensor development efforts.

2.4. Validation (free-field blast testing)

2.4.1. Free-field test arena setup

Free-field blast testing was performed from July 19 – 29, 2010, at ARA's Pecos Research and Development Center (PRTC) located near Pecos, Texas. The helmet sensor tests used one Post Mortem Human Subject (PMHS) head and two FOCUS heads. The first FOCUS headform was recorded by ARA, and the recorded data are discussed in this report. The second FOCUS head was recorded by USAARL personnel, and these data will be discussed separately. Because testing was done in conjunction with another military program, additional mechanical headforms were included: a Hybrid III, NOCSAE, THOR, and GelHead were also present for many of the tests. As many as seven headforms were positioned around the explosive charge at the center. Figure 2.4.1-1 shows a test set up with all seven headforms in position. The charges and the headforms were mounted 5 feet above the ground, to delay and reduce shock wave reflections off the ground. Figure 2.4.1-2 shows a schematic of the layout of each of the headforms and the pie plates used to measure incident pressure.

Figure 2.4.1-1. (left) Test arena with 7 headforms. The standoff distance was 42 inches. (right) blast event from the test series,

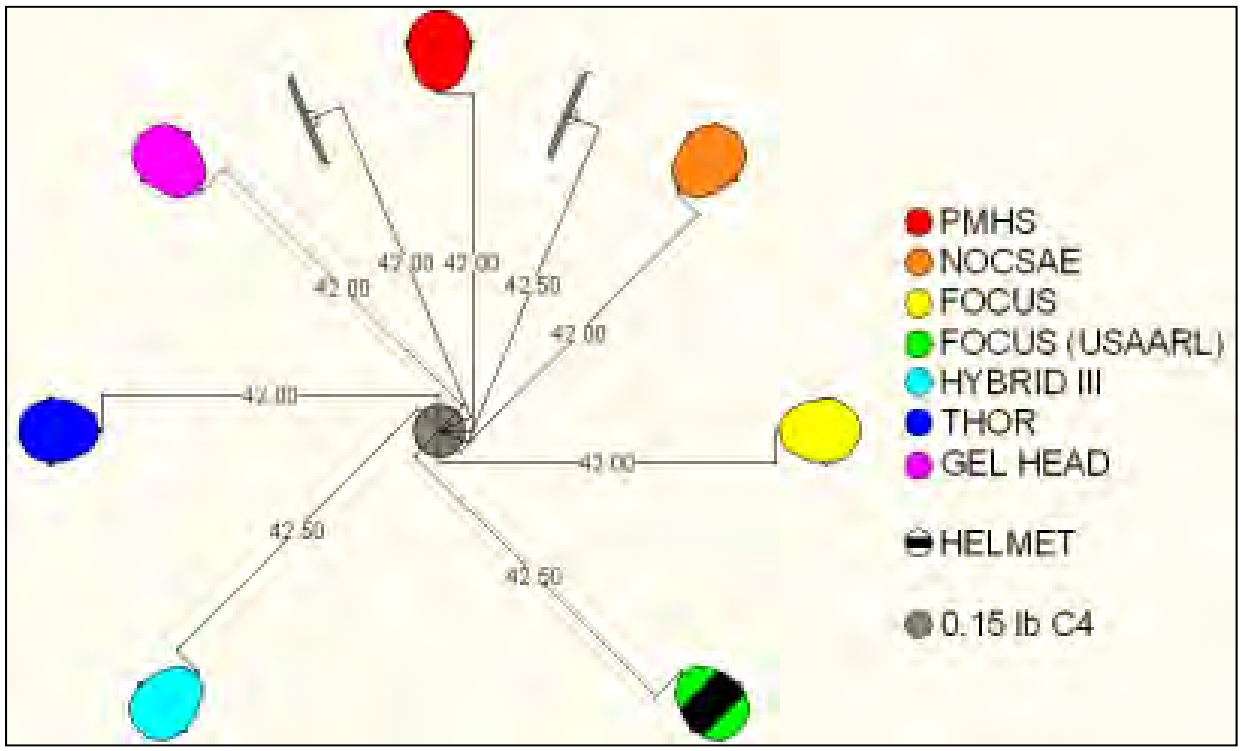

Figure 2.4.1-2. Schematic of headform locations with ideal distances used in test series 1 (tests 1.01 through 1.04). Distance from the charge was measured for each test and varied due to the blast effects on the mounts.

All charges were C-4 explosive formed into a sphere, with the detonator inserted into the center. Detonators were RP-81 exploding bridge wire (Teledyne RISI, Tracy, CA). Three different charge masses were tested at different standoff distances. The FOCUS and PMHS were instrumented and outfitted with ACH helmets in selected tests.

2.4.2. Tests Performed

The tests performed are summarized in Table 2.4.2-1. The charge weight and standoff distances were chosen based on the shock tube testing in Phase 1. The three test conditions correspond to incident pressures of 15 psi with a duration of 1-ms, 15 psi at 3-ms, and 30 psi at 1-ms durations.

Table 2.4.2-1.
Free-Field Test Matrix

Test ID	Date	Charge Wt. (lbs)	Standoff (inches)	Head Type	Helmet	Orientation
Blast_FF_1_01	7/25/10	0.15	39.5	PMHS	None	Front
			42.	Hybrid III	None	Front
			42.	FOCUS	None	Front
			40.5	THOR	None	Front
			42.	NOCSAE	None	Front
			38.5	Gel Head	None	Front
Blast_FF_1_02	7/25/10	0.15	42.	PMHS	None	Front
			42.5	Hybrid III	None	Front
			42.	FOCUS	None	Front
			42.	THOR	None	Front
			42.	NOCSAE	None	Front
			42.	Gel Head	None	Front
Blast_FF_1_03	7/25/10	0.15	42.5	PMHS	None	Front
			42.5	Hybrid III	None	Front
			41.5	FOCUS	None	Front
			42.	THOR	None	Front
			41.75	NOCSAE	None	Front
			41.75	Gel Head	None	Front
Blast_FF_1_04	7/26/10	0.15	42.5	PMHS	None	Front
			42.	Hybrid III	None	Front
			41.5	FOCUS	None	Front
			42.	THOR	None	Front
			41.5	NOCSAE	None	Front
			42.	Gel Head	None	Front
Blast_FF_2_01	7/26/10	1.25	72.	PMHS	None	Front
			72.25	Hybrid III	None	Front
			72.125	FOCUS	None	Front
			72.	THOR	None	Front
			72.	NOCSAE	None	Front
			71.5	Gel Head	None	Front
Blast_FF_2_02	7/26/10	1.25	72.5	PMHS	None	Front
			72.25	Hybrid III	None	Front
			72.	FOCUS	None	Front
			72.25	THOR	None	Front
			72.	NOCSAE	None	Front
			72.	Gel Head	None	Front
Blast_FF_2_03	7/26/10	1.25	72.5	PMHS	None	Front
			72.	Hybrid III	None	Front
			72.	FOCUS	None	Front
			72.	THOR	None	Front
			72.	NOCSAE	None	Front
			72.	Gel Head	None	Front
Blast_FF_2_04	7/27/10	1.625	72.	PMHS	None	Front
			72.5	Hybrid III	None	Front
			72.	FOCUS	None	Front
			72.5	THOR	None	Front
			72.5	NOCSAE	None	Front
			72.5	Gel Head	None	Front
Blast_FF_2_05	7/27/10	1.625	72.	PMHS	None	Front
			72.5	Hybrid III	None	Front
			72.	FOCUS	None	Front
			72.5	THOR	None	Front
			72.5	NOCSAE	None	Front
			72.5	Gel Head	None	Front

Blast_FF_2_06	7/27/10	1.625	72.	PMHS	None	Front
			72.5	Hybrid III	None	Front
			72.	FOCUS	None	Front
			72.5	THOR	None	Front
			72.5	NOCSAE	None	Front
			72.	Gel Head	None	Front
Blast_FF_2_07	7/28/10	1.625	72.	PMHS	ACH	Front
			72.25	Hybrid III	None	Right Side
			72.5	FOCUS	ACH	Front
			72.125	Gel Head	None	Left Side
Blast_FF_2_08	7/28/10	1.625	72	PMHS	ACH	Front
			72.25	Hybrid III	None	Right Side
			72	FOCUS	ACH	Front
			72.5	Gel Head	None	Left Side
Blast_FF_2_09	7/28/10	1.625	72.5	PMHS	ACH	Front
			72.25	Hybrid III	None	Right Side
			72.5	FOCUS	ACH	Front
			72.5	Gel Head	None	Left Side
Blast_FF_3_01	7/29/10	14.0	240	PMHS	ACH	Front
			240	Hybrid III	None	Front
			240	FOCUS	ACH	Front
			240	Gel Head	None	Front
Blast_FF_3_02	7/29/10	14.0	240	PMHS	ACH	Front
			239.25	Hybrid III	None	Front
			240.25	FOCUS	ACH	Front
			239.5	Gel Head	None	Front

2.4.3. Helmet and Headform Instrumentation

Tables 2.4.3-1 and 2.4.3-2 summarize the instrumentation used to capture the head and helmet dynamics. Figure 2.4.3-1 shows the location of the two laboratory accelerometer arrays mounted on the helmets. The laboratory accelerometers were Endevco 7270-A with varying ranges based on their orientation to the blast. The helmets included the helmet-mounted sensor systems (HMSS) A and B, and these data were recorded. HMSS is located inside the helmet at the crown, and HMSS B is located outside the helmet, at the back and is seen in Figure 2.4.3-1.

Incident pressure plates were positioned adjacent to the headforms to measure the free-field pressures. An Endevco 8530-B was mounted in the plate to measure the incident pressure. All data were sampled using a Hi-Techniques (Madison, WI) meDAQ data acquisition system sampling at 1 MHz, with a 100kHz hardware anti-aliasing filter.

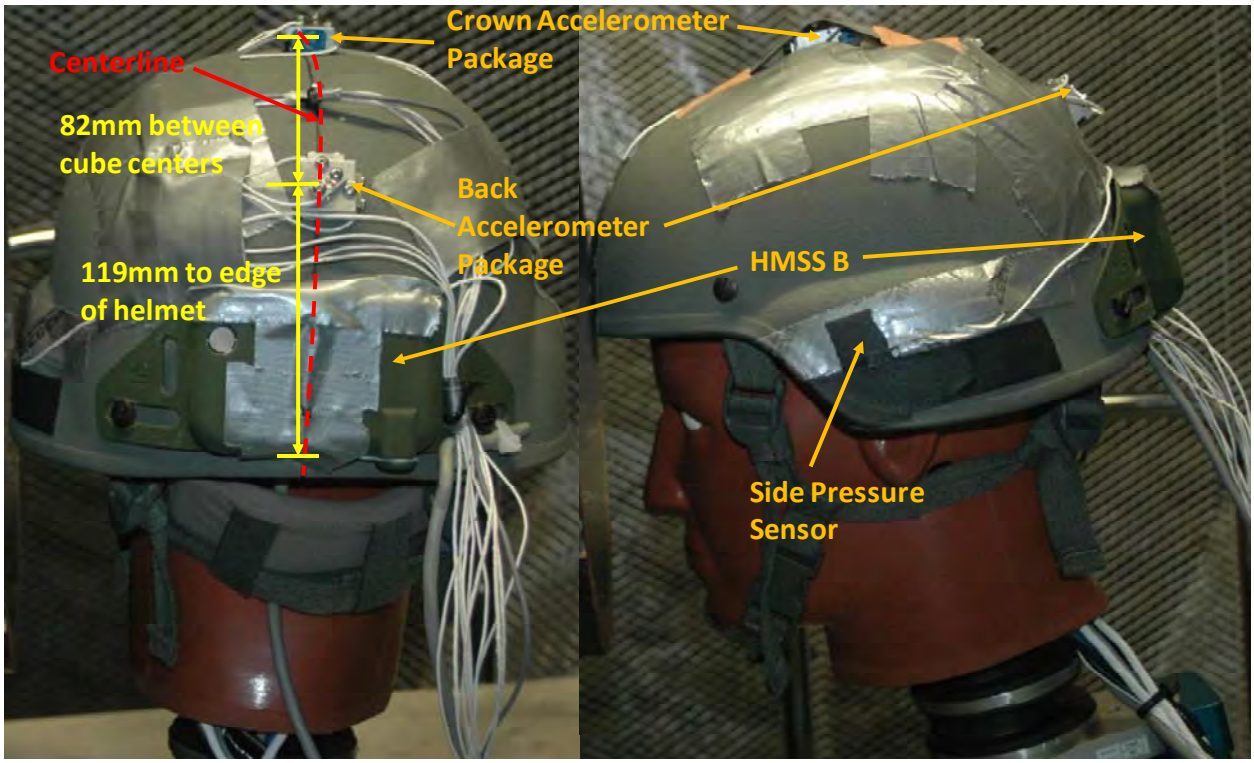

Figure 2.4.3-1. Helmet laboratory grade accelerometer locations

Table 2.4.3-1.
PMHS Instrumentation

Sensor Location	Measurement Type	Units	Channel Number	Channel Name
Upper Palette	Acceleration, X	g	37	CADAccX
Upper Palette	Acceleration, Y	g	38	CADAccY
Upper Palette	Acceleration, Z	g	39	CADAccZ
Lower Neck	Force, X	N	40	CADLNFx
Lower Neck	Force, Z	N	41	CADLNFz
Lower Neck	Moment, Y	N-m	42	CADLNMy
Helmet Crown	Acceleration, X	g	53	CAD HCX
Helmet Crown	Acceleration, Y	g	54	CAD HCY
Helmet Crown	Acceleration, Z	g	55	CAD HCZ
Helmet Rear	Acceleration, X	g	56	CAD HRX
Helmet Rear	Acceleration, Y	g	57	CAD HRY
Helmet Rear	Acceleration, Z	g	58	CAD HRZ
Helmet Front	Pressure	psi	24	HCAD1
Helmet Crown	Pressure	psi	25	HCAD2
Helmet Rear	Pressure	psi	26	HCAD3
Helmet right side	Pressure	psi	36	HCAD4
Adjacent to head	Incident pressure	psi	78	CAD FF

Table 2.4.3-2.
FOCUS Instrumentation.

Sensor Location	Measurement Type	Units	Channel Number	Channel Name
Head CG	Acceleration, X	g	1	FOCAccX
Head CG	Acceleration, Y	g	2	FOCAccY
Head CG	Acceleration, Z	g	3	FOCAccZ
Lower Neck	Force, X	N	12	FOCLNFx
Lower Neck	Force, Z	N	13	FOCLNFz
Lower Neck	Moment, Y	N-m	14	FOCLNMy
Helmet Crown	Acceleration, X	g	47	FOC HCX
Helmet Crown	Acceleration, Y	g	48	FOC HCY
Helmet Crown	Acceleration, Z	g	49	FOC HCZ
Helmet Rear	Acceleration, X	g	50	FOC HRX
Helmet Rear	Acceleration, Y	g	51	FOC HRY
Helmet Rear	Acceleration, Z	g	52	FOC HRZ
Helmet Front	Pressure	psi	43	FOC HP1
Helmet Crown	Pressure	psi	44	FOC HP2
Helmet Rear	Pressure	psi	45	FOC HP3
Helmet right side	Pressure	psi	46	FOC HP4
Adjacent to head	Incident pressure	psi	75	FOC FF

2.4.4. Data Summary

Figure 2.4.4-1 shows the incident pressure profiles seen by the FOCUS and PMHS headforms for shots 2.07, 2.09, 3.01 and 3.02. The traces match up very well with a difference in peak pressure well within the acceptable experimental error. The left chart in Figure 2.4.4-1 compares the free field pressures with the 30 psi-1 ms shock tube tests to demonstrate the similarity of the test conditions for validating the models as discussed in Section 2.1.

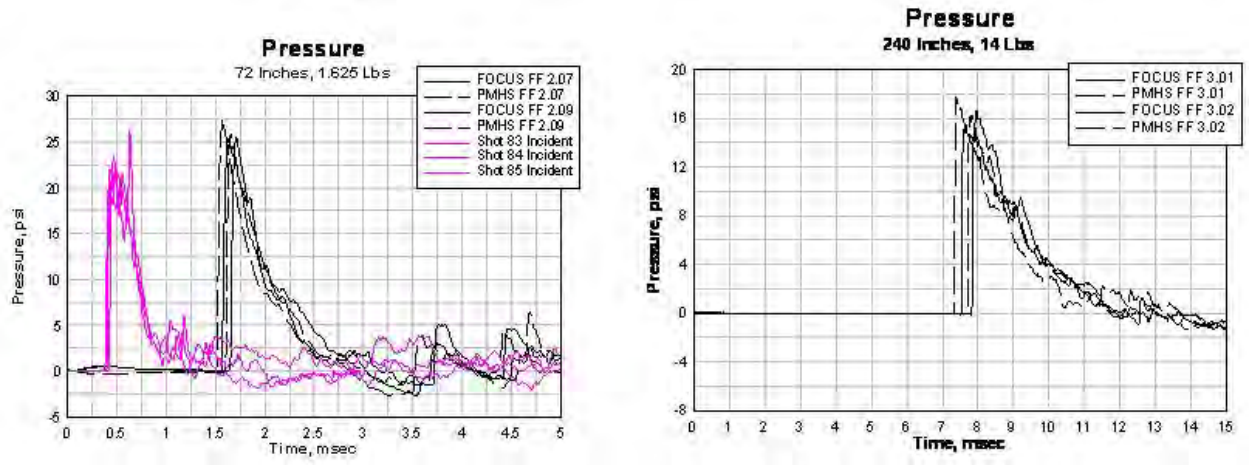

Figure 2.4.4-1. Incident pressure profiles seen by the FOCUS and PMHS headforms for shots (left) 2.07, 2.09 compared to similar shock tube tests, and (right) 3.01 and 3.02.

Figure 2.4.4-2 shows the pressure histories for the incident pressure, the crown of the FOCUS headform under the helmet, the crown of the helmet, and the rear of the helmet. The relatives loads are as expected, with the rear and crown sensors detecting similar magnitudes, but delayed between them, and the under helmet pressure reduced and delayed from the incident pressure.

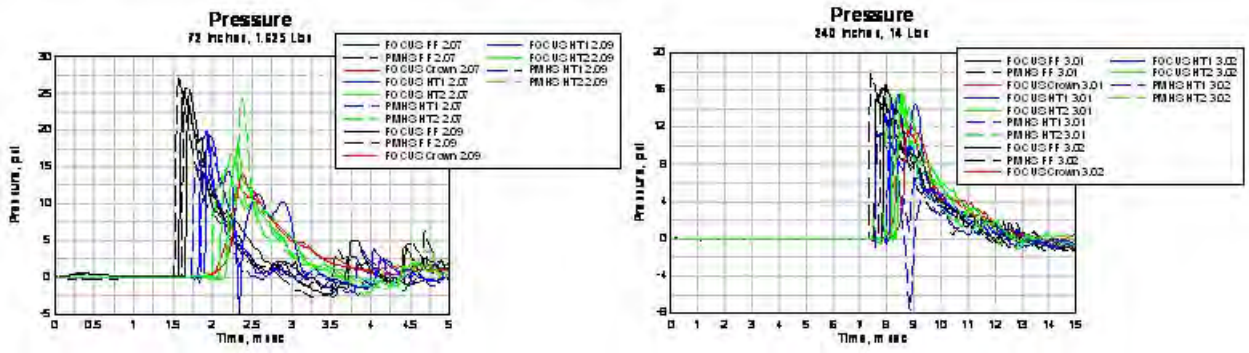

Figure 2.4.4-2. Pressure profiles seen by the FOCUS and PMHS headforms for shots (left) 2.07, 2.09, and (right) 3.01 and 3.02. HT1 is the crown helmet sensor, HT2 is the rear helmet sensor, and crown is under the helmet on the FOCUS headform.

Figure 2.4.4-3 shows the acceleration time histories for the PMHS and FOCUS headform CGs, the Helmet Crown, and Helmet Rear for the same shots, and again the traces are as expected with peak values similar to those seen in the shock tube testing.

The overall responses of the head and helmet pressure traces and acceleration traces behaved as expected. Figure 2.4.4-4 shows the peak pressure measured at the crown of the FOCUS headform for each test plotted against the peak incident pressure from the free field blast. As expected, the crown pressures of the unprotected headform map well with the peak incident pressures. When a helmet was used in the testing, the measured peak pressure was appropriately reduced as well.

Finally, Figure 2.4.4-5 demonstrates the effect of peak incident pressure on the measured peak acceleration in the X-axis. As expected, the acceleration peak of the center of gravity increases with increasing peak incident pressure. However, the acceleration peak of the helmet mounted accelerometer increases significantly with increasing peak pressure.

Figure 2.4.4-6 shows the neck load time histories for the PMHS and FOCUS headform.

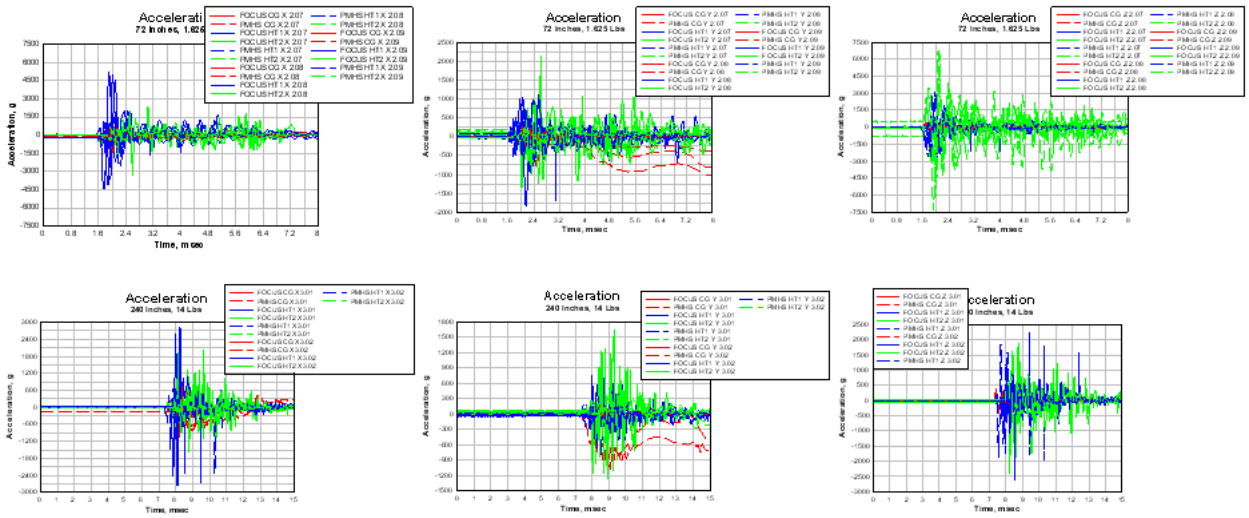

Figure 2.4.4-3. Acceleration profiles seen by the FOCUS and PMHS headforms for shots (top row) 2.07, 2.08, and 2.09, and (bottom row) 3.01 and 3.02. HT1 is the crown helmet sensor, HT2 is the rear helmet sensor. From left to right are X-axis, Y-axis, and Z-axis.

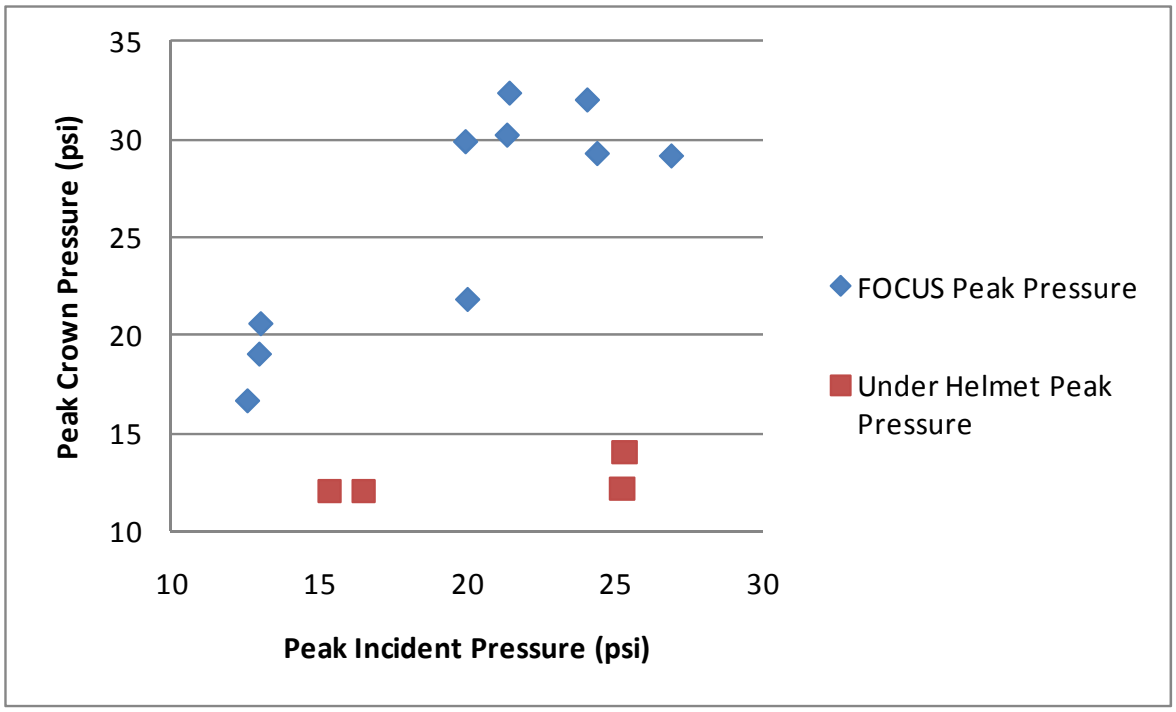

Figure 2.4.4-4. Peak crown pressure for helmeted and unhelmeted heads as a function of peak incident pressure for the free field blast tests.

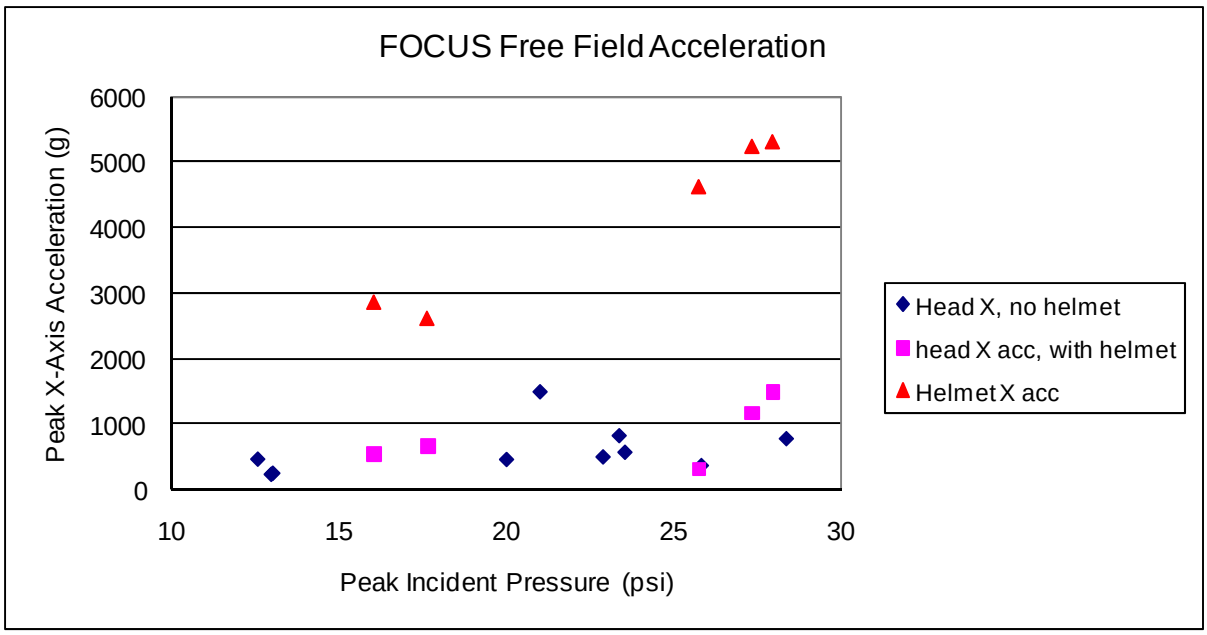

Figure 2.4.4-5. Peak X-axis acceleration as a function of peak incident pressure for the free field blast tests.

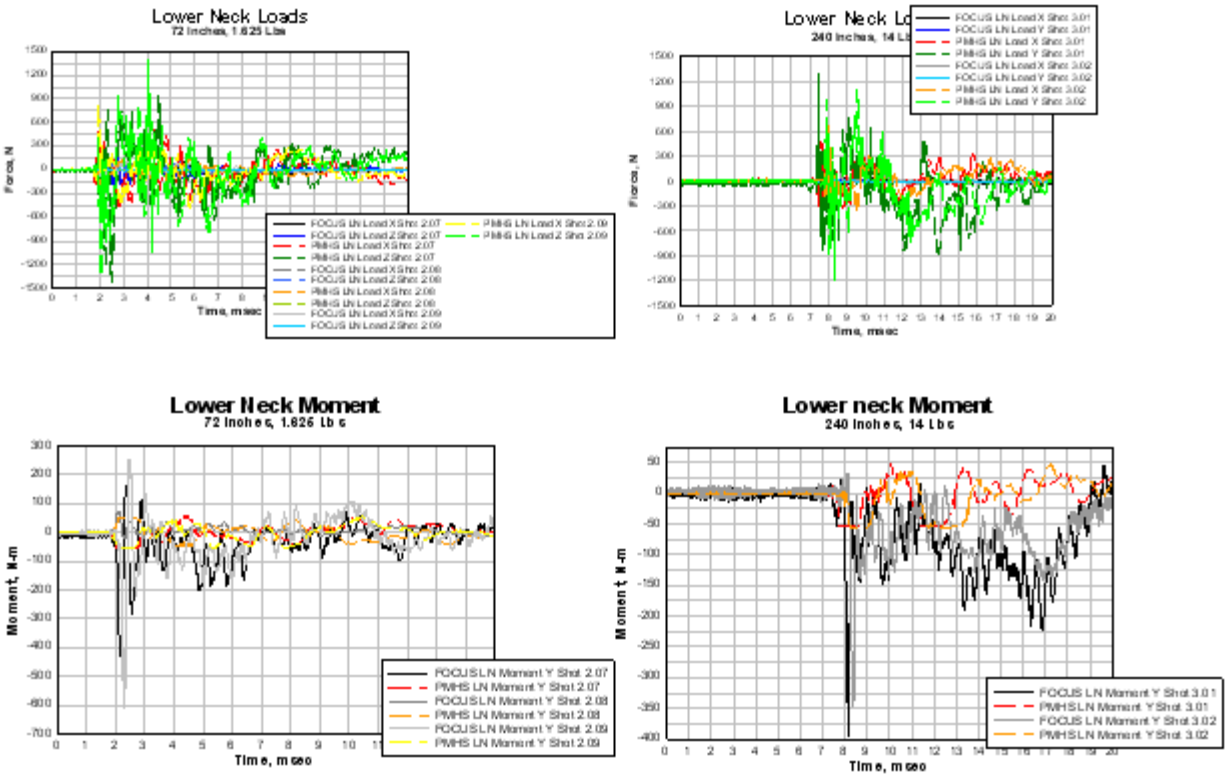

Figure 2.4.4-6: Lower neck load cell time histories for blast test 2 (left) and 3 (right). Top is the neck load forces, and the bottom is the neck moments.

2.4.5. Summary

Free field blast tests were conducted using C-4 as the explosive to acquire validation data to validate the model developed based on the shock tube tests in Phase 1. The path forward from this point is to apply the validation data to Duke and ARA's lumped parameter models. Also, this data will be used to validate the linear model relating helmet acceleration to head CG acceleration. The blast environment generated with the free field blast compared well with the pressure time histories generated by the shock tube tests. Generally, this implies that the free field data will serve as an acceptable validation of the model predictions pending further analysis.

2.5. Overall results and discussion

The results obtained during both the laboratory and field blast testing were very encouraging and showed greater repeatability within a single test condition than originally thought possible for very controlled laboratory conditions and relatively uncontrolled field test conditions. These results were used to develop linear correlations capable of limited predictions of head CG acceleration for a given helmet acceleration using the laboratory sensors ($r_2 > 0.76$), though the correlations were only applicable for a limited number of exposure scenarios.

Several performance capabilities and limitations of the two HMSS systems were identified. Due to this, it is likely incapable for a transfer function to be developed relating HMSS acceleration to headform acceleration. The laboratory sensor transfer function, however should prove to be a good substitute.

3. Key Research Accomplishments

- 100 18" shock tube tests were conducted on an instrumented FOCUS headform wearing an instrumented ACH under a variety of orientations and blast loads.
- 58 12" shock tube tests were conducted on an instrumented FOCUS headform wearing an instrumented ACH under a variety of orientations and blast loads.
- 52 12" shock tube tests were conducted on an instrumented PMHS Head wearing an instrumented ACH under a variety of orientations and blast loads.
- Duke has completed all finite element modeling efforts.
    - Application of finite element model for helmet/head interactions in blast based on an ACH helmet and various padding types including current ACH padding (Team Wendy).
    - Determination of transfer function between helmet and head peak resultant acceleration. Stable nonlinear fit emphasizes potential for developing helmet to head transfer functions.
    - Investigation of padding properties demonstrates the potential for the optimization of pad properties for blast protection.
- ARA has completed all helmet/head lumped-parameter numerical modeling efforts.
    - A lumped-parameter numerical model was created in Matlab.

- The model was used to model the numerous physical shock tube tests performed by ARA.
- Identified limitations of the numerical model and areas to improve model performance.

This report presents an overall flowchart to analyze helmet sensor acceleration data to classify each event as a blunt impact, blast, or ballistic impact. Procedures for determining the direction and magnitude of the pressure wave have been proposed but the procedure needs additional validation under multiple orientations before the procedure can be recommended for use in the analysis of the data from any helmet sensor system. The use of helmet sensor data to quantify ballistics events is discussed. Whole-body helmet motions are small and quite variable depending on the location and direction of projectile impact. Because of the highly localized deformation near the point of impact, we do not believe helmet sensor data will be useful in predicting head motion from ballistic impacts.

Fifteen free-field blast tests were conducted using C-4 as the explosive to acquire validation data to validate the model developed based on the shock tube tests in Phase 1.

4. Reportable Outcomes/Findings

No presentations or publications on this data have been prepared. An abstract on this effort has been submitted to the 2010 Army Science Conference, but was not accepted.

5. Conclusion

Though the data collected during laboratory and field testing was very consistent, more so than originally hypothesized, the performance limitations of the Generation One HMSS were such that they were not able to accurately characterize the blast event and were wholly uncapable of characterizing a ballistic impact.

The obtained ballistic results reveal substantial variability given consistent test conditions. These results are suggestive that a transfer function development may not be supported, at least for the ballistic impact events. Improvements may be realized once advanced signal filtering techniques are applied during continued data reduction efforts and the ongoing effort to develop a transfer function.

Several performance capabilities and limitations of the two HMSS systems have been identified. In fact, the external sensor mounted on the helmet rear failed to remain active and record data. This could have been the result of decayed battery life within the system. The laboratory sensor data will likely prove to be the most useful in the transfer function development. Additional analysis of the data may reveal further limitations of the Gen I Helmet Sensor instrumentation. The laboratory instrumentation data will prove to be extremely valuable to future helmet sensor development efforts.

The following conclusions are made based on the results of the Finite Element Modeling study conducted by the Duke University team:

- The modeling results suggest that the choice of padding materials used in Combat helmets has the potential for improving the protective capabilities in blast events.
- This study also identified certain characteristics of foam materials that may enhance or degrade the protection capabilities of the helmet. However, the helmet protection cannot be truly evaluated until blast brain injury mechanisms are properly identified, and injury metrics are established.
- The helmet reduced the effects of blast exposure relative to the unprotected case in all measures investigated in this study. While use of the helmet augmented the response of the head at low blast levels, helmet attenuation increased with increasing blast pressure such that the helmet offered better protection at blast levels that are considered injurious. Lower foam density decreased peak head acceleration and peak brain pressure.
- Strains induced by the primary blast wave itself were very small, but helmet-head coupling post-blast intensified the relative motion between the skull and the brain leading to greater tissue deformation. Coupling was reduced with crushable foams, which generated lower HIC values and lower brain strain than flexible foams. Furthermore, crushable foams reduced the magnitude of KE of the head by dissipated energy owing to the crushing action during the loading phase of impact.
- The blunt impact criterion specified for the Army current combat helmet (150G peak acceleration) is easily exceeded for even relatively mild blast levels.
- The results of this study imply that the computation of ACH-like helmet response to head response is well behaved under the controlled circumstances modeled in this limited study. It is also clear that padding choice has the potential for improving the protective capabilities of military helmets in blast, confirming previous experimental studies [3]. This study also identified certain characteristics of foam materials that may enhance or degrade the protection capabilities of the helmet. These assessments were based on analyzing the global response of the head and the local response of the brain subsequent to blast impingement. However, the helmet protection cannot be truly evaluated until blast brain injury mechanisms are properly identified, and injury metrics are established.
- Based on the metrics used in this study, the helmet reduced the effects of blast exposure relative to the unprotected case in all measures investigated in this study. While use of the helmet augmented the response of the head at low blast levels, helmet attenuation increased with increasing blast pressure such that the helmet offered better protection at blast levels that are considered injurious. Lower foam density decreased peak head acceleration and peak brain pressure. Strains induced by the primary blast wave itself were very small, but helmet-head coupling post-blast intensified the relative motion between the skull and the brain leading to greater tissue deformation. Coupling was reduced with crushable foams, which generated lower HIC values and lower brain strain than flexible foams. Furthermore, crushable foams reduced the magnitude of KE of the head by dissipated energy owing to the crushing action during the loading phase of impact.
- Limitations of this study include the assumption of plane strain; the predicted values reported in this study will change if modeling the three dimensional head and helmet. Helmet and head aerodynamics decrease the acceleration of the head and pressures seen in the brain. Helmet straps, although not likely to have substantial effect in the pressure propagation phase, may have an effect during the helmet/head coupling phase. However, as this study was comparative (helmet cases to non-helmet cases), it is likely that the

relative results reported in this study would still apply in three dimensions, and that relative response between helmet configurations will be consistent.

The following conclusions are made based on the results of the Lumped-Parameter Modeling study conducted by the ARA team:

- The lumped-parameter numerical model best fit the exposure data from the 15 psi incident pressure, 3 ms duration test condition
- The lumped parameter model uses padding forces to predict head movement. To accurately predict these forces we need a better characterization of padding forces as a function of strain and strain rate. The dual-density foam used in the padding would have very different stress-strain properties than the single density foam characterized by Chou. The strain rate-dependent effects need to be characterized at the high rates that were encountered here, up to 20,000 %/sec. This is not as daunting as it seems: impact testing at 4 m/s on helmet pads would be sufficient.
- Neck response could be brought into the model, using data from the neck load cell. Neck forces could not be measured in a field-able unit, but this would facilitate improvements in model fidelity. The shock tube tests measured forces and moments from the lower neck load cell. The upper neck load cell measures forces directly to/from the head and would be better.
- The model could be adjusted and evaluated at slower strain rates, such as from blunt impact tests.
- All of these could be done without significantly complicating the model.

6. References

[1] Warden, D.L., Military TBI During the Iraq and Afghanistan Wars. 21 (5) (2006), 398.
[2] Warden, D.L., et al., Case Report of a Soldier with Primary Blast Brain Injury. Neuroimage, 47 (Supplement 2) (2009), T152-T153.
[3] Keown, M., et al., Characterization of Helmet Energy Absorbing Liner Materials. PASS. Leeds, UK. (2006)
[4] Palm, E.J., et al., Test Methodology for the Assessment of Blast Trauma Behind Military Helmets. PASS. Quebec City, QC. (*Submitted)* (2010)
[5] US Army, Purchase Description, Helmet, Advanced Combat (ACH). CO/PD-05-04. (2007)
[6] Bicycle Helmet Safety Institute. Foams Used in Bicycle Helmets. 2008 [cited 2009 December 4]; Available from: http://www.bhsi.org/foam.htm
[7] Yang, K.H., et al., Development of Numerical Models for Injury Biomechanics Research: A Review of 50 Years of Publications in the Stapp Car Crash Conference. Stapp Car C J, 50 (2006).
[8] Cronin, D.S., et al., Numerical Modeling of Blast Loading to the Head. PASS. Brussels, Belgium. (2008)
[9] Moore, D.F., et al., Computational Biology — Modeling of Primary Blast Effects on the Central Nervous System. 47 (Supplementary 2) (2009), T10-T20.
[10] Cronin, D.S., et al., Numerical Modeling of Blast Trauma to the Human Torso. PASS. Rijswijk, The Netherlands. (2004)
[11] Ackerman, M.J., The Visible Human Project. Proc IEEE, 86 (3) (1998), 504-511.

[12] Gordon, C.C., et al., Anthropometric Survey of US Army Personnel: Methods and Summary Statistics, U.S. Army, Editor. 1989: Natick, MA. p. 325.
[13] Lynnerup, N., et al., Thickness of the Human Cranial Diploe in Relation to Age, Sex and General Body Build. Head Face Med, 1 (1) (2005), 1-13.
[14] Nicolle, S., et al., Shear Properties of Brain Tissue over a Frequency Range Relevant for Automotive Impact Situations: New Experimental Results. Stapp Car C J, 48 (2004), 239-258.
[15] van Hoof, J., et al., Backplane Response of Ballistically Impacted Composites. J Phys-Paris, 10 (2000), 659-664.
[16] Galford, J.E., et al., A Viscoelastic Study of Scalp, Brain, and Dura. J Biomech, 3 (2) (1970), 211-221.
[17] McElhaney, J.H., Dynamic response of bone and muscle tissue. 21 (4) (1966), 1231-1236.
[18] Chou, C.C., et al., A Constitutive Model for Polyurethane Foams with Strain-Rate and Temperature Effects. SAE Int C. Detroit, MI. (1998)
[19] McElhaney, J.H., et al., Mechanical Properties on Cranial Bone. J Biomech, 3 (5) (1970), 495-511.
[20] Boyd, R., et al., Simulation and Validation of UNDEX Phenomena Relating to Axisymmetric Structures. Int LS-DYNA C. Detroit, MI. (2000)
[21] Bloomfield, I.G., et al., Effects of proteins, blood cells and glucose on the viscosity of cerebrospinal fluid. Pediatr Neurosurg, 28 (1998), 246-251.
[22] Bouix, R., et al., Polypropylene Foam Behaviour under Dynamic Loadings: Strain Rate, Density and Microstructure effects. Int J Impact Eng, 36 (2) (2009), 329-342.
[23] Ouellet, S., et al., Compressive Response of Polymeric Foams under Quasi-Static, Medium and High Strain Rate Conditions. Polym Test, 25 (6) (2006), 731-743.
[24] Richmond, D.R., et al., Physical Correlates of Eardrum Rupture. Ann Oto Rhinol Laryn, 140 (1989), 35-41.
[25] Bass, C.R., et al., Pulmonary Injury Risk Assessment for Short-Duration Blasts. J Trauma, 65 (3) (2008), 604-615.
[26] Rafaels, K.A., et al., Injury Risk Assessment for Brain Injuries from Primary Blast. J Neurotrauma, *(Submitted)* (2010).
[27] Versace, J., A Review of the Severity Index. Stapp Car C J, 15 (1971), 771-796.
[28] Bass, C.R., et al., A Methodology for Assesing Blast Protection in Explosive Ordinance Disposal Bomb Suits. JOSE, 11 (4) (2005), 347-361.
[29] Iremonger, M.J., Blast Overpressure Injury. Scientific Foundations of Trauma, ed. G.J. Cooper, et al. 1997: Butterworth Heinemann. 189-199.

Appendices

Appendix A

Test and modeling time-history plots for the frontal blast direction.

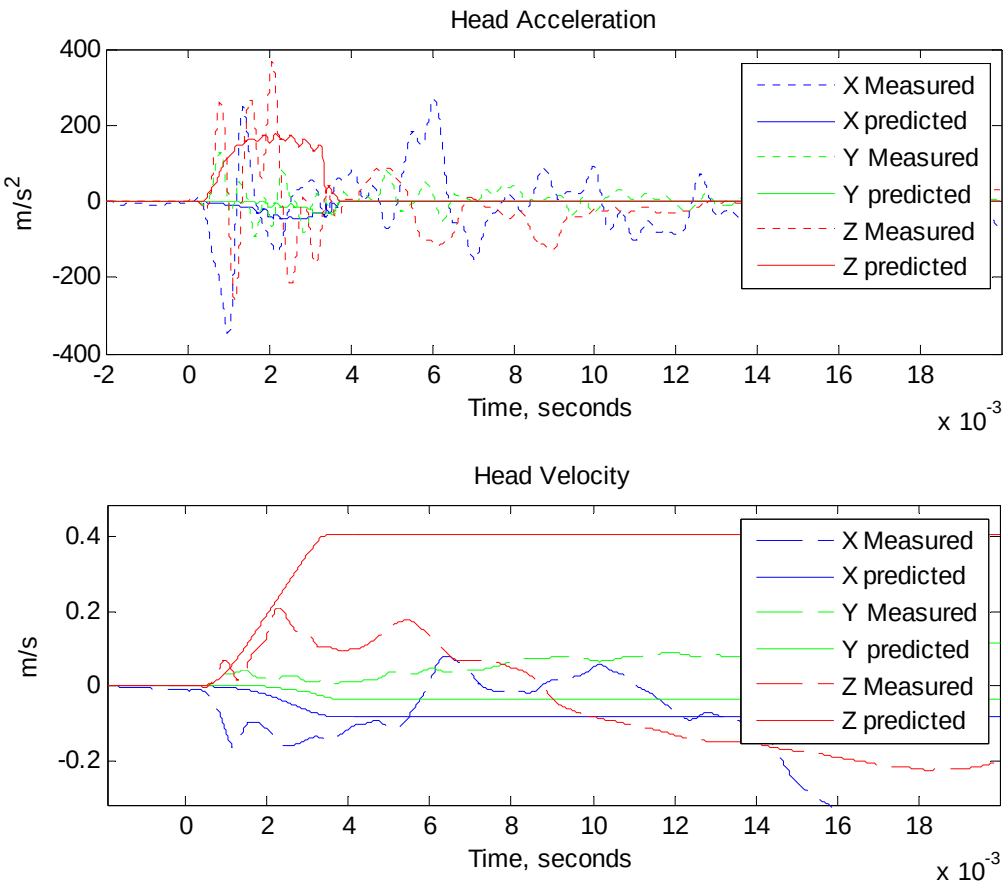

Figure A1. Head accelerations and velocities predicted by the model compared to measured head accelerations. From Test 6: Frontal - toward the blast, 15 psi -1 ms pulse.

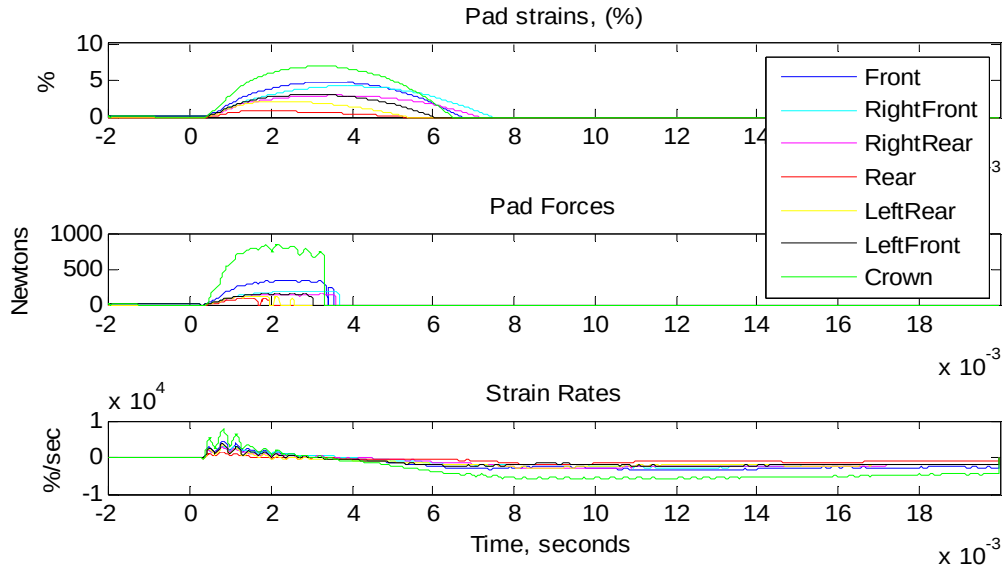

Figure A2. Helmet padding strains and forces from Test 6.

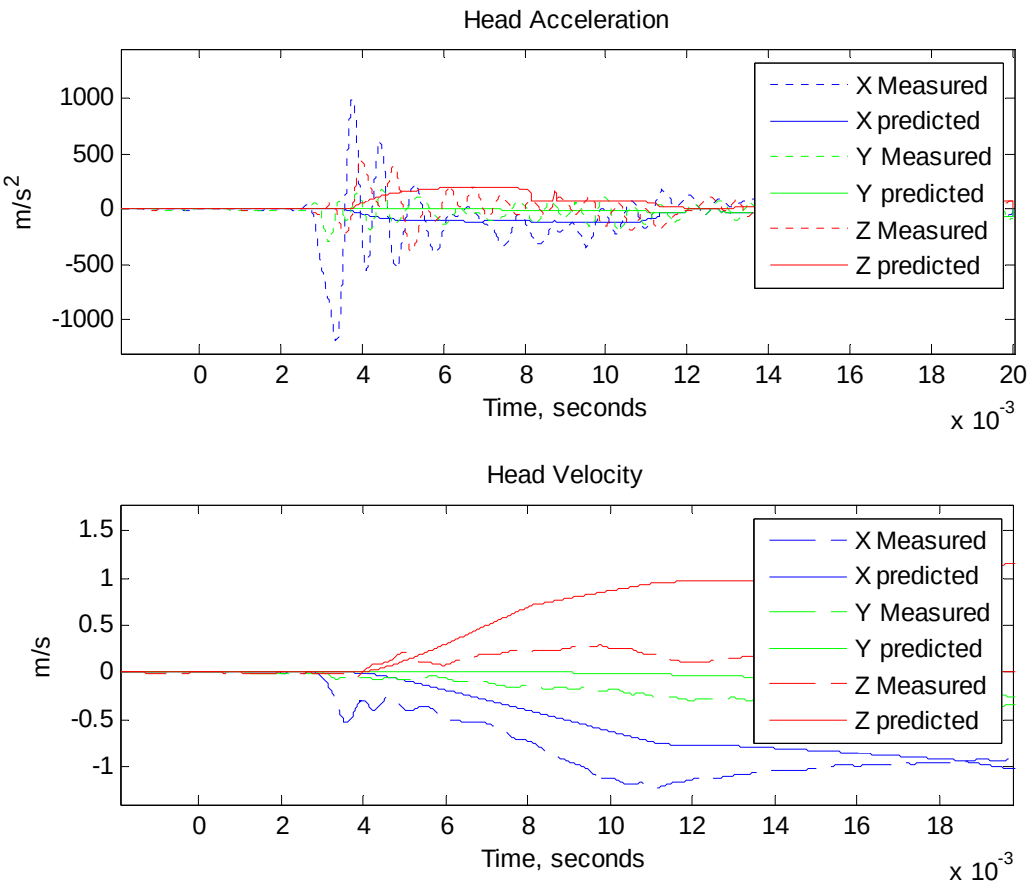

Figure A3. Head accelerations and velocities predicted by the model compared to measured head accelerations. From Test 45: Frontal - toward the blast, 15 psi - 3 ms pulse.

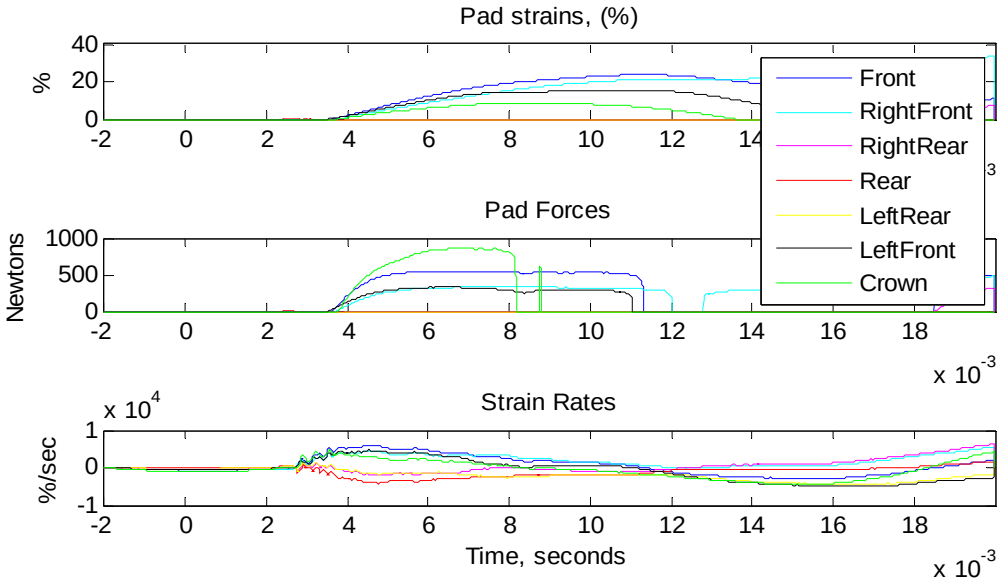

Figure A4. Helmet padding strains and forces from Test 45.

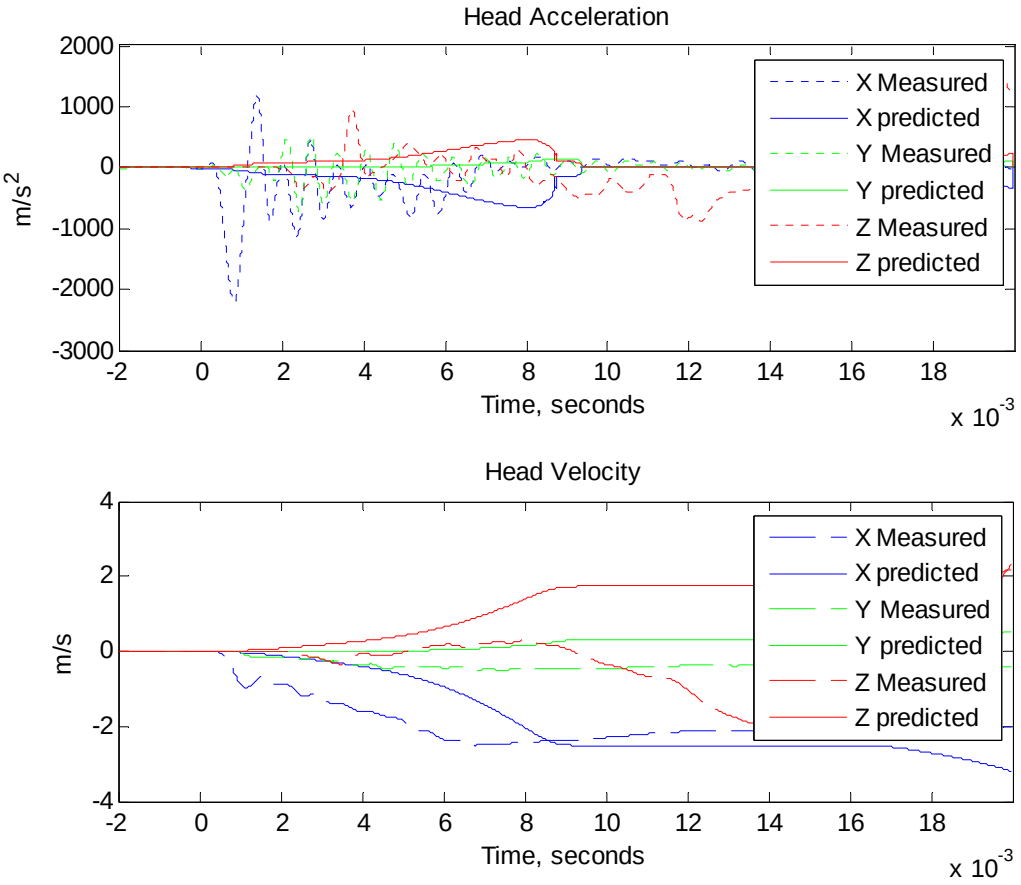

Figure A5. Head accelerations and velocities predicted by the model compared to measured head accelerations. From Test 88: Frontal - toward the blast, 30 psi - 1 ms pulse.

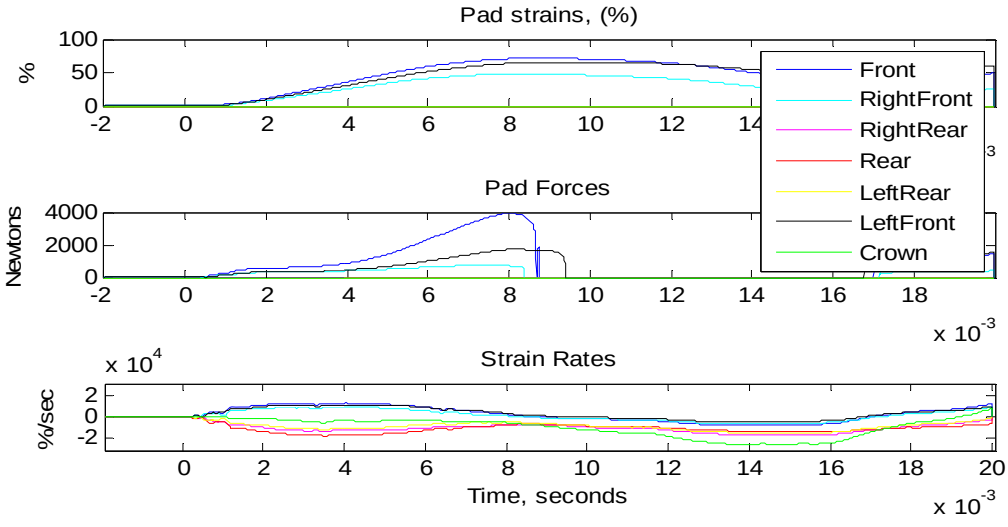

Figure A6. Helmet padding strains and forces from Test 88.

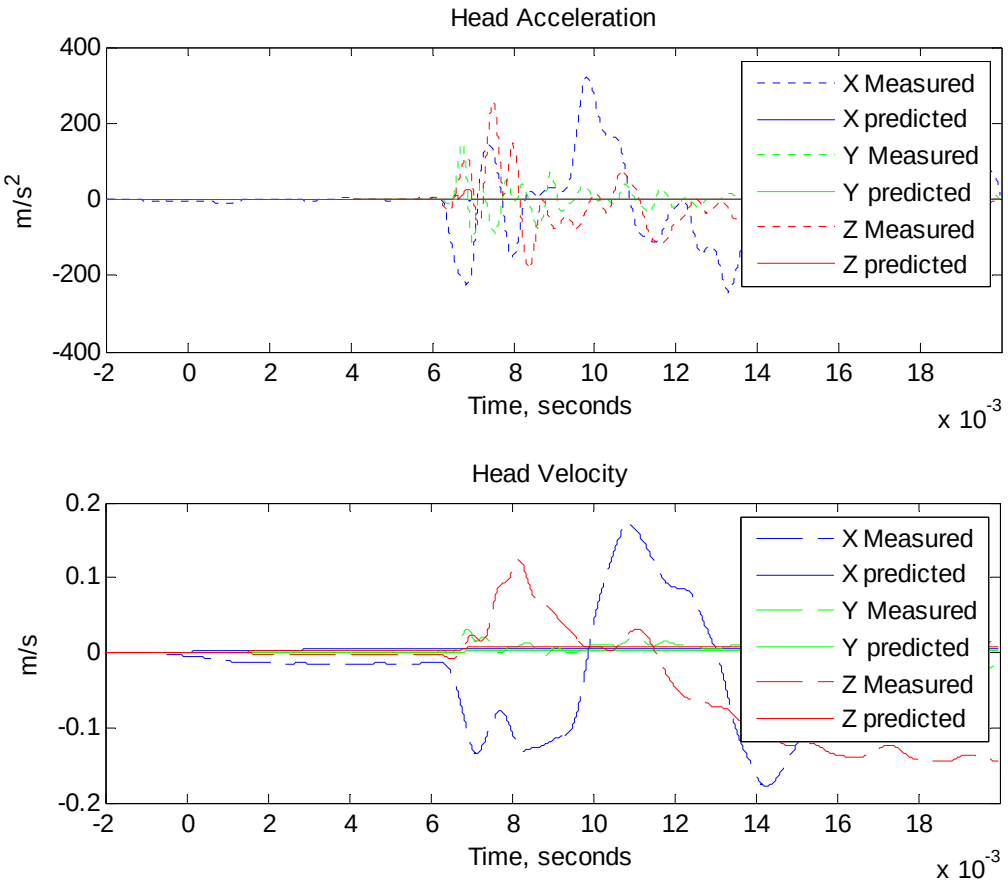

Figure A7. Head accelerations and velocities predicted by the model compared to measured head accelerations. From Test 3: Frontal - level with the blast, 15 psi - 1 ms pulse.

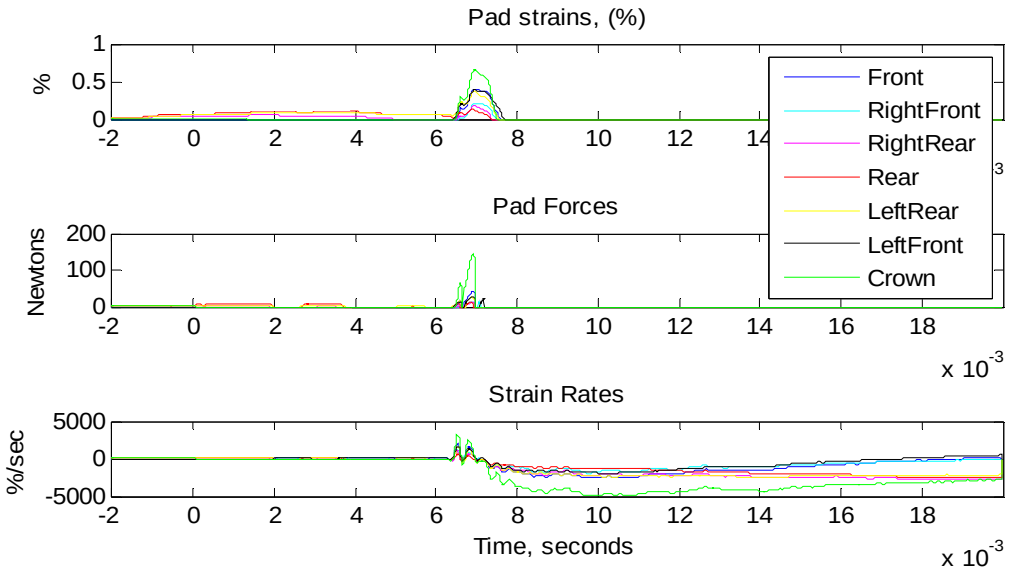

Figure A8. Helmet padding strains and forces from Test 3.

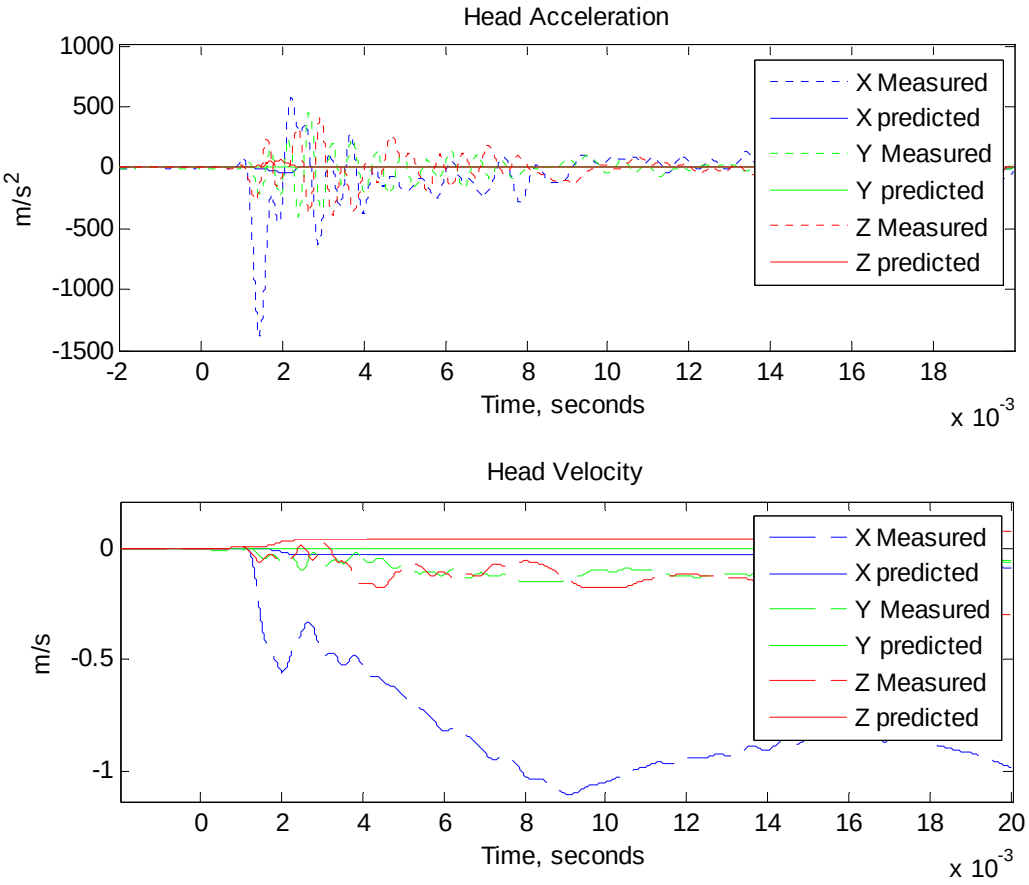

Figure A9. Head accelerations and velocities predicted by the model compared to measured head accelerations. From Test 40: Frontal - level with the blast, 15 psi - 3 ms pulse.

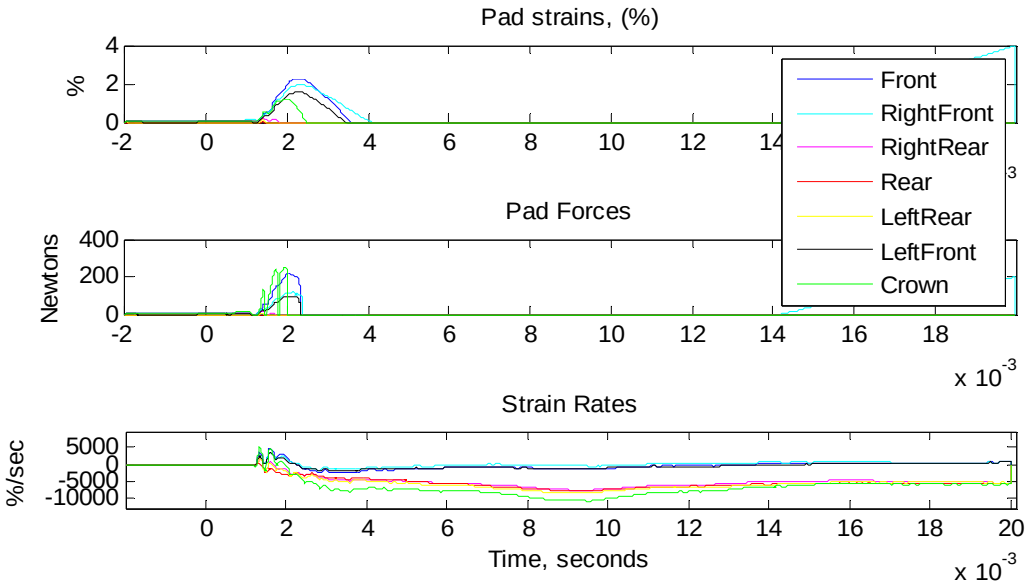

Figure A10. Helmet padding strains and forces from Test 40.

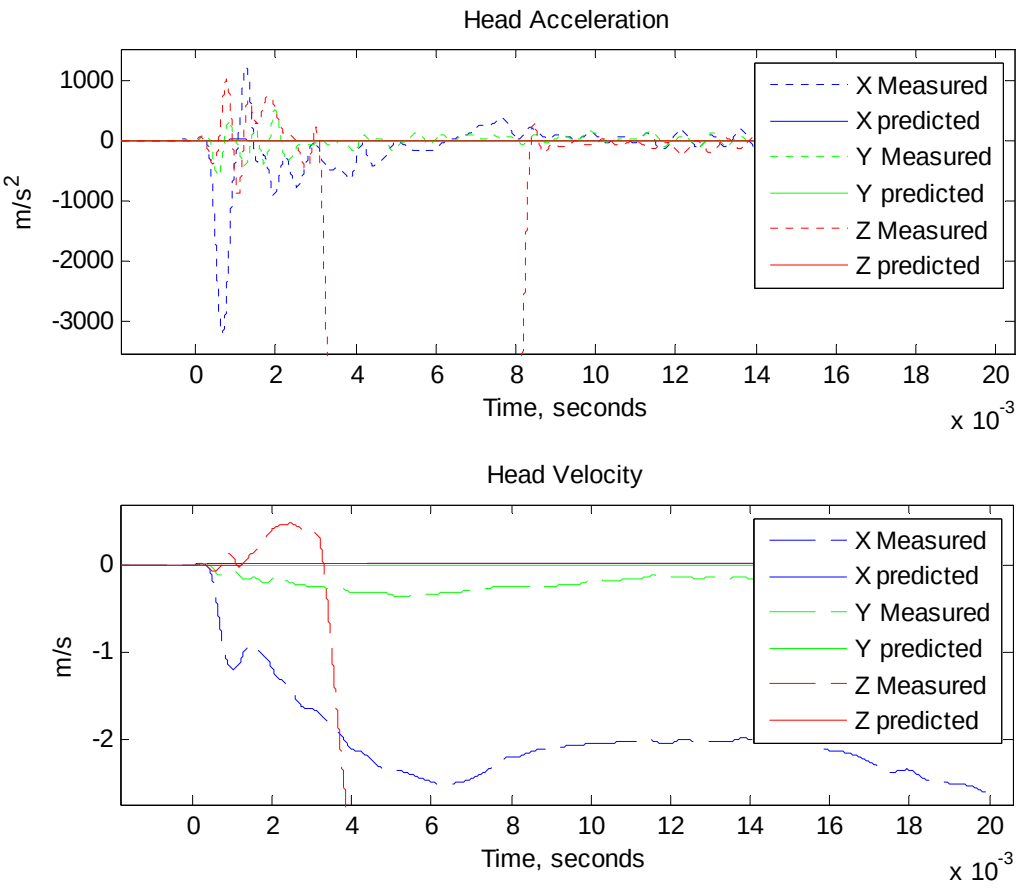

Figure A11. Head accelerations and velocities predicted by the model compared to measured head accelerations. From Test 84: Frontal - level, 30 psi - 1 ms pulse.

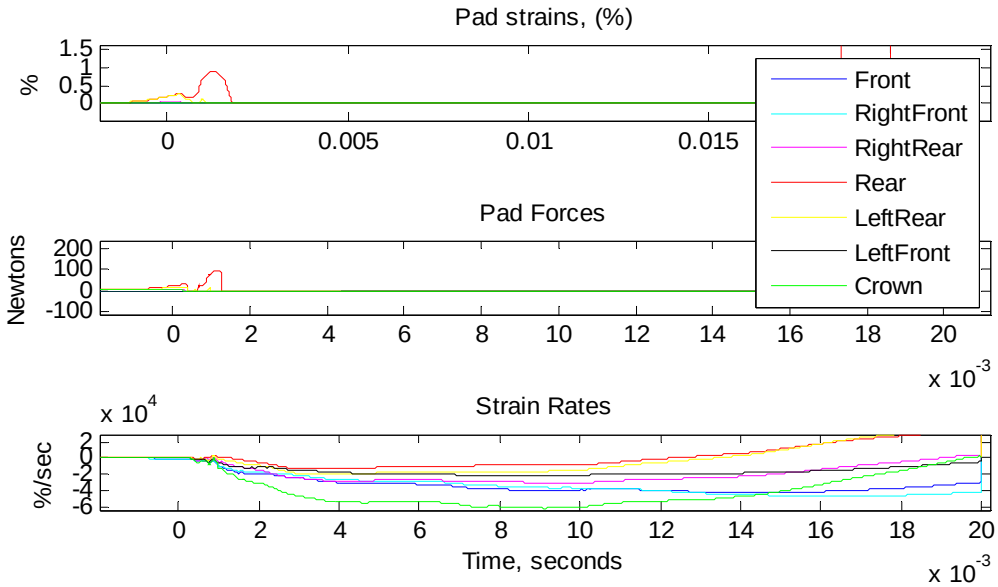

Figure A12. Helmet padding strains and forces from Test 84.

Appendix B

Test and modeling time-history plots for the sideward blast direction.

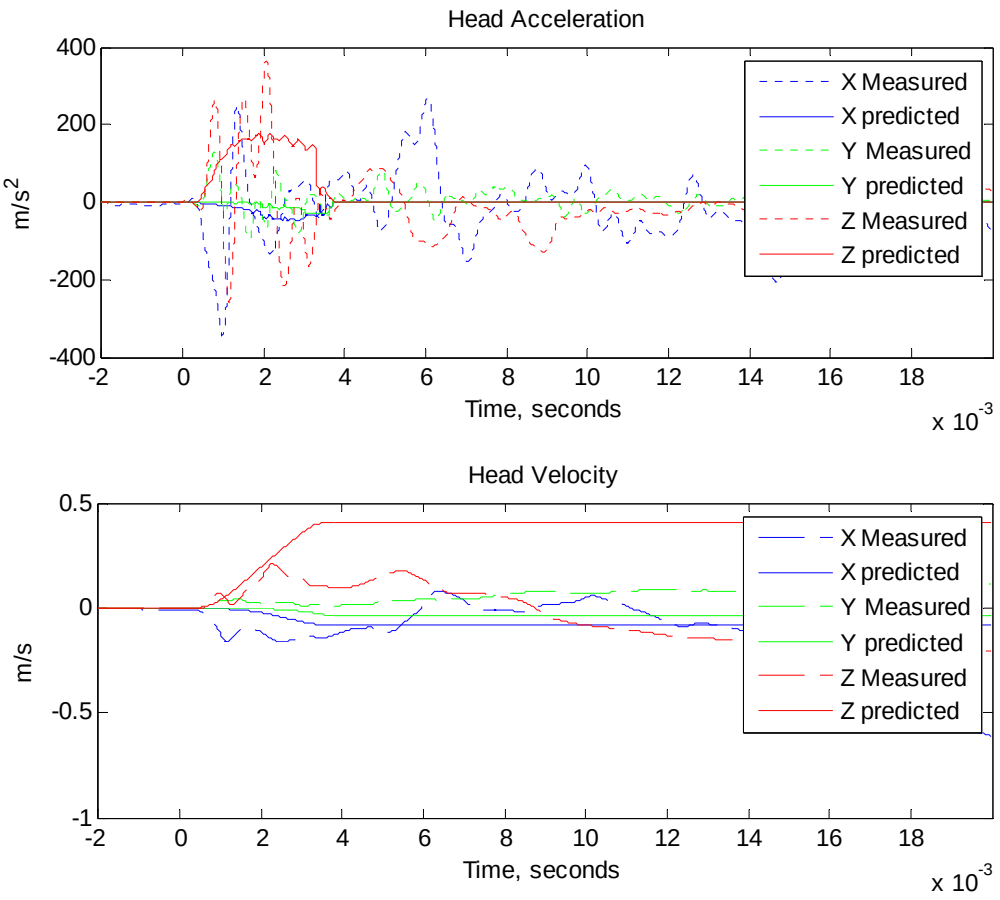

Figure B1. Head accelerations and velocities predicted by the model compared to measured head accelerations. From Test 6: Side – toward the blast, 15 psi - 1 ms pulse.

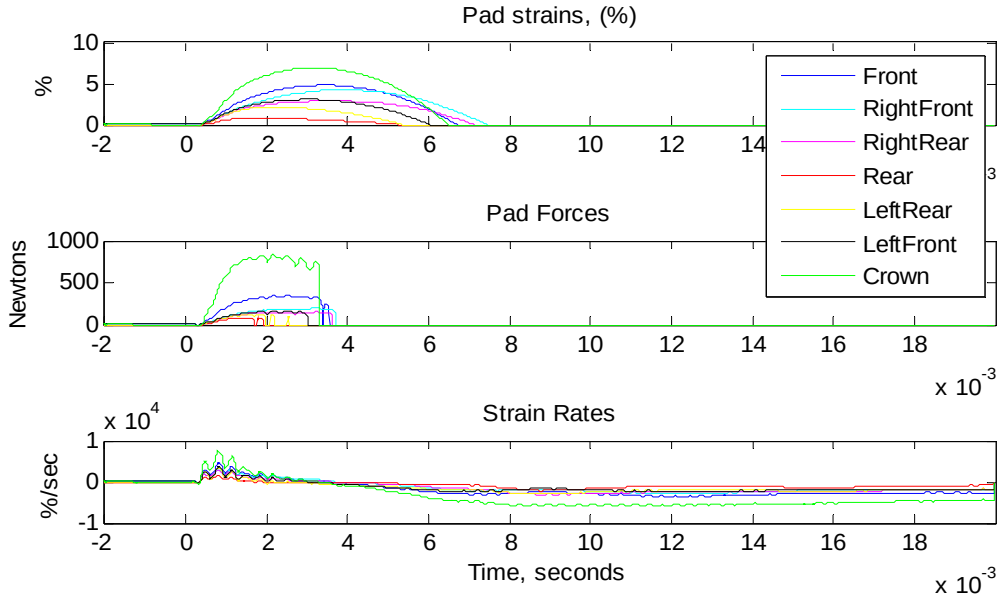

Figure B2. Helmet padding strains and forces from Test 6.

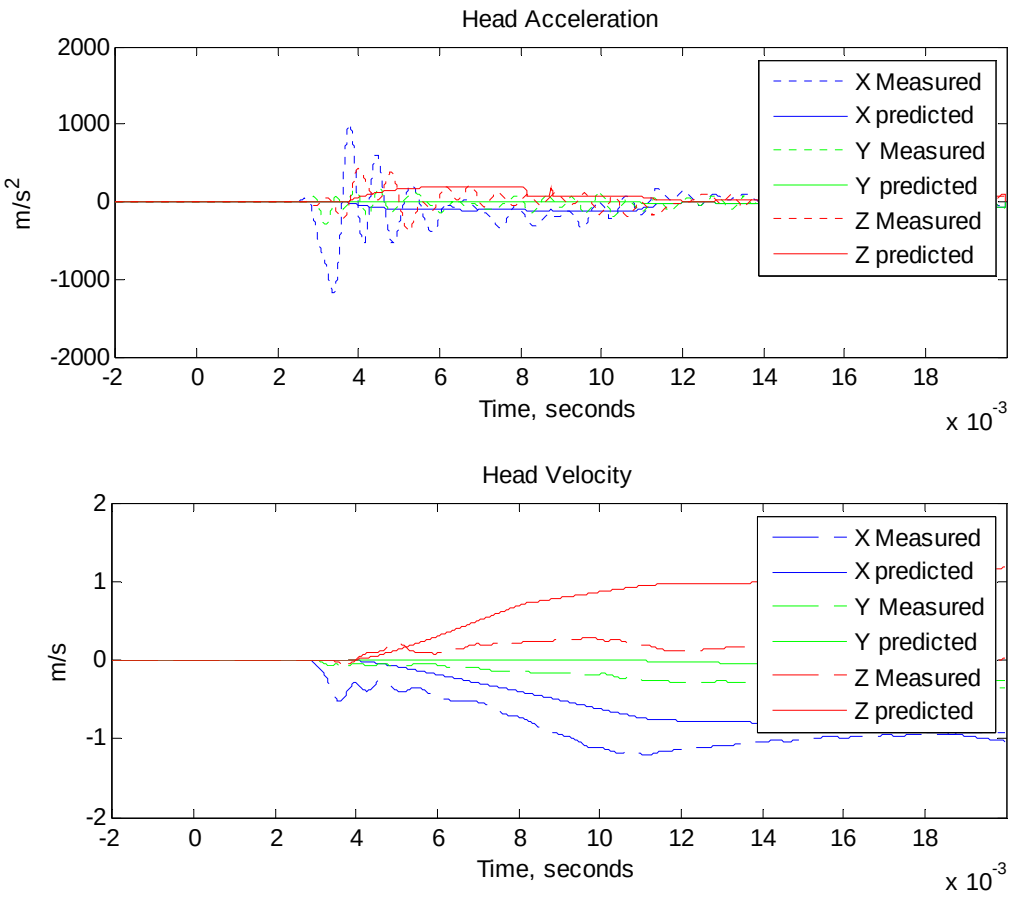

Figure B3. Head accelerations and velocities predicted by the model compared to measured head accelerations. From Test 45 : Side - toward blast, 15 psi - 3 ms pulse.

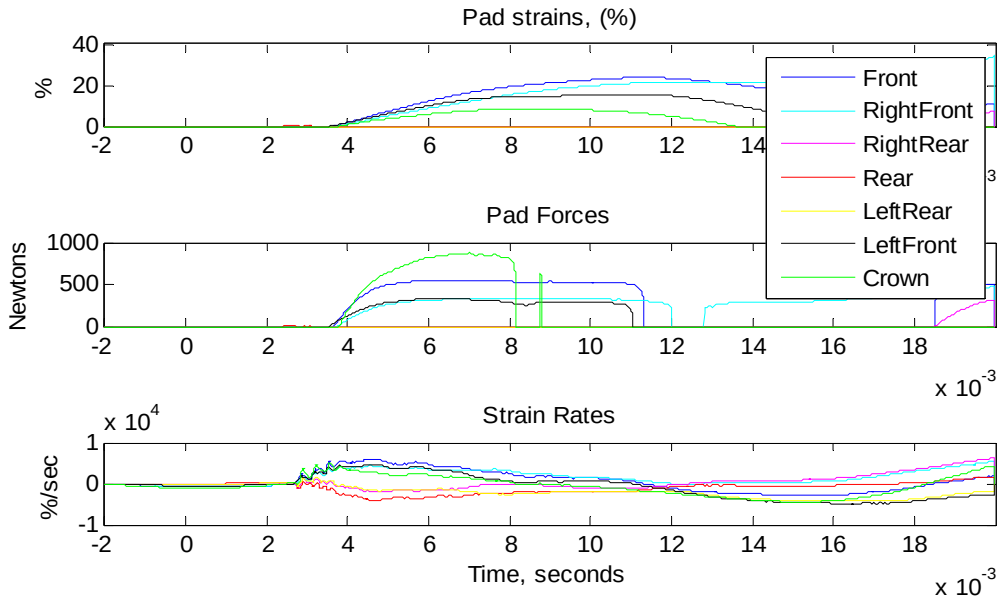

Figure B4. Helmet padding strains and forces from Test 45.

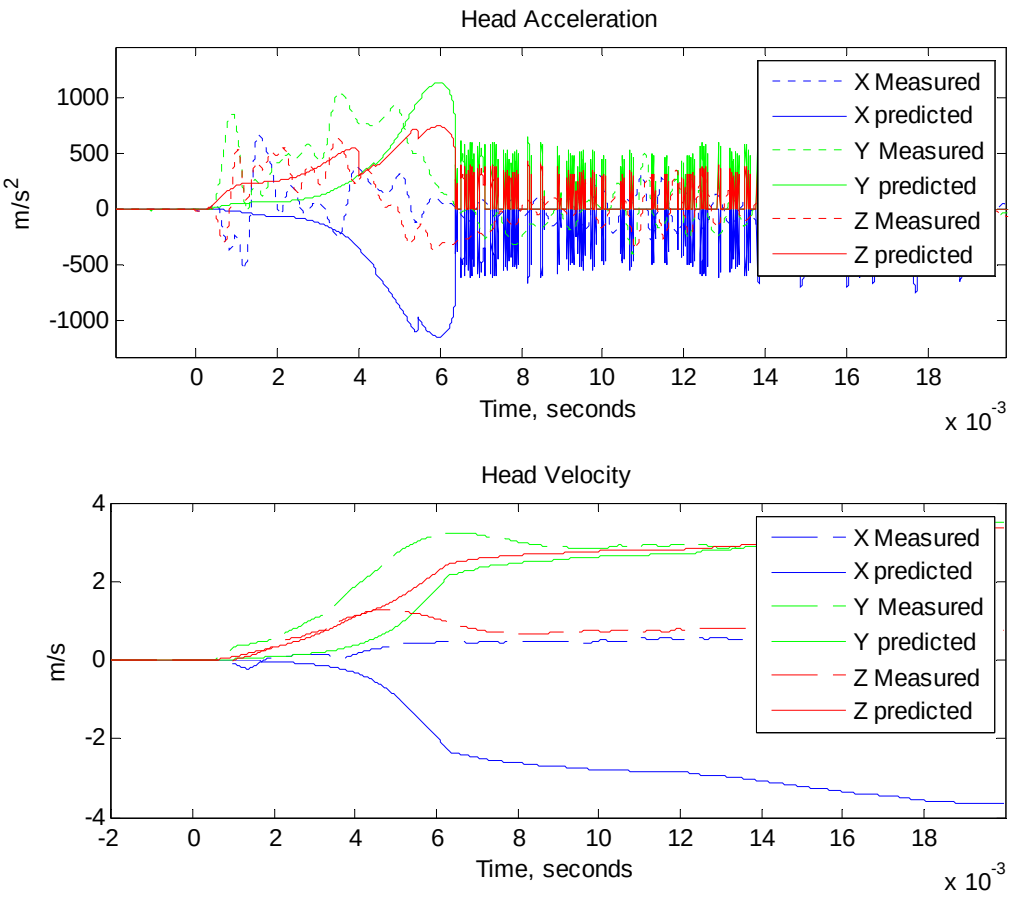

Figure B5. Head accelerations and velocities predicted by the model compared to measured head accelerations. From Test 75: Side - toward blast, 30 psi - 1 ms pulse.

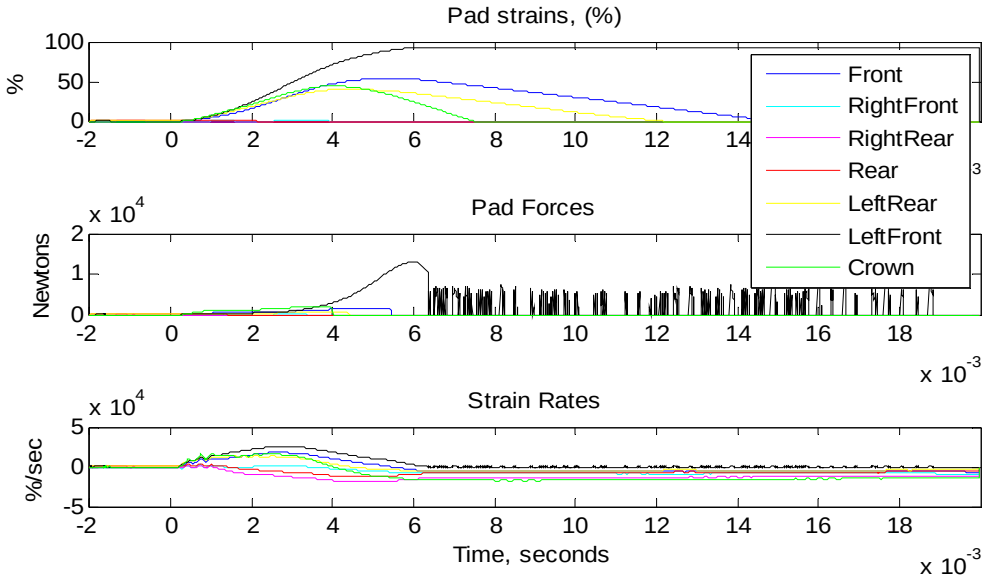

Figure B6. Helmet padding strains and forces from Test 75.

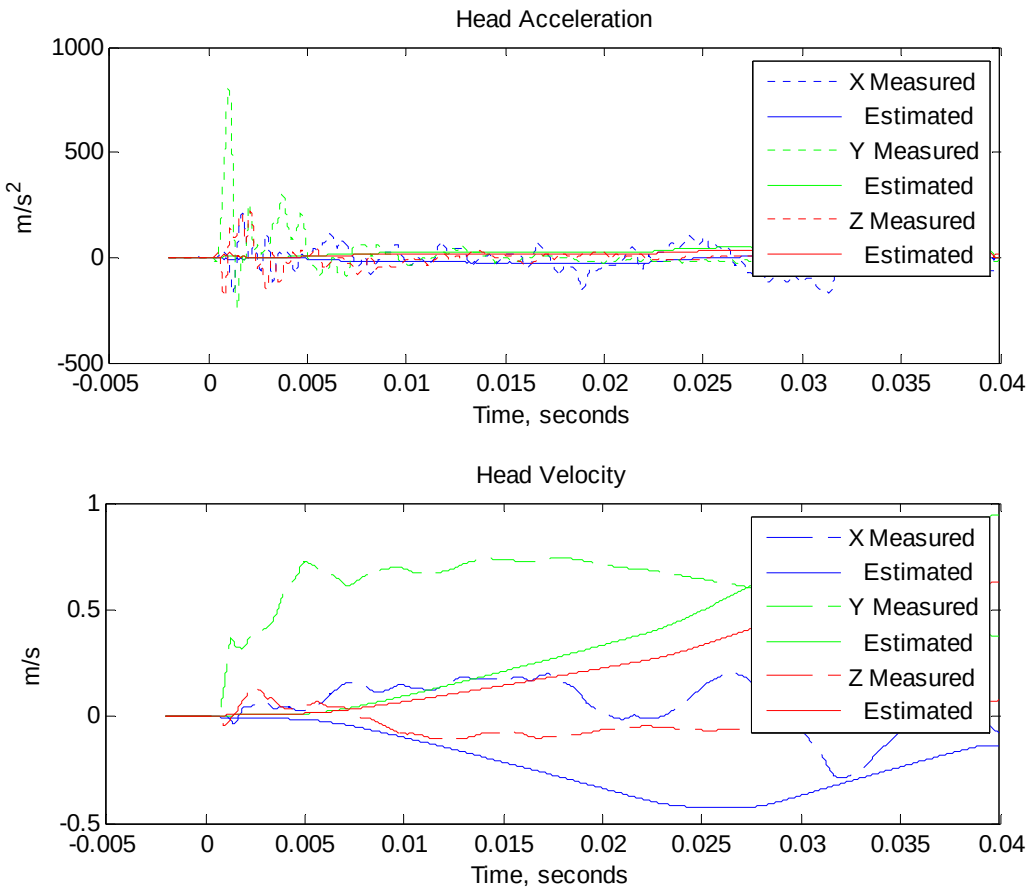

Figure B7. Head accelerations and velocities predicted by the model compared to measured head accelerations. From Test 28: Side - level, 15 psi - 1 ms pulse.

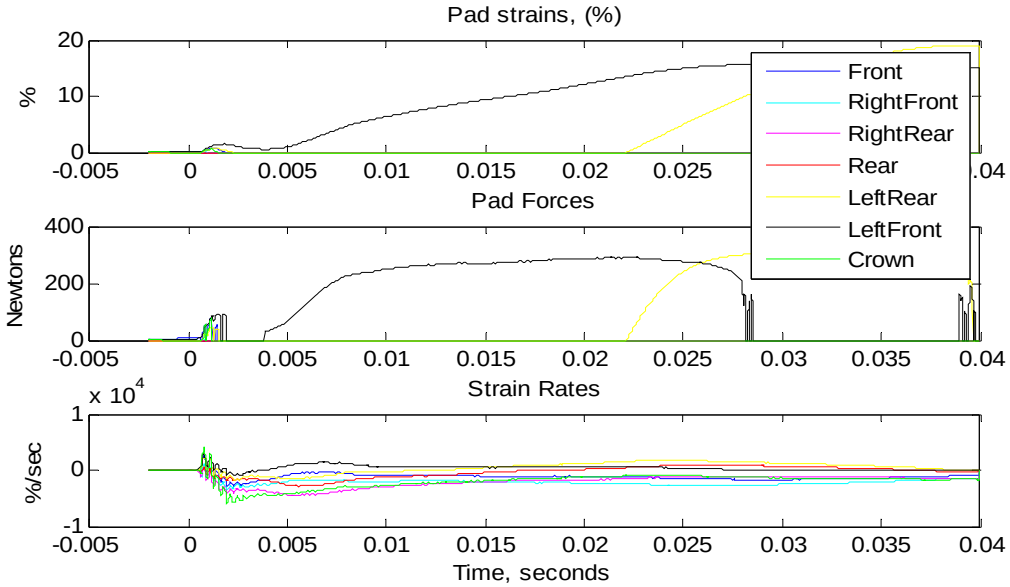

Figure B8. Helmet padding strains and forces from Test 28.

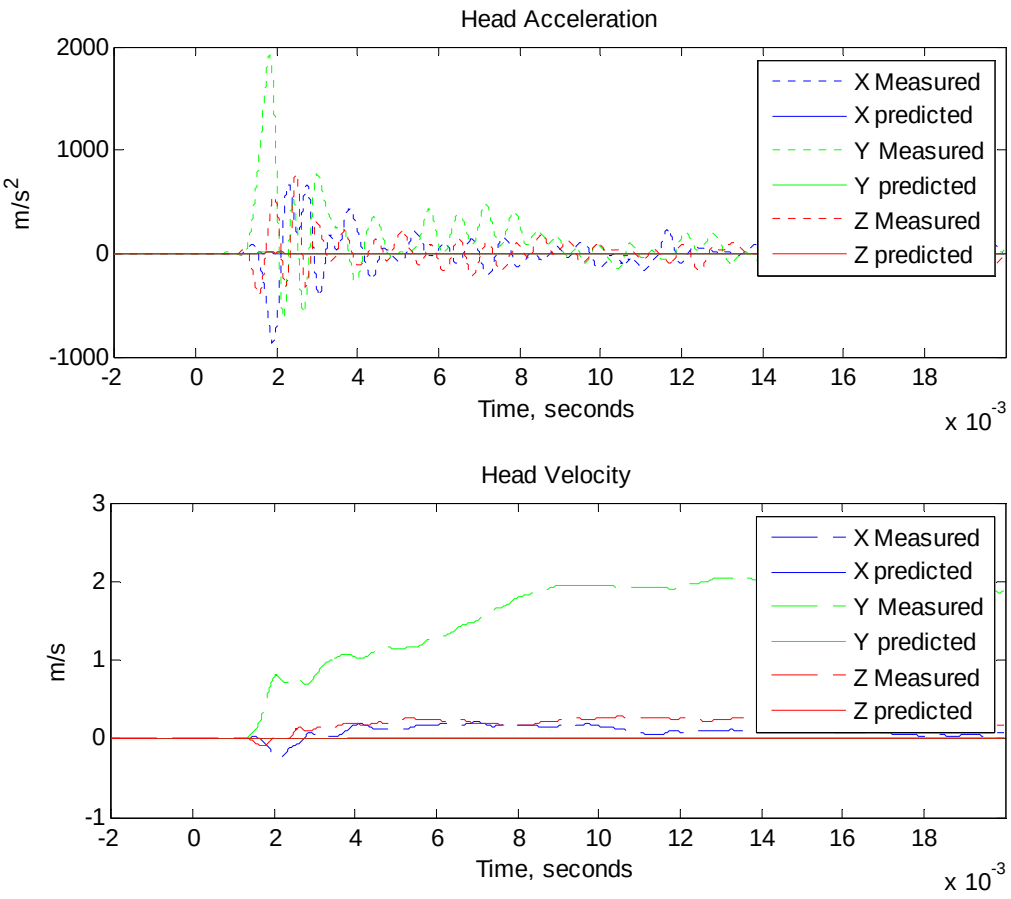

Figure B9. Head accelerations and velocities predicted by the model compared to measured head accelerations. From Test 62: Side - level, 15 psi - 3 ms pulse.

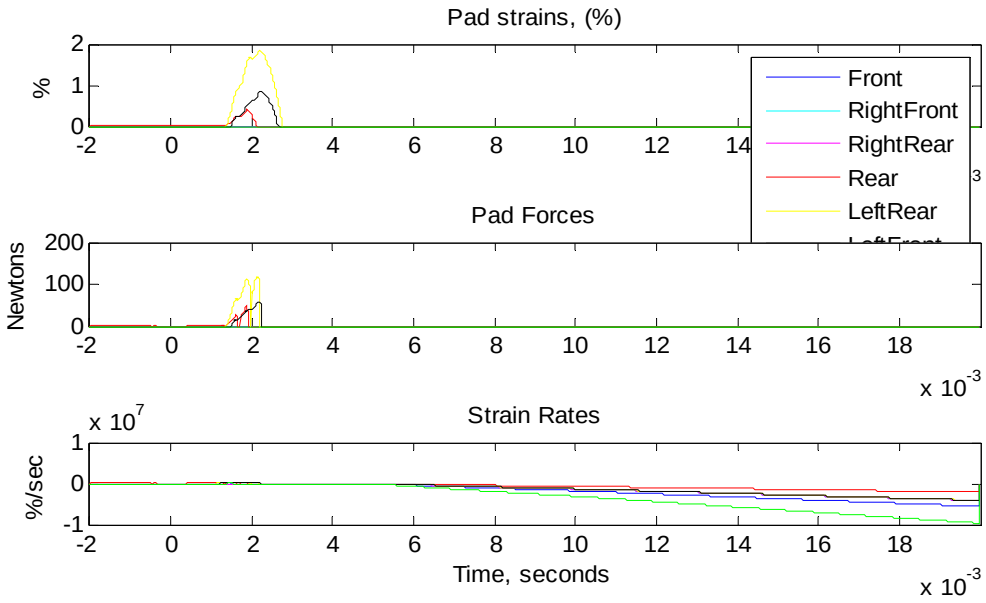

Figure B10. Helmet padding strains and forces from Test 62.

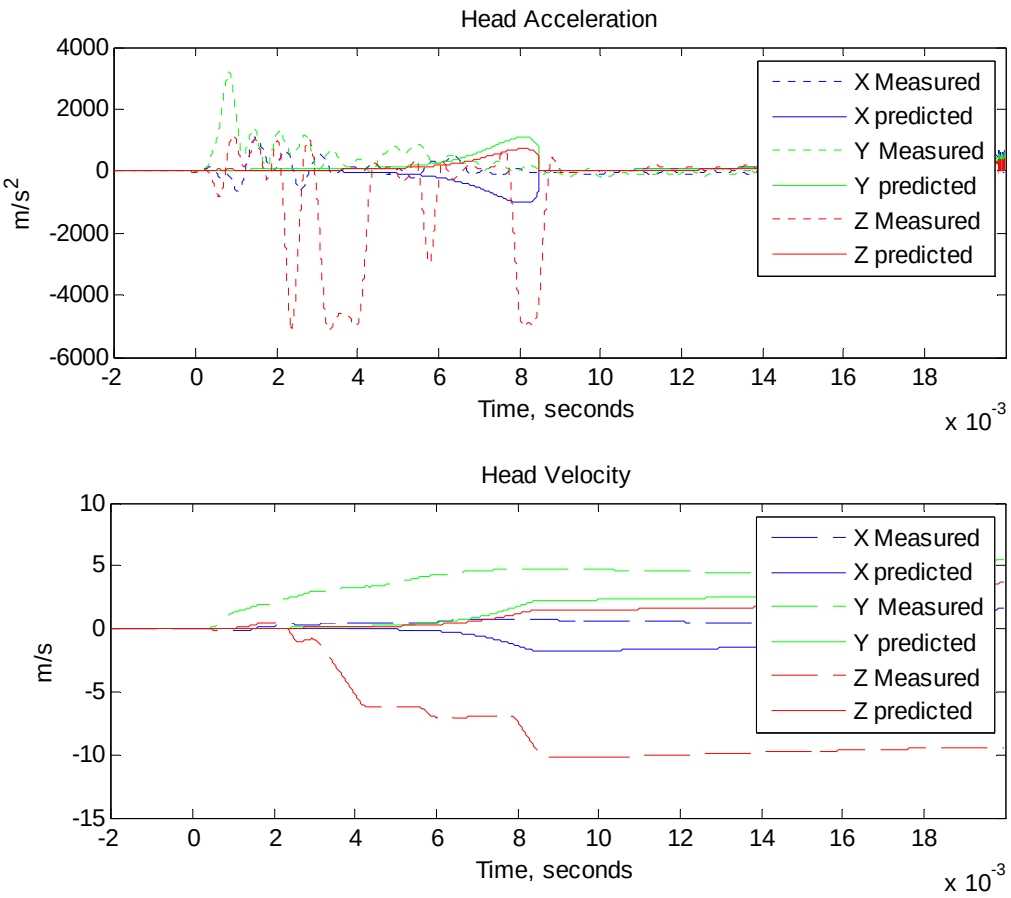

Figure B11. Head accelerations and velocities predicted by the model compared to measured head accelerations. From Test 77: Side - level, 30 psi - 1 ms pulse. Head Z data is bad after 3.2 ms.

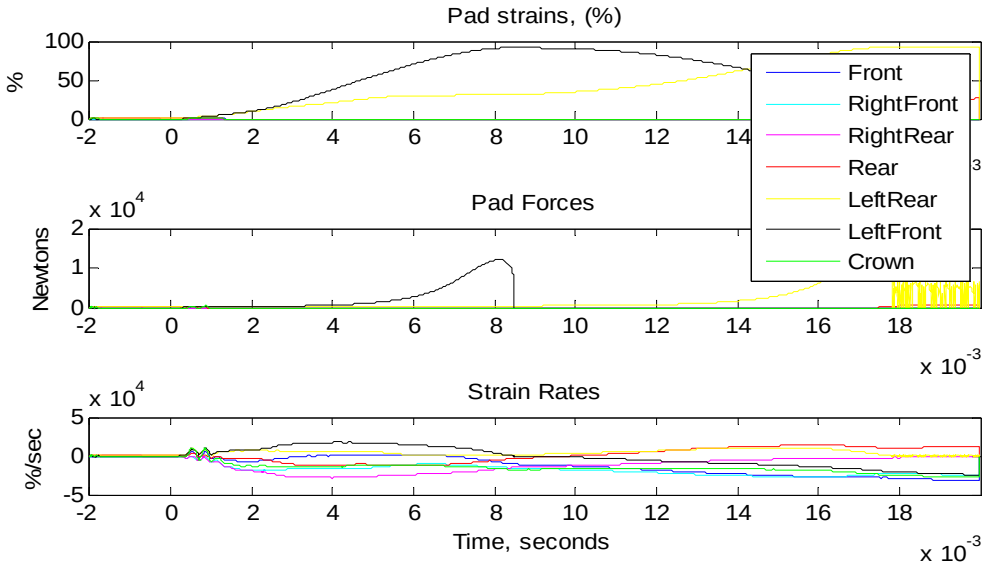

Figure B12. Helmet padding strains and forces from Test 77.

Appendix C

Plots of the measured frequency response function (FRF) and the corresponding modes. The coherence function was used as a validation for the peaks picked on the FRF.

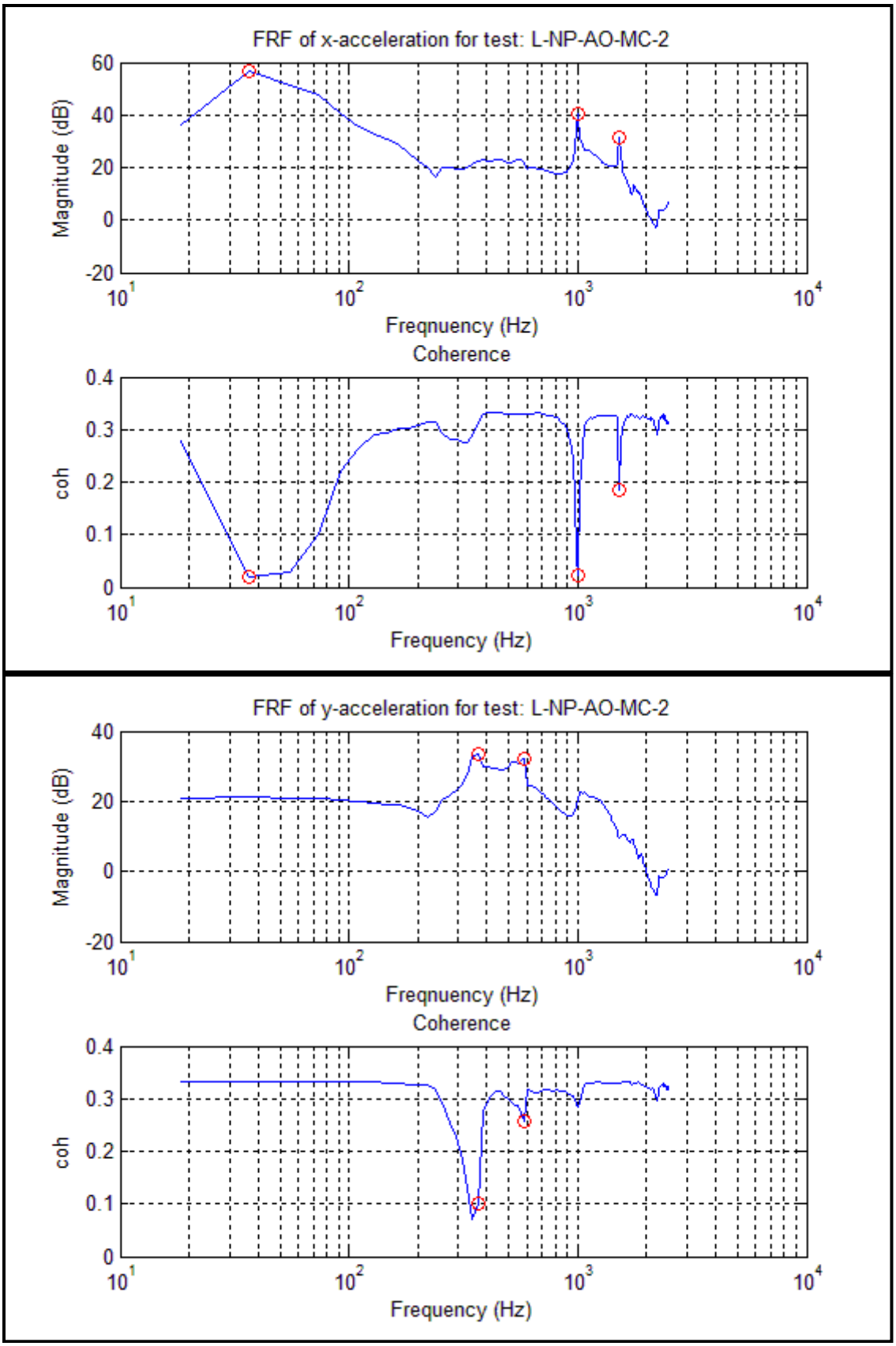
FRF of x-acceleration for test: L-NP-AO-MC-2
Magnitude (dB)
60
40
20
0
-20
10^1
10^2
10^3
10^4
Freqnuency (Hz)
Coherence
coh
0.4
0.3
0.2
0.1
0
Frequency (Hz)
FRF of y-acceleration for test: L-NP-AO-MC-2
Magnitude (dB)
40
20
0
-20
Freqnuency (Hz)
Coherence
coh
0.4
0.3
0.2
0.1
0
Frequency (Hz)

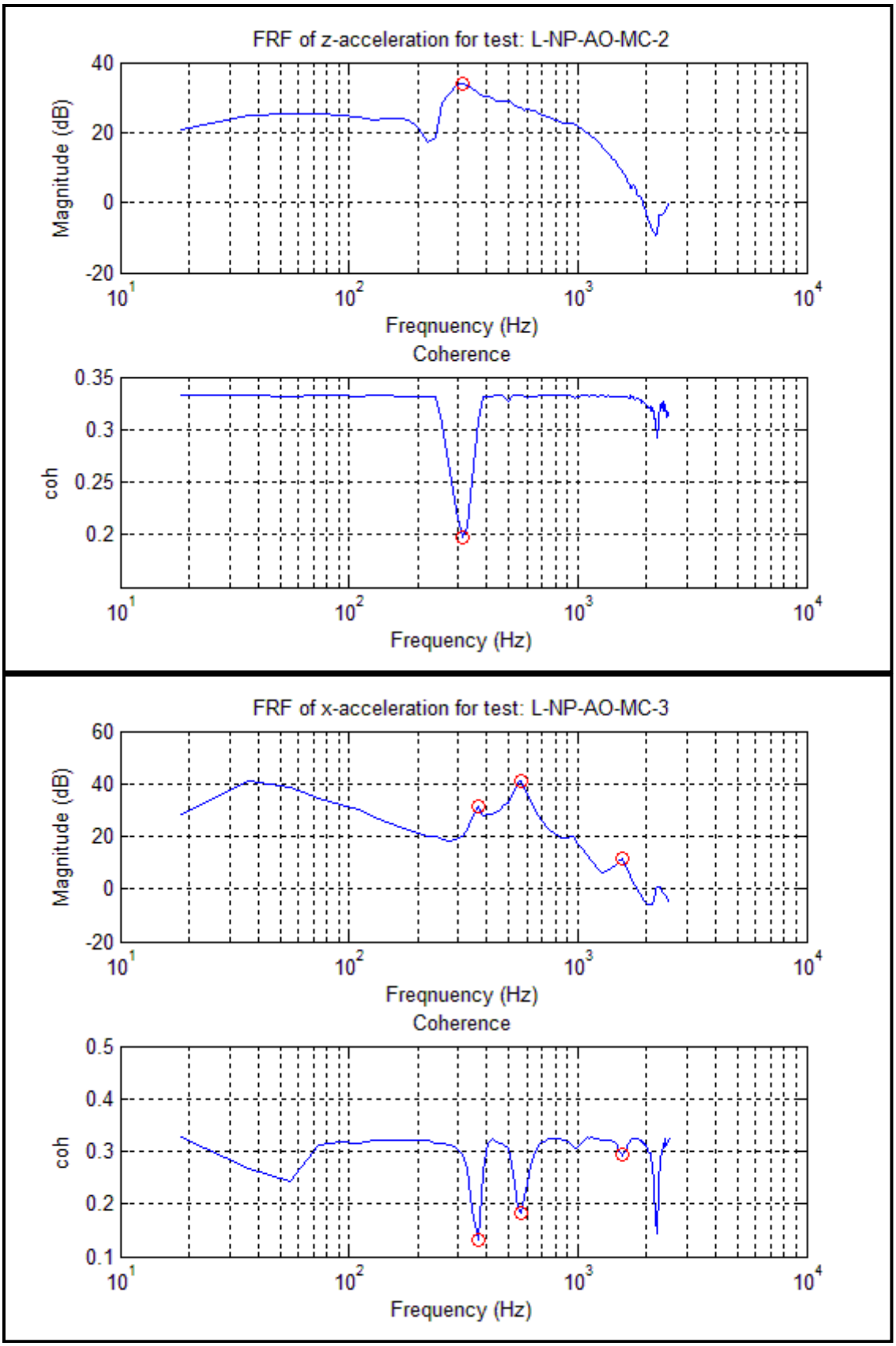
FRF of z-acceleration for test: L-NP-AO-MC-2
Magnitude (dB)
40
20
0
-20
10^1
10^2
10^3
10^4
Freqnuency (Hz)
Coherence
coh
0.35
0.3
0.25
0.2
10^1
10^2
10^3
10^4
Frequency (Hz)
FRF of x-acceleration for test: L-NP-AO-MC-3
Magnitude (dB)
60
40
20
0
-20
10^1
10^2
10^3
10^4
Freqnuency (Hz)
Coherence
coh
0.5
0.4
0.3
0.2
0.1
10^1
10^2
10^3
10^4
Frequency (Hz)

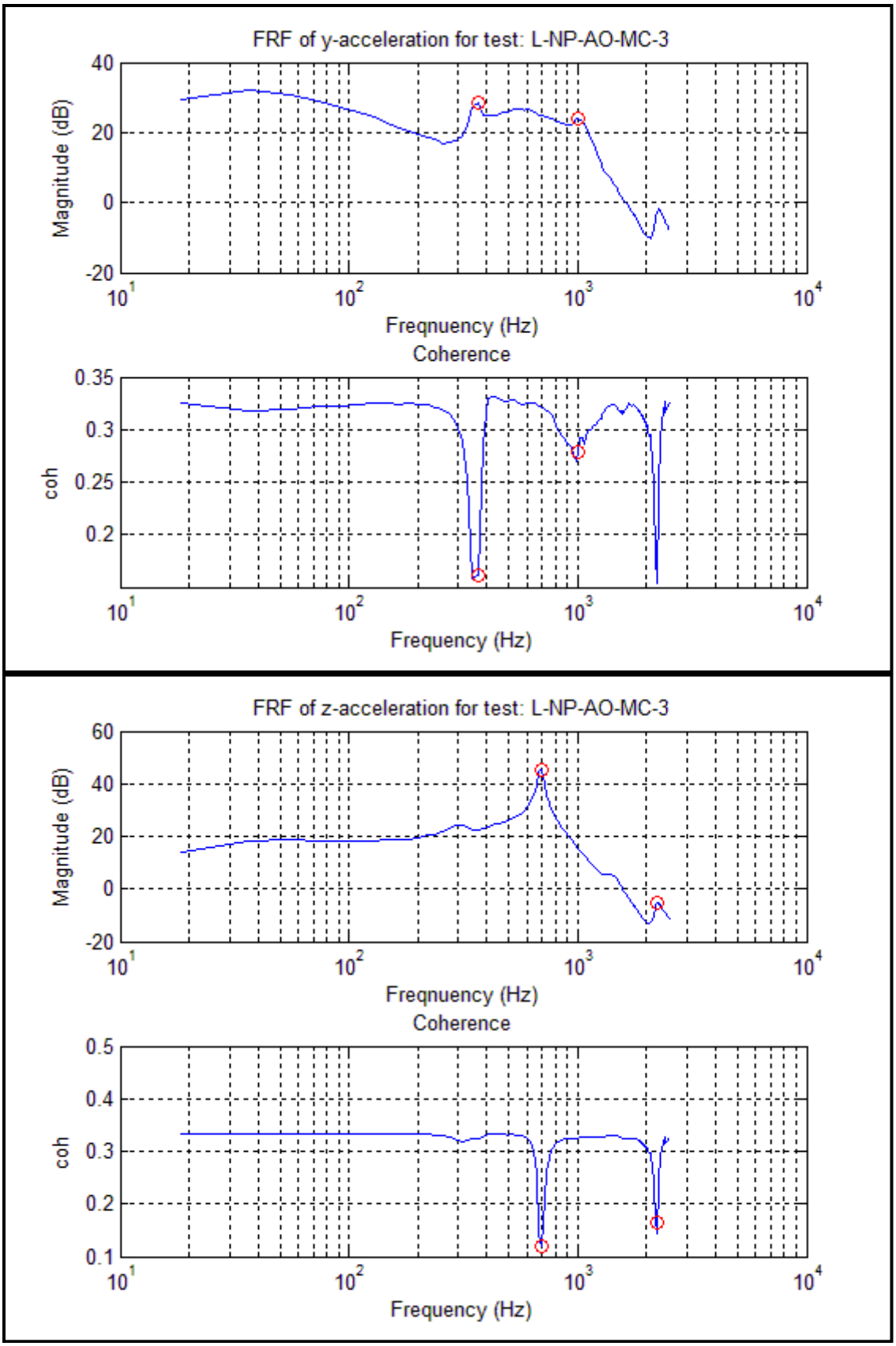
FRF of y-acceleration for test: L-NP-AO-MC-3
Magnitude (dB)
40
20
0
-20
10^1
10^2
10^3
10^4
Freqnuency (Hz)
Coherence
coh
0.35
0.3
0.25
0.2
Frequency (Hz)
FRF of z-acceleration for test: L-NP-AO-MC-3
Magnitude (dB)
60
40
20
0
-20
Freqnuency (Hz)
Coherence
coh
0.5
0.4
0.3
0.2
0.1
Frequency (Hz)

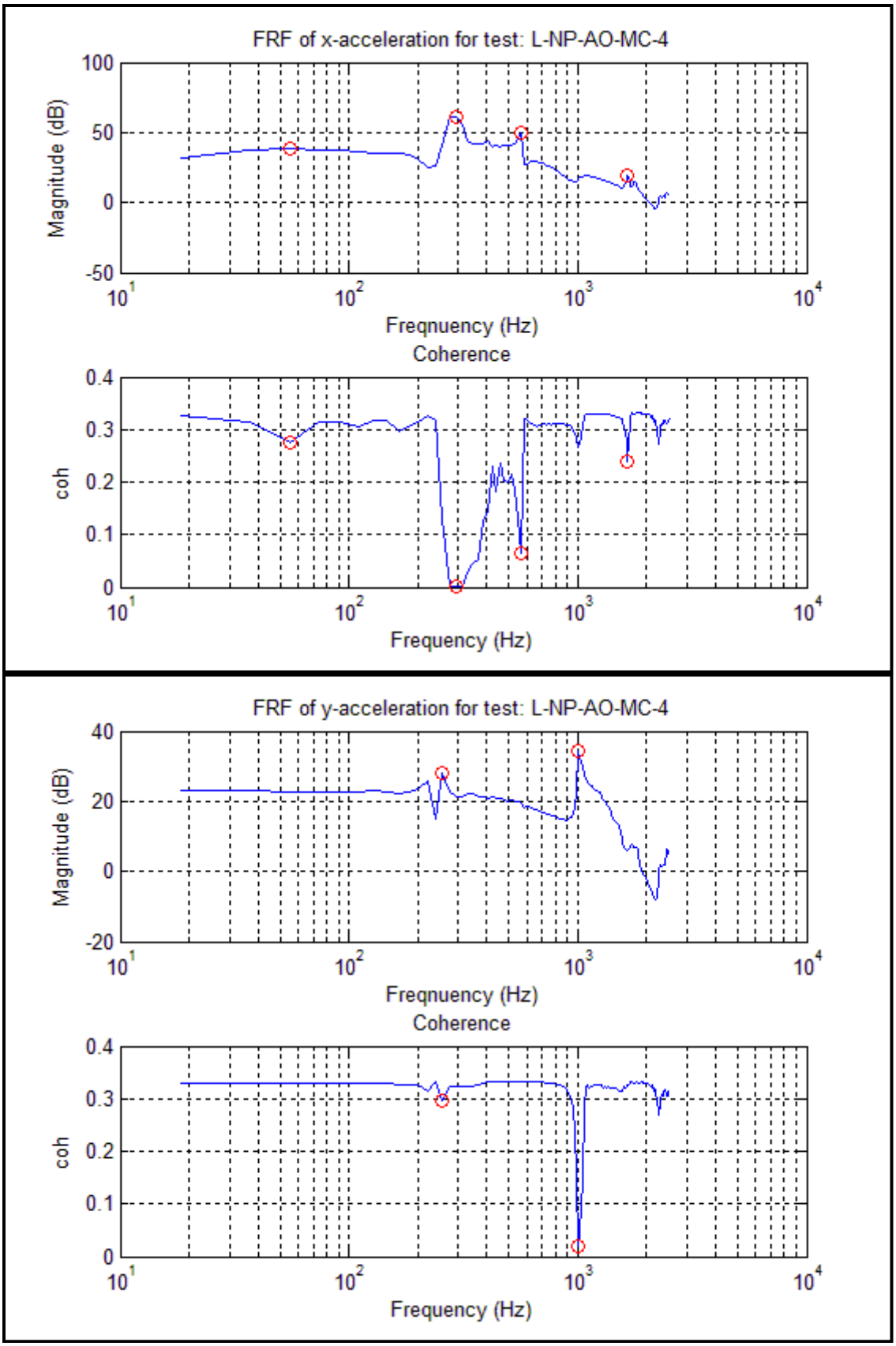
FRF of x-acceleration for test: L-NP-AO-MC-4
Magnitude (dB)
100
50
0
-50
10^1
10^2
10^3
10^4
Freqnuency (Hz)
Coherence
coh
0.4
0.3
0.2
0.1
0
Frequency (Hz)
FRF of y-acceleration for test: L-NP-AO-MC-4
Magnitude (dB)
40
20
0
-20
Freqnuency (Hz)
Coherence
coh
Frequency (Hz)

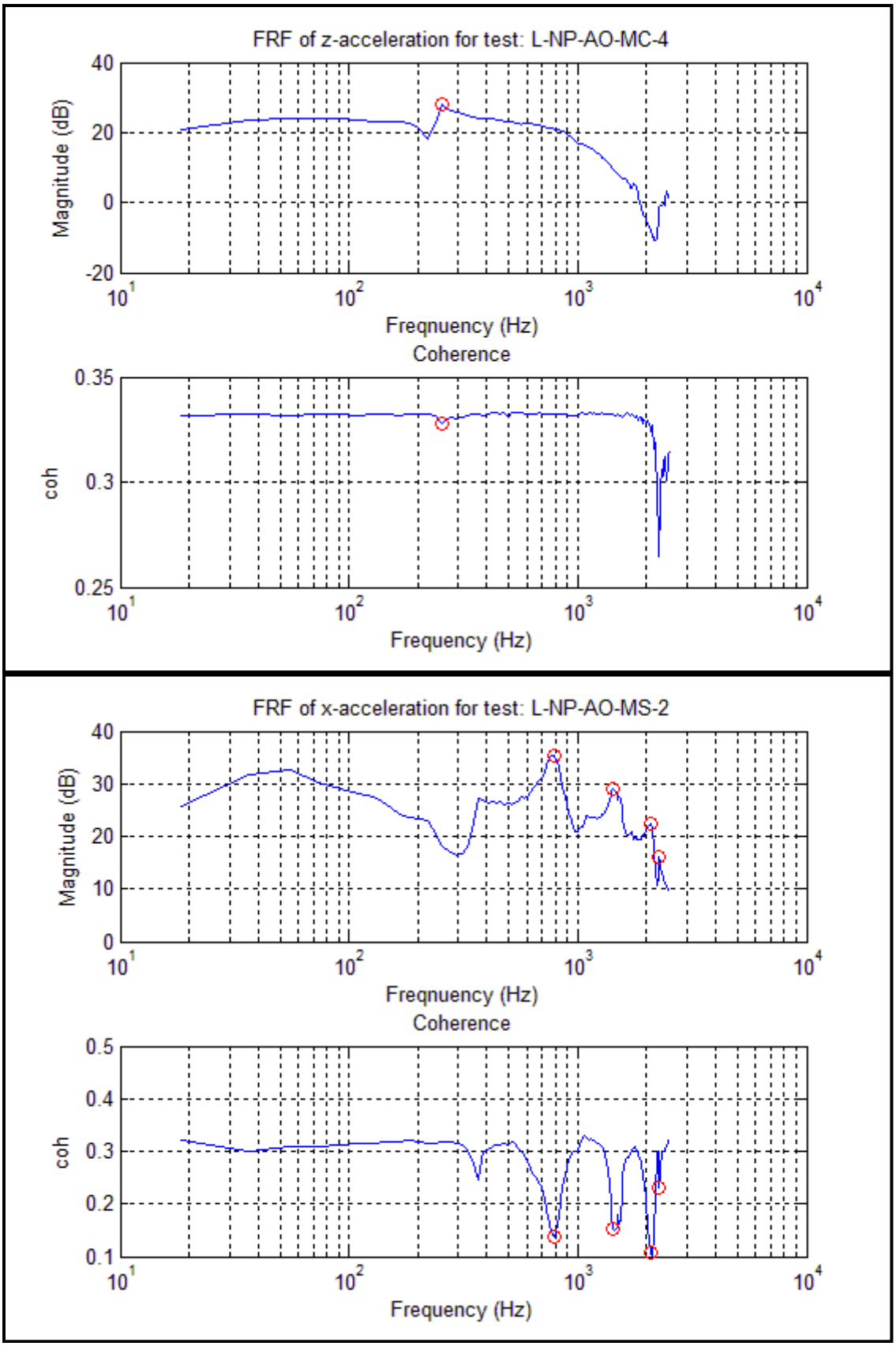
FRF of z-acceleration for test: L-NP-AO-MC-4
Magnitude (dB)
40
20
0
-20
10^1
10^2
10^3
10^4
Freqnuency (Hz)
Coherence
coh
0.35
0.3
0.25
Frequency (Hz)
FRF of x-acceleration for test: L-NP-AO-MS-2
Magnitude (dB)
40
30
20
10
0
Freqnuency (Hz)
Coherence
coh
0.5
0.4
0.3
0.2
0.1
Frequency (Hz)

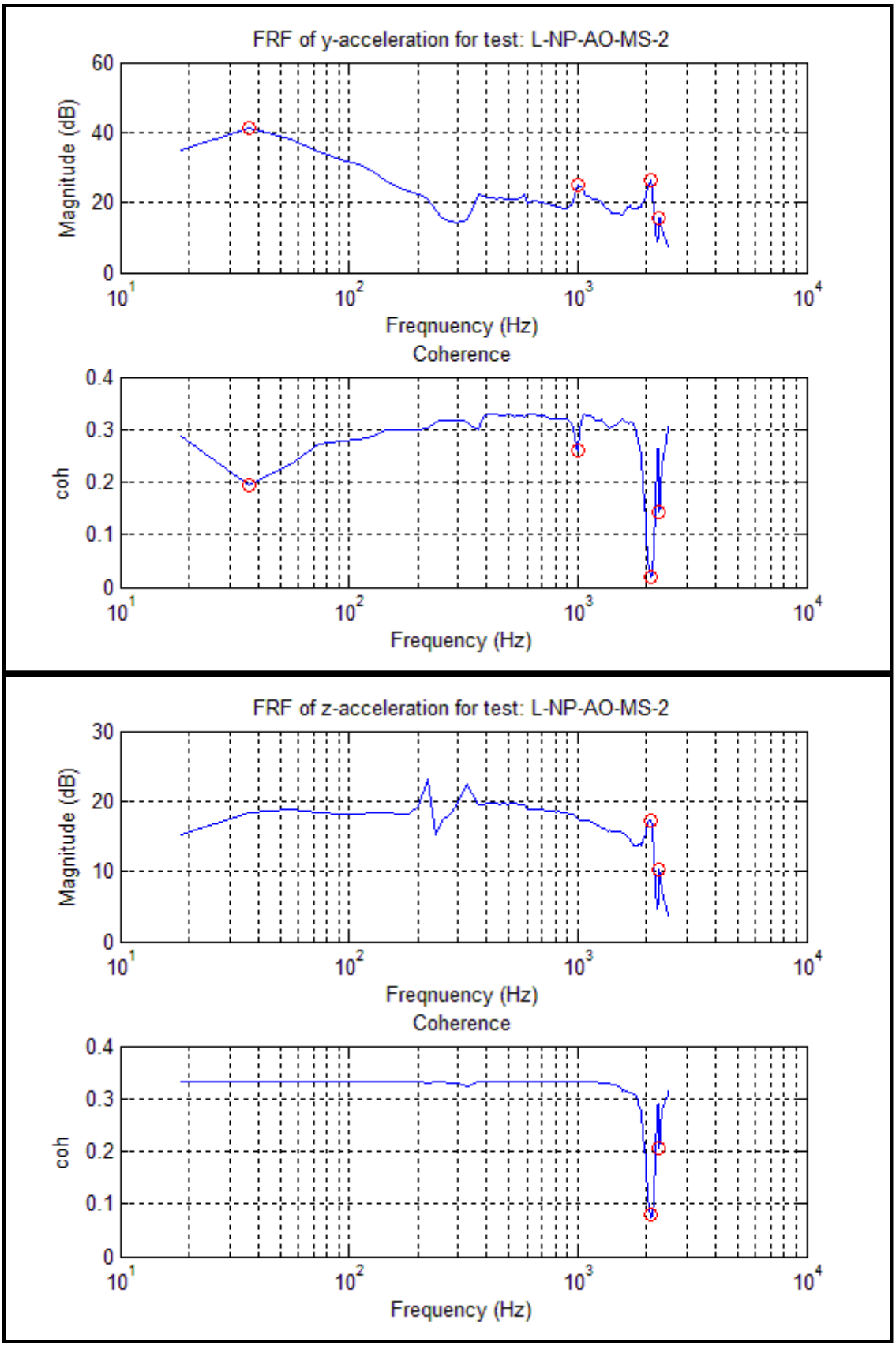
FRF of y-acceleration for test: L-NP-AO-MS-2
Magnitude (dB)
Freqnuency (Hz)
Coherence
coh
Frequency (Hz)
FRF of z-acceleration for test: L-NP-AO-MS-2
Magnitude (dB)
Freqnuency (Hz)
Coherence
coh
Frequency (Hz)

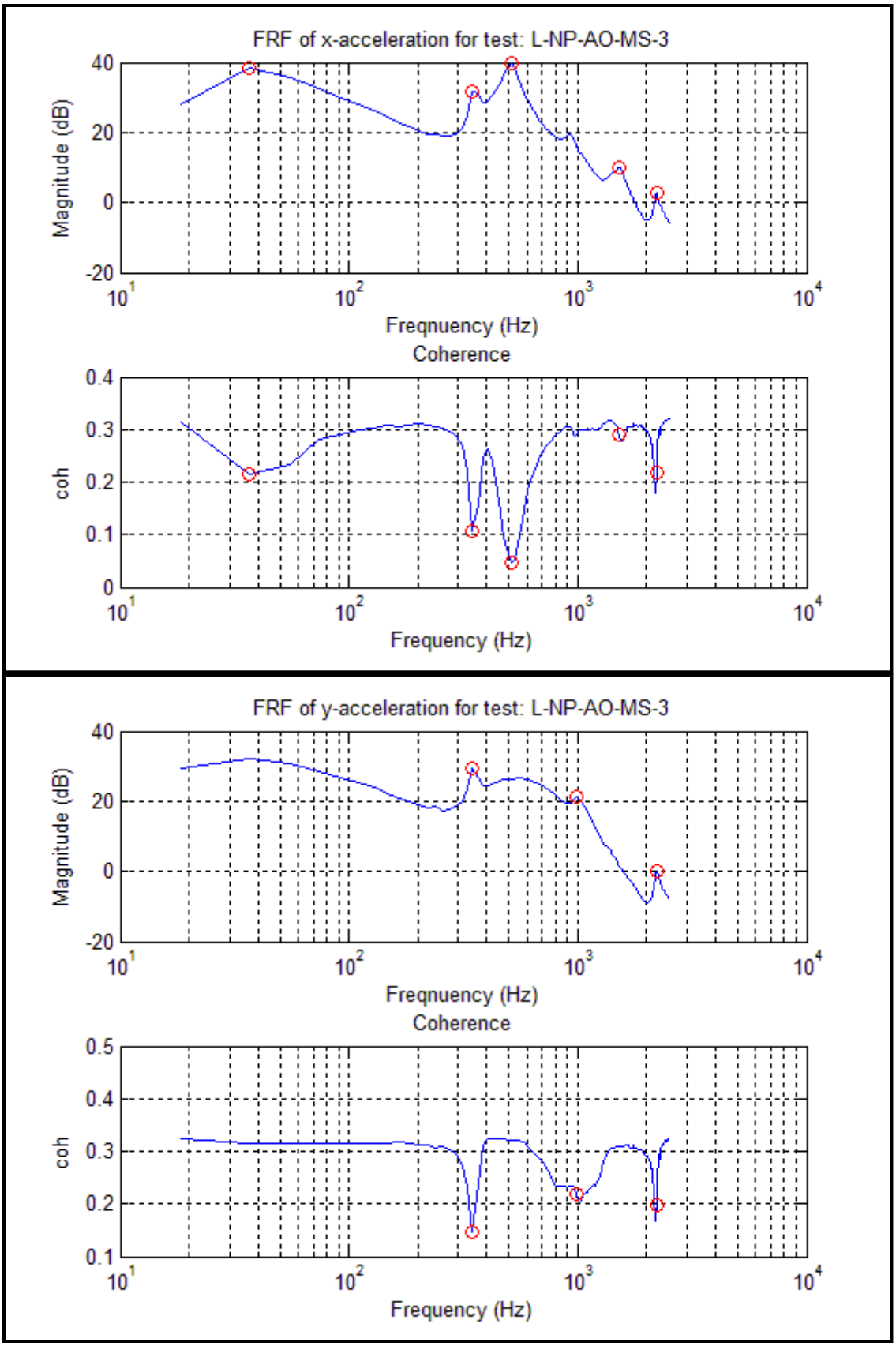
FRF of x-acceleration for test: L-NP-AO-MS-3
Magnitude (dB)
40
20
0
-20
10^1
10^2
10^3
10^4
Freqnuency (Hz)
Coherence
coh
0.4
0.3
0.2
0.1
0
Frequency (Hz)
FRF of y-acceleration for test: L-NP-AO-MS-3
Magnitude (dB)
Freqnuency (Hz)
Coherence
coh
0.5
0.4
0.3
0.2
0.1
Frequency (Hz)

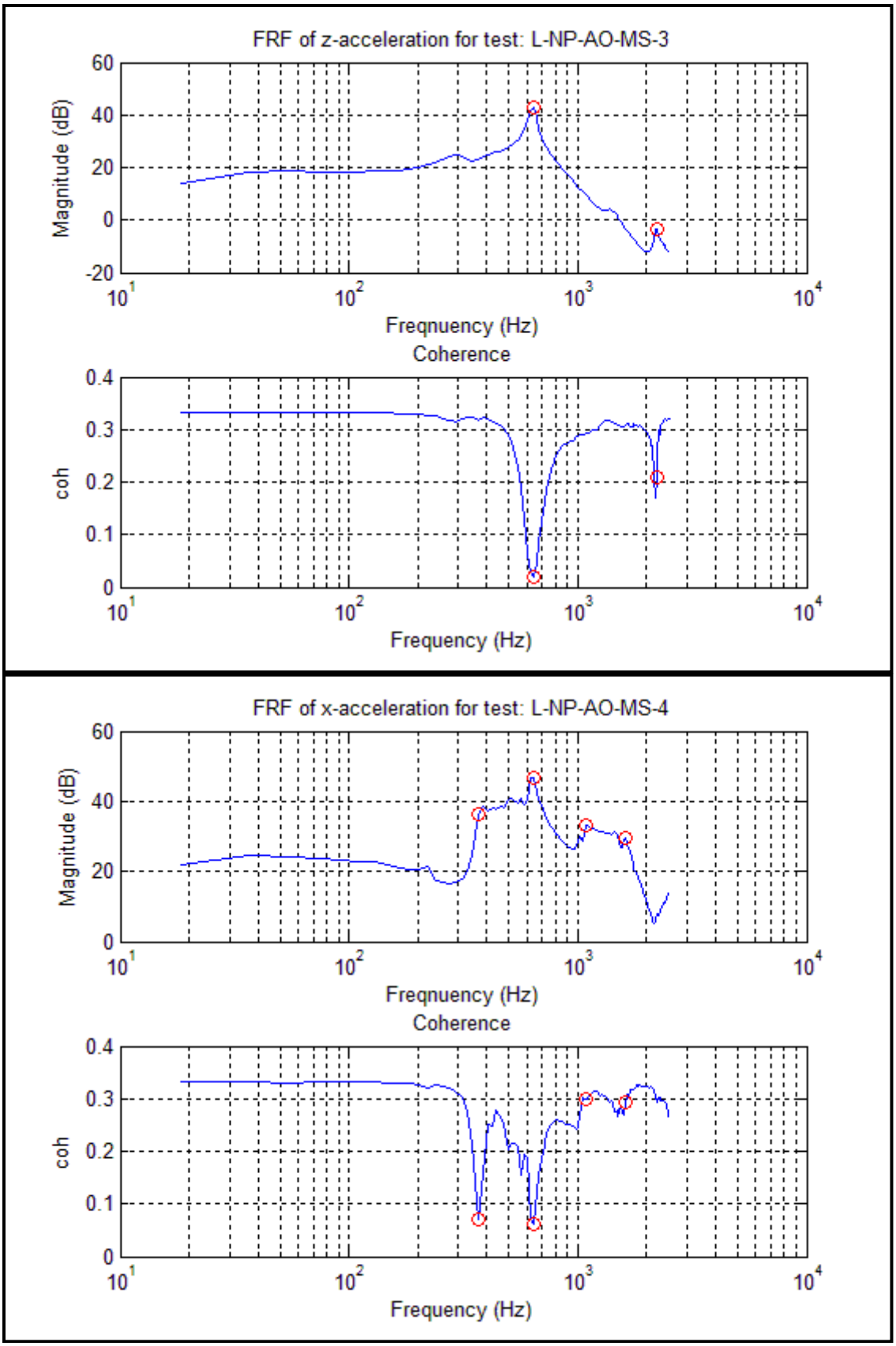
FRF of z-acceleration for test: L-NP-AO-MS-3
Magnitude (dB)
60
40
20
0
-20
10^1
10^2
10^3
10^4
Freqnuency (Hz)
Coherence
coh
0.4
0.3
0.2
0.1
0
Frequency (Hz)
FRF of x-acceleration for test: L-NP-AO-MS-4
Magnitude (dB)
Freqnuency (Hz)
Coherence
coh
Frequency (Hz)

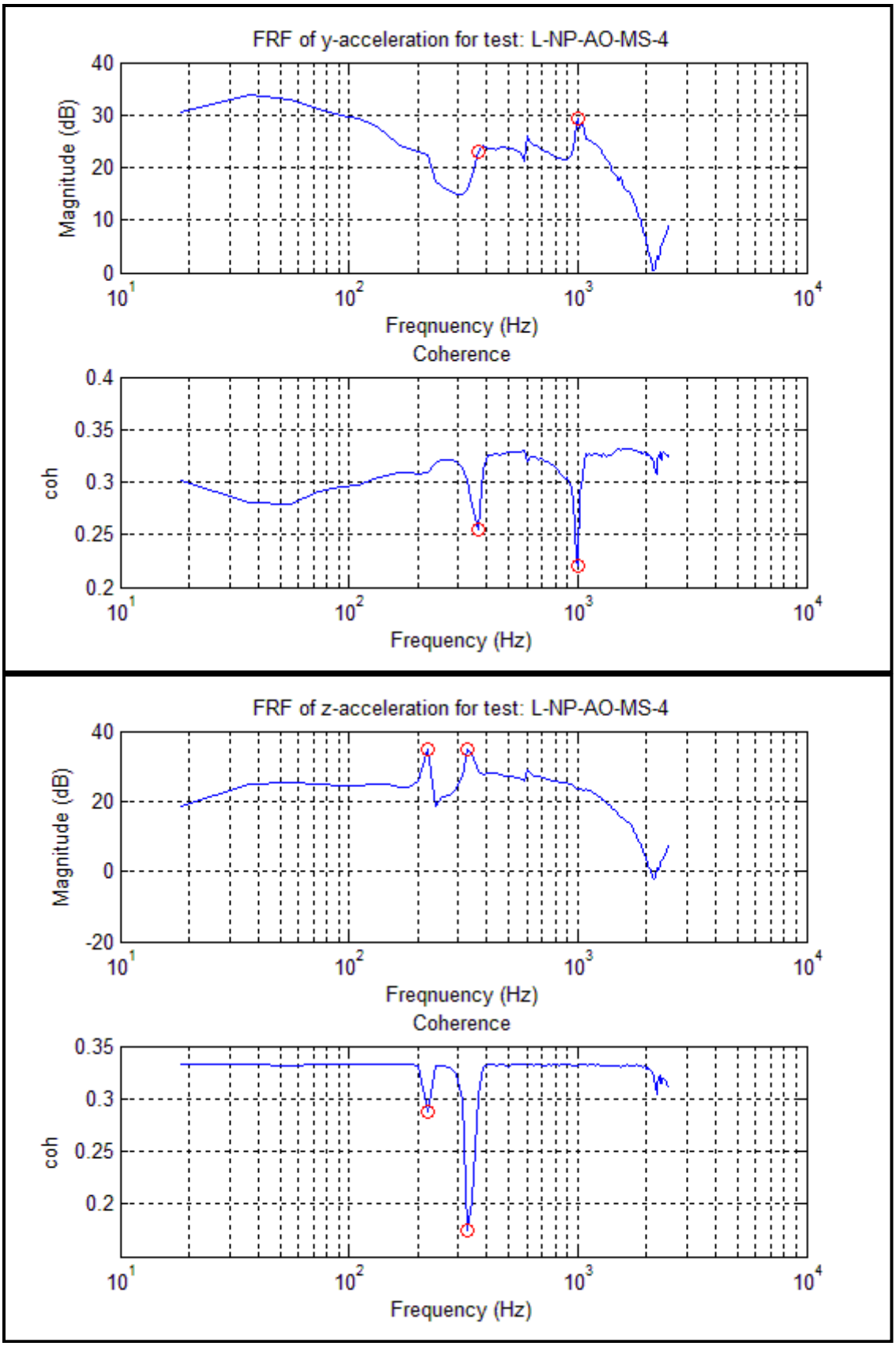
FRF of y-acceleration for test: L-NP-AO-MS-4
Magnitude (dB)
Freqnuency (Hz)
Coherence
coh
Frequency (Hz)
FRF of z-acceleration for test: L-NP-AO-MS-4
Magnitude (dB)
Freqnuency (Hz)
Coherence
coh
Frequency (Hz)

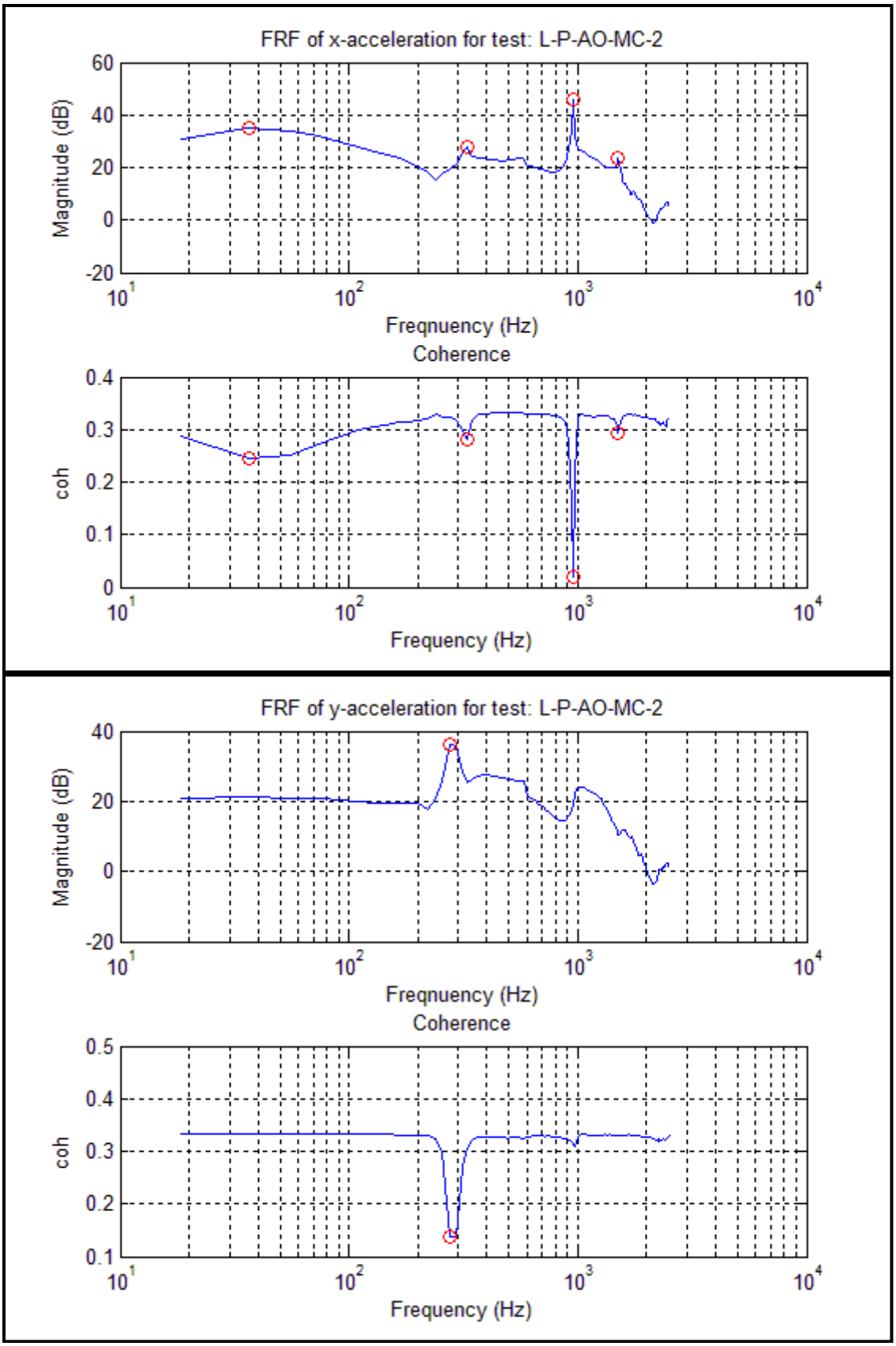
FRF of x-acceleration for test: L-P-AO-MC-2
Magnitude (dB)
60
40
20
0
-20
10^1
10^2
10^3
10^4
Freqnuency (Hz)
Coherence
coh
0.4
0.3
0.2
0.1
0
Frequency (Hz)
FRF of y-acceleration for test: L-P-AO-MC-2
Magnitude (dB)
40
20
0
-20
Freqnuency (Hz)
Coherence
coh
0.5
0.4
0.3
0.2
0.1
Frequency (Hz)

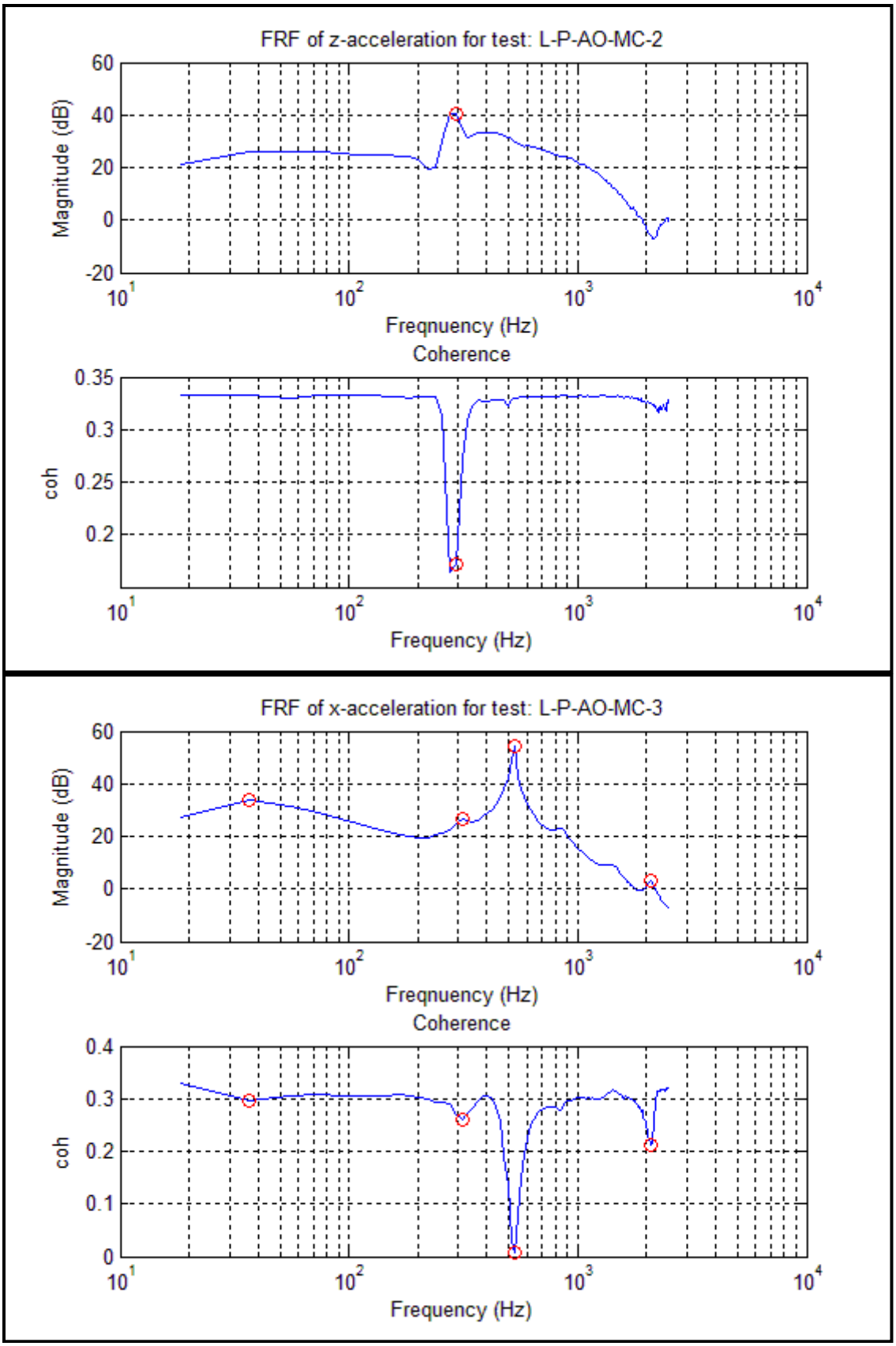
FRF of z-acceleration for test: L-P-AO-MC-2
Magnitude (dB)
60
40
20
0
-20
10^1
10^2
10^3
10^4
Freqnuency (Hz)
Coherence
coh
0.35
0.3
0.25
0.2
Frequency (Hz)
FRF of x-acceleration for test: L-P-AO-MC-3
Magnitude (dB)
Freqnuency (Hz)
Coherence
coh
0.4
0.3
0.2
0.1
0
Frequency (Hz)

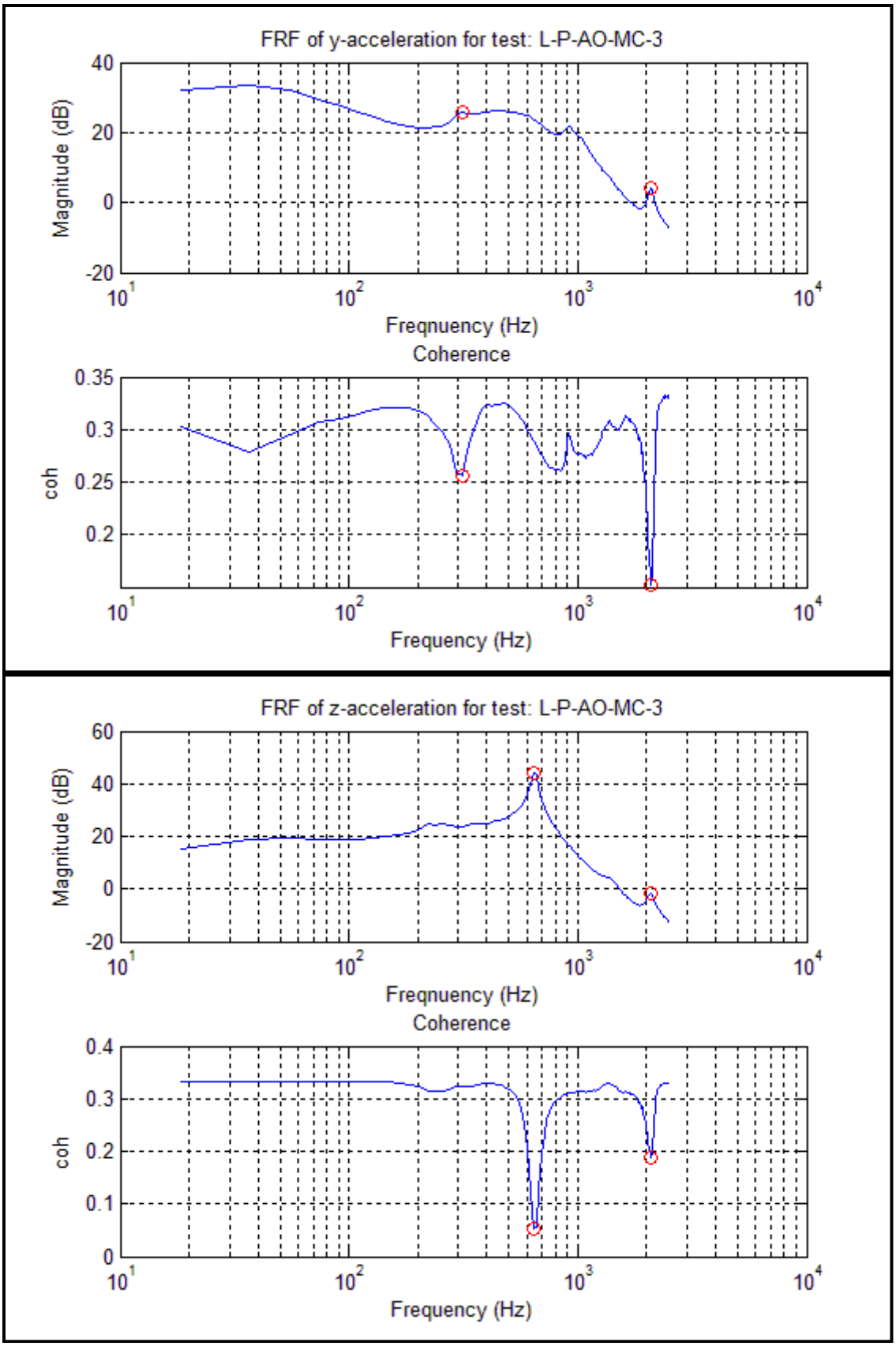
FRF of y-acceleration for test: L-P-AO-MC-3
Magnitude (dB)
40
20
0
-20
10^1
10^2
10^3
10^4
Freqnuency (Hz)
Coherence
coh
0.35
0.3
0.25
0.2
Frequency (Hz)
FRF of z-acceleration for test: L-P-AO-MC-3
Magnitude (dB)
60
40
20
0
-20
Freqnuency (Hz)
Coherence
coh
0.4
0.3
0.2
0.1
0
Frequency (Hz)

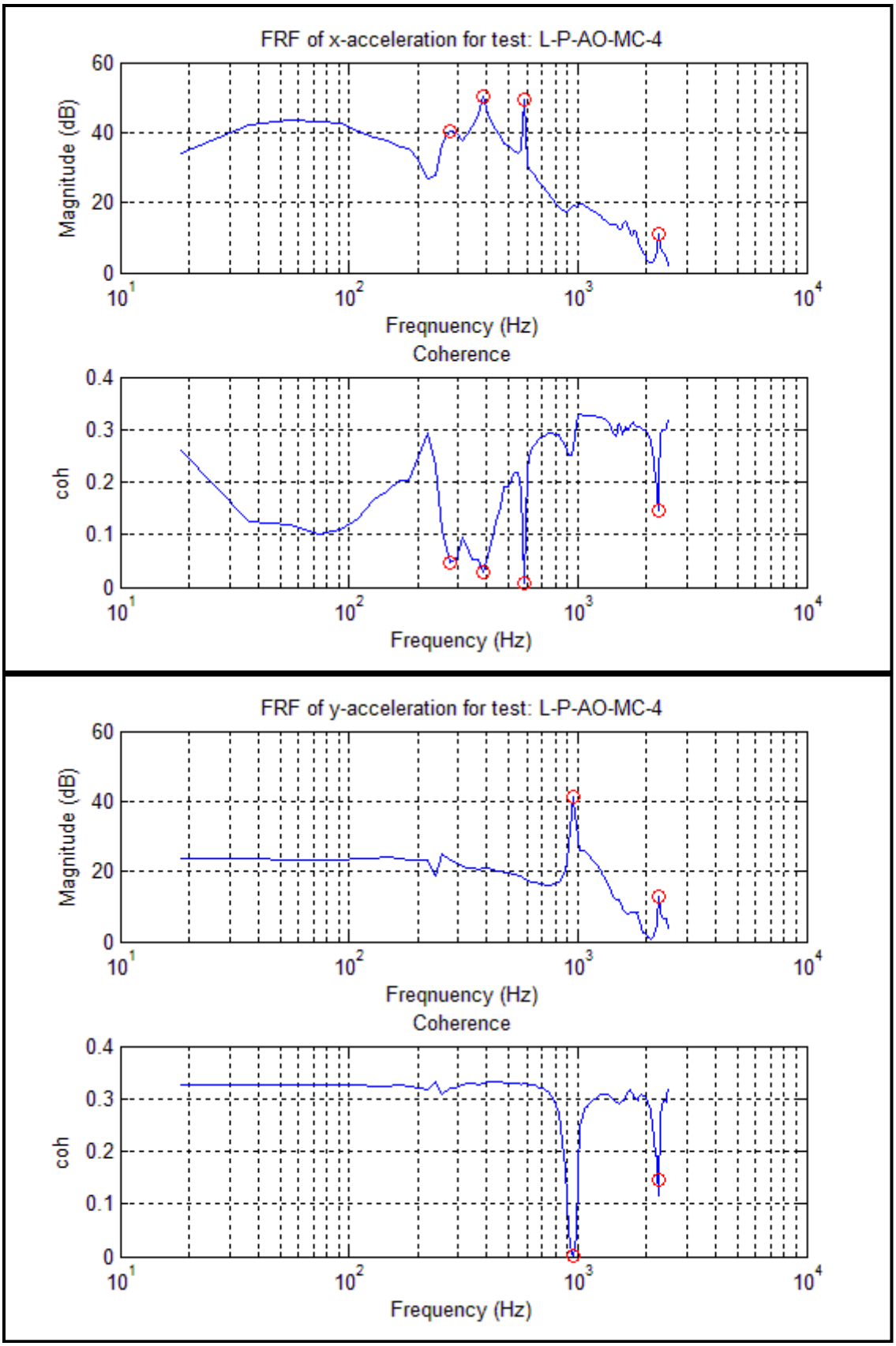
FRF of x-acceleration for test: L-P-AO-MC-4
Magnitude (dB)
Freqnuency (Hz)
Coherence
coh
Frequency (Hz)
FRF of y-acceleration for test: L-P-AO-MC-4
Magnitude (dB)
Freqnuency (Hz)
Coherence
coh
Frequency (Hz)

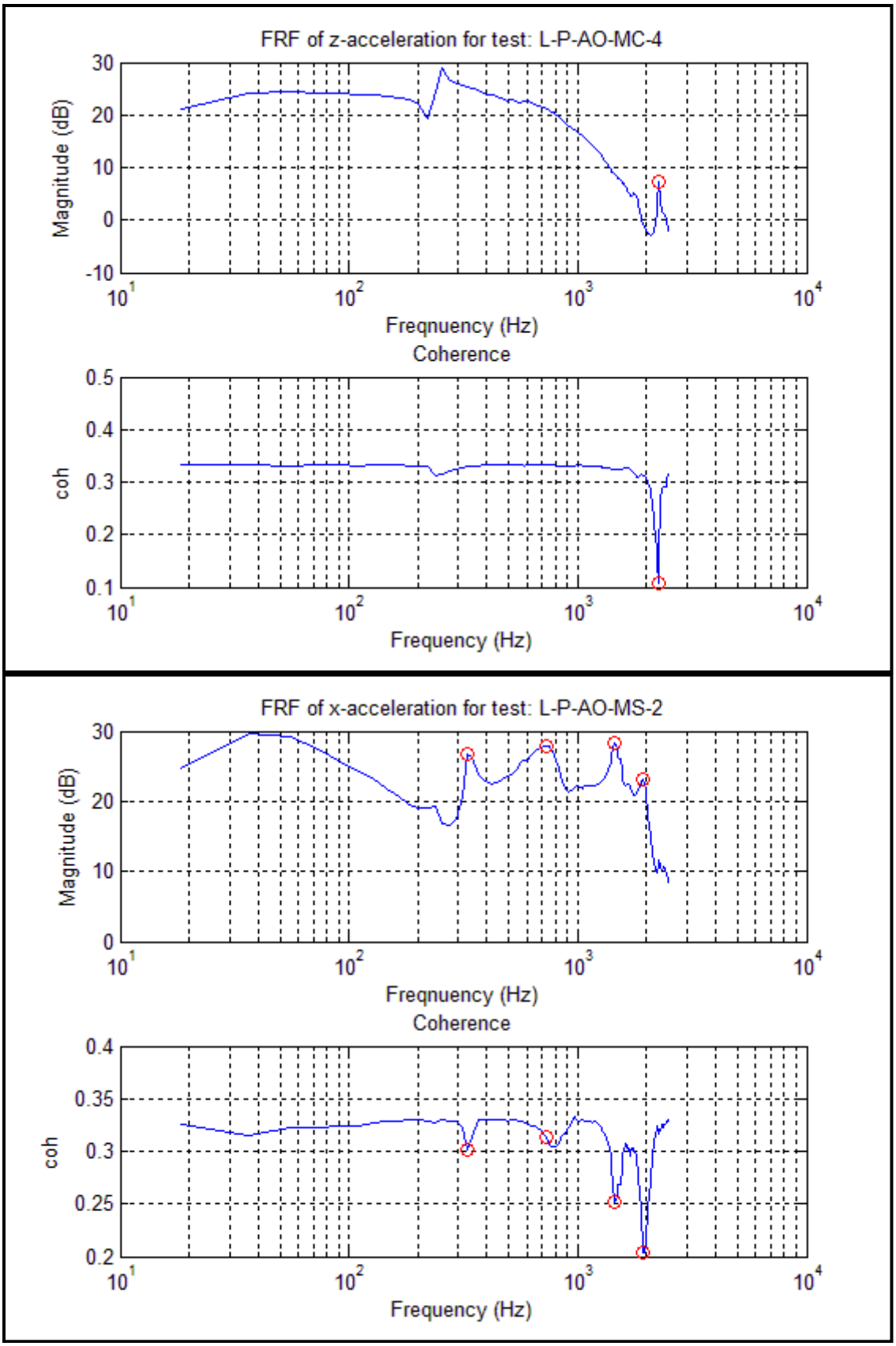
FRF of z-acceleration for test: L-P-AO-MC-4
Magnitude (dB)
Freqnuency (Hz)
Coherence
coh
Frequency (Hz)
FRF of x-acceleration for test: L-P-AO-MS-2
Magnitude (dB)
Freqnuency (Hz)
Coherence
coh
Frequency (Hz)

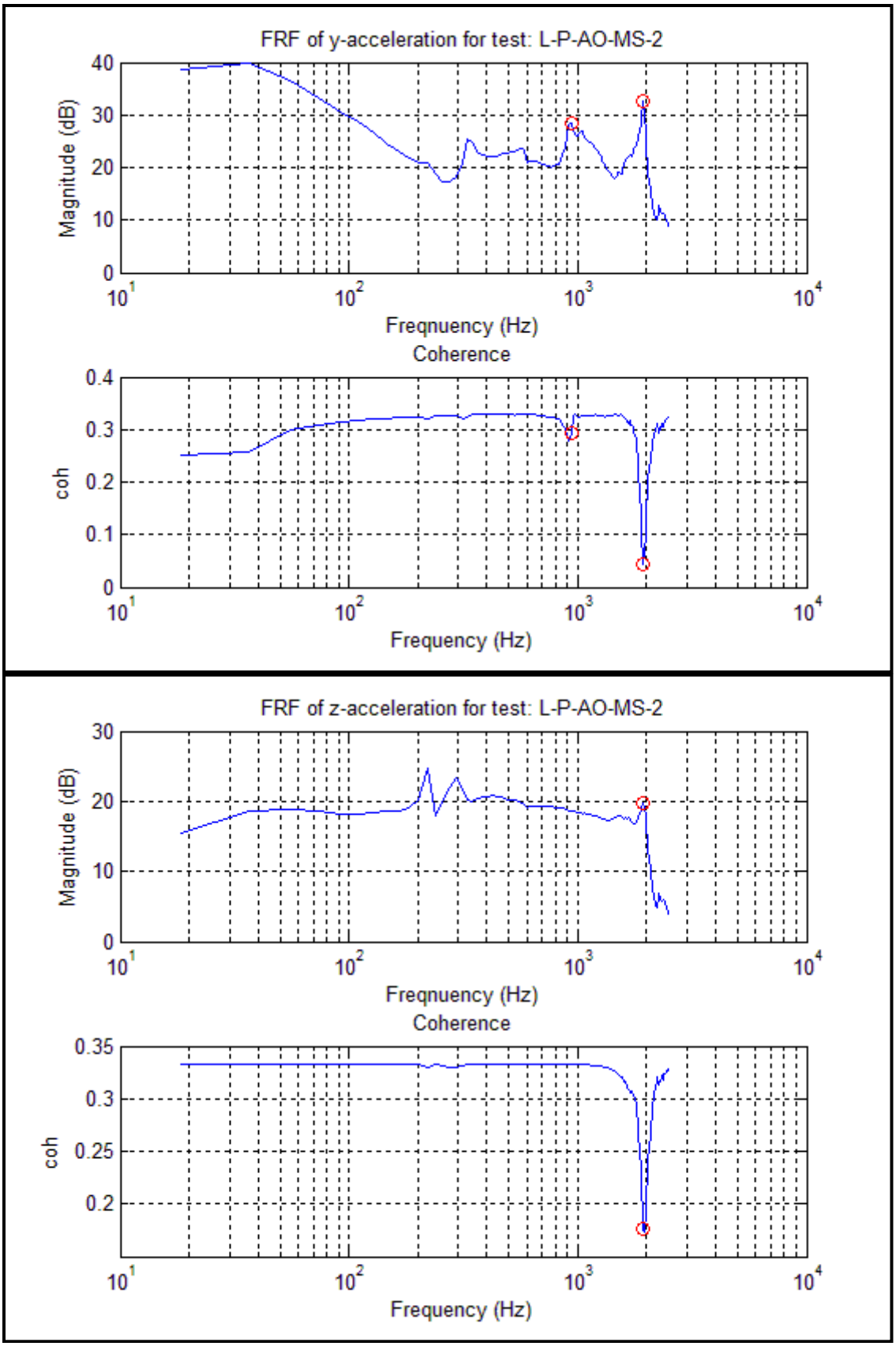
FRF of y-acceleration for test: L-P-AO-MS-2
Magnitude (dB)
Freqnuency (Hz)
Coherence
coh
Frequency (Hz)
FRF of z-acceleration for test: L-P-AO-MS-2
Magnitude (dB)
Freqnuency (Hz)
Coherence
coh
Frequency (Hz)

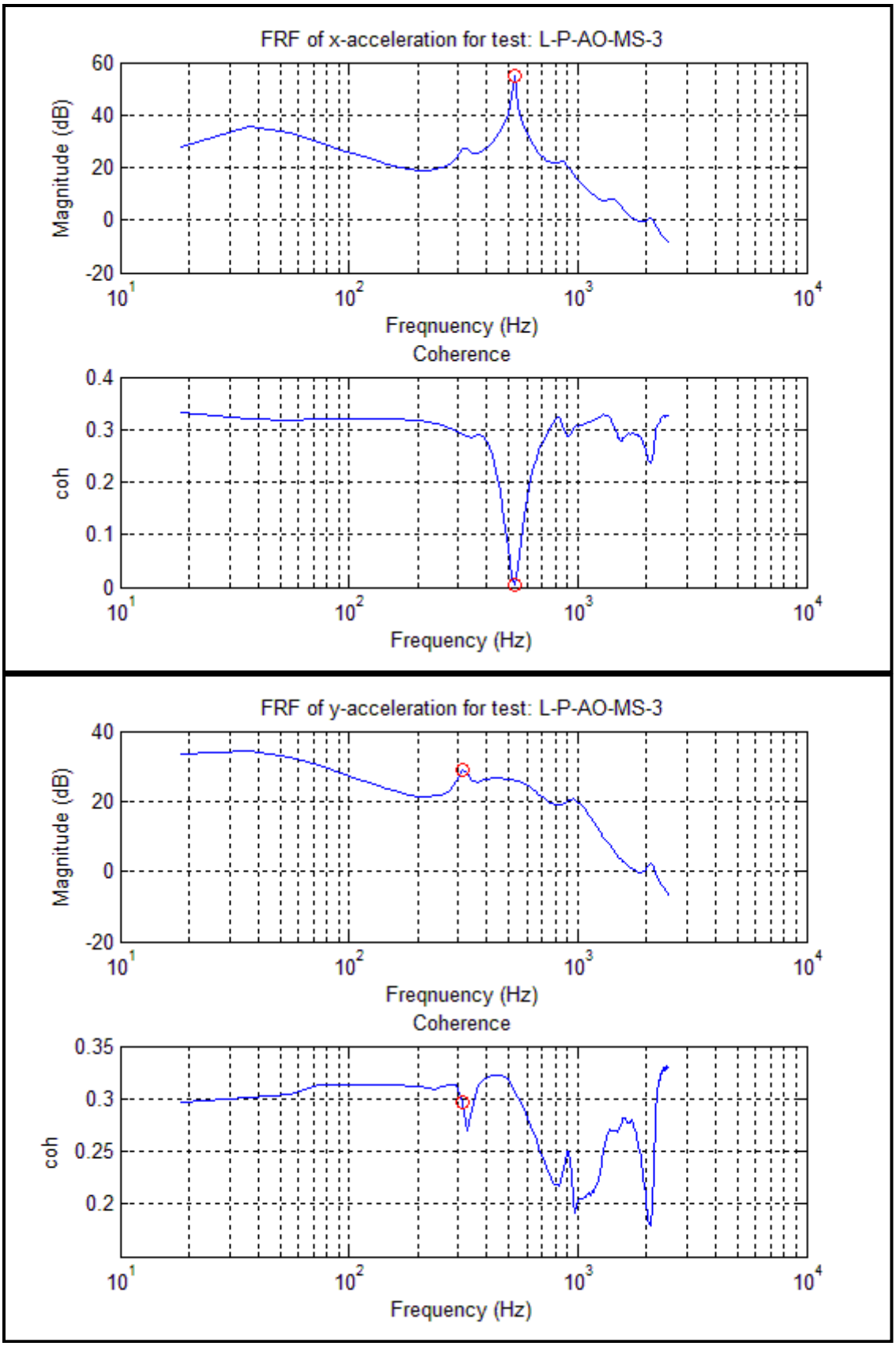
FRF of x-acceleration for test: L-P-AO-MS-3
Magnitude (dB)
60
40
20
0
-20
10^1
10^2
10^3
10^4
Freqnuency (Hz)
Coherence
coh
0.4
0.3
0.2
0.1
0
Frequency (Hz)
FRF of y-acceleration for test: L-P-AO-MS-3
Magnitude (dB)
40
20
0
-20
Freqnuency (Hz)
Coherence
coh
0.35
0.3
0.25
0.2
Frequency (Hz)

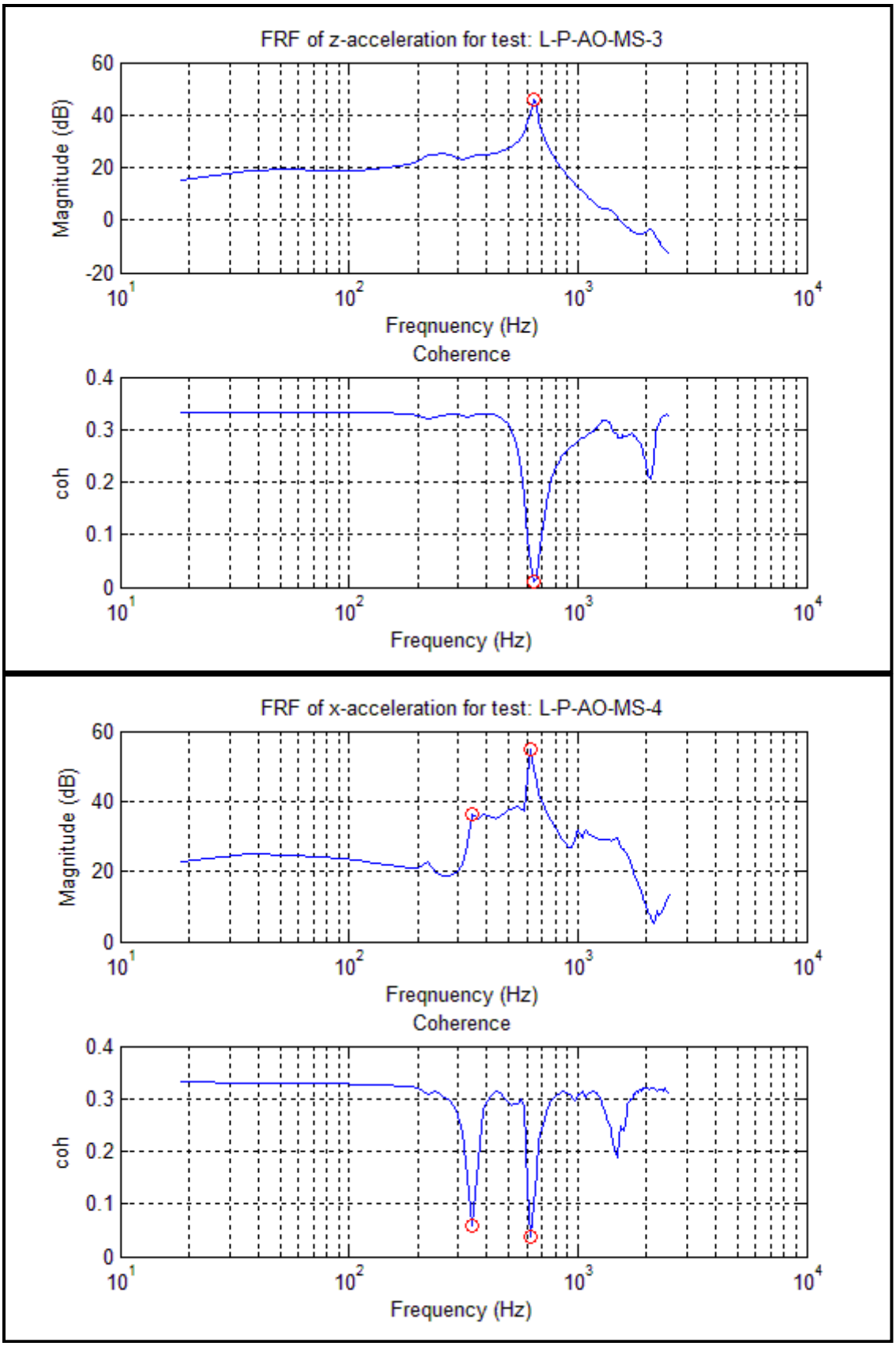
FRF of z-acceleration for test: L-P-AO-MS-3
Magnitude (dB)
60
40
20
0
-20
10^1
10^2
10^3
10^4
Freqnuency (Hz)
Coherence
coh
0.4
0.3
0.2
0.1
0
Frequency (Hz)
FRF of x-acceleration for test: L-P-AO-MS-4
Magnitude (dB)
Freqnuency (Hz)
Coherence
coh
Frequency (Hz)

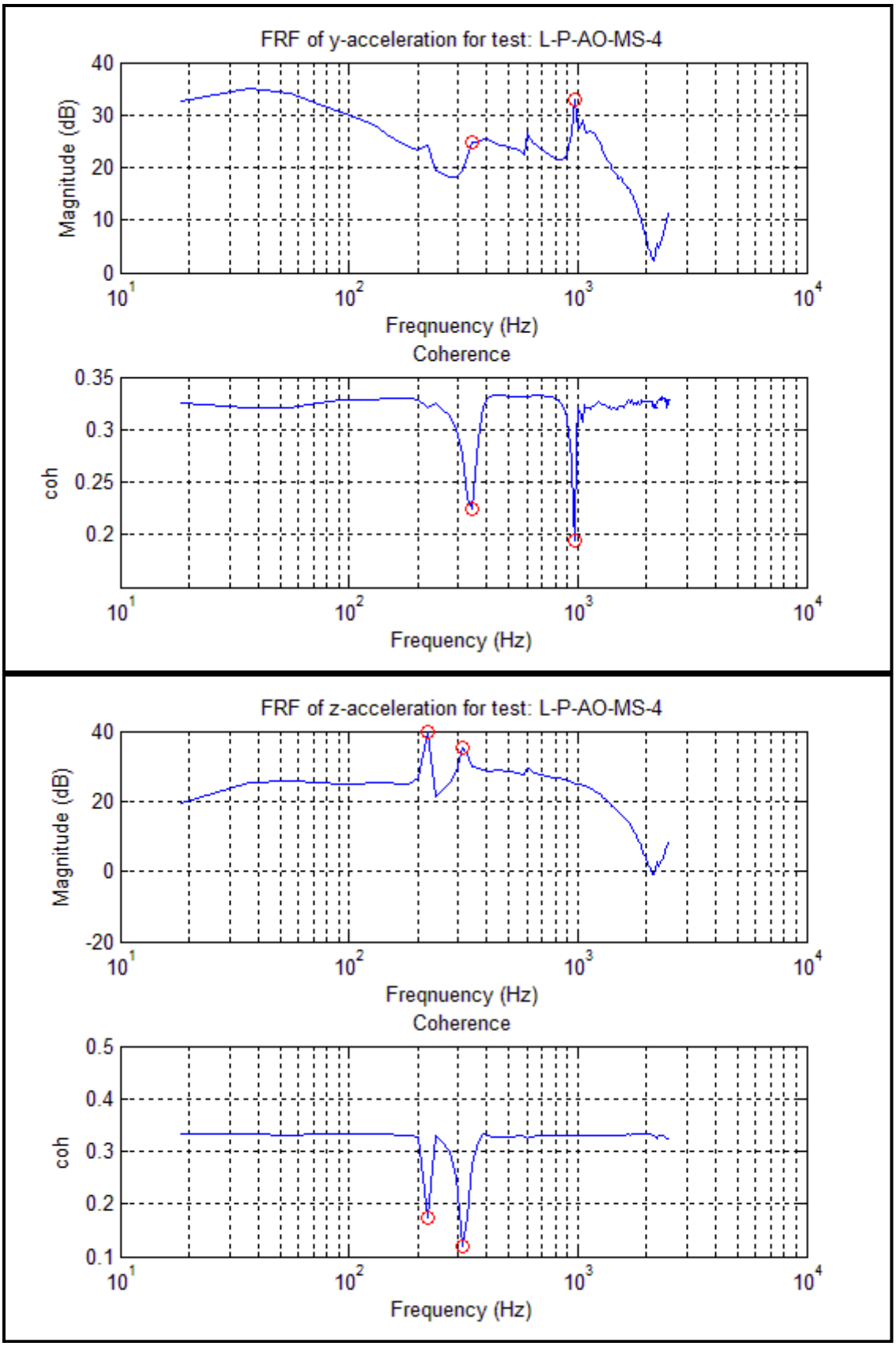
FRF of y-acceleration for test: L-P-AO-MS-4
Magnitude (dB)
Freqnuency (Hz)
Coherence
coh
Frequency (Hz)
FRF of z-acceleration for test: L-P-AO-MS-4
Magnitude (dB)
Freqnuency (Hz)
Coherence
coh
Frequency (Hz)

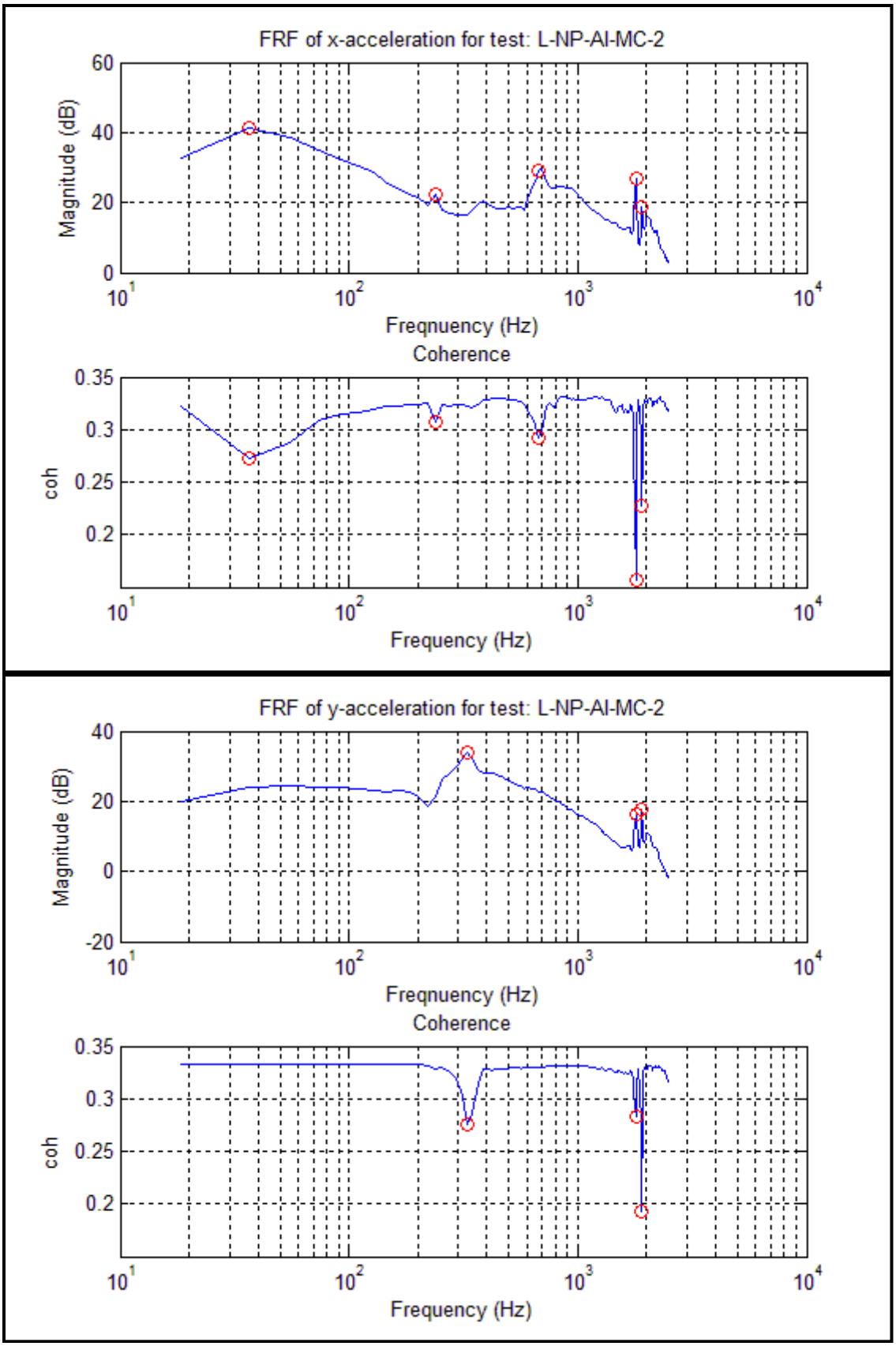
FRF of x-acceleration for test: L-NP-AI-MC-2
Magnitude (dB)
60
40
20
0
10^1
10^2
10^3
10^4
Freqnuency (Hz)
Coherence
coh
0.35
0.3
0.25
0.2
10^1
10^2
10^3
10^4
Frequency (Hz)
FRF of y-acceleration for test: L-NP-AI-MC-2
Magnitude (dB)
40
20
0
-20
10^1
10^2
10^3
10^4
Freqnuency (Hz)
Coherence
coh
0.35
0.3
0.25
0.2
10^1
10^2
10^3
10^4
Frequency (Hz)

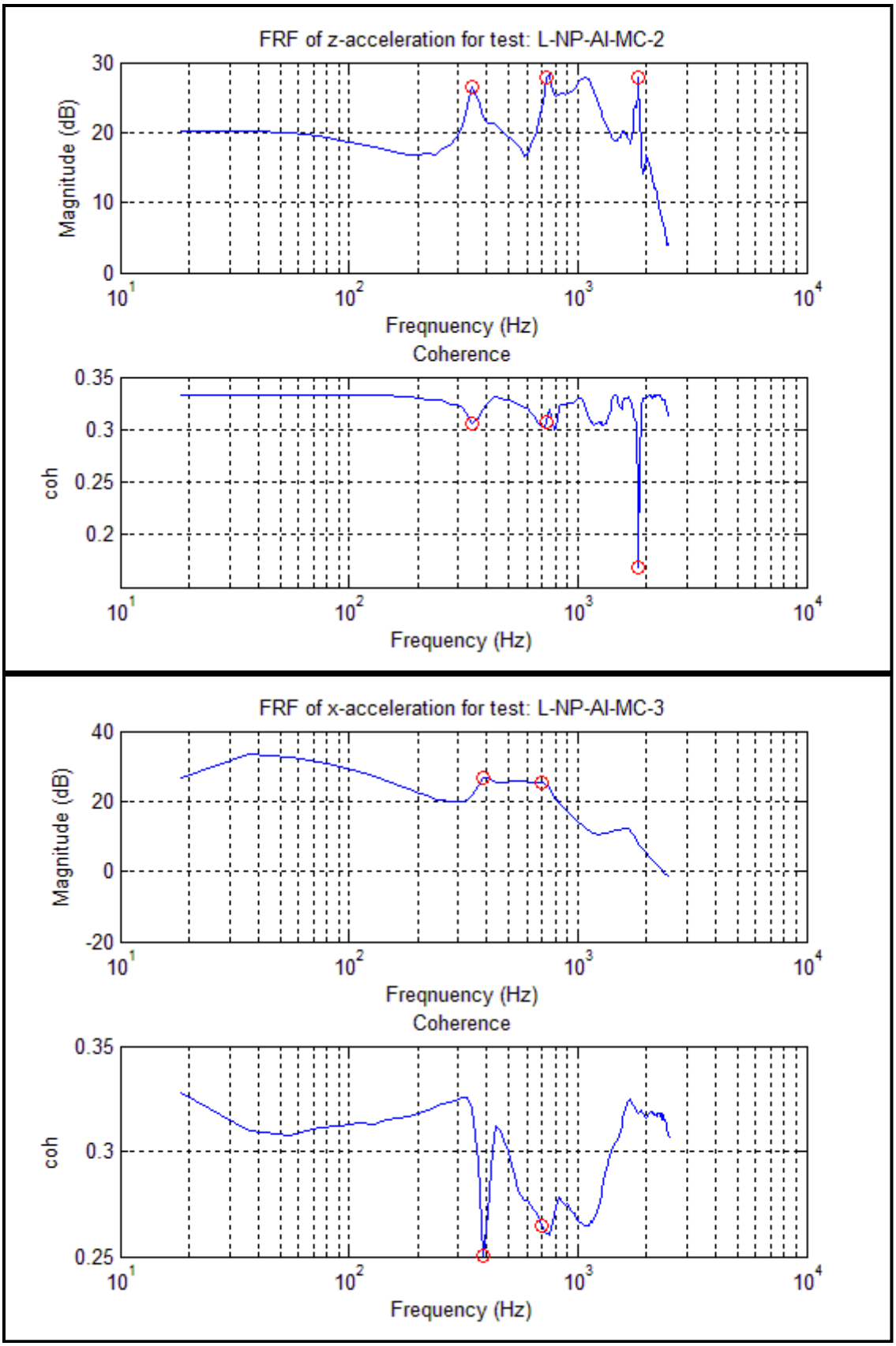
FRF of z-acceleration for test: L-NP-AI-MC-2
Magnitude (dB)
30
20
10
0
10^1
10^2
10^3
10^4
Freqnuency (Hz)
Coherence
coh
0.35
0.3
0.25
0.2
Frequency (Hz)
FRF of x-acceleration for test: L-NP-AI-MC-3
Magnitude (dB)
40
20
0
-20
Freqnuency (Hz)
Coherence
coh
0.35
0.3
0.25
Frequency (Hz)

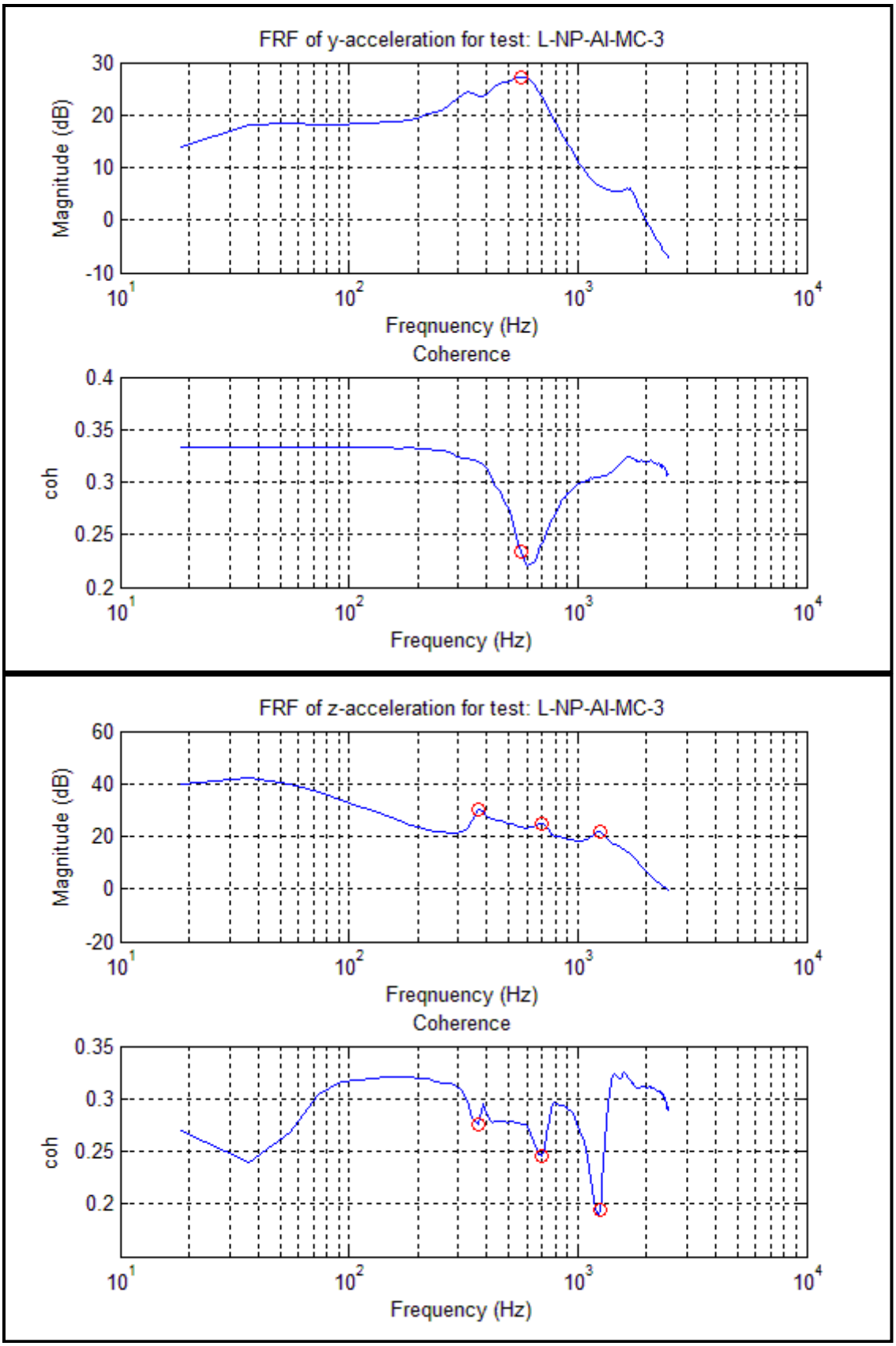
FRF of y-acceleration for test: L-NP-AI-MC-3
Magnitude (dB)
30
20
10
0
-10
10^1
10^2
10^3
10^4
Freqnuency (Hz)
Coherence
coh
0.4
0.35
0.3
0.25
0.2
10^1
10^2
10^3
10^4
Frequency (Hz)
FRF of z-acceleration for test: L-NP-AI-MC-3
Magnitude (dB)
60
40
20
0
-20
10^1
10^2
10^3
10^4
Freqnuency (Hz)
Coherence
coh
0.35
0.3
0.25
0.2
10^1
10^2
10^3
10^4
Frequency (Hz)

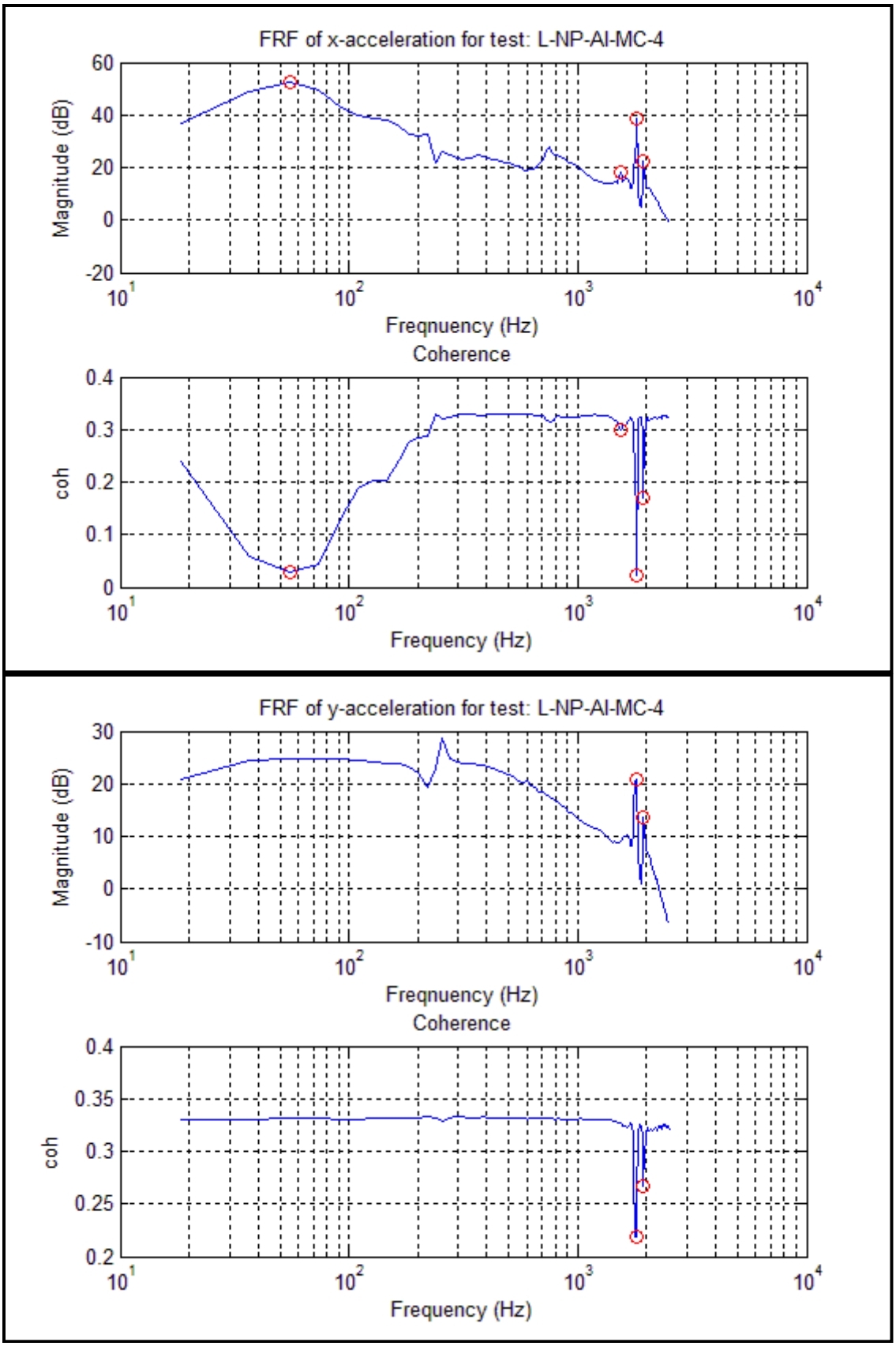
FRF of x-acceleration for test: L-NP-AI-MC-4
Magnitude (dB)
60
40
20
0
-20
10^1
10^2
10^3
10^4
Freqnuency (Hz)
Coherence
coh
0.4
0.3
0.2
0.1
0
Frequency (Hz)
FRF of y-acceleration for test: L-NP-AI-MC-4
Magnitude (dB)
30
20
10
0
-10
Freqnuency (Hz)
Coherence
coh
0.4
0.35
0.3
0.25
0.2
Frequency (Hz)

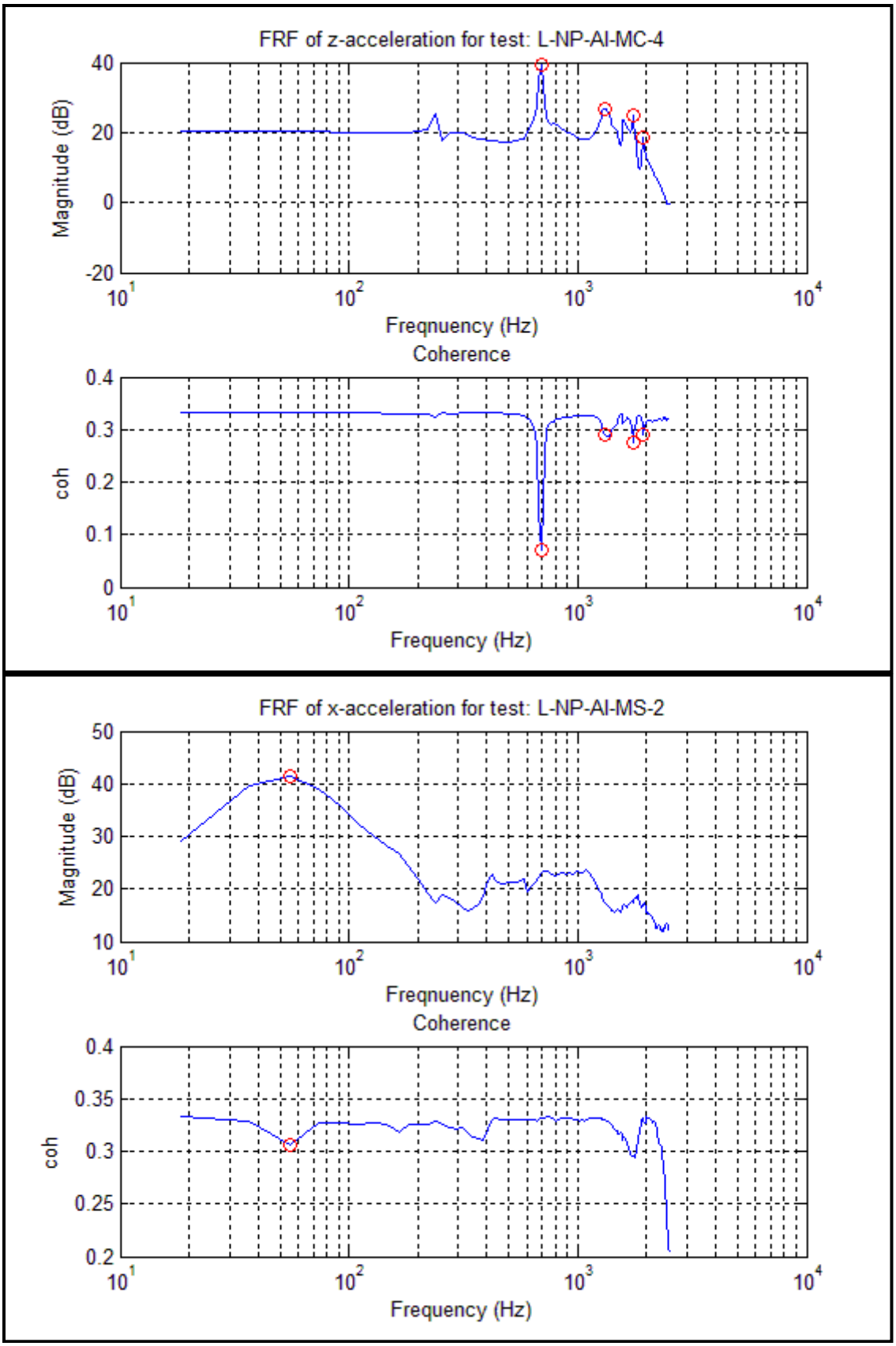
FRF of z-acceleration for test: L-NP-AI-MC-4
Magnitude (dB)
40
20
0
-20
10^1
10^2
10^3
10^4
Freqnuency (Hz)
Coherence
coh
0.4
0.3
0.2
0.1
0
10^1
10^2
10^3
10^4
Frequency (Hz)
FRF of x-acceleration for test: L-NP-AI-MS-2
Magnitude (dB)
50
40
30
20
10
10^1
10^2
10^3
10^4
Freqnuency (Hz)
Coherence
coh
0.4
0.35
0.3
0.25
0.2
10^1
10^2
10^3
10^4
Frequency (Hz)

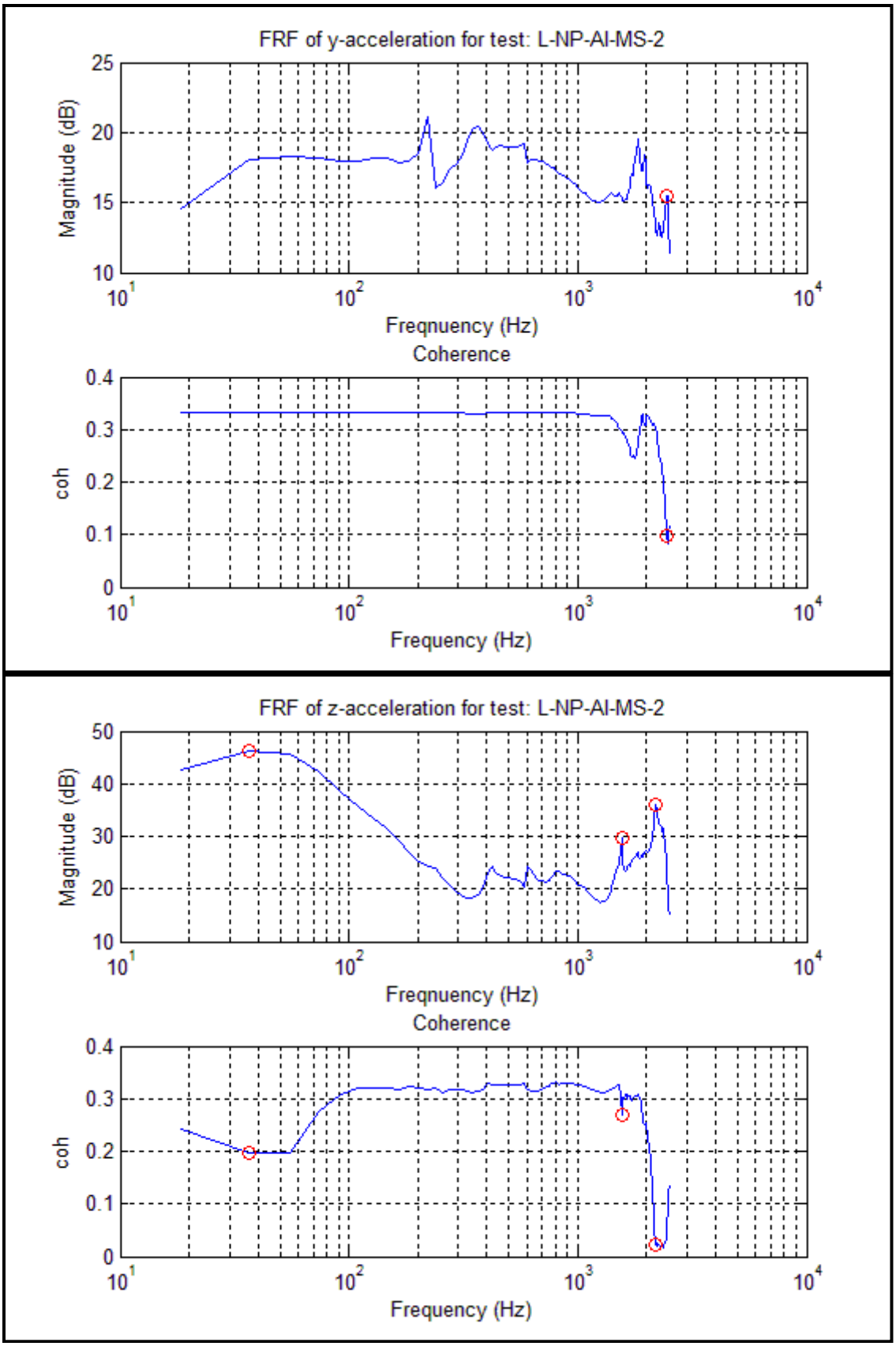
FRF of y-acceleration for test: L-NP-AI-MS-2
Magnitude (dB)
Freqnuency (Hz)
Coherence
coh
Frequency (Hz)
FRF of z-acceleration for test: L-NP-AI-MS-2
Magnitude (dB)
Freqnuency (Hz)
Coherence
coh
Frequency (Hz)

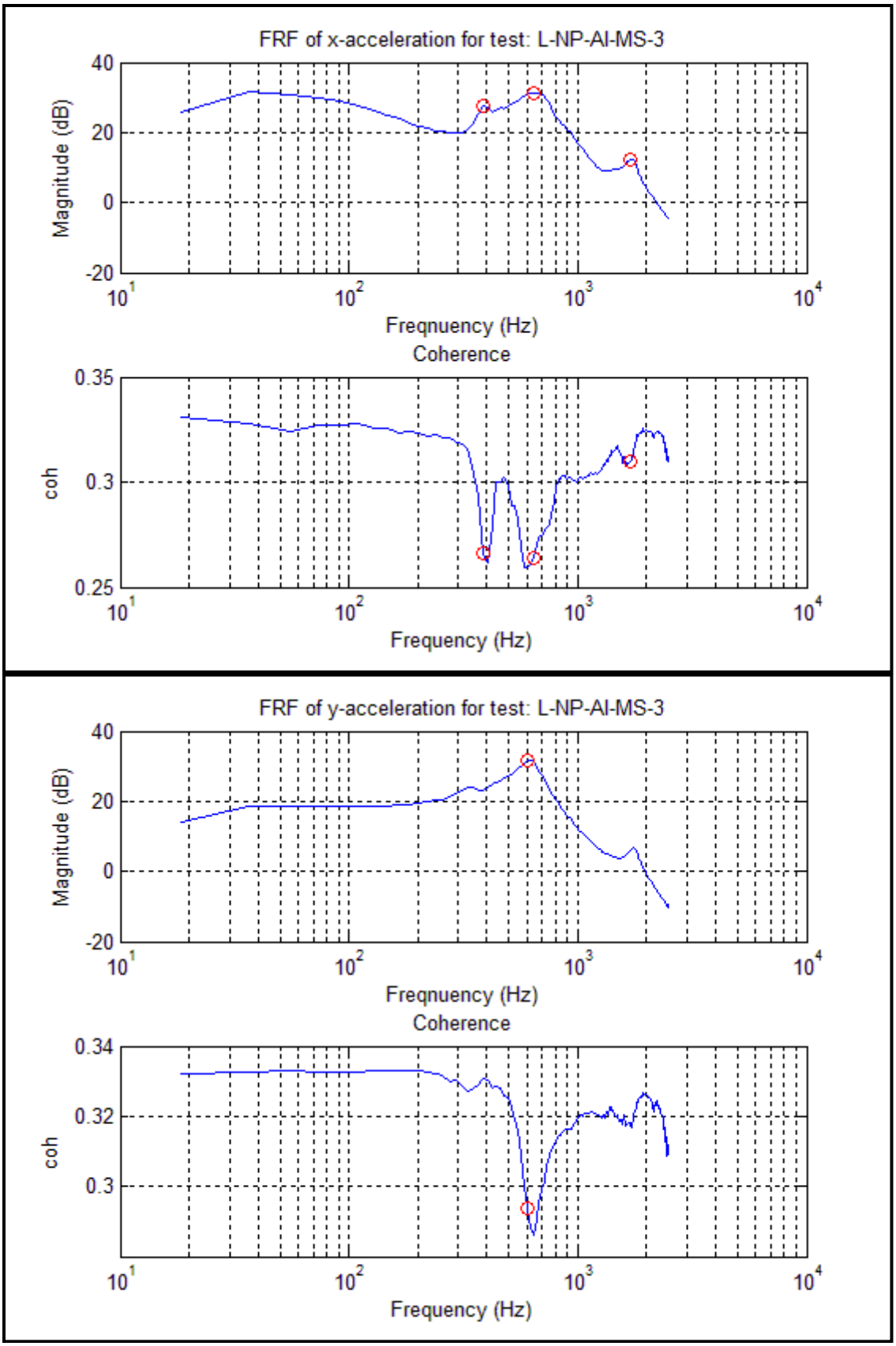
FRF of x-acceleration for test: L-NP-AI-MS-3
Magnitude (dB)
40
20
0
-20
10^1
10^2
10^3
10^4
Freqnuency (Hz)
Coherence
coh
0.35
0.3
0.25
Frequency (Hz)
FRF of y-acceleration for test: L-NP-AI-MS-3
Magnitude (dB)
Freqnuency (Hz)
Coherence
coh
0.34
0.32
0.3
Frequency (Hz)

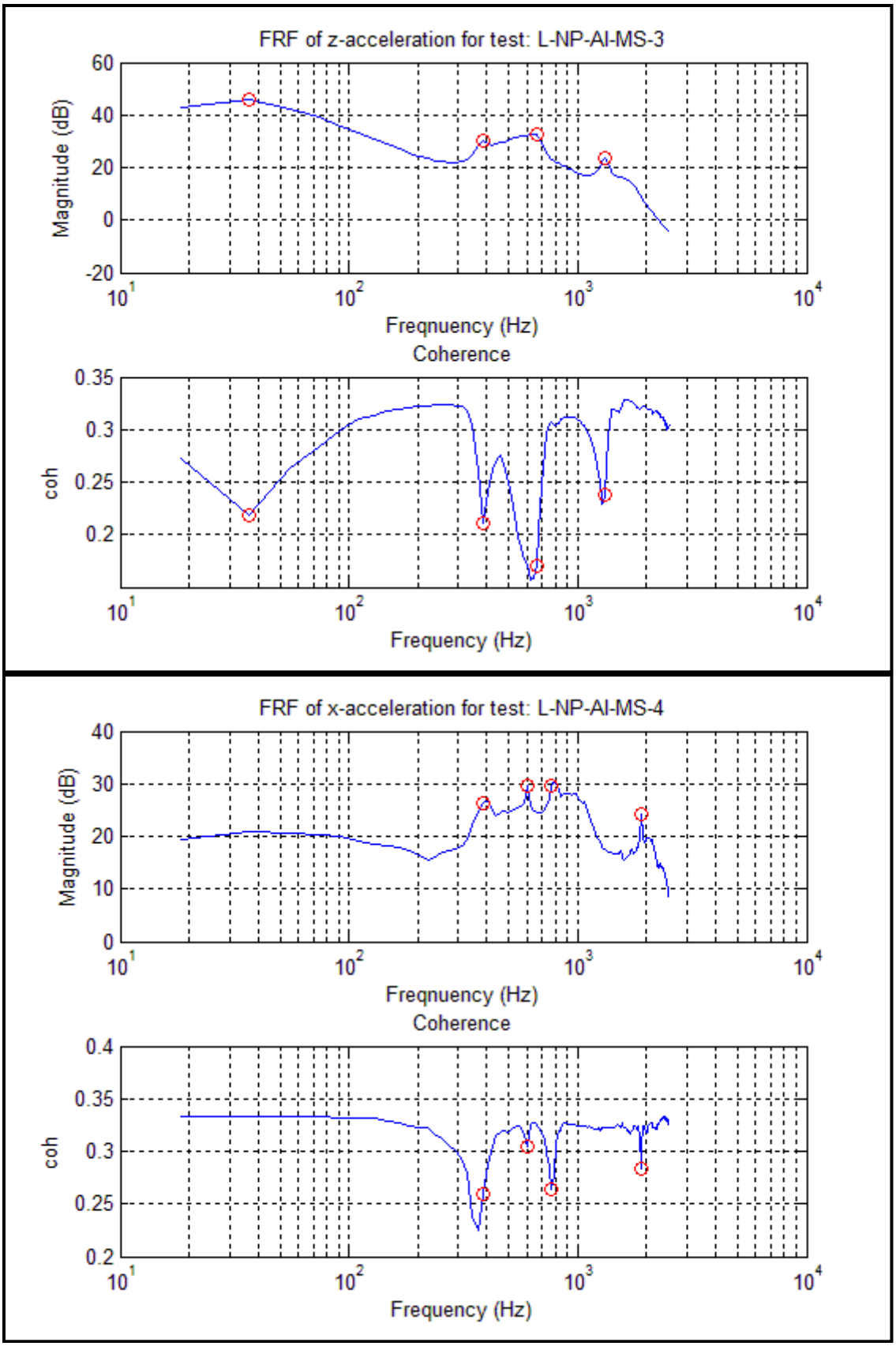
FRF of z-acceleration for test: L-NP-AI-MS-3
Magnitude (dB)
60
40
20
0
-20
10^1
10^2
10^3
10^4
Freqnuency (Hz)
Coherence
coh
0.35
0.3
0.25
0.2
10^1
10^2
10^3
10^4
Frequency (Hz)
FRF of x-acceleration for test: L-NP-AI-MS-4
Magnitude (dB)
40
30
20
10
0
10^1
10^2
10^3
10^4
Freqnuency (Hz)
Coherence
coh
0.4
0.35
0.3
0.25
0.2
10^1
10^2
10^3
10^4
Frequency (Hz)

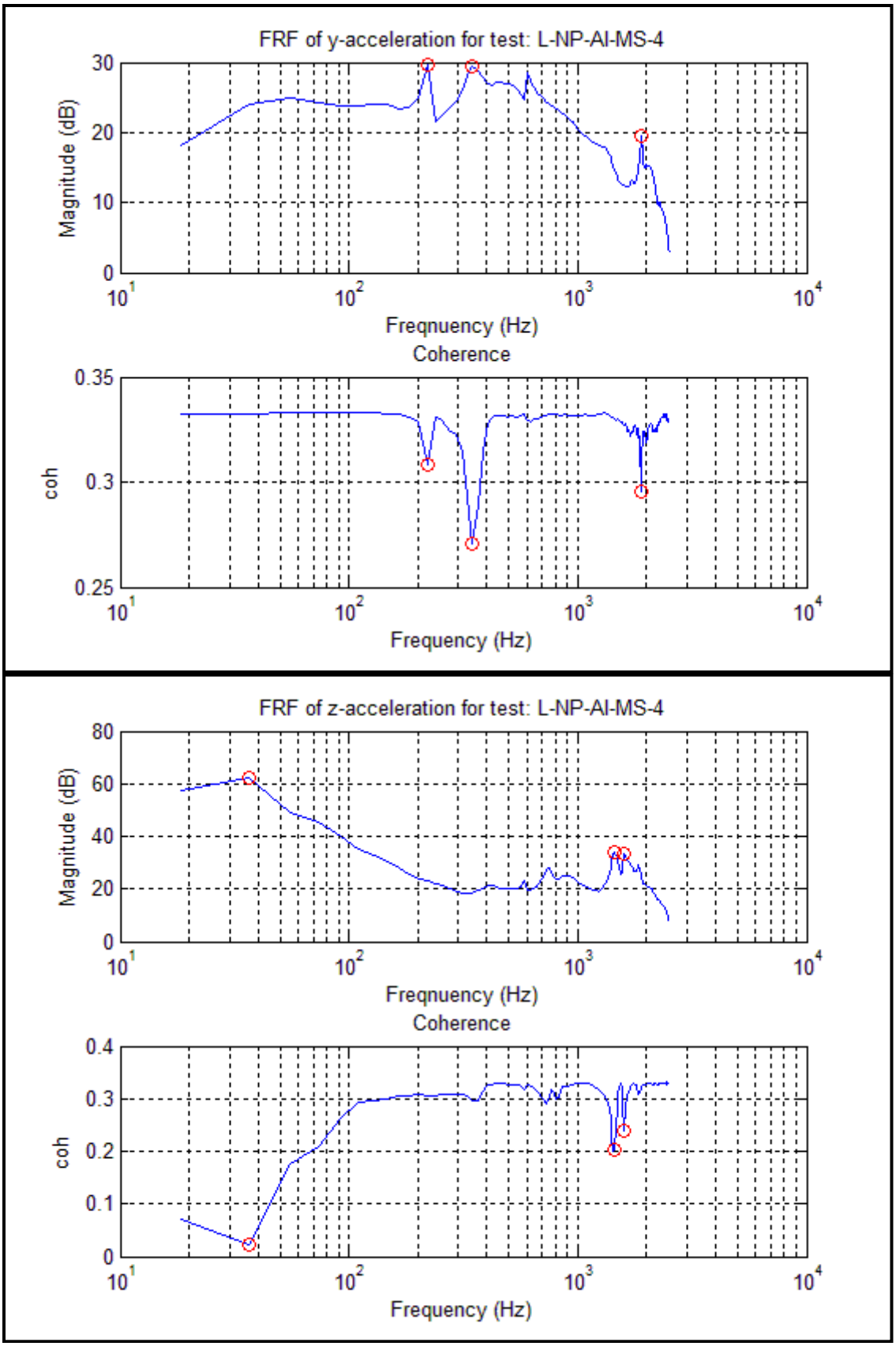
FRF of y-acceleration for test: L-NP-AI-MS-4
Magnitude (dB)
30
20
10
0
10^1
10^2
10^3
10^4
Freqnuency (Hz)
Coherence
coh
0.35
0.3
0.25
Frequency (Hz)
FRF of z-acceleration for test: L-NP-AI-MS-4
Magnitude (dB)
80
60
40
20
0
Freqnuency (Hz)
Coherence
coh
0.4
0.3
0.2
0.1
0
Frequency (Hz)

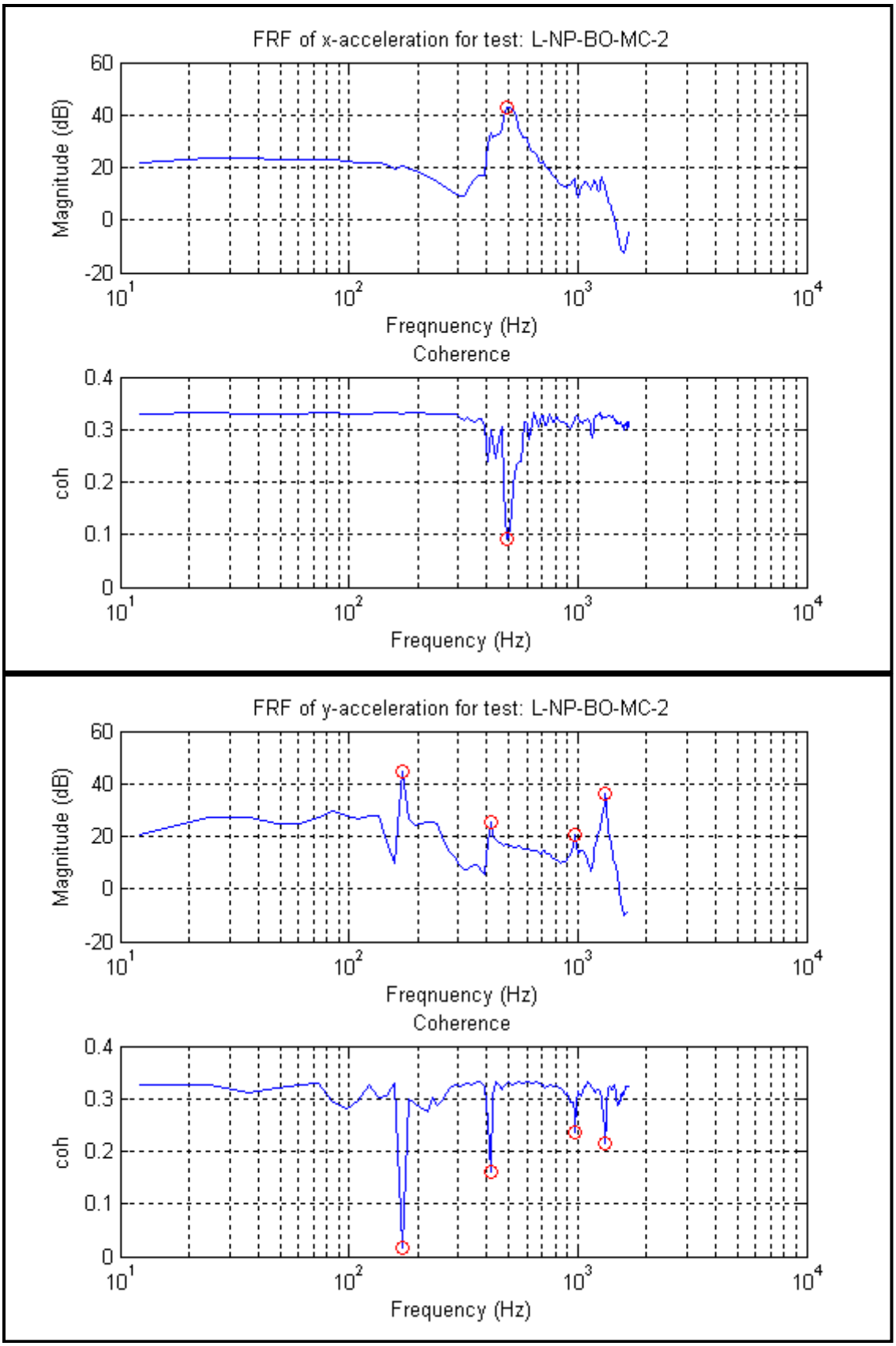
FRF of x-acceleration for test: L-NP-BO-MC-2
Magnitude (dB)
60
40
20
0
-20
10^1
10^2
10^3
10^4
Freqnuency (Hz)
Coherence
coh
0.4
0.3
0.2
0.1
0
Frequency (Hz)
FRF of y-acceleration for test: L-NP-BO-MC-2
Magnitude (dB)
Freqnuency (Hz)
Coherence
coh
Frequency (Hz)

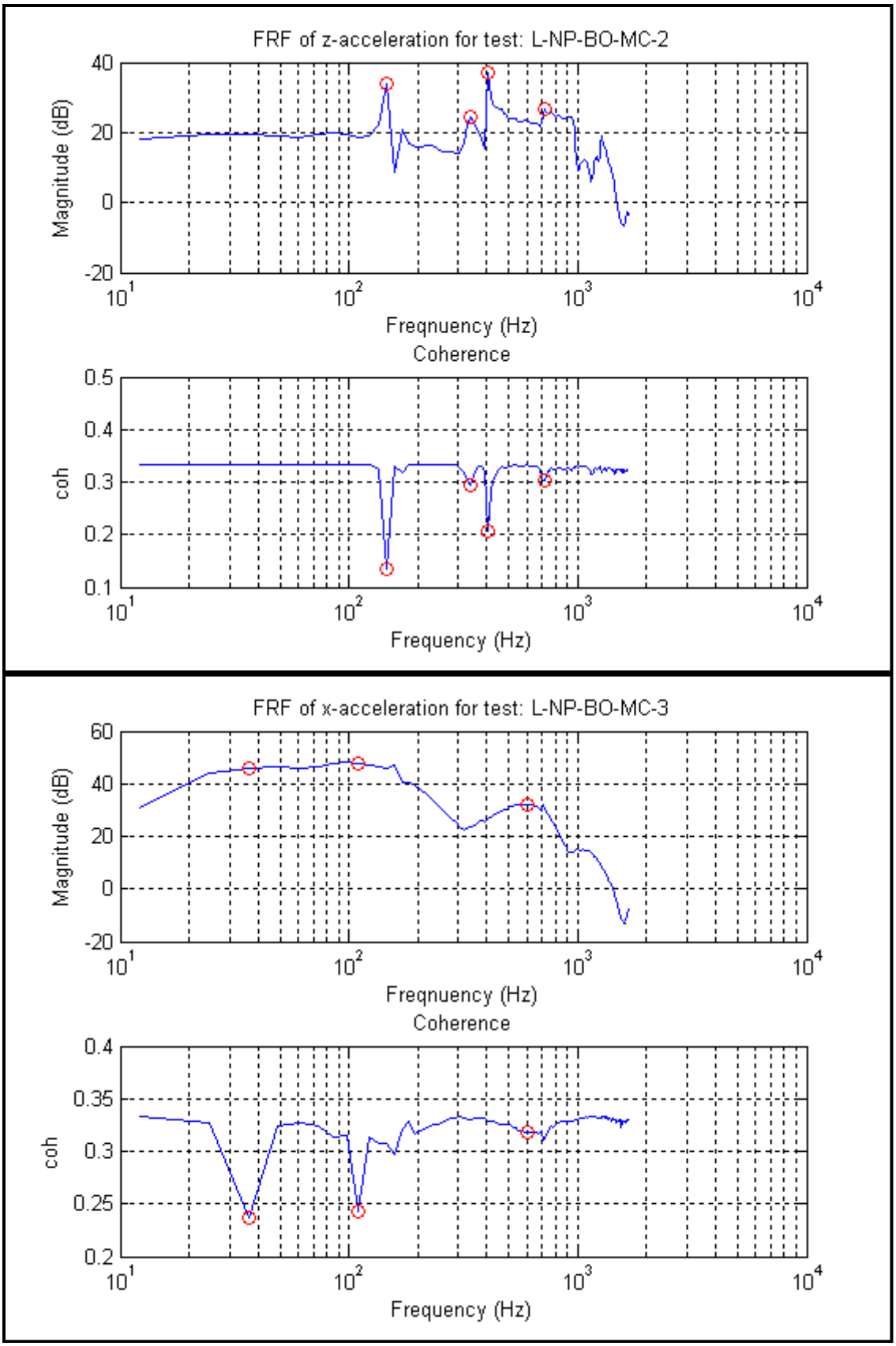
FRF of z-acceleration for test: L-NP-BO-MC-2
Magnitude (dB)
40
20
0
-20
10^1
10^2
10^3
10^4
Freqnuency (Hz)
Coherence
coh
0.5
0.4
0.3
0.2
0.1
10^1
10^2
10^3
10^4
Frequency (Hz)
FRF of x-acceleration for test: L-NP-BO-MC-3
Magnitude (dB)
60
40
20
0
-20
10^1
10^2
10^3
10^4
Freqnuency (Hz)
Coherence
coh
0.4
0.35
0.3
0.25
0.2
10^1
10^2
10^3
10^4
Frequency (Hz)

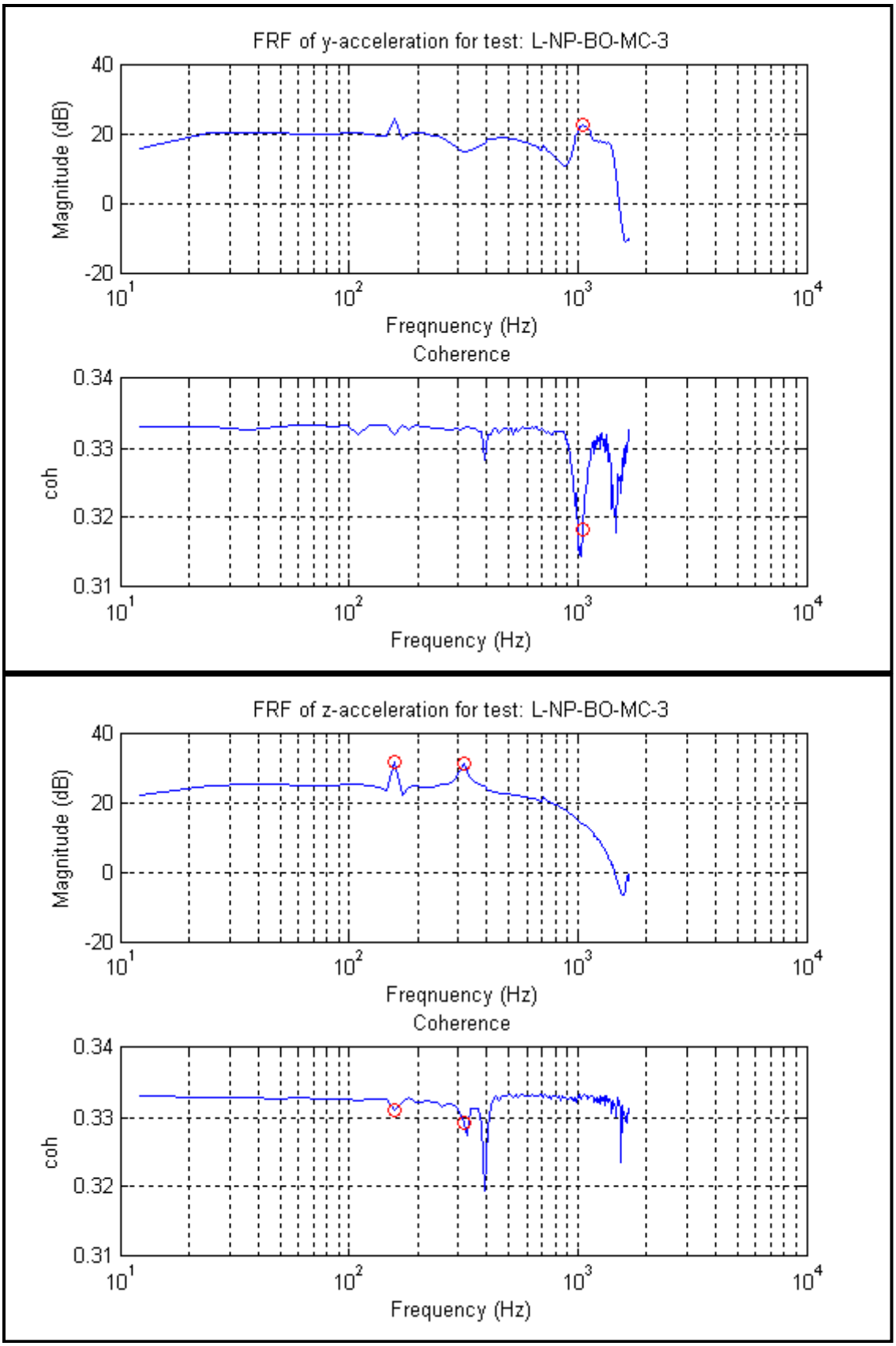
FRF of y-acceleration for test: L-NP-BO-MC-3
Magnitude (dB)
40
20
0
-20
10^1
10^2
10^3
10^4
Freqnuency (Hz)
Coherence
coh
0.34
0.33
0.32
0.31
Frequency (Hz)
FRF of z-acceleration for test: L-NP-BO-MC-3
Magnitude (dB)
Freqnuency (Hz)
Coherence
coh
Frequency (Hz)

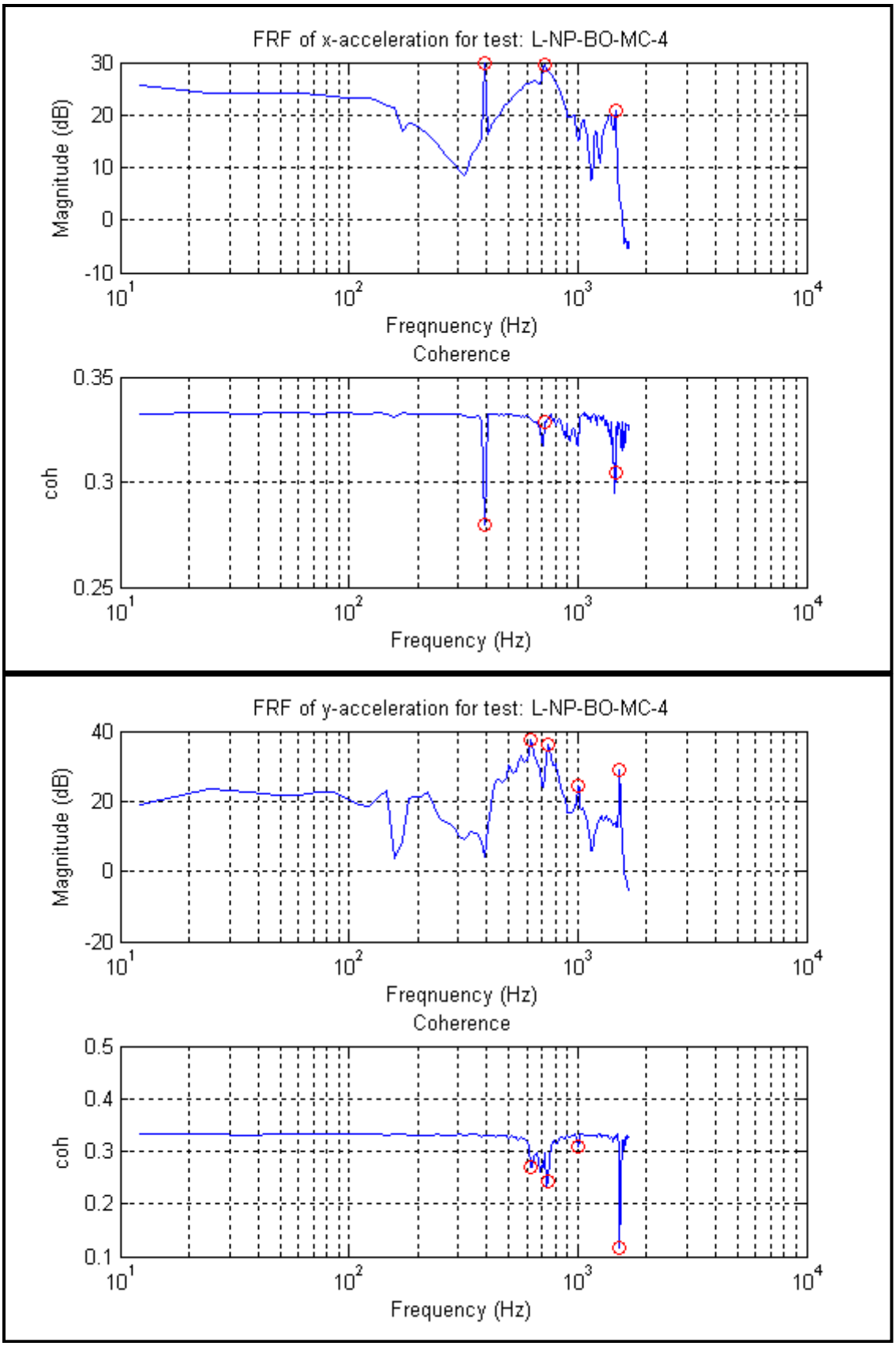
FRF of x-acceleration for test: L-NP-BO-MC-4
Magnitude (dB)
30
20
10
0
-10
10^1
10^2
10^3
10^4
Freqnuency (Hz)
Coherence
coh
0.35
0.3
0.25
Frequency (Hz)
FRF of y-acceleration for test: L-NP-BO-MC-4
Magnitude (dB)
40
20
0
-20
Freqnuency (Hz)
Coherence
coh
0.5
0.4
0.3
0.2
0.1
Frequency (Hz)

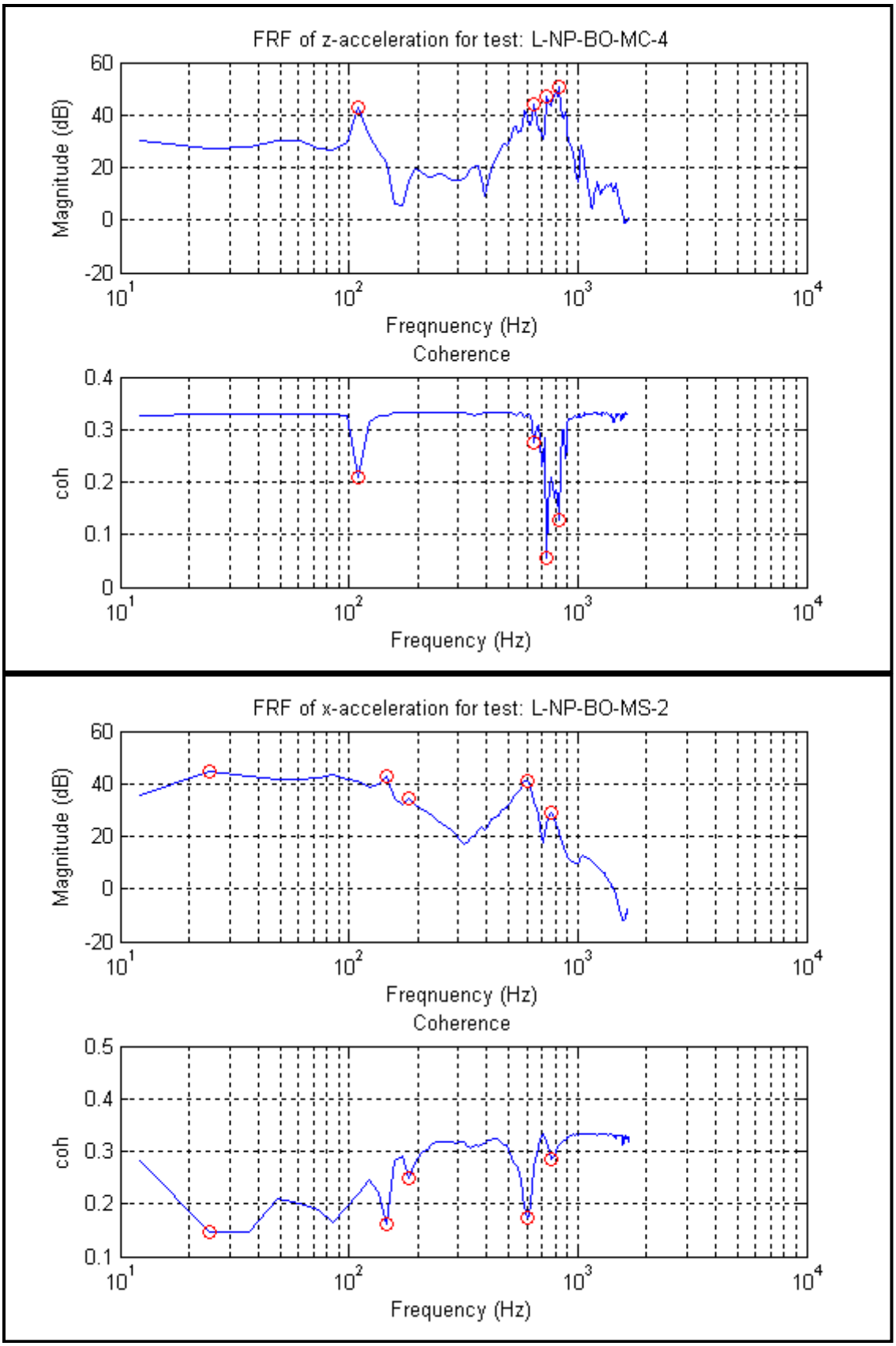
FRF of z-acceleration for test: L-NP-BO-MC-4
Magnitude (dB)
60
40
20
0
-20
10^1
10^2
10^3
10^4
Freqnuency (Hz)
Coherence
coh
0.4
0.3
0.2
0.1
0
Frequency (Hz)
FRF of x-acceleration for test: L-NP-BO-MS-2
Magnitude (dB)
Freqnuency (Hz)
Coherence
coh
0.5
0.4
0.3
0.2
0.1
Frequency (Hz)

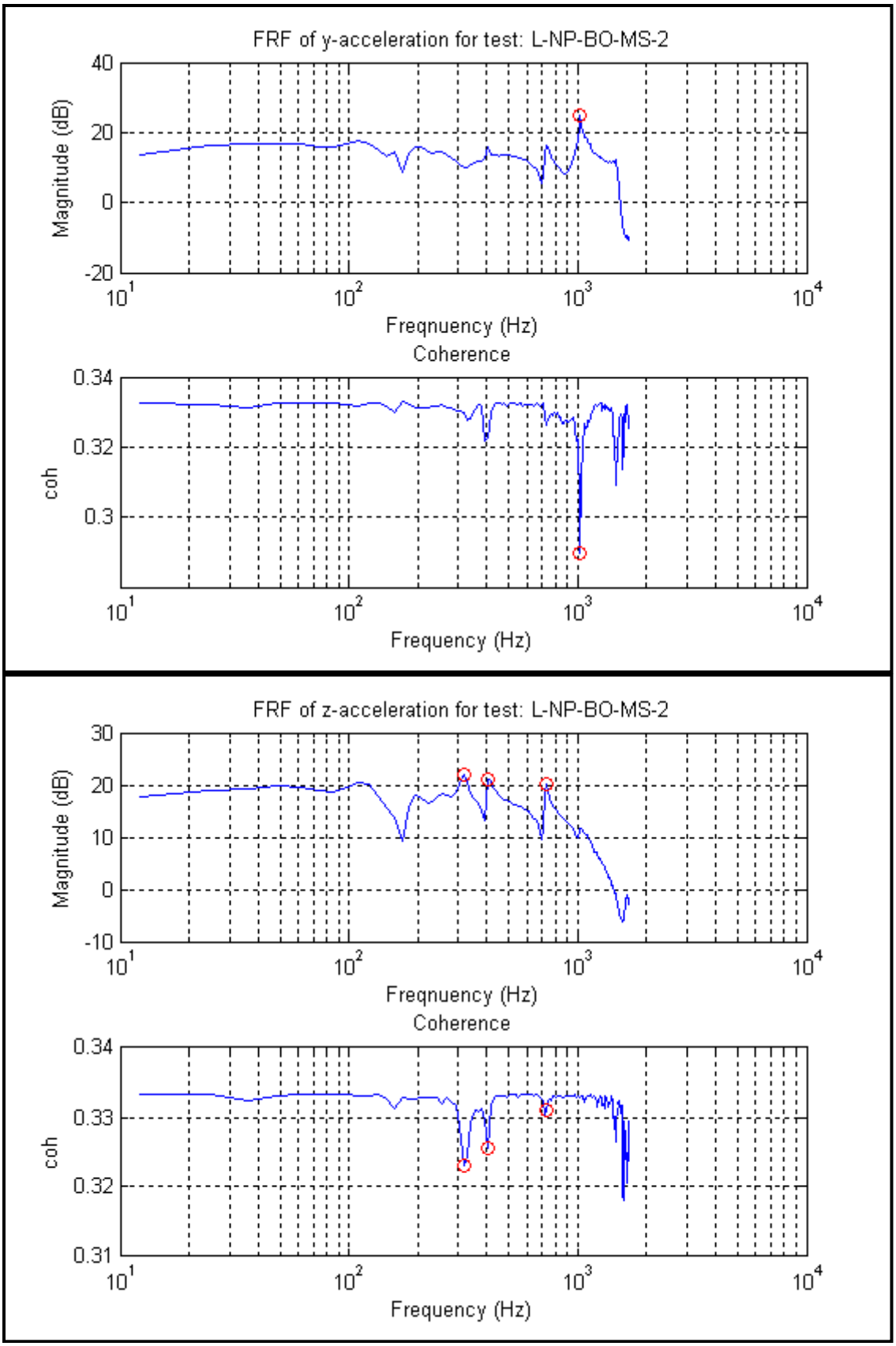
FRF of y-acceleration for test: L-NP-BO-MS-2
Magnitude (dB)
40
20
0
-20
10^1
10^2
10^3
10^4
Freqnuency (Hz)
Coherence
coh
0.34
0.32
0.3
Frequency (Hz)
FRF of z-acceleration for test: L-NP-BO-MS-2
Magnitude (dB)
30
20
10
0
-10
Freqnuency (Hz)
Coherence
coh
0.34
0.33
0.32
0.31
Frequency (Hz)

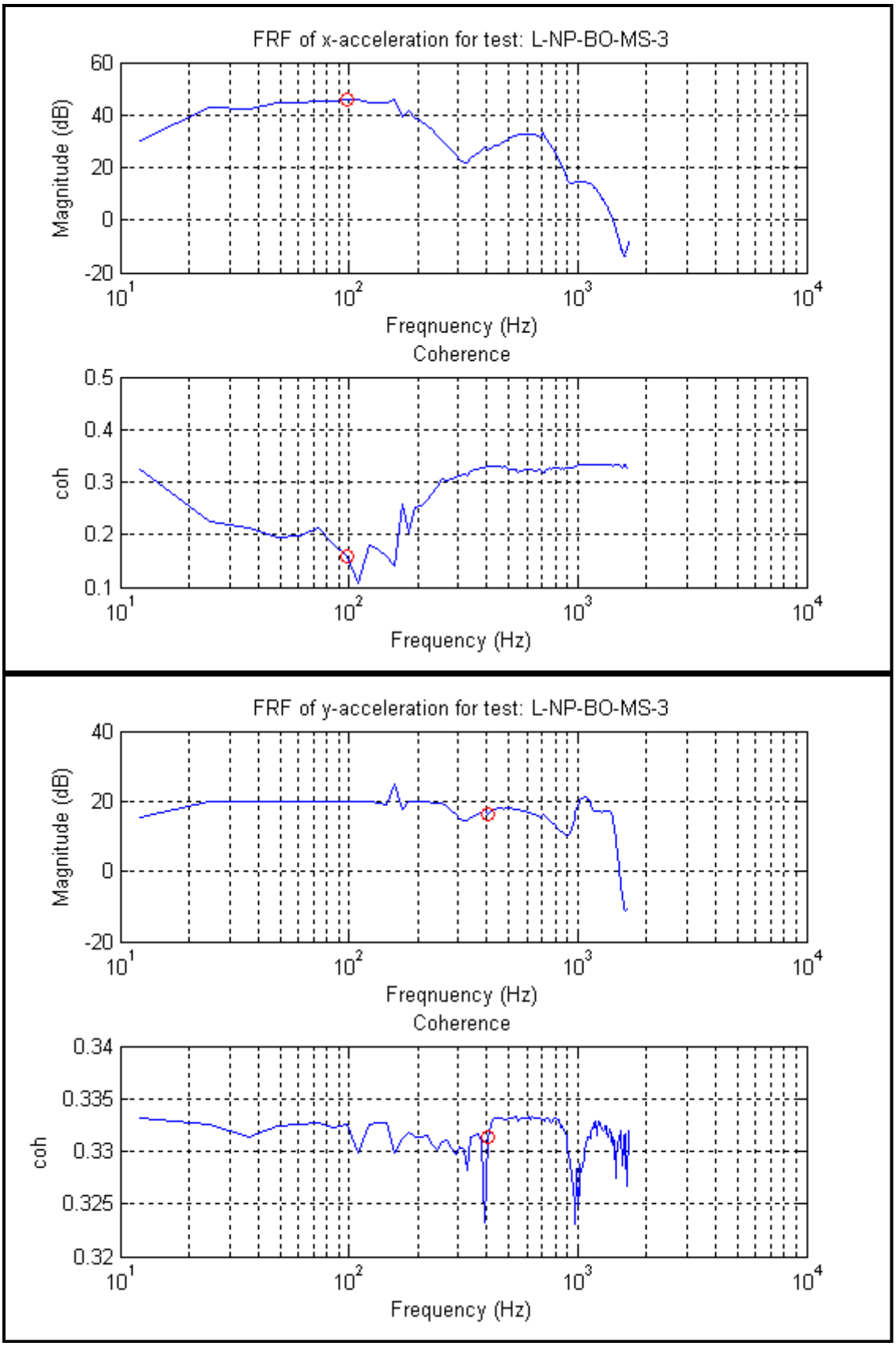
FRF of x-acceleration for test: L-NP-BO-MS-3
Magnitude (dB)
60
40
20
0
-20
10^1
10^2
10^3
10^4
Freqnuency (Hz)
Coherence
coh
0.5
0.4
0.3
0.2
0.1
Frequency (Hz)
FRF of y-acceleration for test: L-NP-BO-MS-3
Magnitude (dB)
40
20
0
-20
Freqnuency (Hz)
Coherence
coh
0.34
0.335
0.33
0.325
0.32
Frequency (Hz)

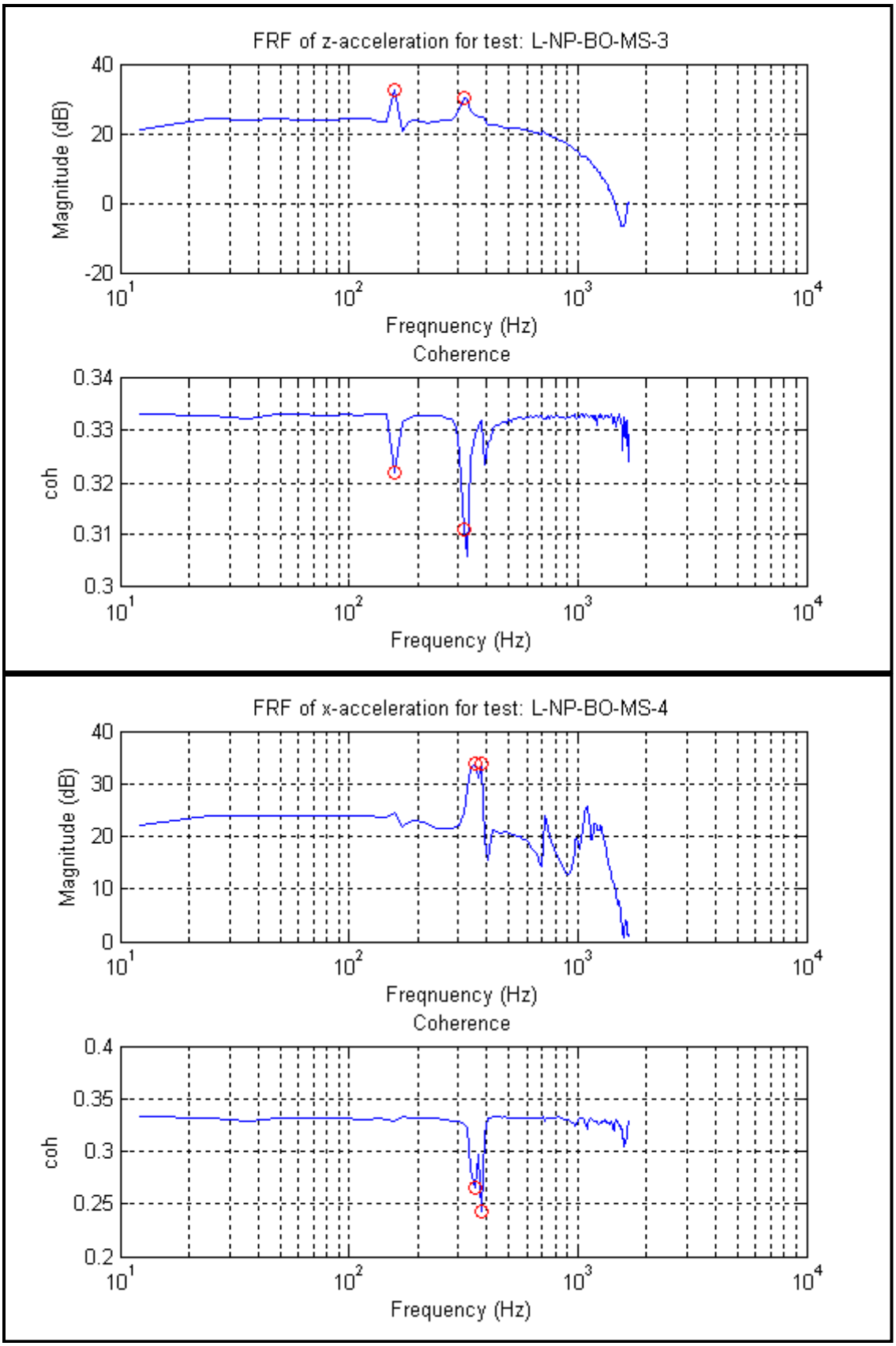
FRF of z-acceleration for test: L-NP-BO-MS-3
Magnitude (dB)
40
20
0
-20
10^1
10^2
10^3
10^4
Freqnuency (Hz)
Coherence
coh
0.34
0.33
0.32
0.31
0.3
Frequency (Hz)
FRF of x-acceleration for test: L-NP-BO-MS-4
Magnitude (dB)
40
30
20
10
0
Freqnuency (Hz)
Coherence
coh
0.4
0.35
0.3
0.25
0.2
Frequency (Hz)

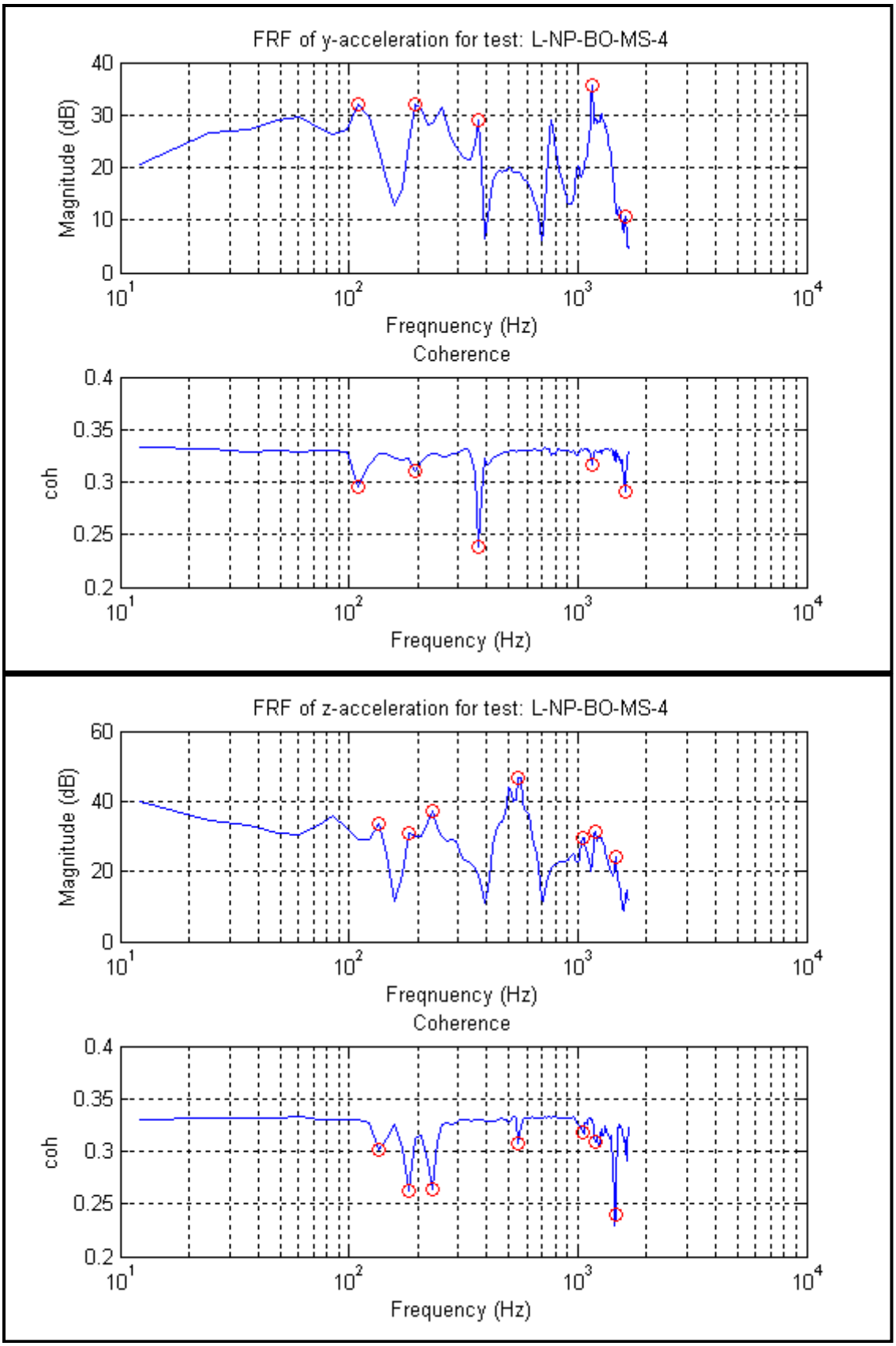
FRF of y-acceleration for test: L-NP-BO-MS-4
Magnitude (dB)
Freqnuency (Hz)
Coherence
coh
Frequency (Hz)
FRF of z-acceleration for test: L-NP-BO-MS-4
Magnitude (dB)
Freqnuency (Hz)
Coherence
coh
Frequency (Hz)

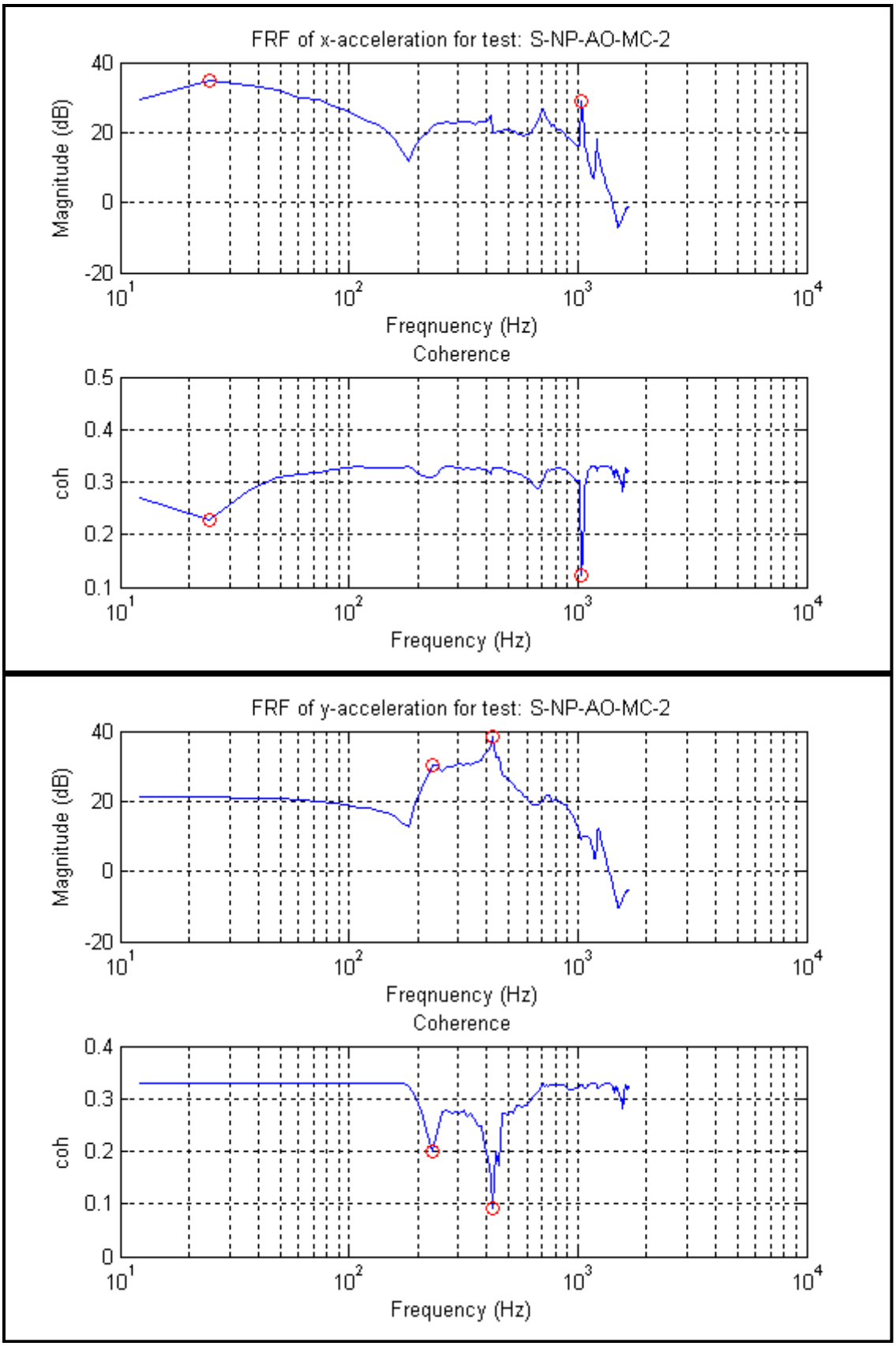
FRF of x-acceleration for test: S-NP-AO-MC-2
Magnitude (dB)
40
20
0
-20
10^1
10^2
10^3
10^4
Freqnuency (Hz)
Coherence
coh
0.5
0.4
0.3
0.2
0.1
Frequency (Hz)
FRF of y-acceleration for test: S-NP-AO-MC-2
Magnitude (dB)
Freqnuency (Hz)
Coherence
coh
0.4
0.3
0.2
0.1
0
Frequency (Hz)

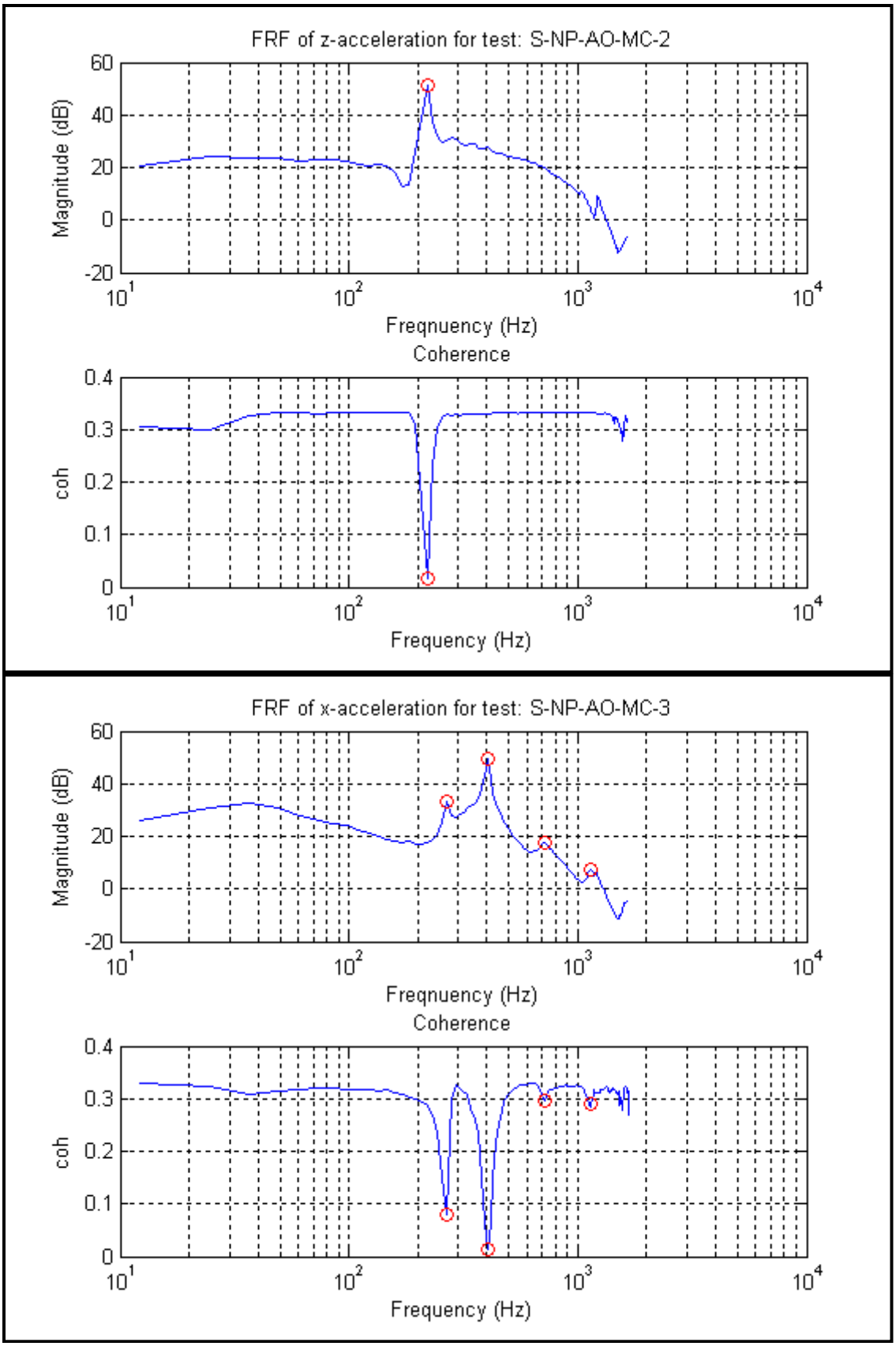
FRF of z-acceleration for test: S-NP-AO-MC-2
Magnitude (dB)
Freqnuency (Hz)
Coherence
coh
Frequency (Hz)
FRF of x-acceleration for test: S-NP-AO-MC-3
Magnitude (dB)
Freqnuency (Hz)
Coherence
coh
Frequency (Hz)

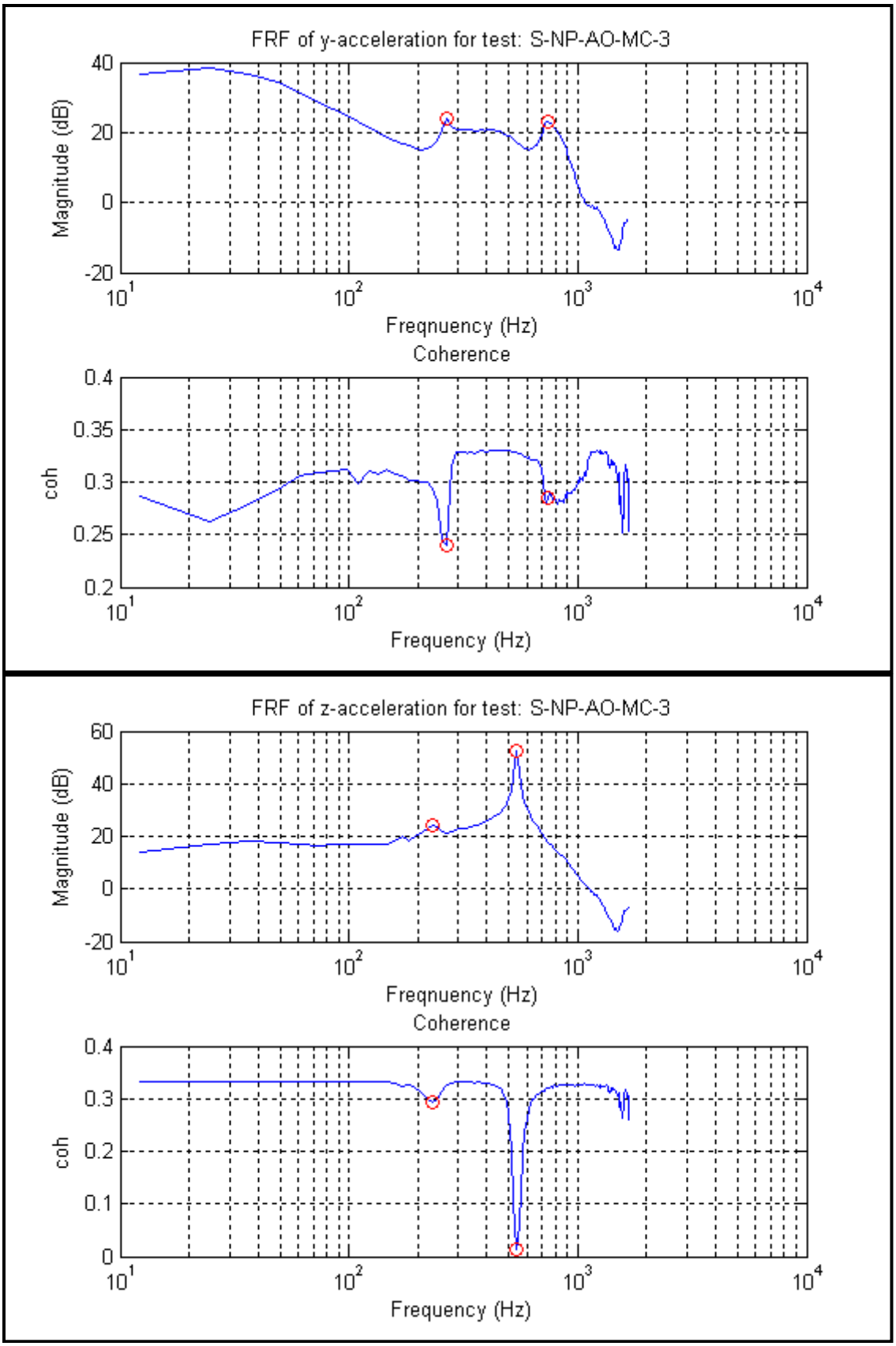
FRF of y-acceleration for test: S-NP-AO-MC-3
Magnitude (dB)
Freqnuency (Hz)
Coherence
coh
Frequency (Hz)
FRF of z-acceleration for test: S-NP-AO-MC-3
Magnitude (dB)
Freqnuency (Hz)
Coherence
coh
Frequency (Hz)

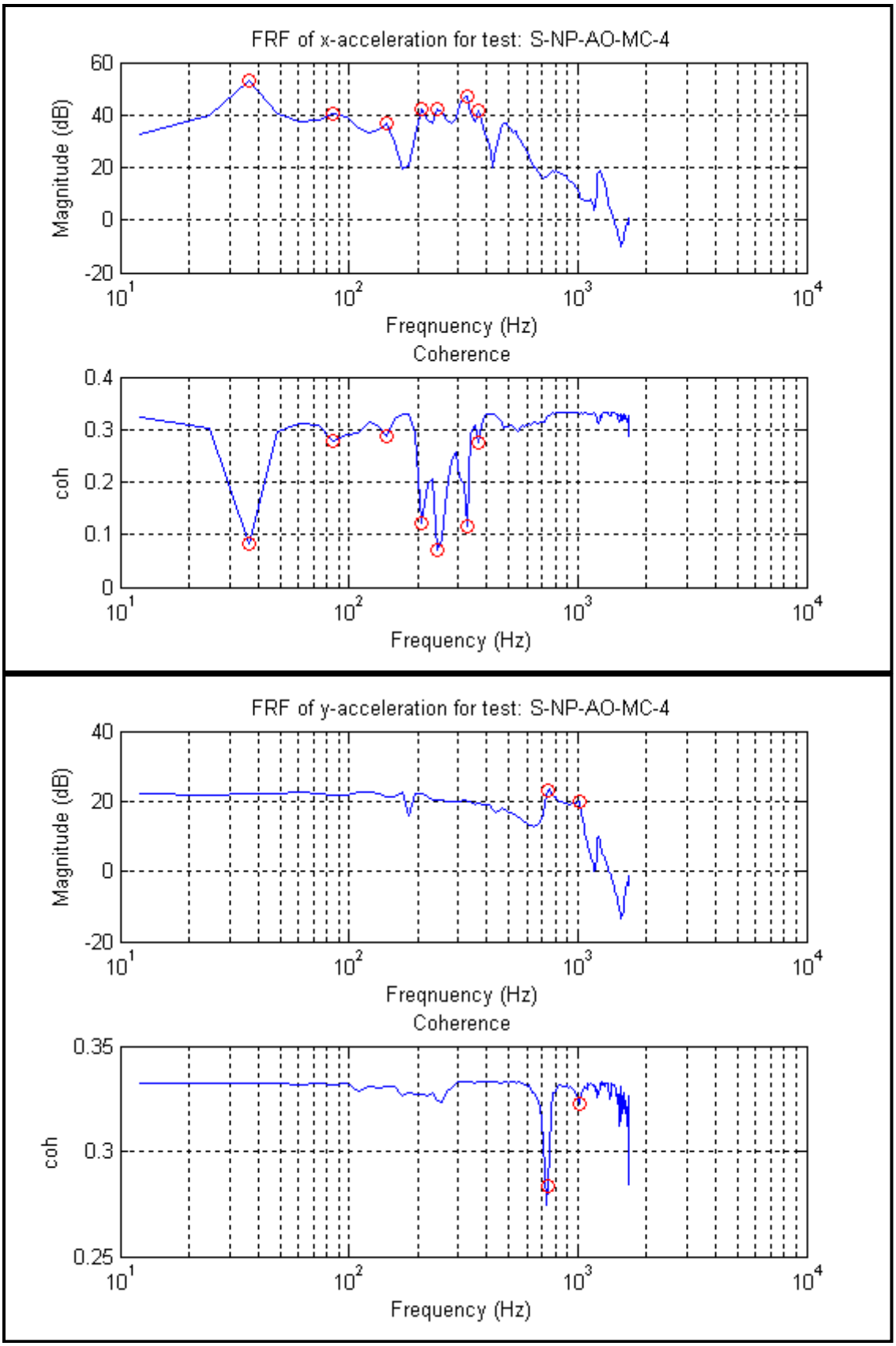
FRF of x-acceleration for test: S-NP-AO-MC-4
Magnitude (dB)
60
40
20
0
-20
10^1
10^2
10^3
10^4
Freqnuency (Hz)
Coherence
coh
0.4
0.3
0.2
0.1
0
Frequency (Hz)
FRF of y-acceleration for test: S-NP-AO-MC-4
Magnitude (dB)
40
20
0
-20
Freqnuency (Hz)
Coherence
coh
0.35
0.3
0.25
Frequency (Hz)

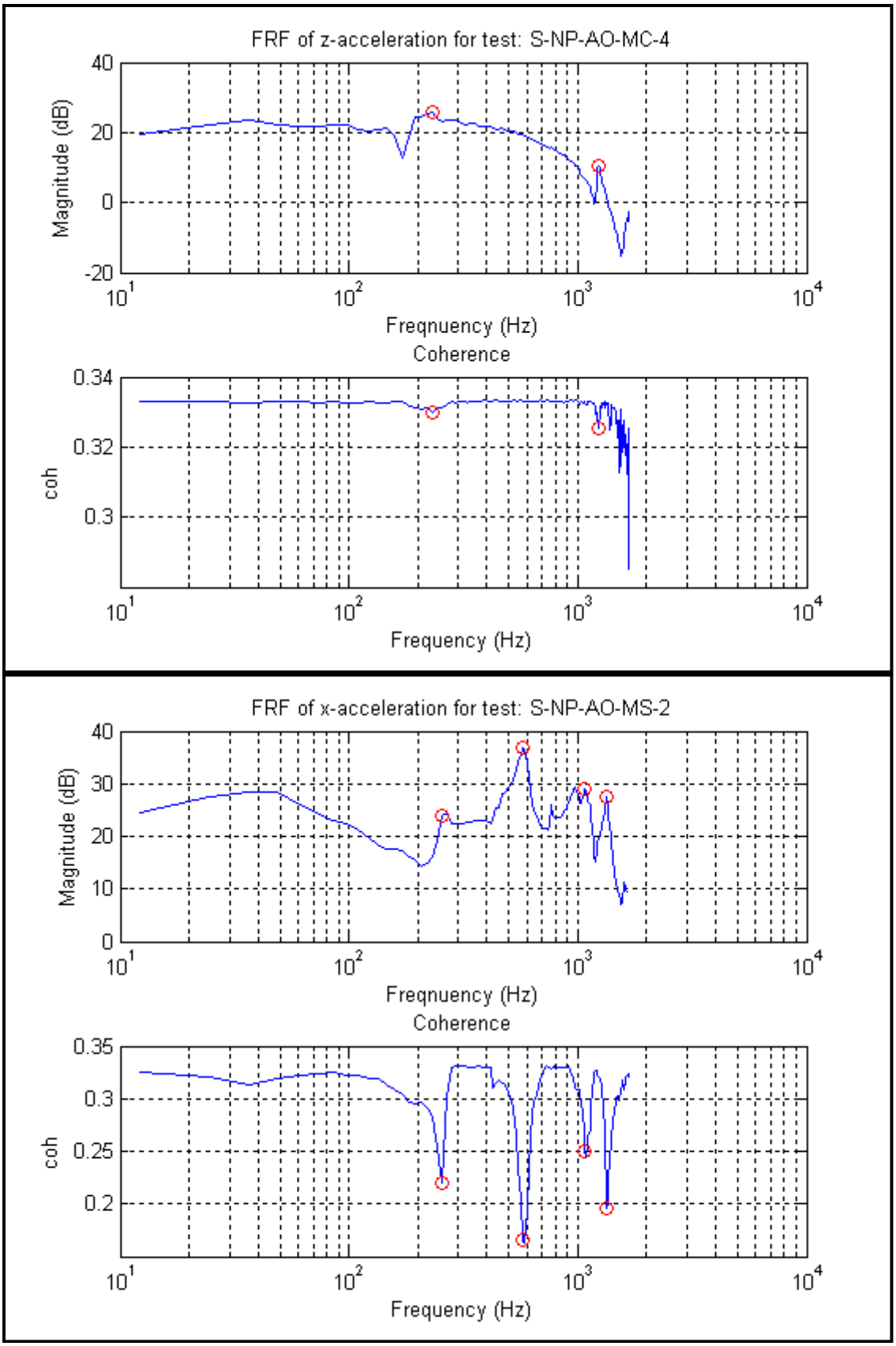
FRF of z-acceleration for test: S-NP-AO-MC-4
Magnitude (dB)
40
20
0
-20
10^1
10^2
10^3
10^4
Freqnuency (Hz)
Coherence
coh
0.34
0.32
0.3
Frequency (Hz)
FRF of x-acceleration for test: S-NP-AO-MS-2
Magnitude (dB)
40
30
20
10
0
Freqnuency (Hz)
Coherence
coh
0.35
0.3
0.25
0.2
Frequency (Hz)

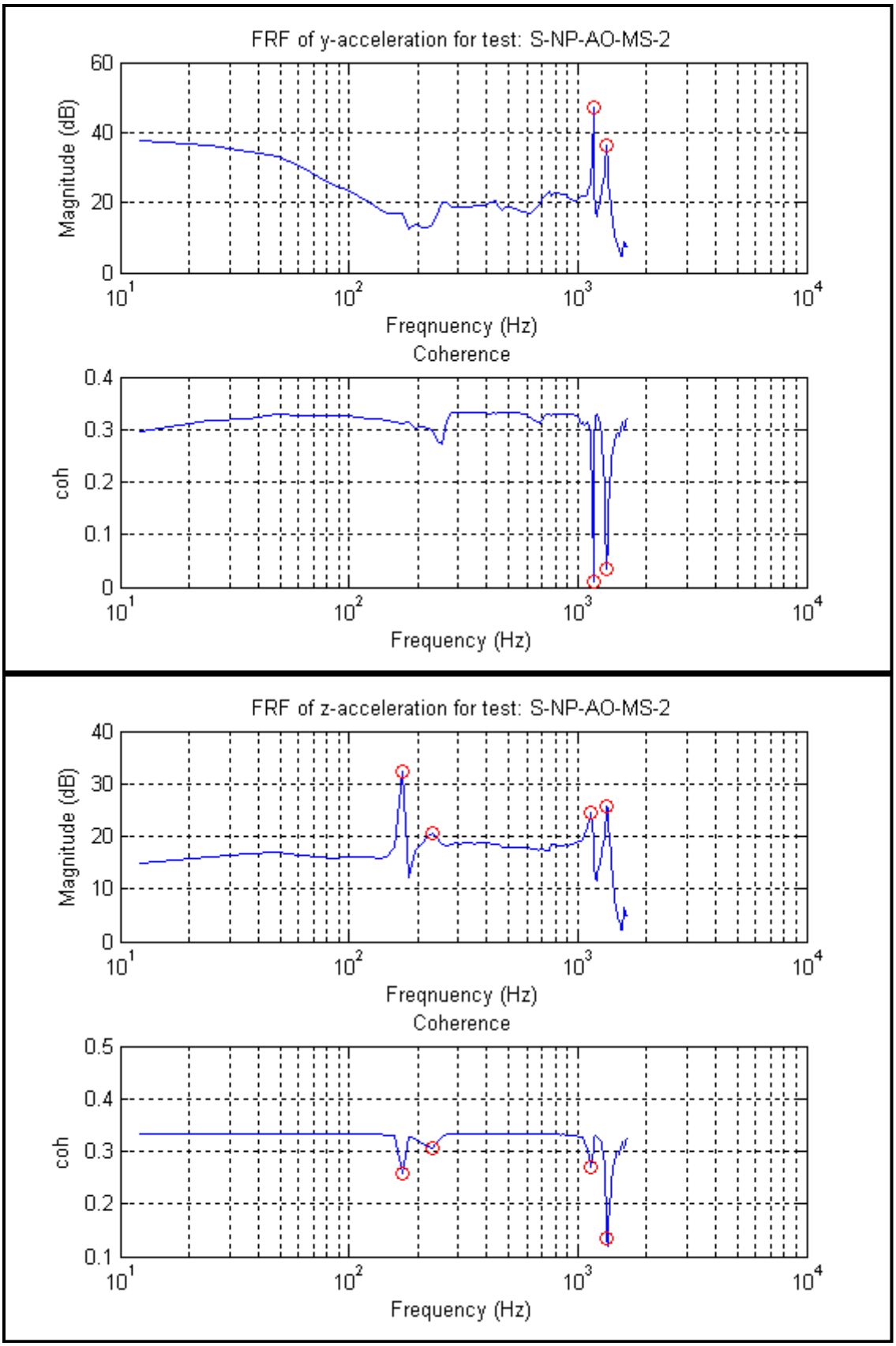
FRF of y-acceleration for test: S-NP-AO-MS-2
Magnitude (dB)
Freqnuency (Hz)
Coherence
coh
Frequency (Hz)
FRF of z-acceleration for test: S-NP-AO-MS-2
Magnitude (dB)
Freqnuency (Hz)
Coherence
coh
Frequency (Hz)

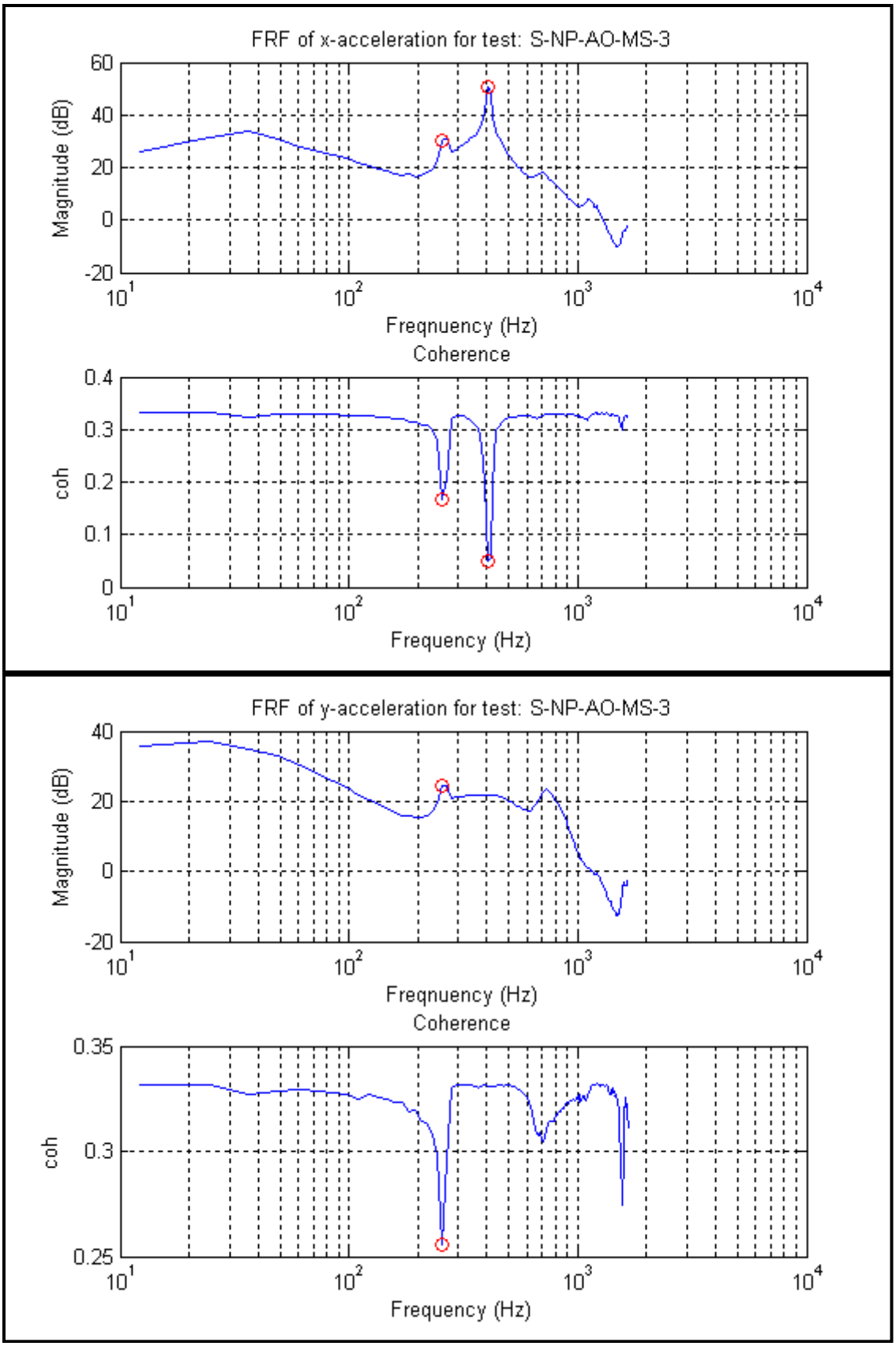
FRF of x-acceleration for test: S-NP-AO-MS-3
Magnitude (dB)
60
40
20
0
-20
10^1
10^2
10^3
10^4
Freqnuency (Hz)
Coherence
coh
0.4
0.3
0.2
0.1
0
Frequency (Hz)
FRF of y-acceleration for test: S-NP-AO-MS-3
Magnitude (dB)
40
20
0
-20
Freqnuency (Hz)
Coherence
coh
0.35
0.3
0.25
Frequency (Hz)

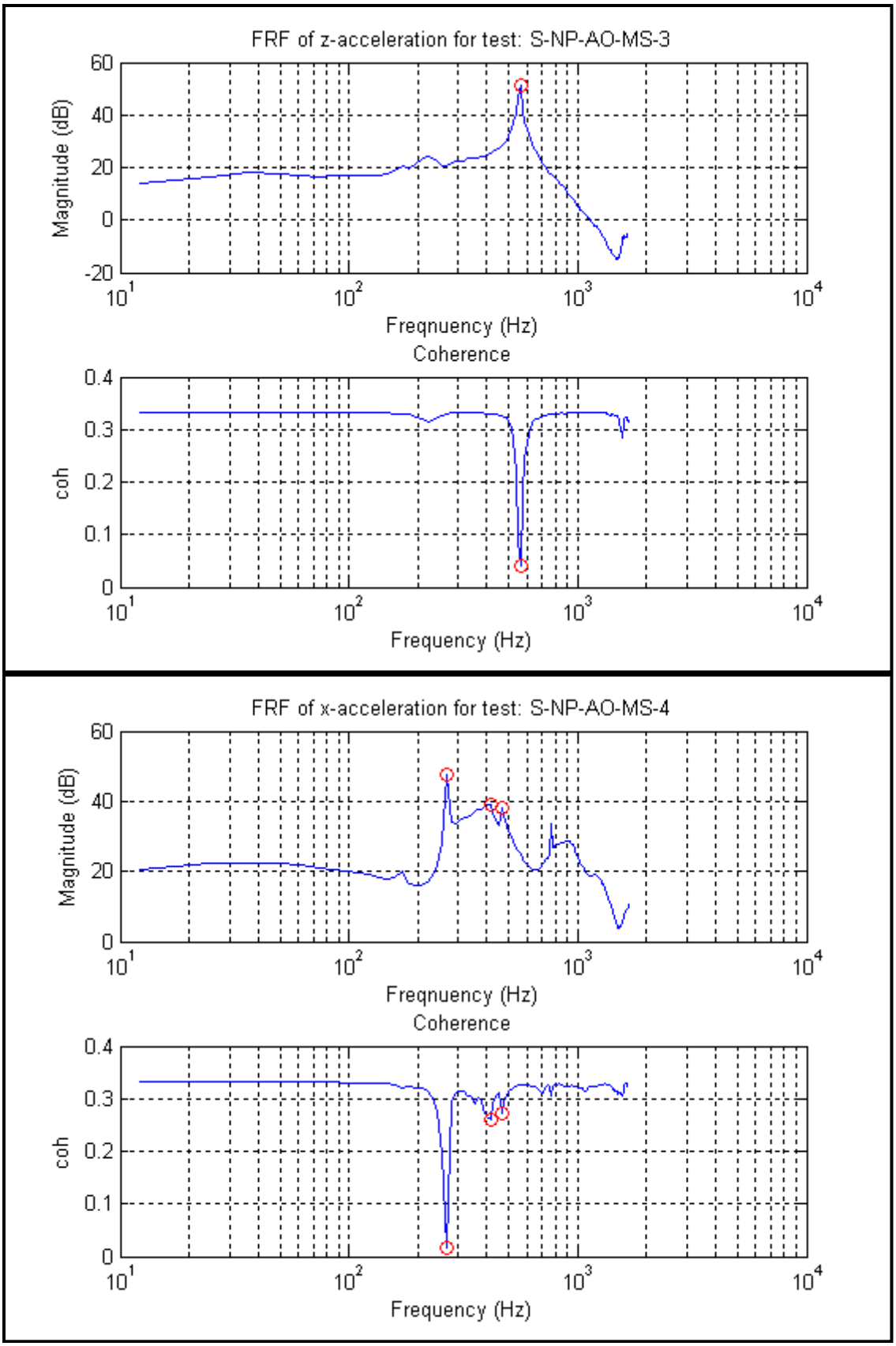
FRF of z-acceleration for test: S-NP-AO-MS-3
Magnitude (dB)
60
40
20
0
-20
10^1
10^2
10^3
10^4
Freqnuency (Hz)
Coherence
coh
0.4
0.3
0.2
0.1
0
Frequency (Hz)
FRF of x-acceleration for test: S-NP-AO-MS-4
Magnitude (dB)
Freqnuency (Hz)
Coherence
coh
Frequency (Hz)

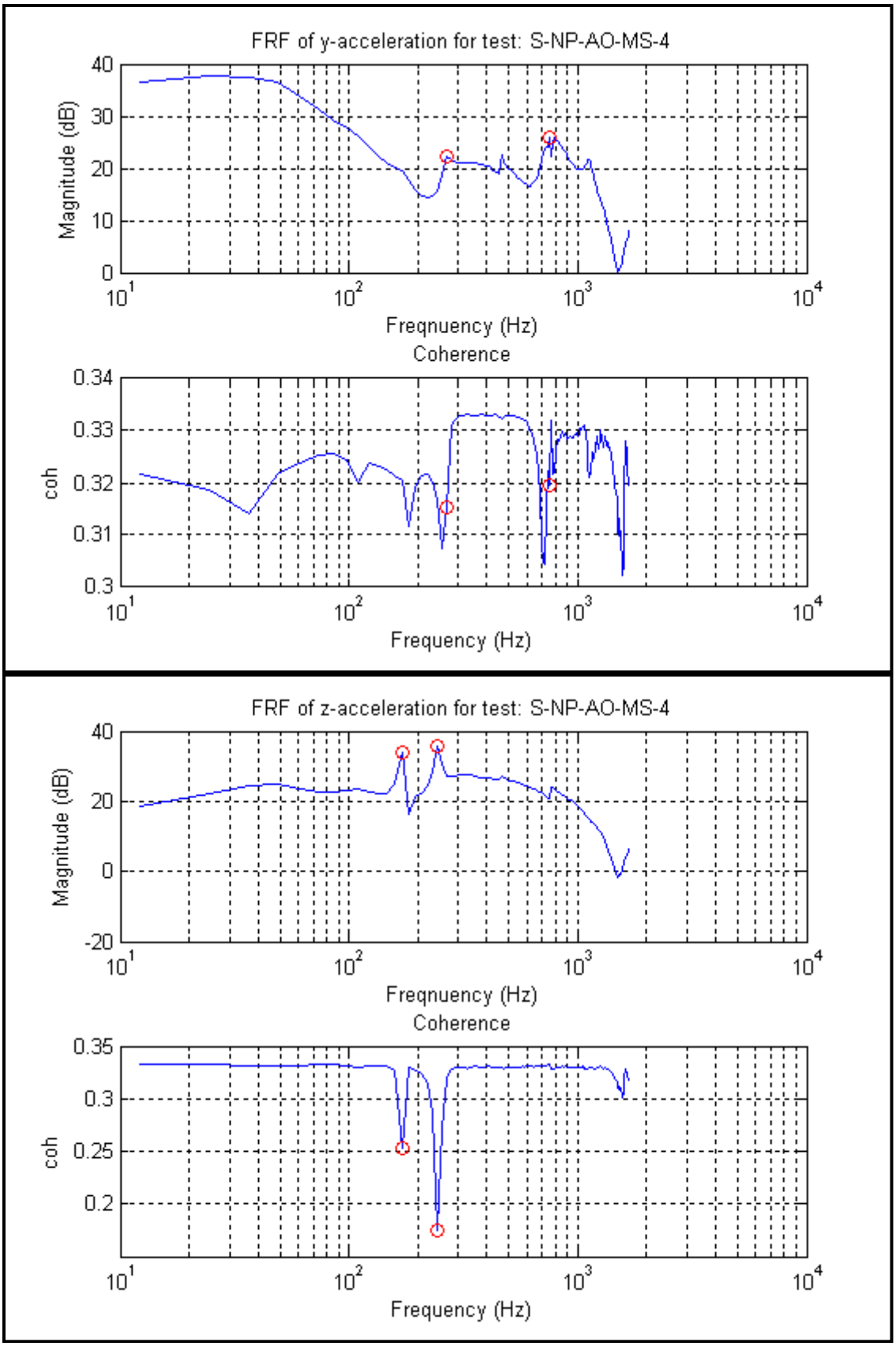
FRF of y-acceleration for test: S-NP-AO-MS-4
Magnitude (dB)
Freqnuency (Hz)
Coherence
coh
Frequency (Hz)
FRF of z-acceleration for test: S-NP-AO-MS-4
Magnitude (dB)
Freqnuency (Hz)
Coherence
coh
Frequency (Hz)

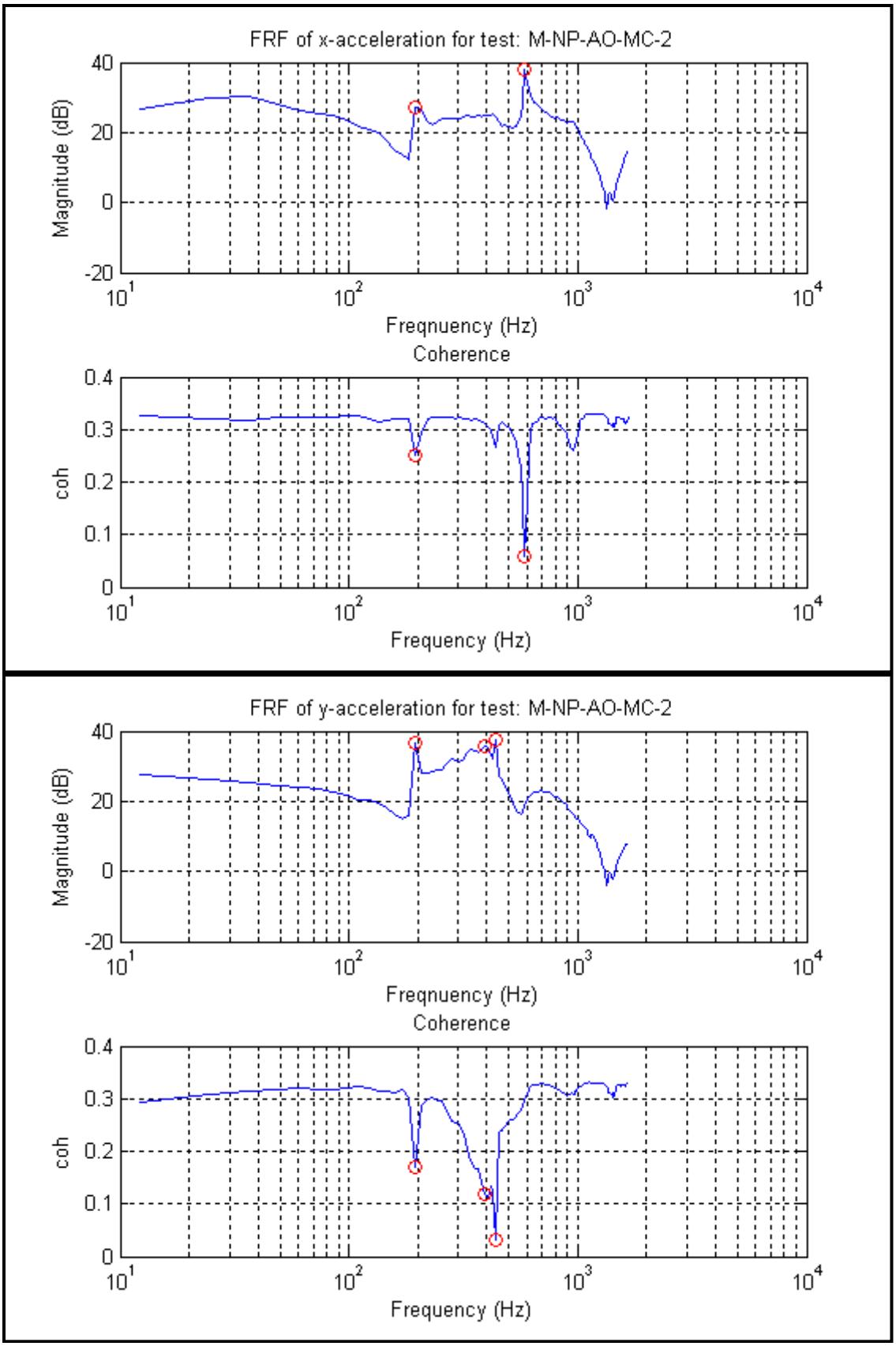
FRF of x-acceleration for test: M-NP-AO-MC-2
Magnitude (dB)
40
20
0
-20
10^1
10^2
10^3
10^4
Freqnuency (Hz)
Coherence
coh
0.4
0.3
0.2
0.1
0
Frequency (Hz)
FRF of y-acceleration for test: M-NP-AO-MC-2
Magnitude (dB)
Freqnuency (Hz)
Coherence
coh
Frequency (Hz)

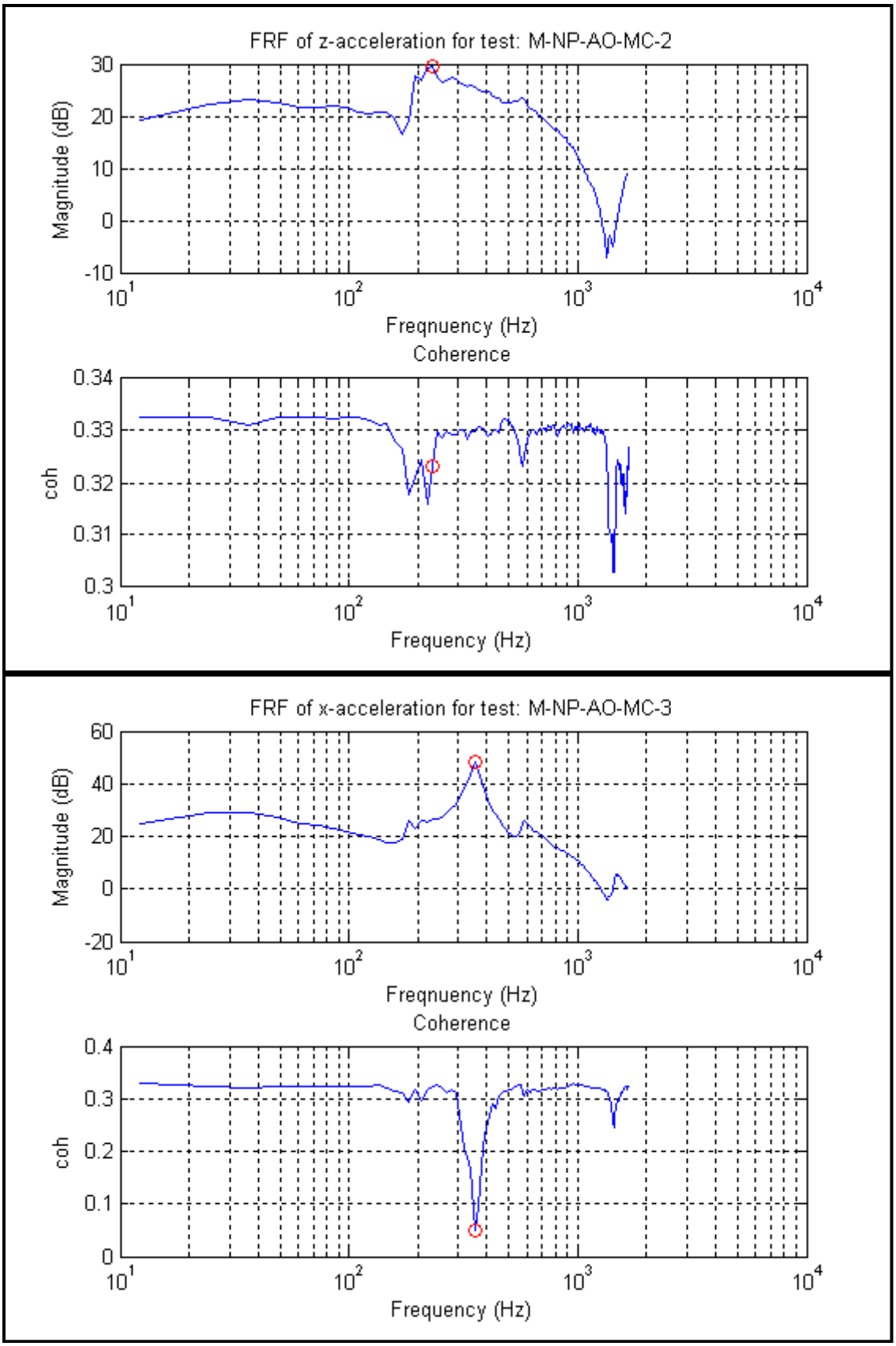
FRF of z-acceleration for test: M-NP-AO-MC-2
Magnitude (dB)
30
20
10
0
-10
10^1
10^2
10^3
10^4
Freqnuency (Hz)
Coherence
coh
0.34
0.33
0.32
0.31
0.3
Frequency (Hz)
FRF of x-acceleration for test: M-NP-AO-MC-3
Magnitude (dB)
60
40
20
0
-20
Freqnuency (Hz)
Coherence
coh
0.4
0.3
0.2
0.1
0
Frequency (Hz)

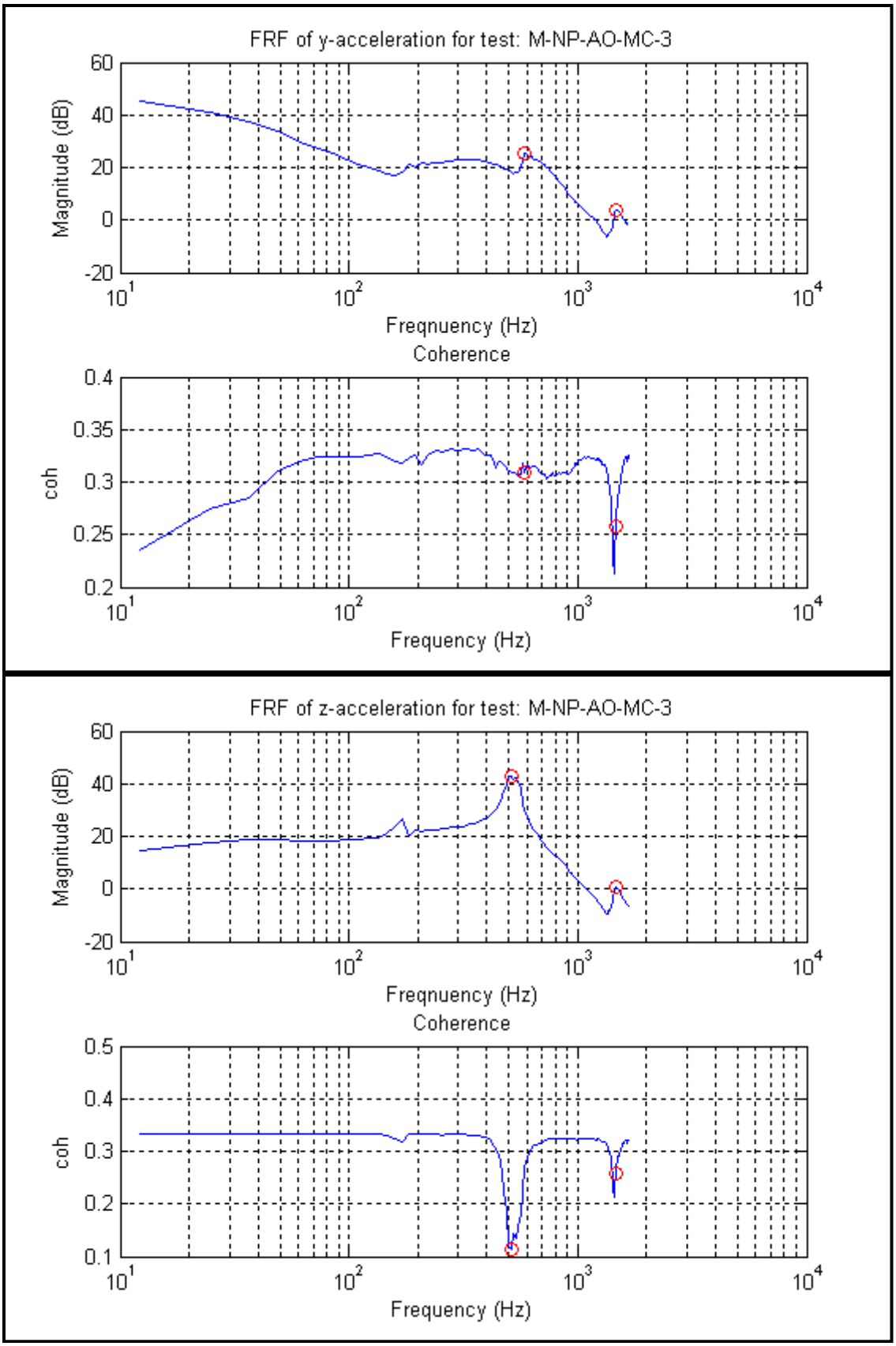
FRF of y-acceleration for test: M-NP-AO-MC-3
Magnitude (dB)
Freqnuency (Hz)
Coherence
coh
Frequency (Hz)
FRF of z-acceleration for test: M-NP-AO-MC-3
Magnitude (dB)
Freqnuency (Hz)
Coherence
coh
Frequency (Hz)

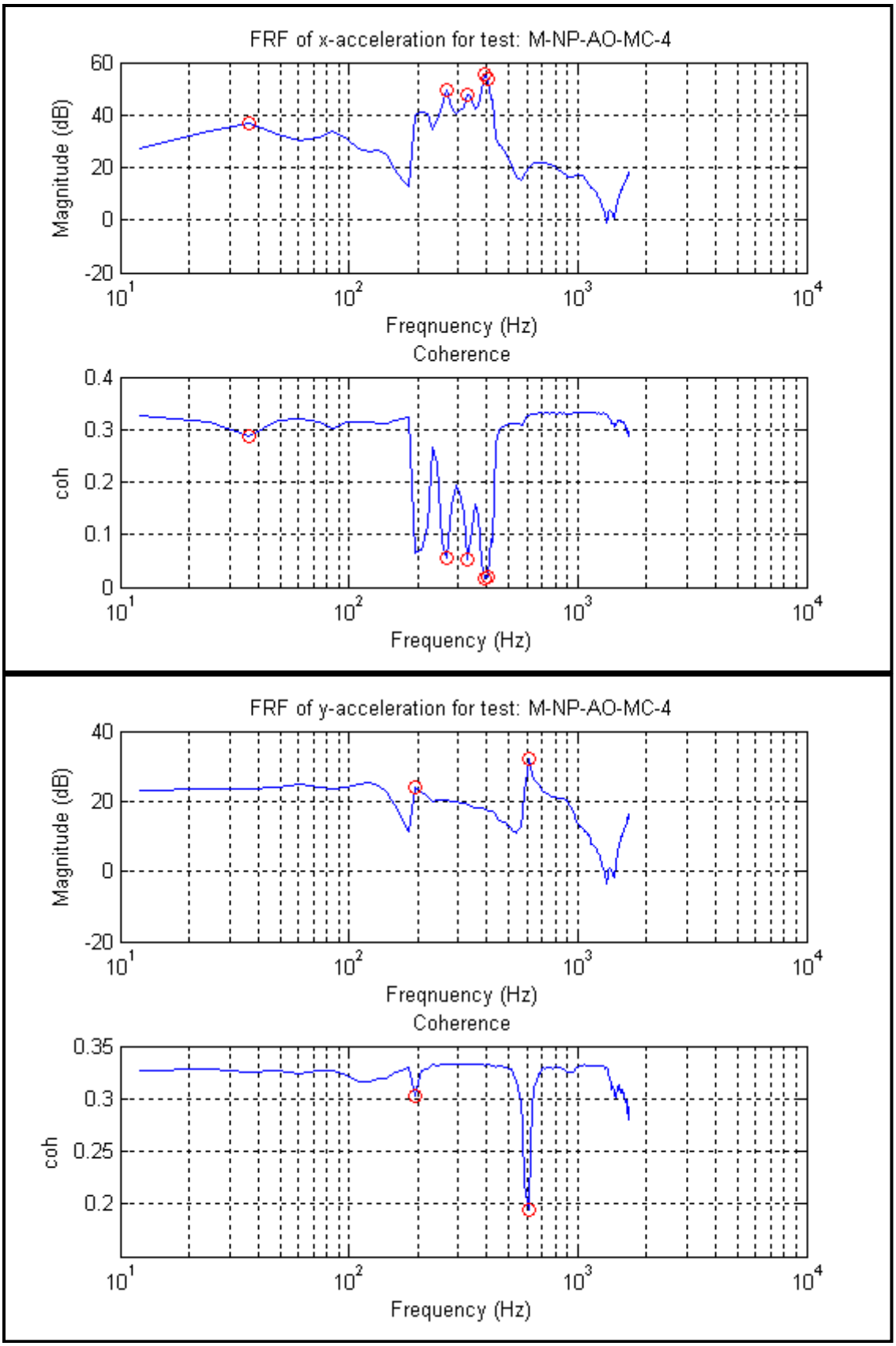
FRF of x-acceleration for test: M-NP-AO-MC-4
Magnitude (dB)
60
40
20
0
-20
10^1
10^2
10^3
10^4
Freqnuency (Hz)
Coherence
coh
0.4
0.3
0.2
0.1
0
Frequency (Hz)
FRF of y-acceleration for test: M-NP-AO-MC-4
Magnitude (dB)
40
20
0
-20
Freqnuency (Hz)
Coherence
coh
0.35
0.3
0.25
0.2
Frequency (Hz)

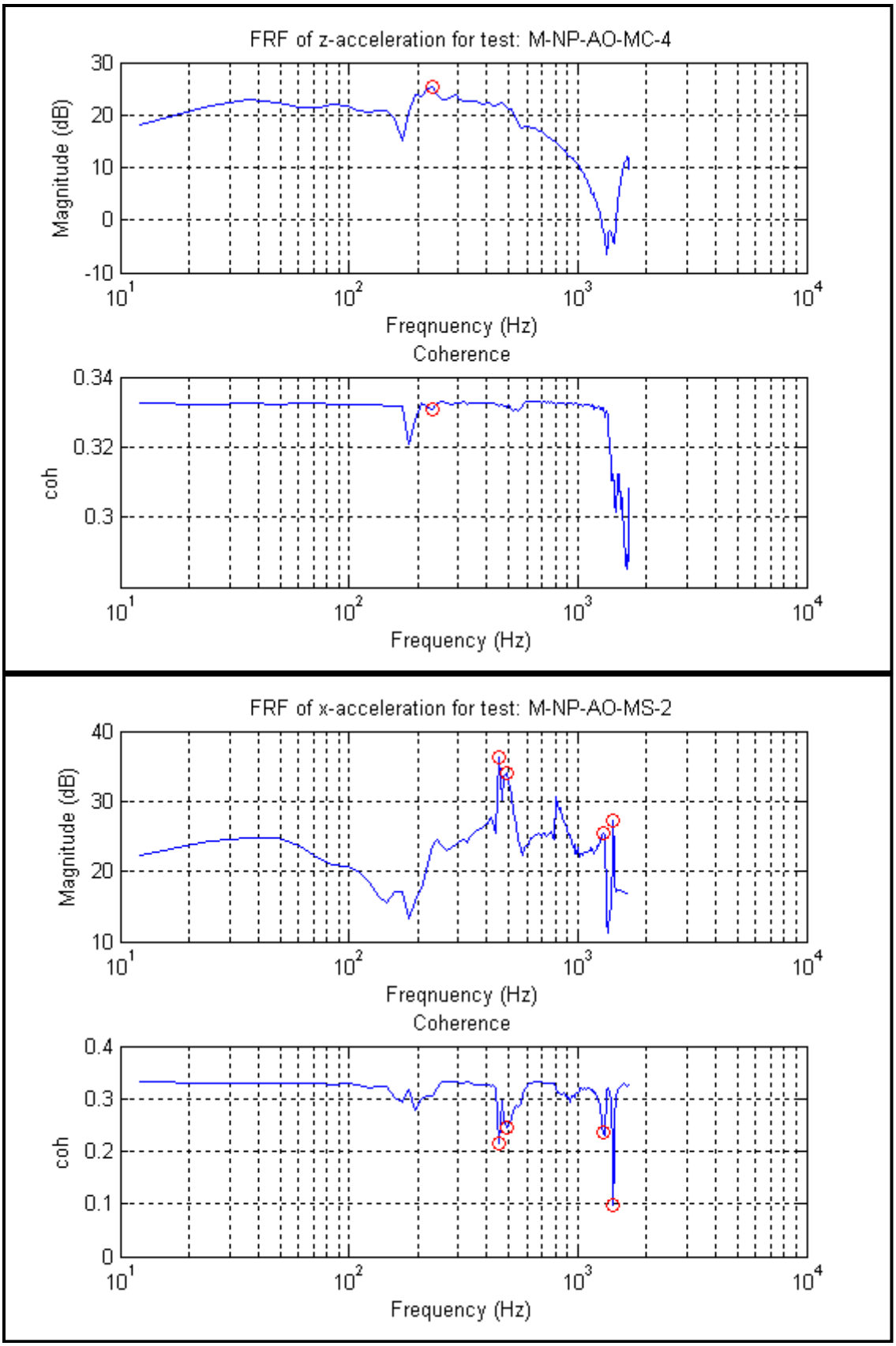
FRF of z-acceleration for test: M-NP-AO-MC-4
Magnitude (dB)
30
20
10
0
-10
10^1
10^2
10^3
10^4
Freqnuency (Hz)
Coherence
coh
0.34
0.32
0.3
Frequency (Hz)
FRF of x-acceleration for test: M-NP-AO-MS-2
Magnitude (dB)
40
30
20
10
Freqnuency (Hz)
Coherence
coh
0.4
0.3
0.2
0.1
0
Frequency (Hz)

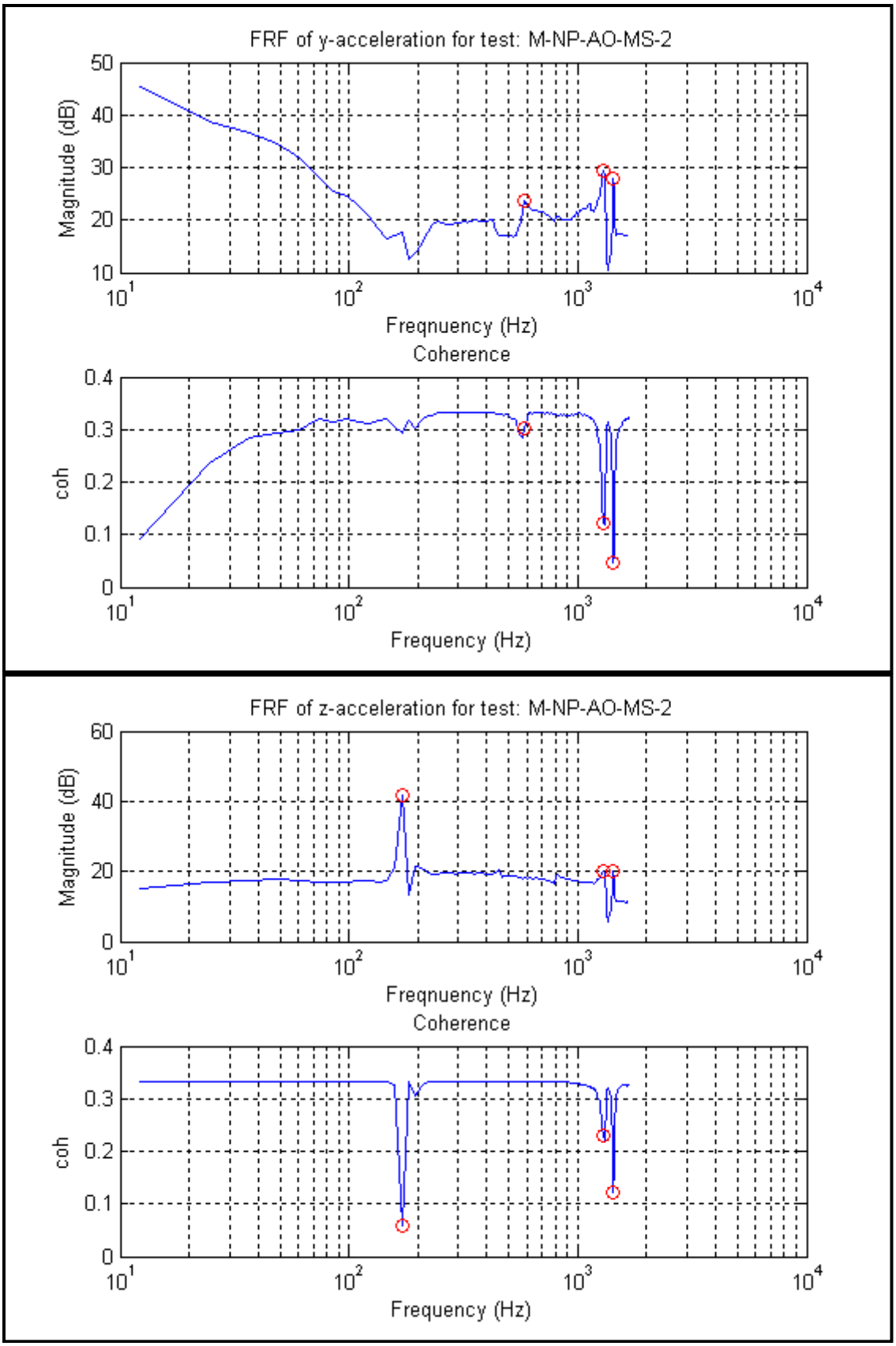
FRF of y-acceleration for test: M-NP-AO-MS-2
Magnitude (dB)
Freqnuency (Hz)
Coherence
coh
Frequency (Hz)
FRF of z-acceleration for test: M-NP-AO-MS-2
Magnitude (dB)
Freqnuency (Hz)
Coherence
coh
Frequency (Hz)

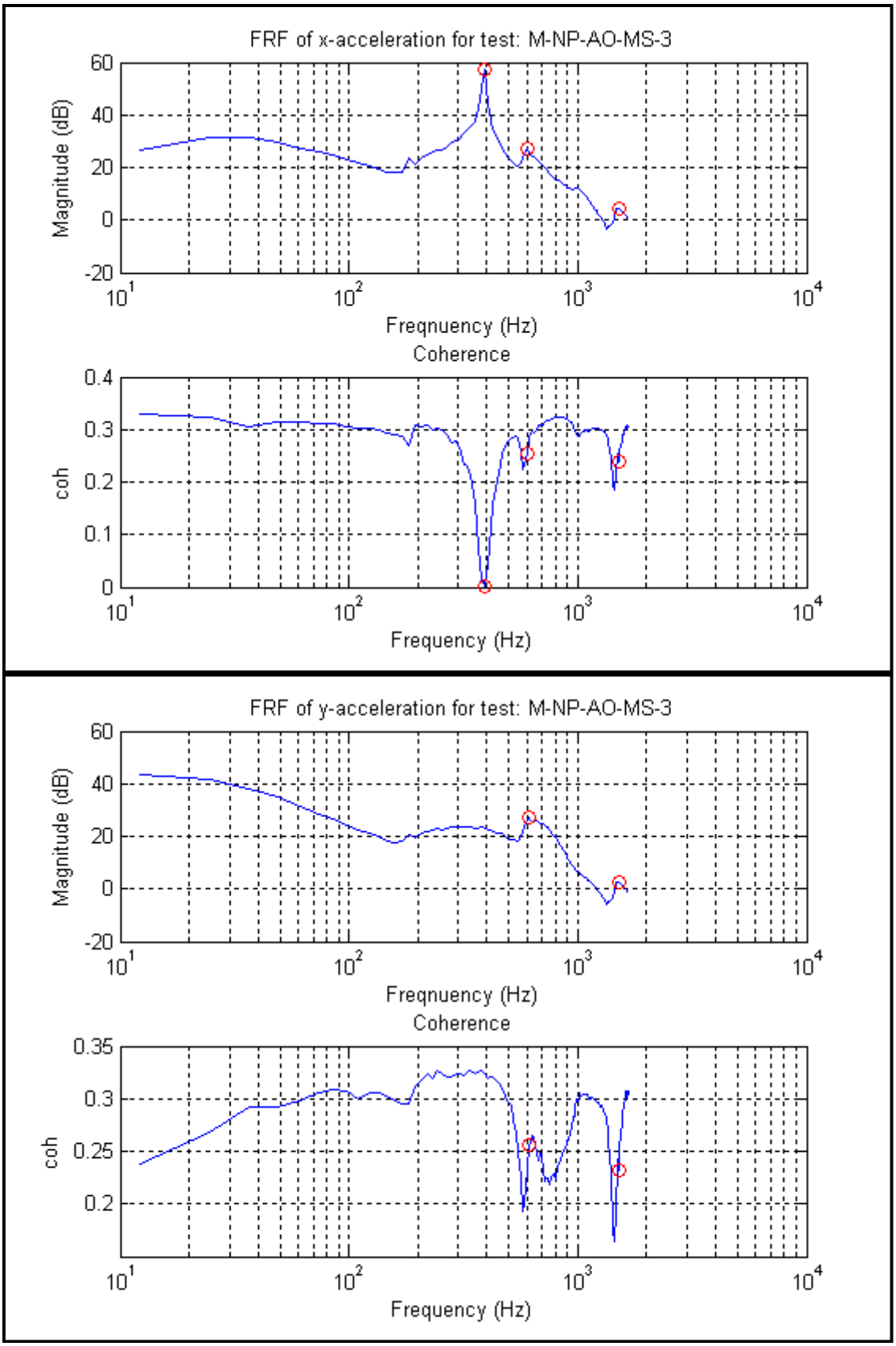
FRF of x-acceleration for test: M-NP-AO-MS-3
Magnitude (dB)
60
40
20
0
-20
10^1
10^2
10^3
10^4
Freqnuency (Hz)
Coherence
coh
0.4
0.3
0.2
0.1
0
Frequency (Hz)
FRF of y-acceleration for test: M-NP-AO-MS-3
Magnitude (dB)
Freqnuency (Hz)
Coherence
coh
0.35
0.3
0.25
0.2
Frequency (Hz)

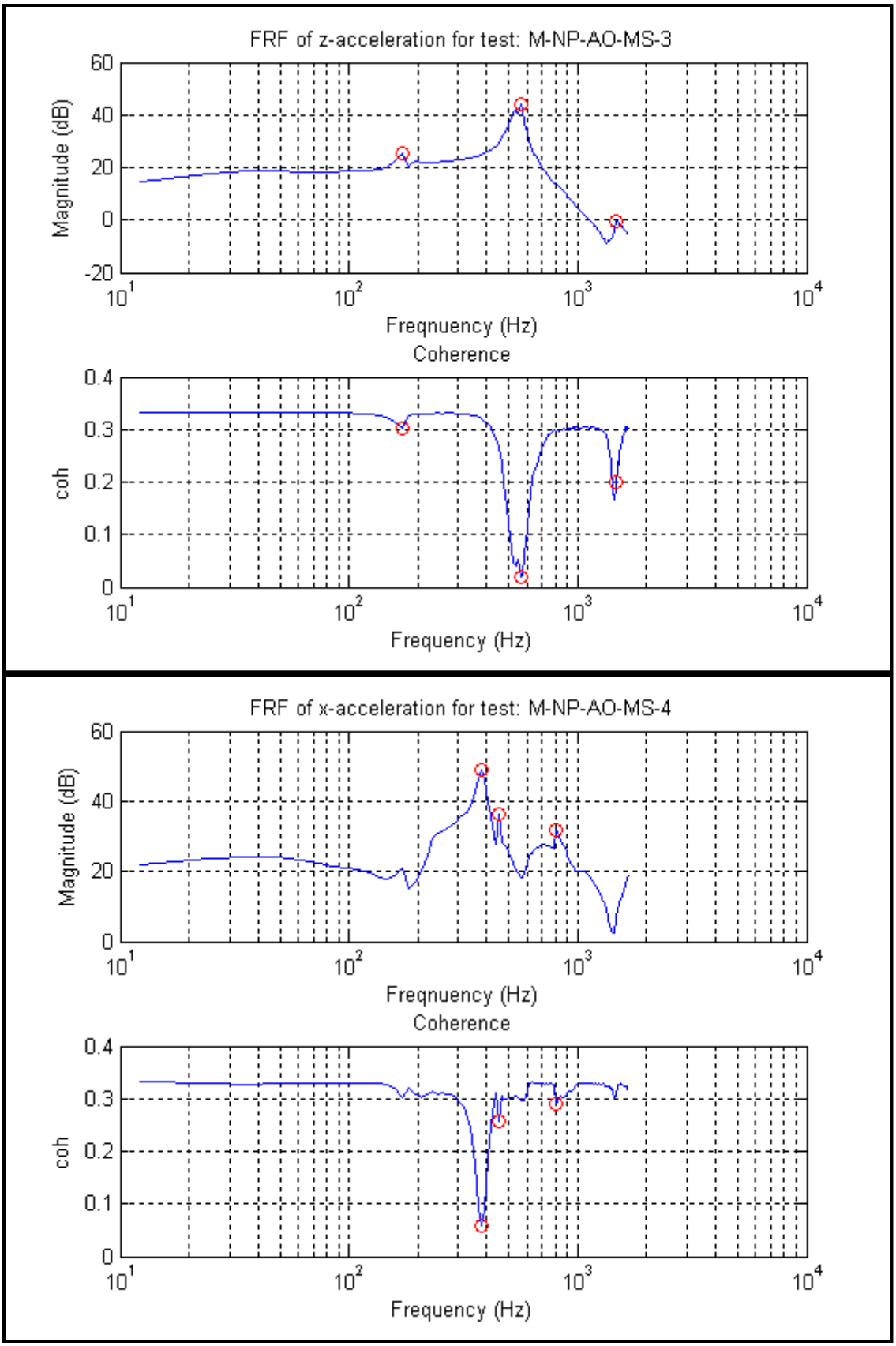
FRF of z-acceleration for test: M-NP-AO-MS-3
Magnitude (dB)
Freqnuency (Hz)
Coherence
coh
Frequency (Hz)
FRF of x-acceleration for test: M-NP-AO-MS-4
Magnitude (dB)
Freqnuency (Hz)
Coherence
coh
Frequency (Hz)

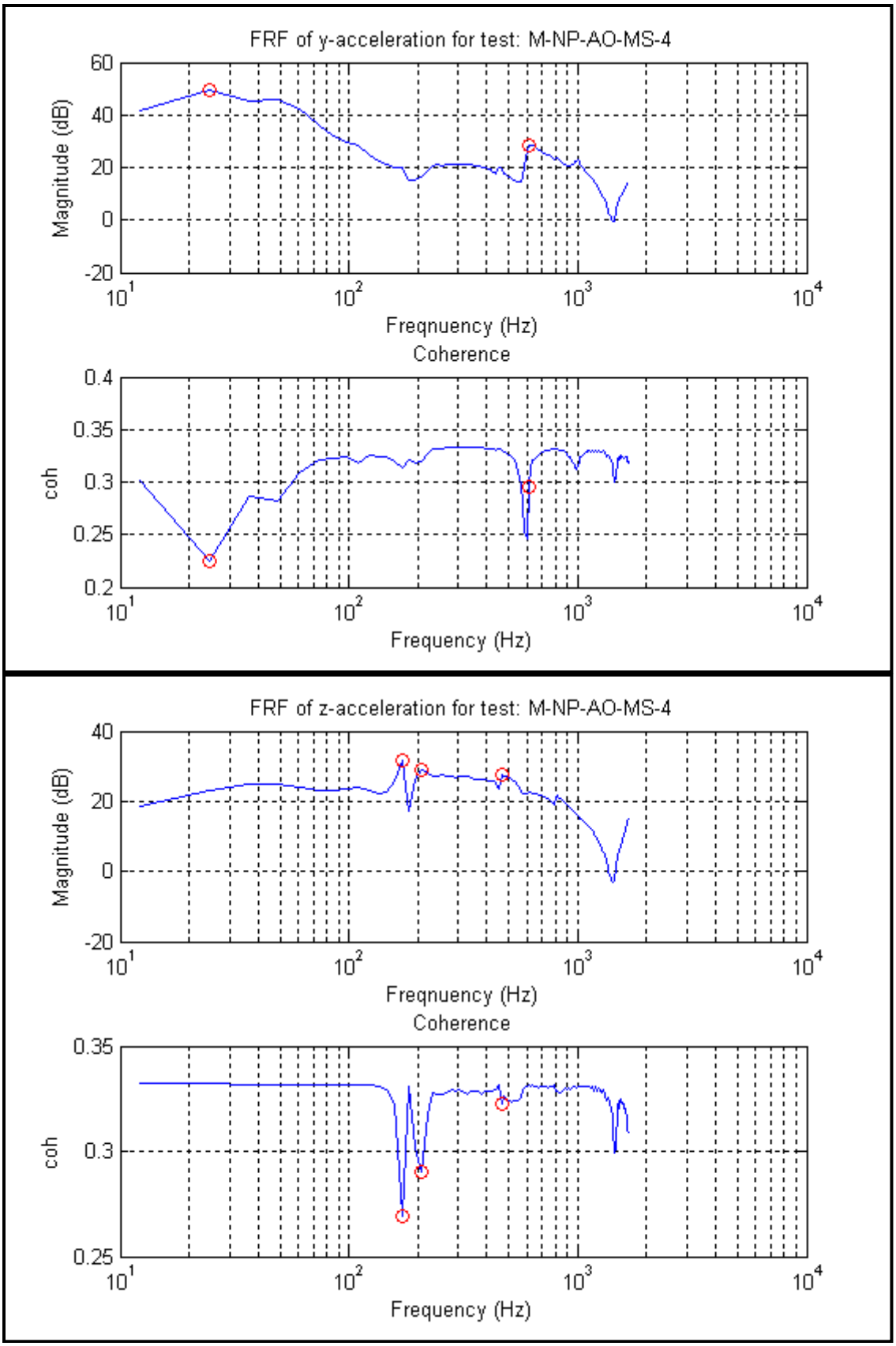
FRF of y-acceleration for test: M-NP-AO-MS-4
Magnitude (dB)
Freqnuency (Hz)
Coherence
coh
Frequency (Hz)
FRF of z-acceleration for test: M-NP-AO-MS-4
Magnitude (dB)
Freqnuency (Hz)
Coherence
coh
Frequency (Hz)

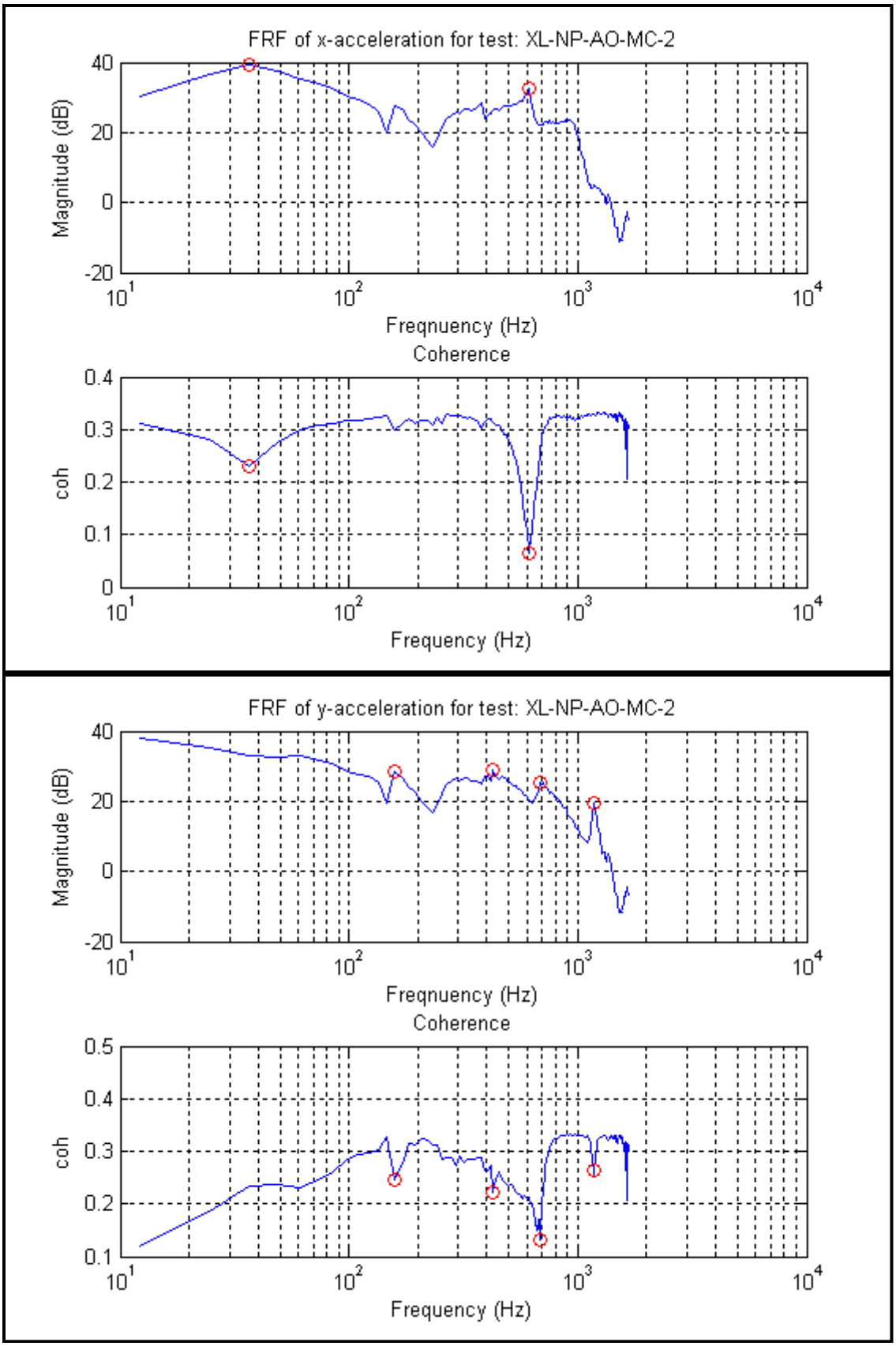
FRF of x-acceleration for test: XL-NP-AO-MC-2
Magnitude (dB)
40
20
0
-20
10^1
10^2
10^3
10^4
Freqnuency (Hz)
Coherence
coh
0.4
0.3
0.2
0.1
0
Frequency (Hz)
FRF of y-acceleration for test: XL-NP-AO-MC-2
Magnitude (dB)
Freqnuency (Hz)
Coherence
coh
0.5
0.4
0.3
0.2
0.1
Frequency (Hz)

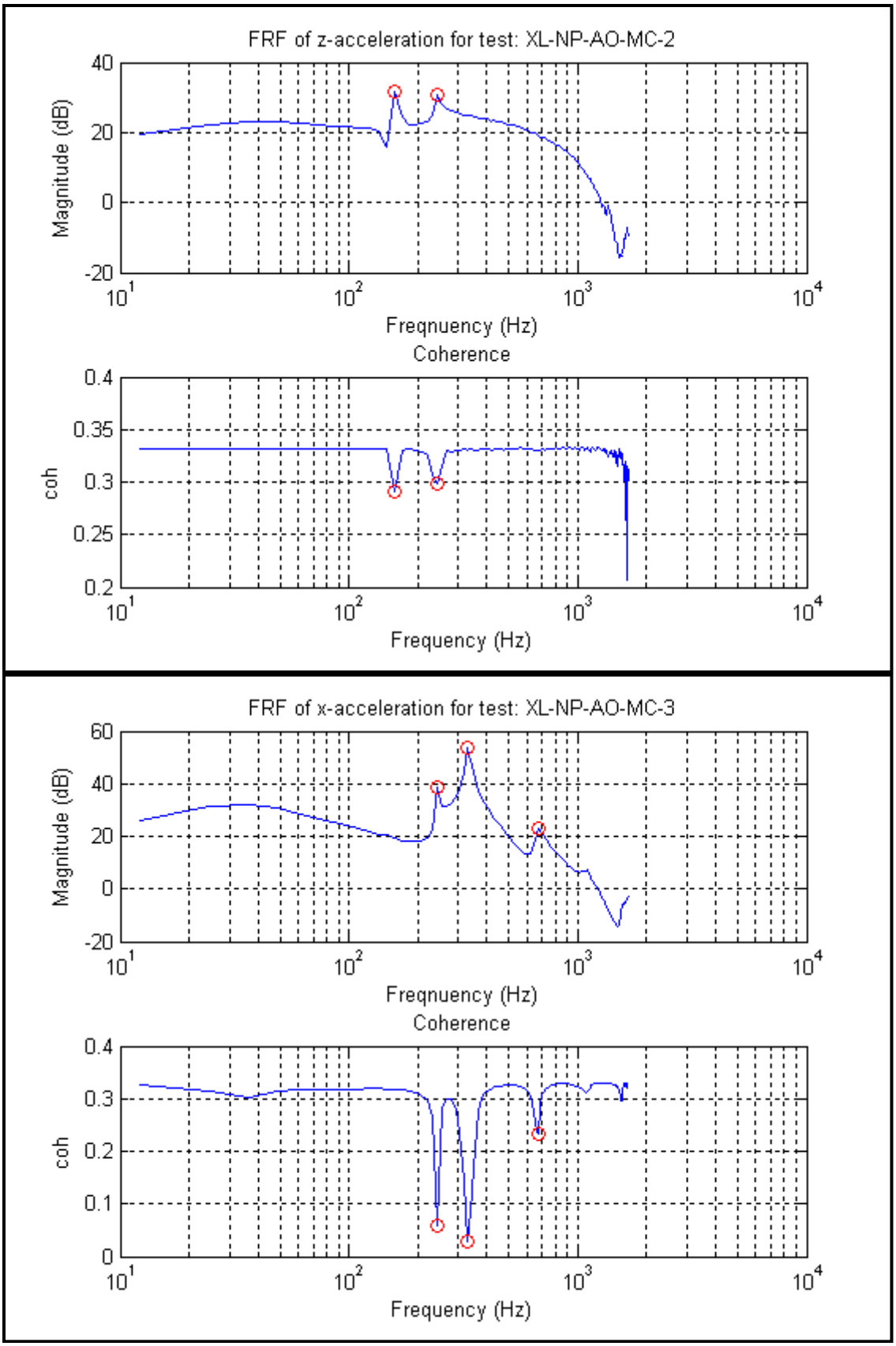
FRF of z-acceleration for test: XL-NP-AO-MC-2
Magnitude (dB)
Freqnuency (Hz)
Coherence
coh
Frequency (Hz)
FRF of x-acceleration for test: XL-NP-AO-MC-3
Magnitude (dB)
Freqnuency (Hz)
Coherence
coh
Frequency (Hz)

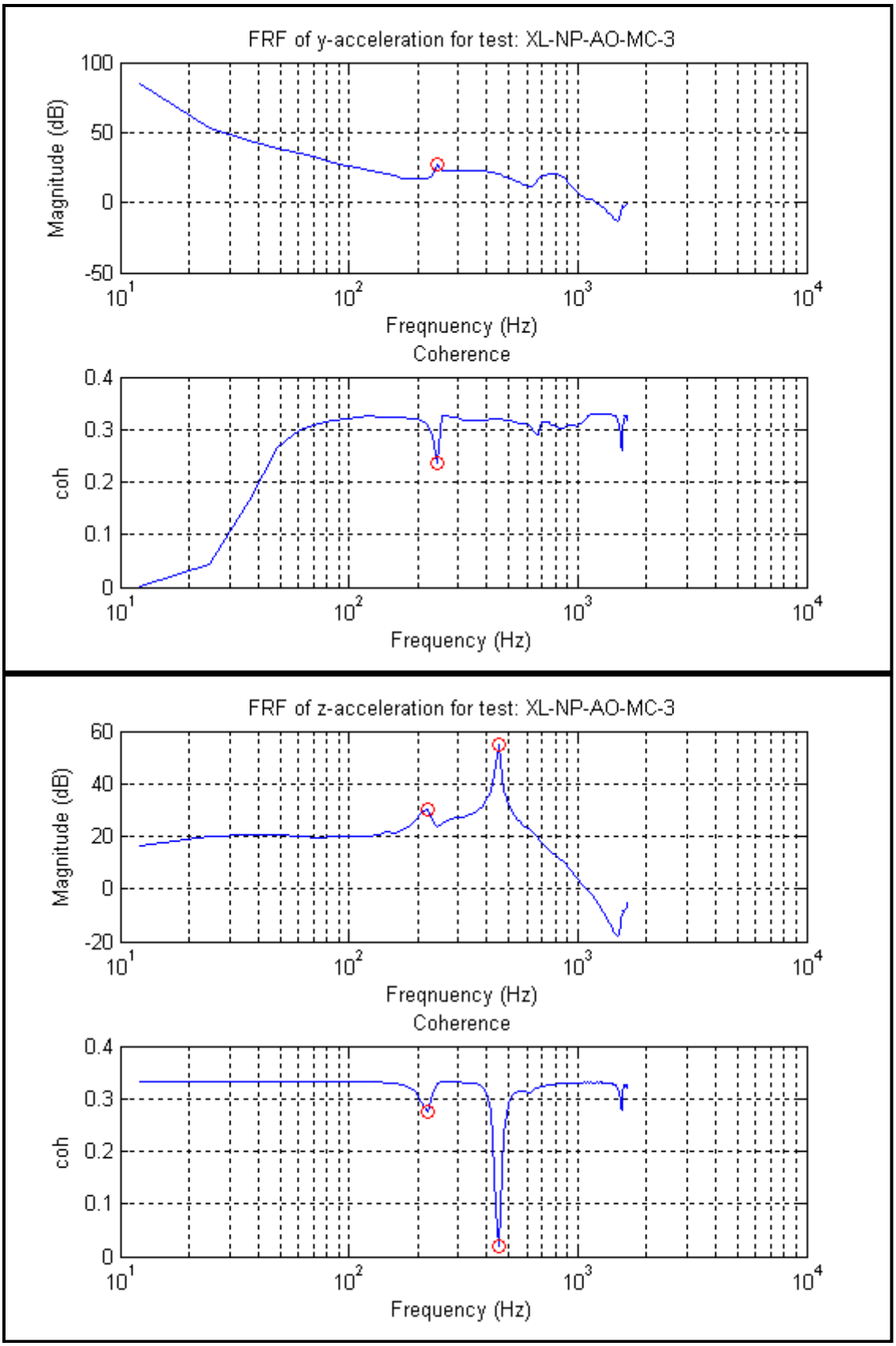
FRF of y-acceleration for test: XL-NP-AO-MC-3
Magnitude (dB)
Freqnuency (Hz)
Coherence
coh
Frequency (Hz)
FRF of z-acceleration for test: XL-NP-AO-MC-3
Magnitude (dB)
Freqnuency (Hz)
Coherence
coh
Frequency (Hz)

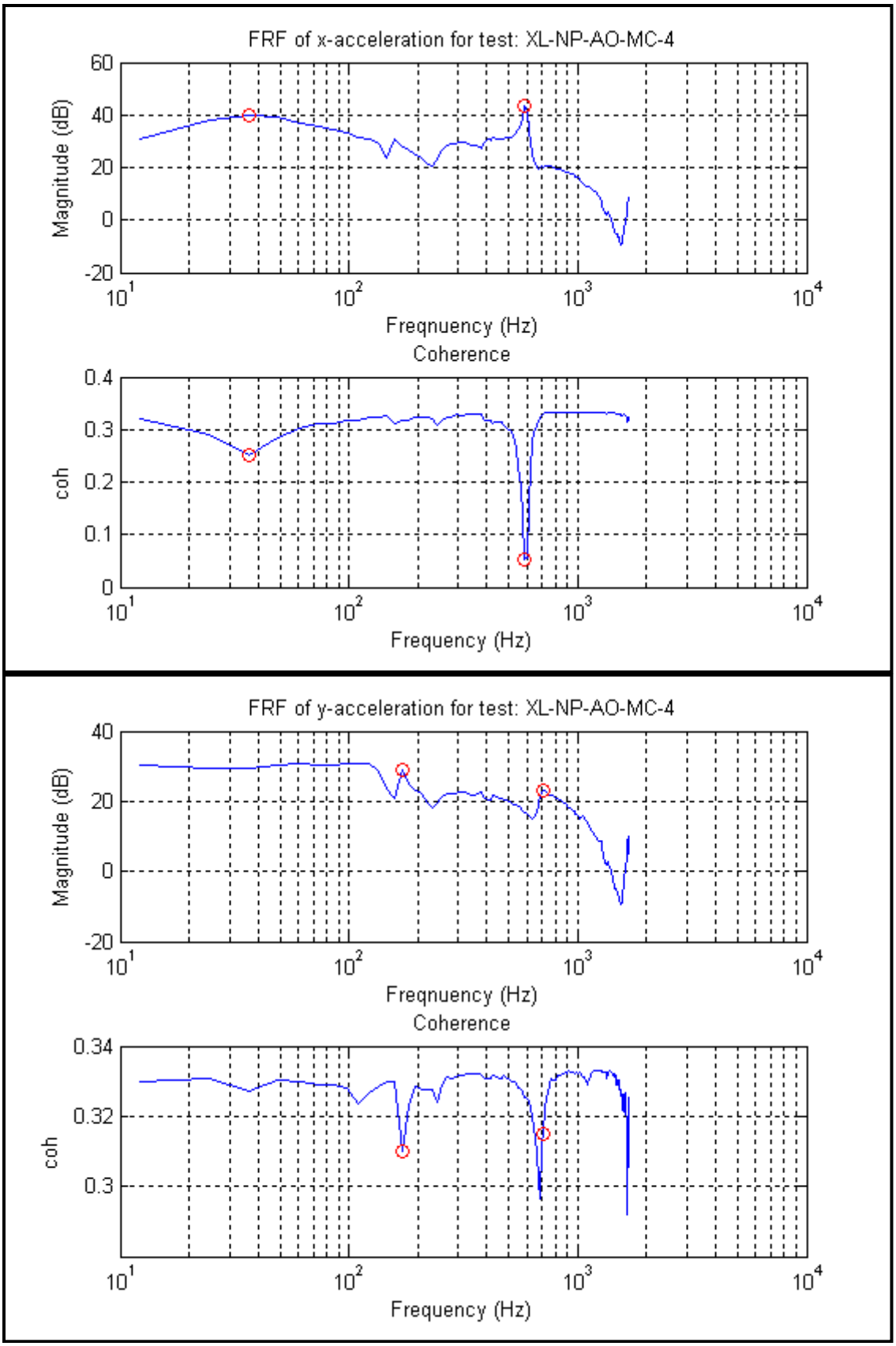
FRF of x-acceleration for test: XL-NP-AO-MC-4
Magnitude (dB)
60
40
20
0
-20
10^1
10^2
10^3
10^4
Freqnuency (Hz)
Coherence
coh
0.4
0.3
0.2
0.1
0
Frequency (Hz)
FRF of y-acceleration for test: XL-NP-AO-MC-4
Magnitude (dB)
40
20
0
-20
Freqnuency (Hz)
Coherence
coh
0.34
0.32
0.3
Frequency (Hz)

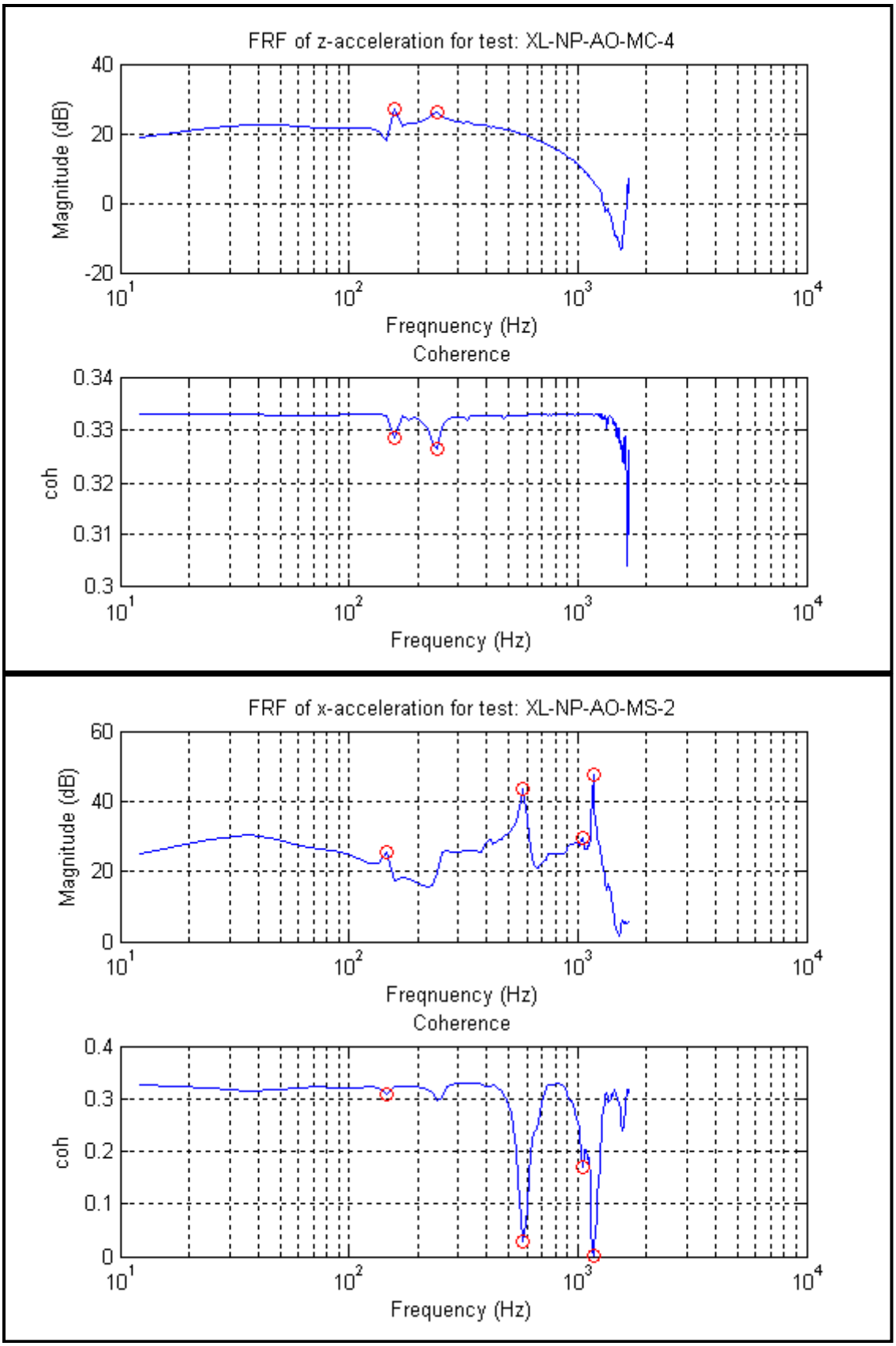
FRF of z-acceleration for test: XL-NP-AO-MC-4
Magnitude (dB)
40
20
0
-20
10^1
10^2
10^3
10^4
Freqnuency (Hz)
Coherence
coh
0.34
0.33
0.32
0.31
0.3
Frequency (Hz)
FRF of x-acceleration for test: XL-NP-AO-MS-2
Magnitude (dB)
60
40
20
0
Freqnuency (Hz)
Coherence
coh
0.4
0.3
0.2
0.1
0
Frequency (Hz)

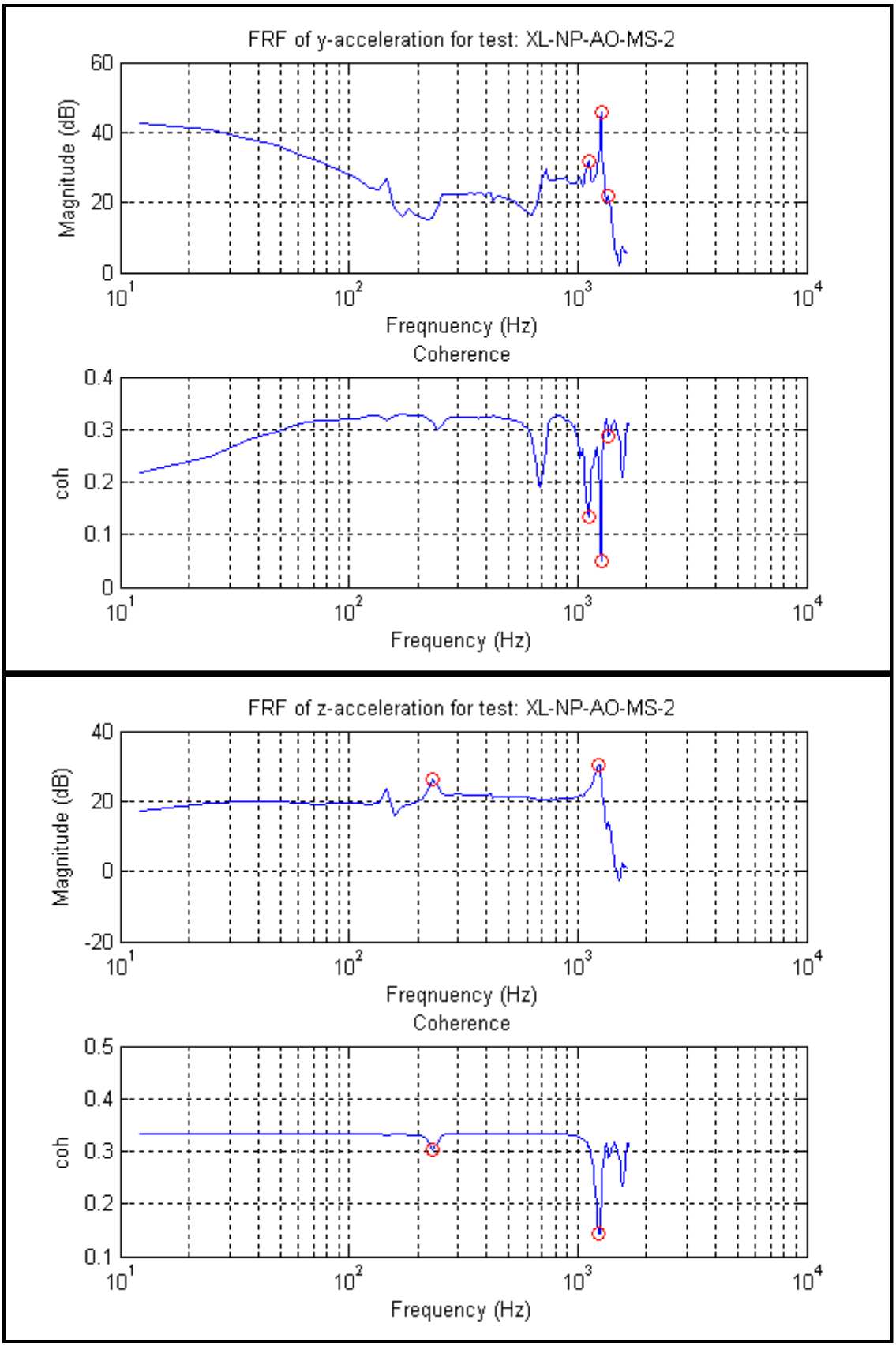
FRF of y-acceleration for test: XL-NP-AO-MS-2
Magnitude (dB)
Freqnuency (Hz)
Coherence
coh
Frequency (Hz)
FRF of z-acceleration for test: XL-NP-AO-MS-2
Magnitude (dB)
Freqnuency (Hz)
Coherence
coh
Frequency (Hz)

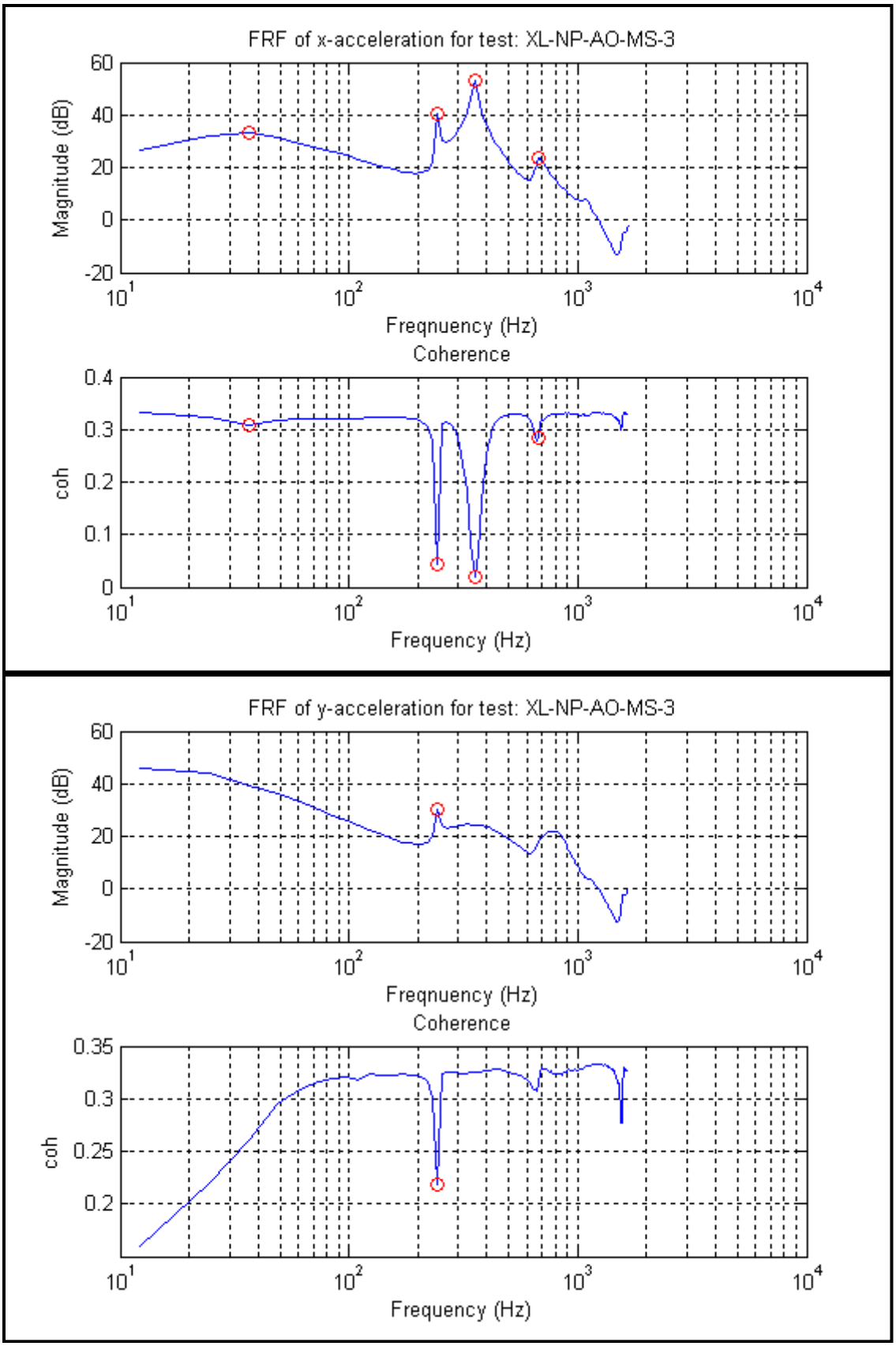
FRF of x-acceleration for test: XL-NP-AO-MS-3
Magnitude (dB)
Freqnuency (Hz)
Coherence
coh
Frequency (Hz)
FRF of y-acceleration for test: XL-NP-AO-MS-3
Magnitude (dB)
Freqnuency (Hz)
Coherence
coh
Frequency (Hz)

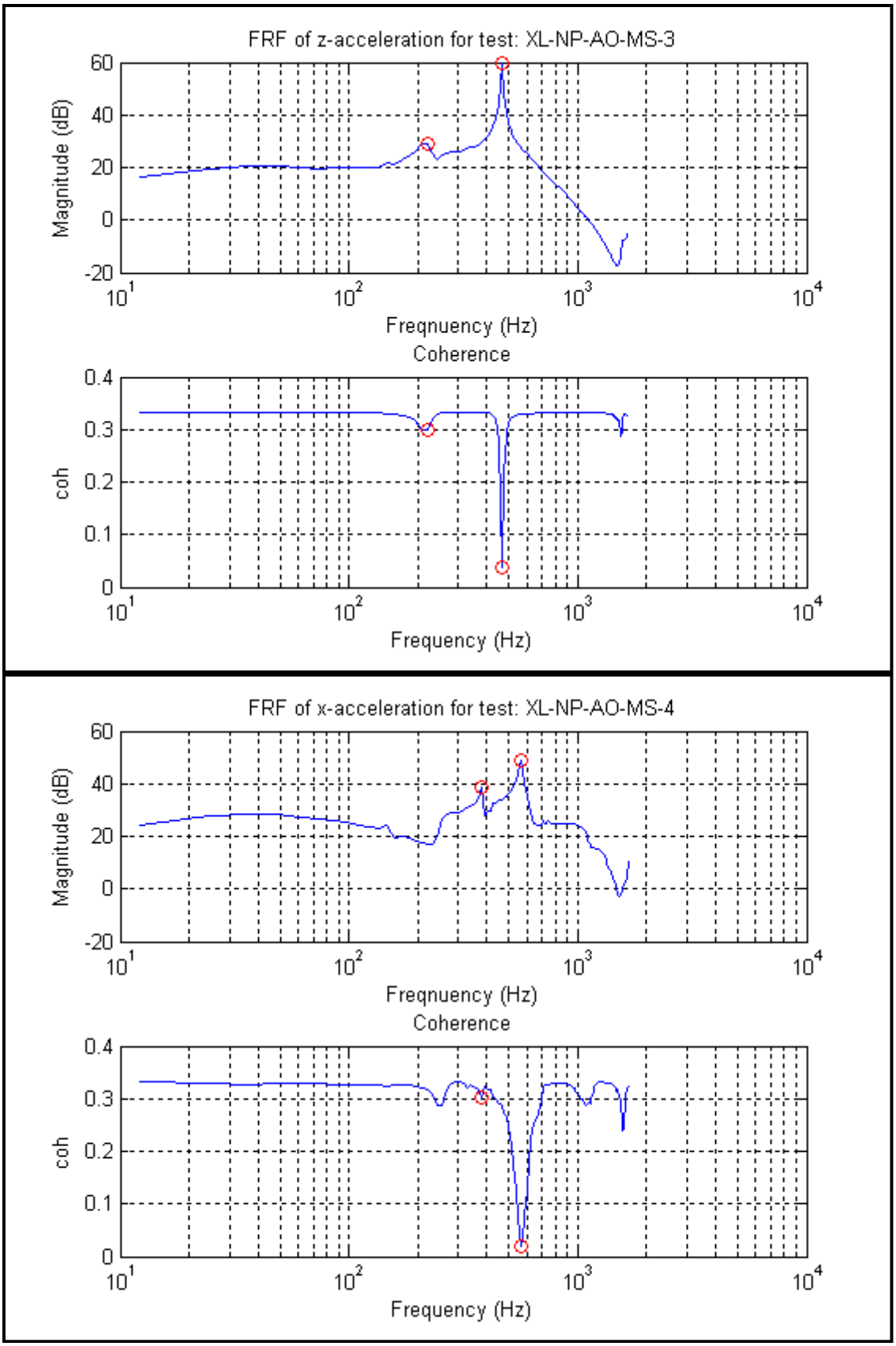
FRF of z-acceleration for test: XL-NP-AO-MS-3
Magnitude (dB)
60
40
20
0
-20
10^1
10^2
10^3
10^4
Freqnuency (Hz)
Coherence
coh
0.4
0.3
0.2
0.1
0
Frequency (Hz)
FRF of x-acceleration for test: XL-NP-AO-MS-4
Magnitude (dB)
Freqnuency (Hz)
Coherence
coh
Frequency (Hz)

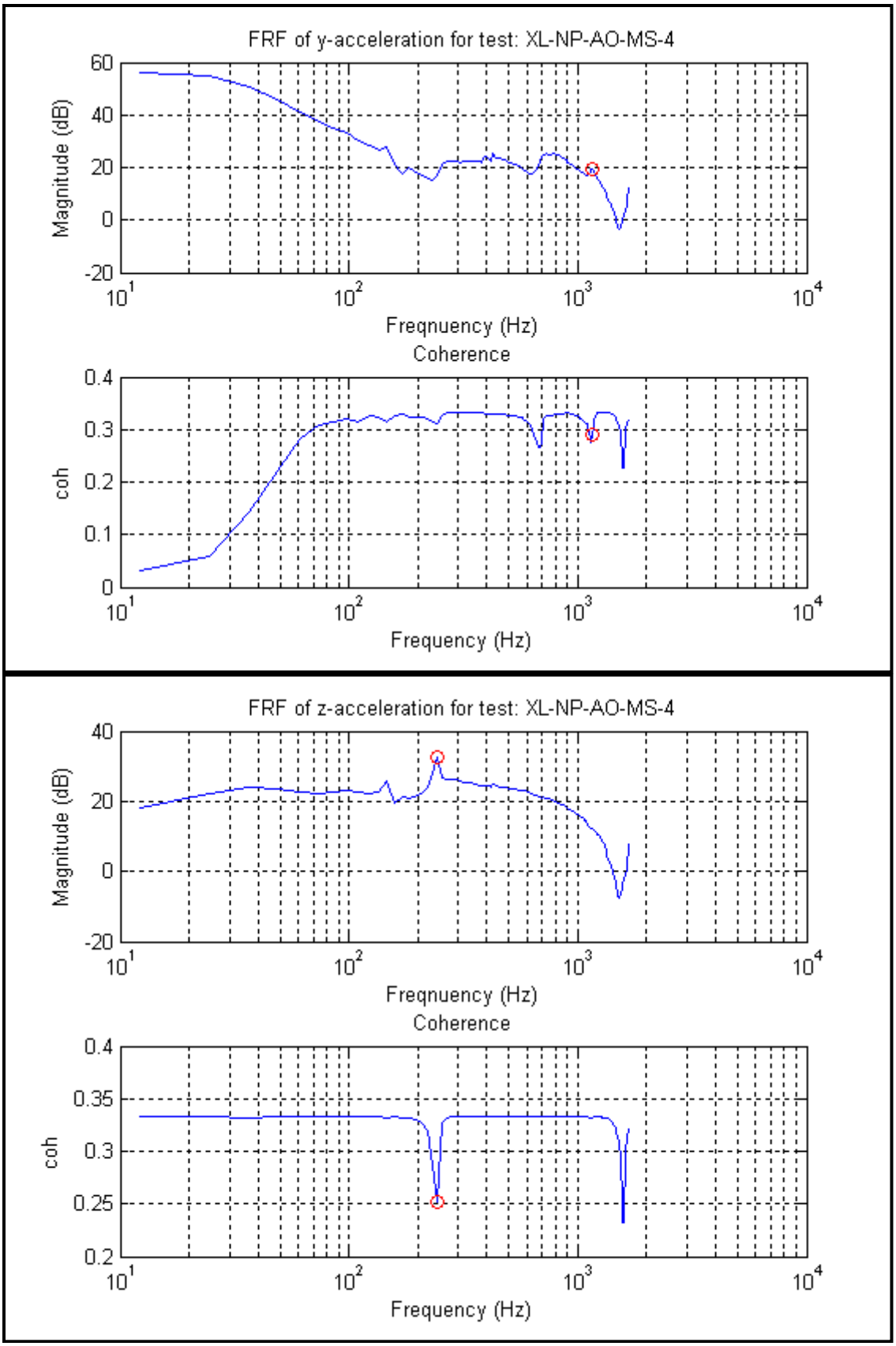
FRF of y-acceleration for test: XL-NP-AO-MS-4
Magnitude (dB)
Freqnuency (Hz)
Coherence
coh
Frequency (Hz)
FRF of z-acceleration for test: XL-NP-AO-MS-4
Magnitude (dB)
Freqnuency (Hz)
Coherence
coh
Frequency (Hz)

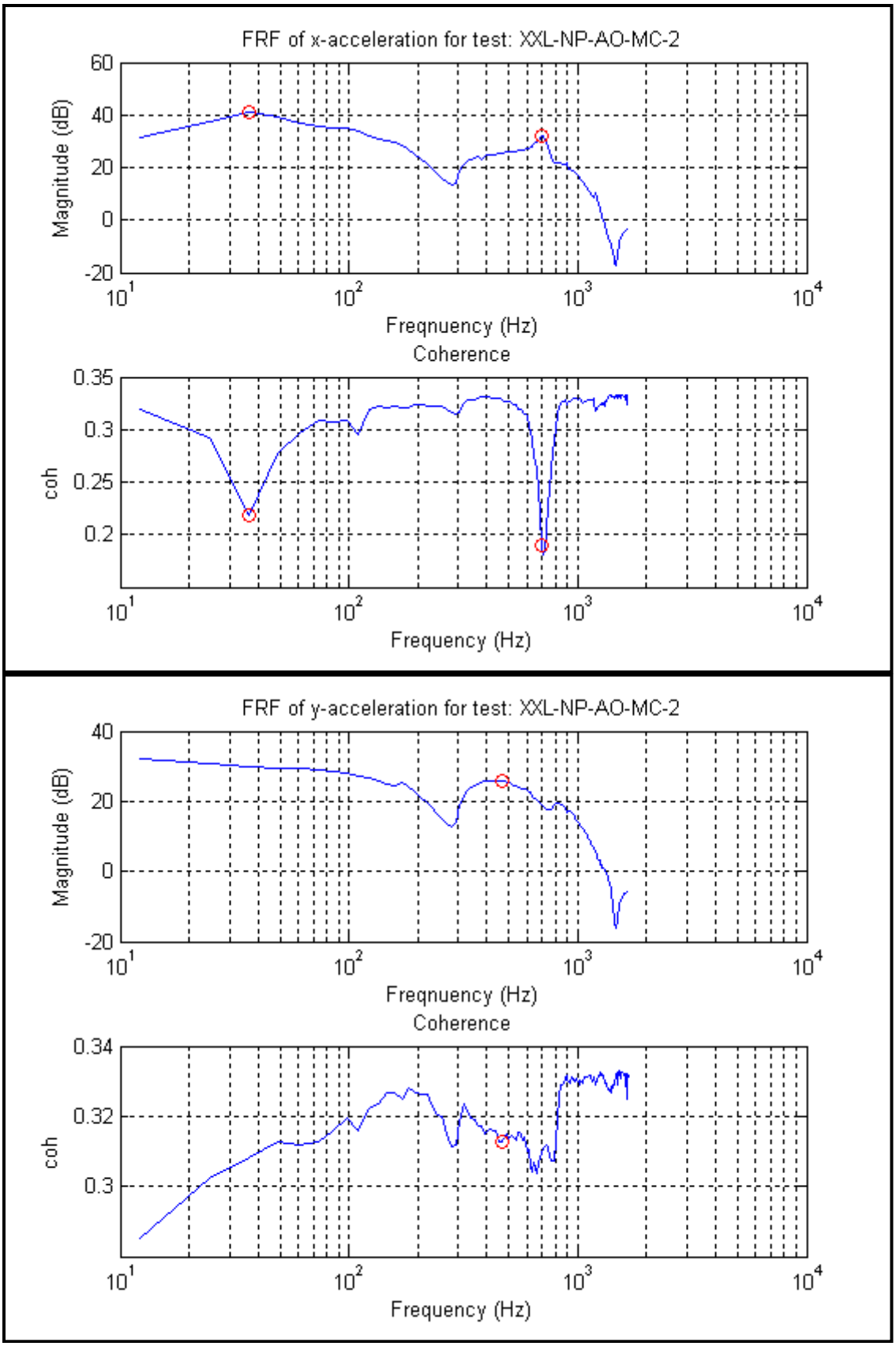
FRF of x-acceleration for test: XXL-NP-AO-MC-2
Magnitude (dB)
60
40
20
0
-20
10^1
10^2
10^3
10^4
Freqnuency (Hz)
Coherence
coh
0.35
0.3
0.25
0.2
10^1
10^2
10^3
10^4
Frequency (Hz)
FRF of y-acceleration for test: XXL-NP-AO-MC-2
Magnitude (dB)
40
20
0
-20
10^1
10^2
10^3
10^4
Freqnuency (Hz)
Coherence
coh
0.34
0.32
0.3
10^1
10^2
10^3
10^4
Frequency (Hz)

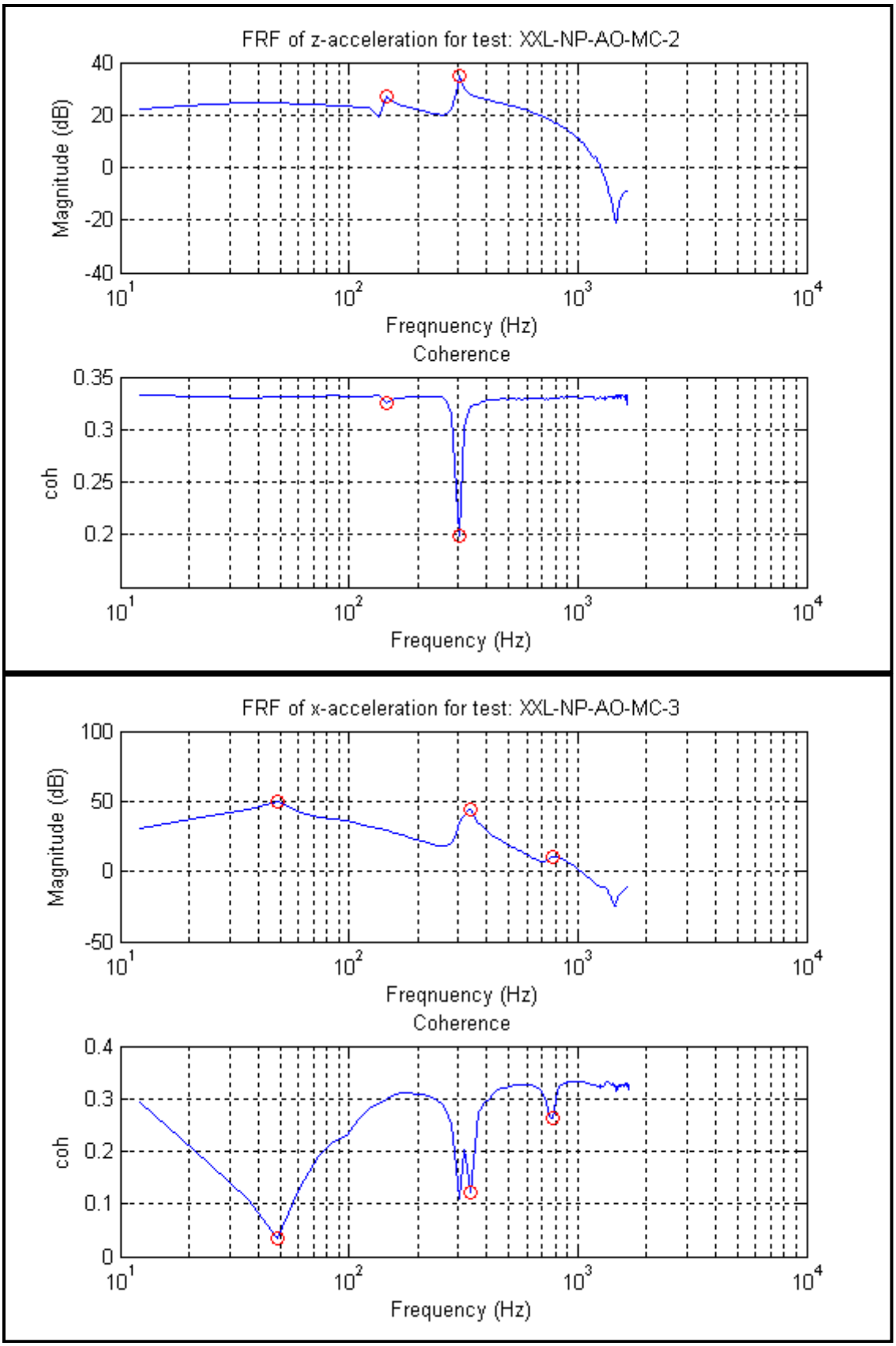
FRF of z-acceleration for test: XXL-NP-AO-MC-2
Magnitude (dB)
40
20
0
-20
-40
10^1
10^2
10^3
10^4
Freqnuency (Hz)
Coherence
coh
0.35
0.3
0.25
0.2
Frequency (Hz)
FRF of x-acceleration for test: XXL-NP-AO-MC-3
Magnitude (dB)
100
50
0
-50
Freqnuency (Hz)
Coherence
coh
0.4
0.3
0.2
0.1
0
Frequency (Hz)

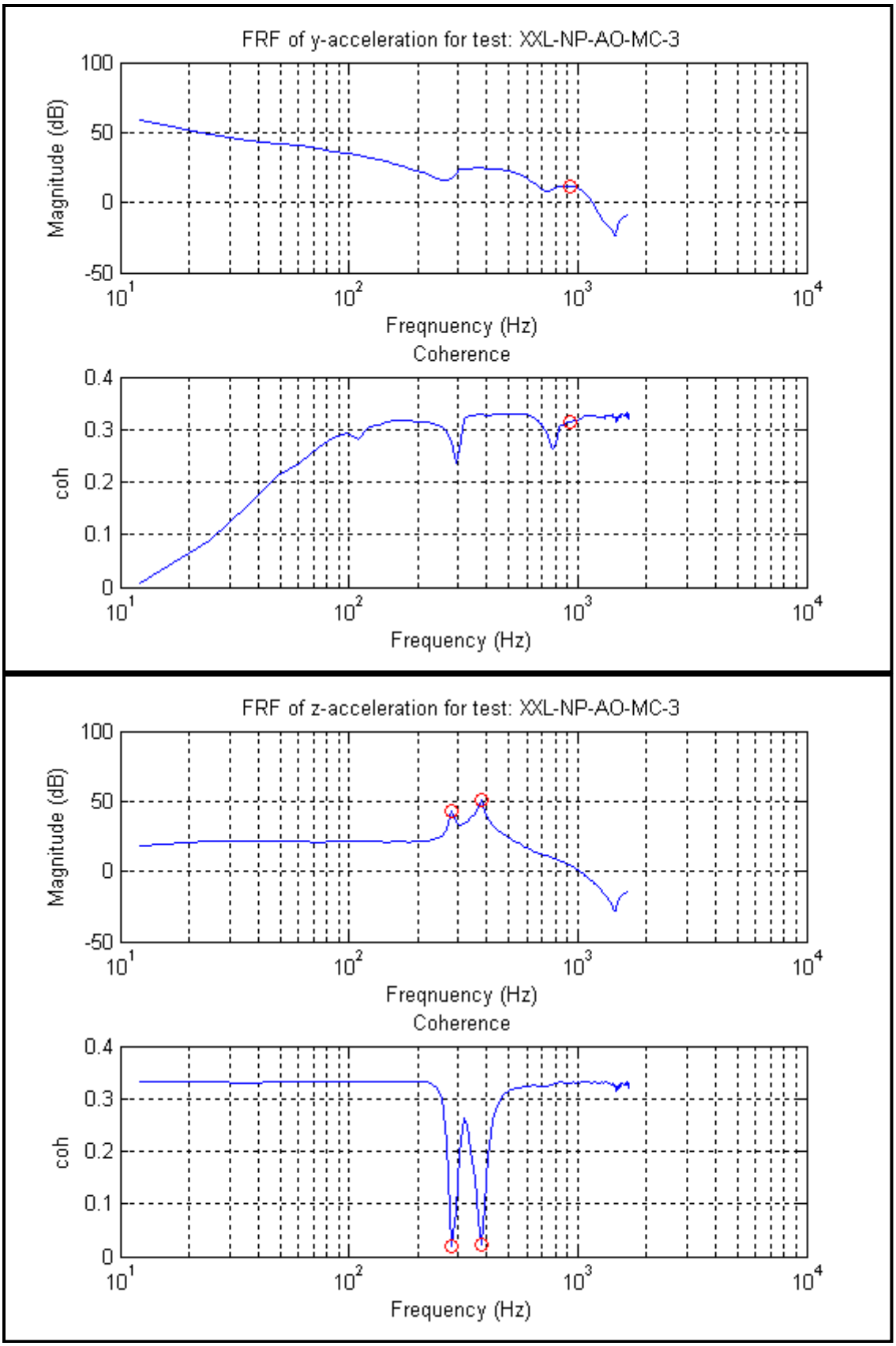
FRF of y-acceleration for test: XXL-NP-AO-MC-3
Magnitude (dB)
Freqnuency (Hz)
Coherence
coh
Frequency (Hz)
FRF of z-acceleration for test: XXL-NP-AO-MC-3
Magnitude (dB)
Freqnuency (Hz)
Coherence
coh
Frequency (Hz)

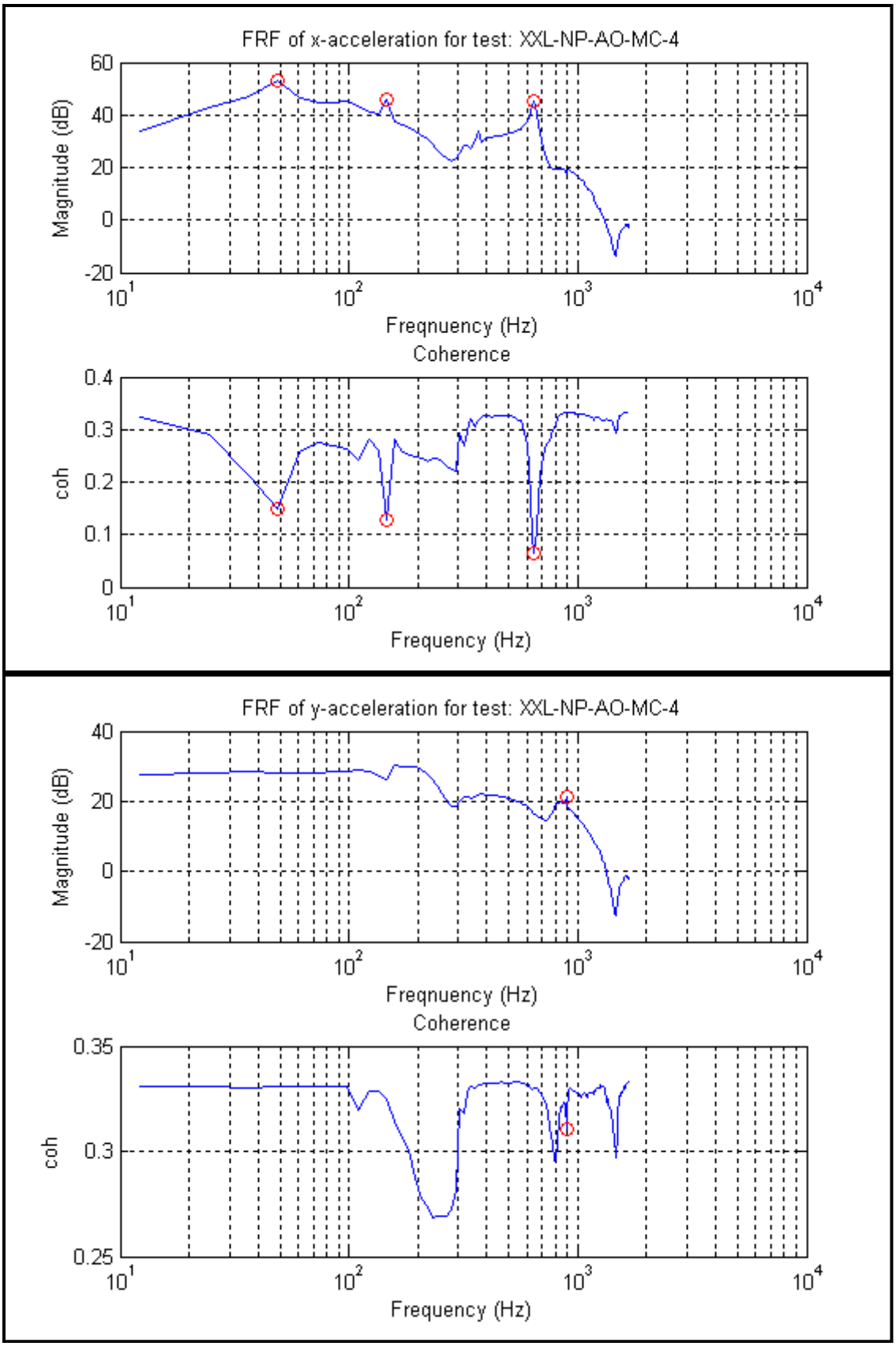
FRF of x-acceleration for test: XXL-NP-AO-MC-4
Magnitude (dB)
Freqnuency (Hz)
Coherence
coh
Frequency (Hz)
FRF of y-acceleration for test: XXL-NP-AO-MC-4
Magnitude (dB)
Freqnuency (Hz)
Coherence
coh
Frequency (Hz)

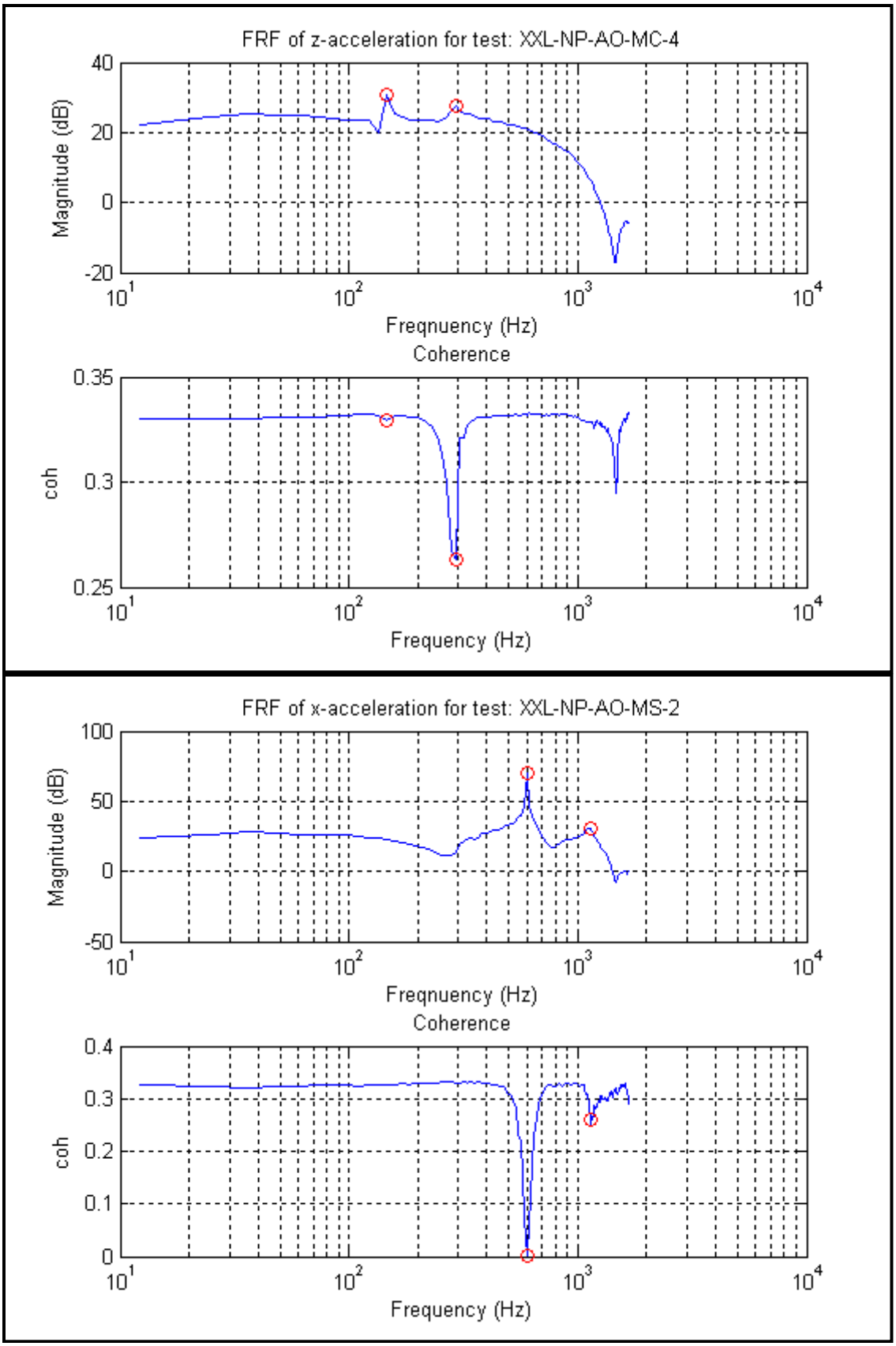
FRF of z-acceleration for test: XXL-NP-AO-MC-4
Magnitude (dB)
40
20
0
-20
10^1
10^2
10^3
10^4
Freqnuency (Hz)
Coherence
coh
0.35
0.3
0.25
Frequency (Hz)
FRF of x-acceleration for test: XXL-NP-AO-MS-2
Magnitude (dB)
100
50
0
-50
Freqnuency (Hz)
Coherence
coh
0.4
0.3
0.2
0.1
0
Frequency (Hz)

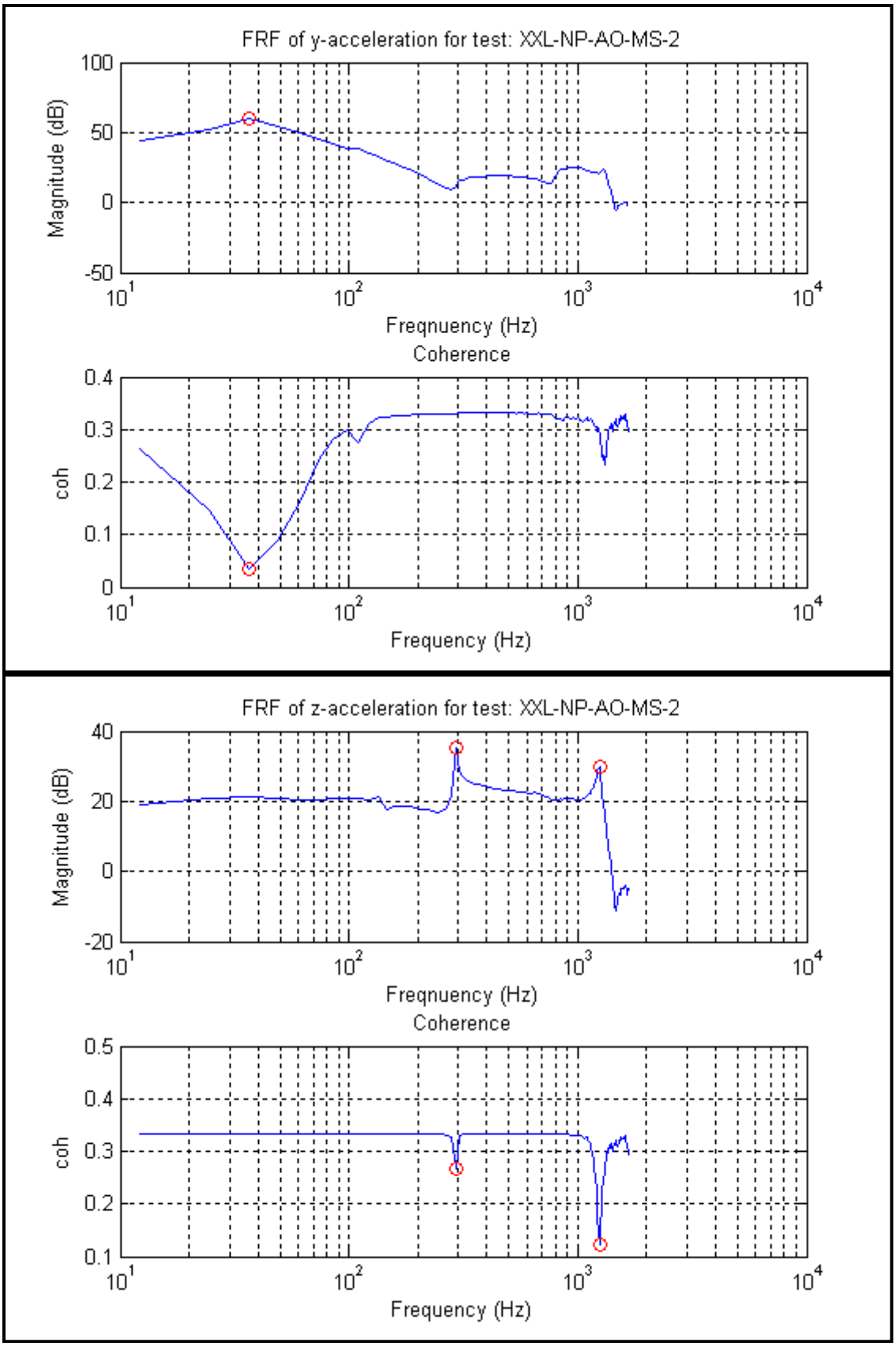
FRF of y-acceleration for test: XXL-NP-AO-MS-2
Magnitude (dB)
Freqnuency (Hz)
Coherence
coh
Frequency (Hz)
FRF of z-acceleration for test: XXL-NP-AO-MS-2
Magnitude (dB)
Freqnuency (Hz)
Coherence
coh
Frequency (Hz)

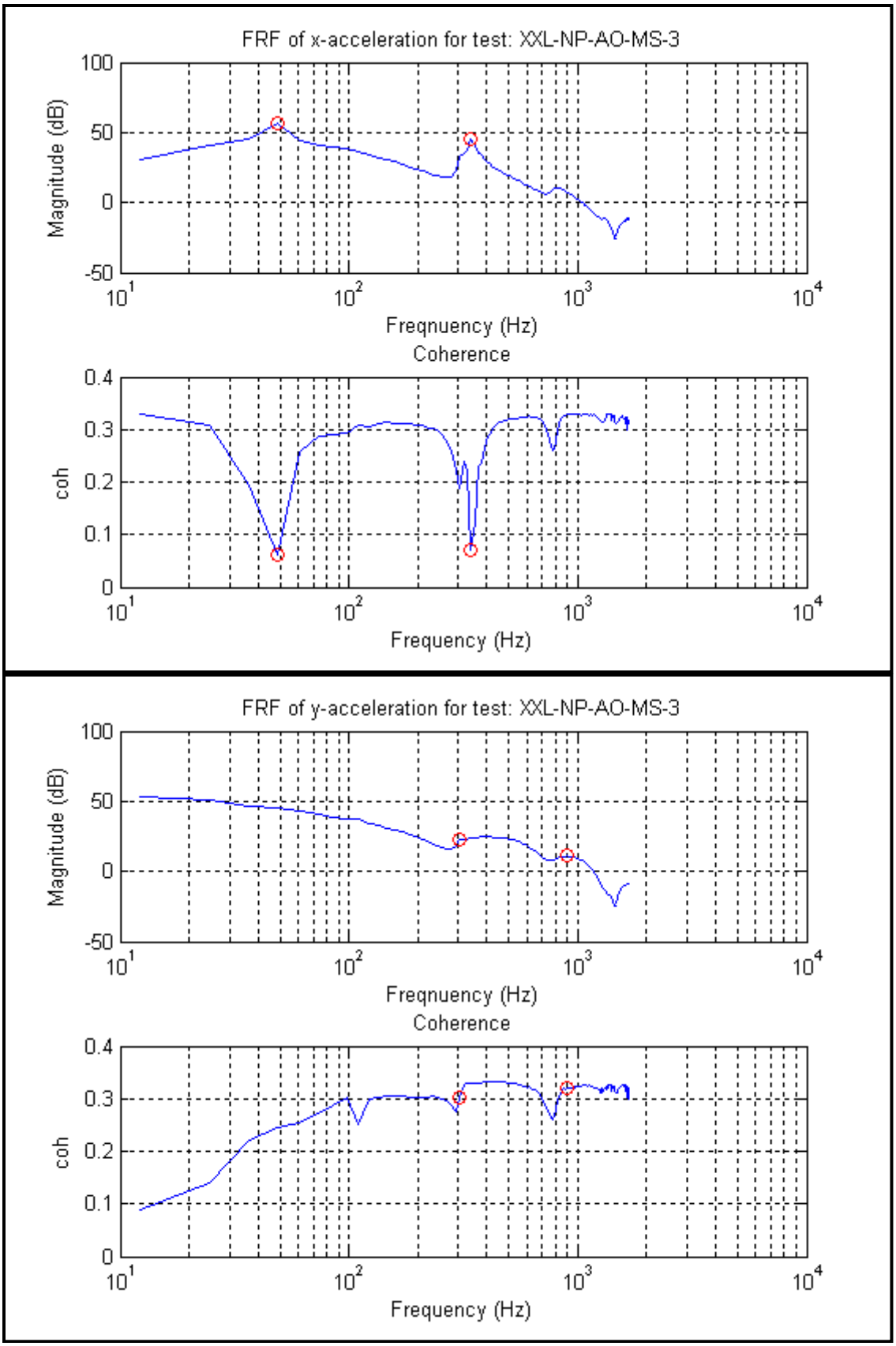
FRF of x-acceleration for test: XXL-NP-AO-MS-3
Magnitude (dB)
Freqnuency (Hz)
Coherence
coh
Frequency (Hz)
FRF of y-acceleration for test: XXL-NP-AO-MS-3
Magnitude (dB)
Freqnuency (Hz)
Coherence
coh
Frequency (Hz)

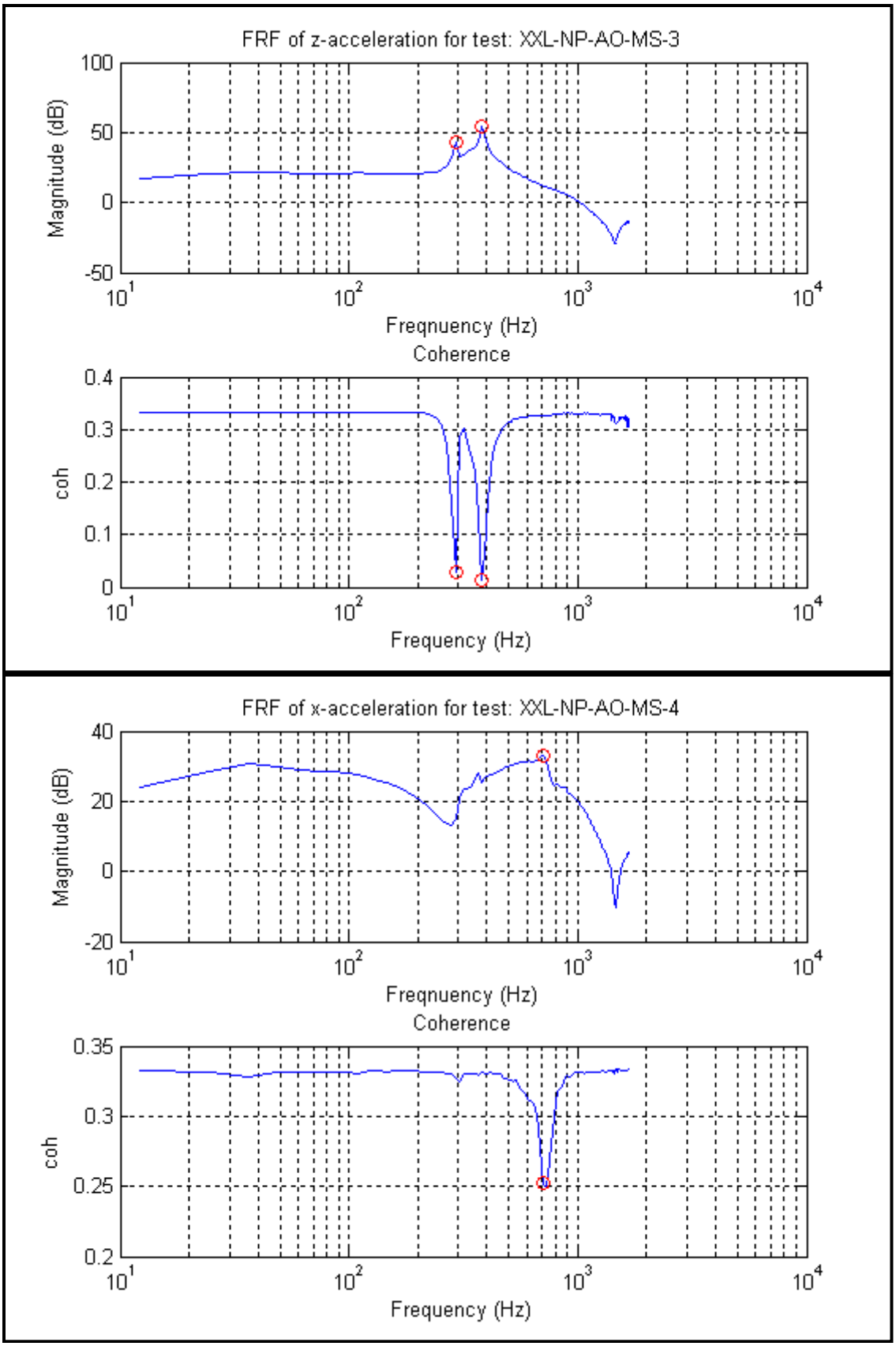
FRF of z-acceleration for test: XXL-NP-AO-MS-3
Magnitude (dB)
100
50
0
-50
10^1
10^2
10^3
10^4
Freqnuency (Hz)
Coherence
coh
0.4
0.3
0.2
0.1
0
Frequency (Hz)
FRF of x-acceleration for test: XXL-NP-AO-MS-4
Magnitude (dB)
40
20
0
-20
Freqnuency (Hz)
Coherence
coh
0.35
0.3
0.25
0.2
Frequency (Hz)

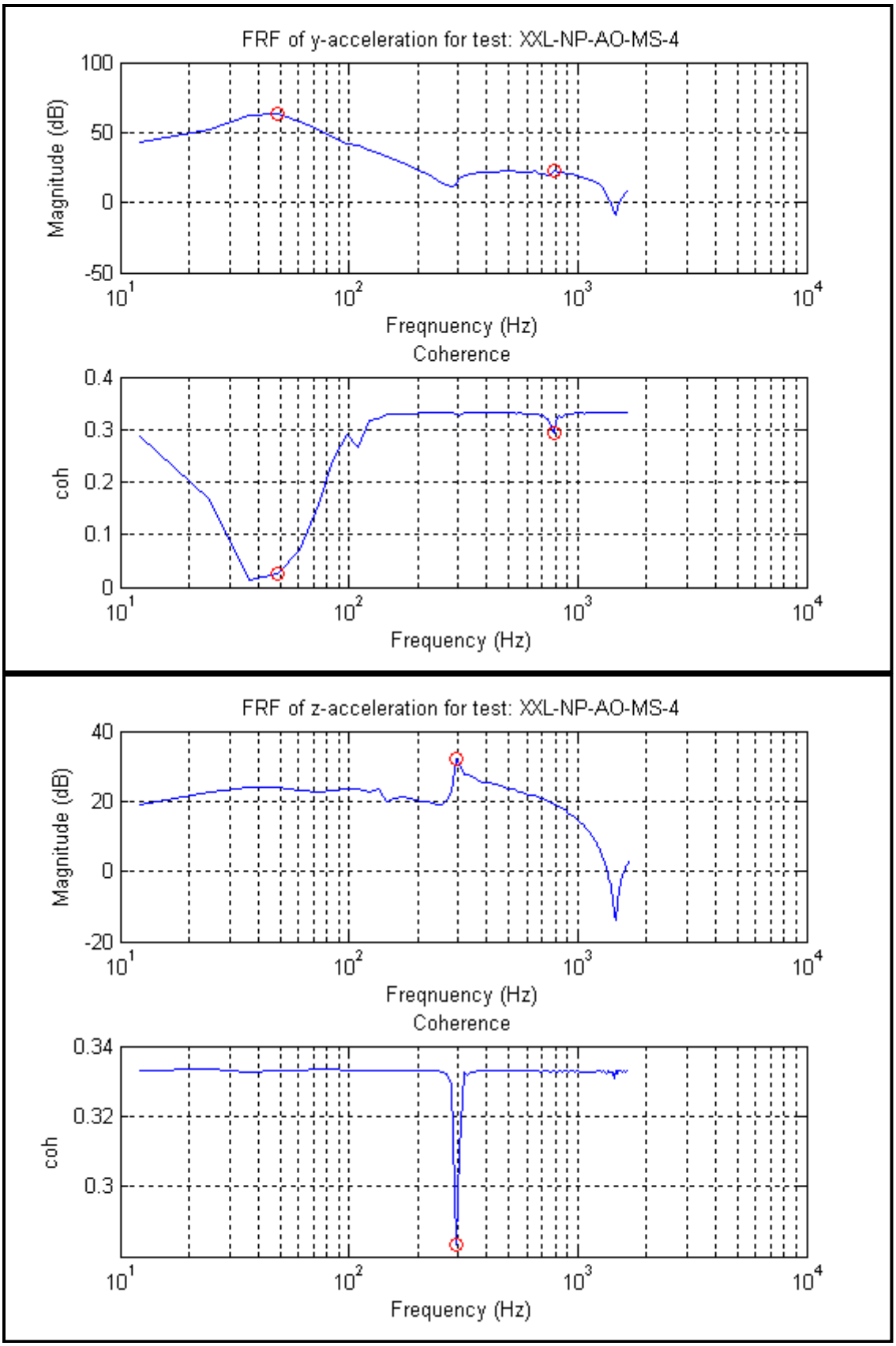
FRF of y-acceleration for test: XXL-NP-AO-MS-4
Magnitude (dB)
Freqnuency (Hz)
Coherence
coh
Frequency (Hz)
FRF of z-acceleration for test: XXL-NP-AO-MS-4
Magnitude (dB)
Freqnuency (Hz)
Coherence
coh
Frequency (Hz)

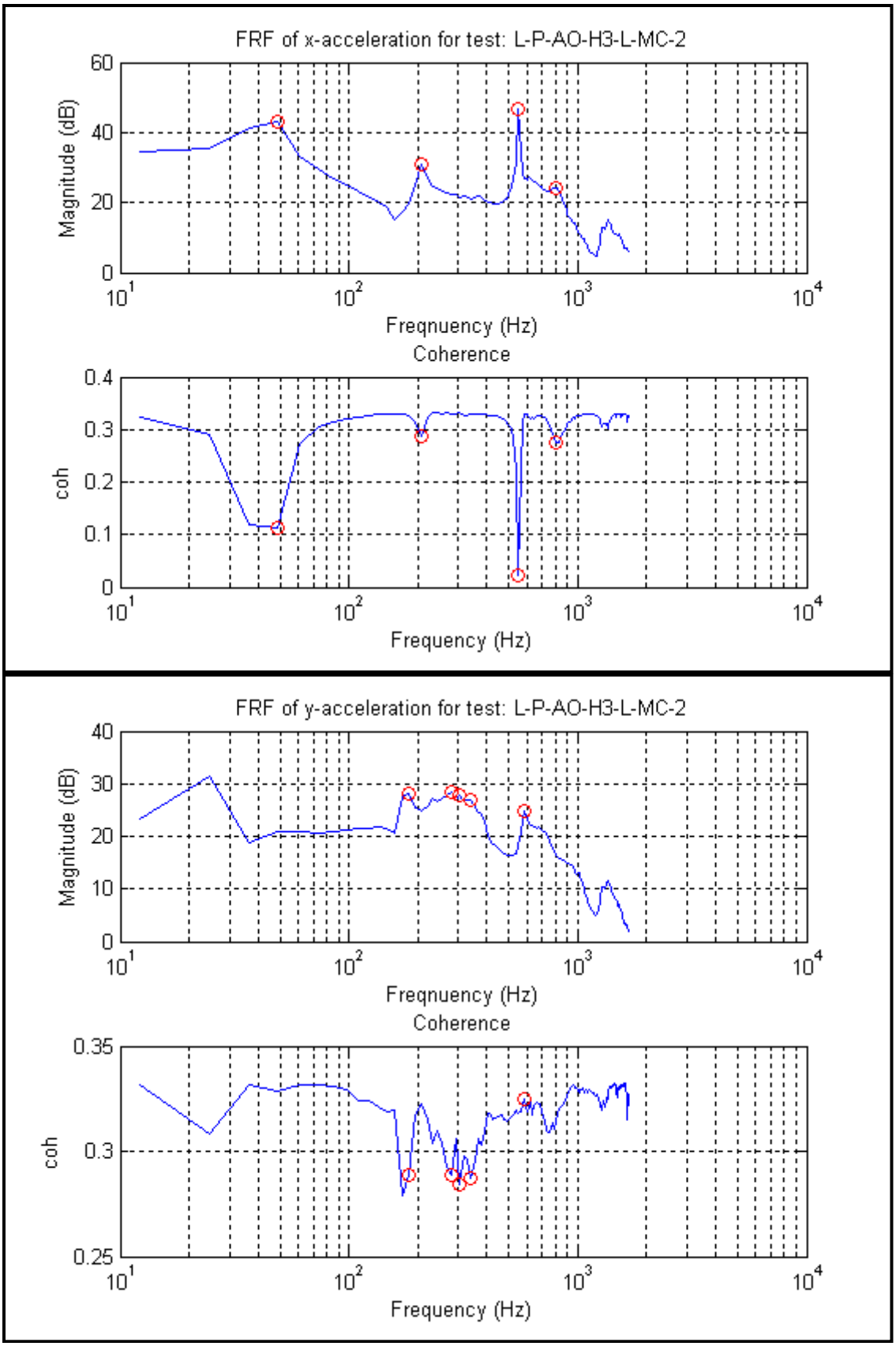
FRF of x-acceleration for test: L-P-AO-H3-L-MC-2
Magnitude (dB)
Freqnuency (Hz)
Coherence
coh
Frequency (Hz)
FRF of y-acceleration for test: L-P-AO-H3-L-MC-2
Magnitude (dB)
Freqnuency (Hz)
Coherence
coh
Frequency (Hz)

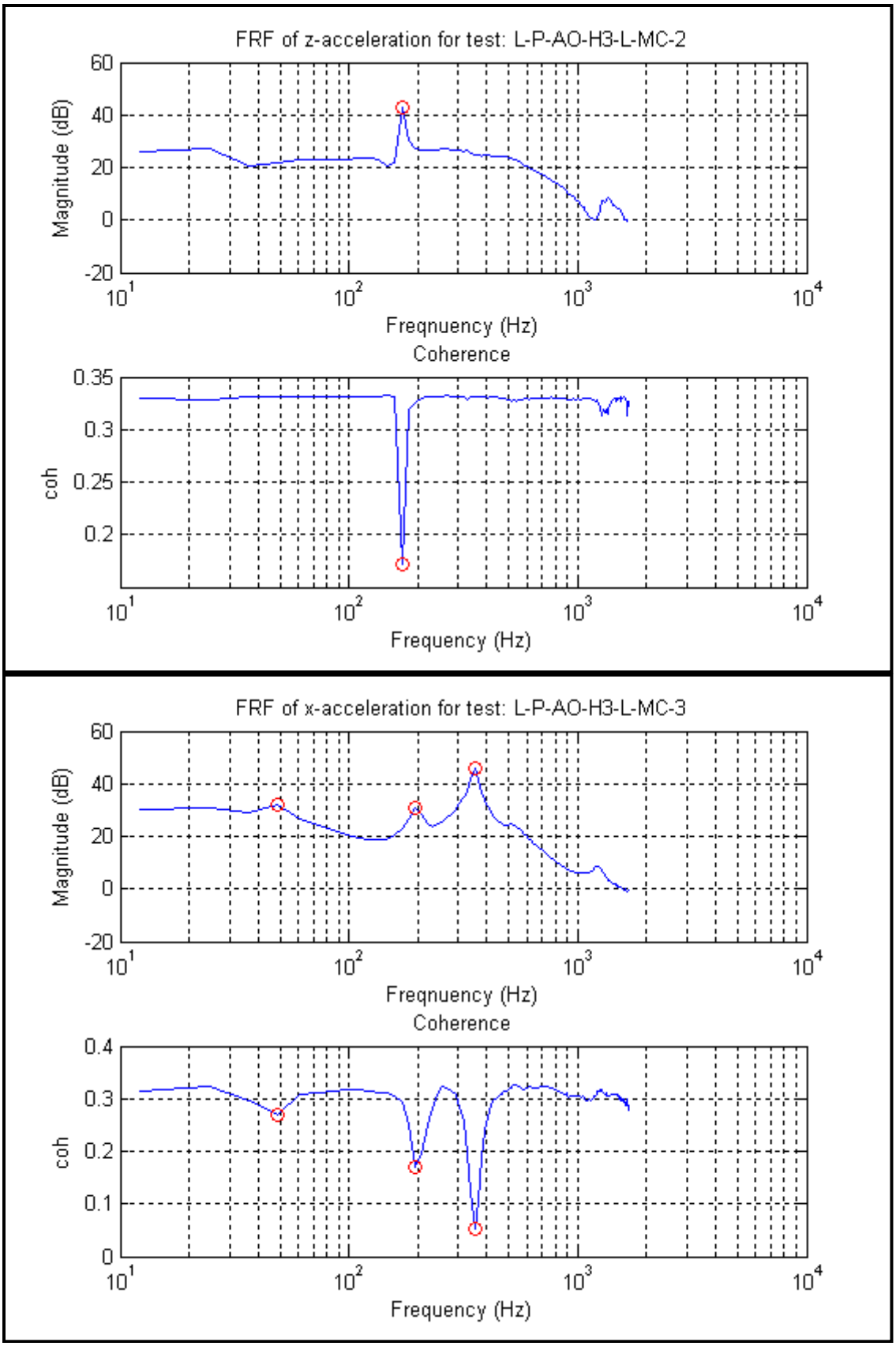
FRF of z-acceleration for test: L-P-AO-H3-L-MC-2
Magnitude (dB)
Freqnuency (Hz)
Coherence
coh
Frequency (Hz)
FRF of x-acceleration for test: L-P-AO-H3-L-MC-3
Magnitude (dB)
Freqnuency (Hz)
Coherence
coh
Frequency (Hz)

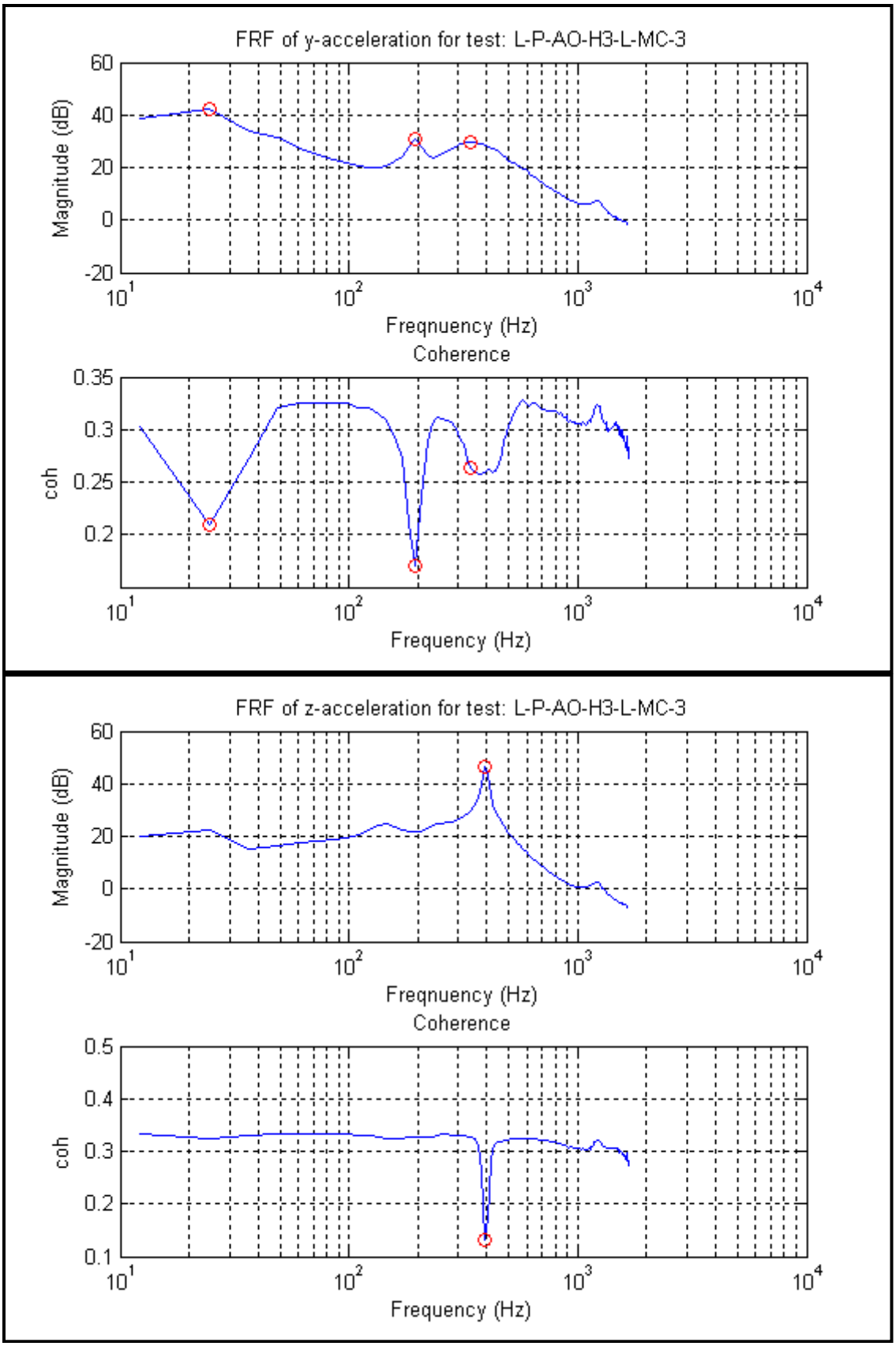
FRF of y-acceleration for test: L-P-AO-H3-L-MC-3
Magnitude (dB)
60
40
20
0
-20
10^1
10^2
10^3
10^4
Freqnuency (Hz)
Coherence
coh
0.35
0.3
0.25
0.2
Frequency (Hz)
FRF of z-acceleration for test: L-P-AO-H3-L-MC-3
Magnitude (dB)
Freqnuency (Hz)
Coherence
coh
0.5
0.4
0.3
0.2
0.1
Frequency (Hz)

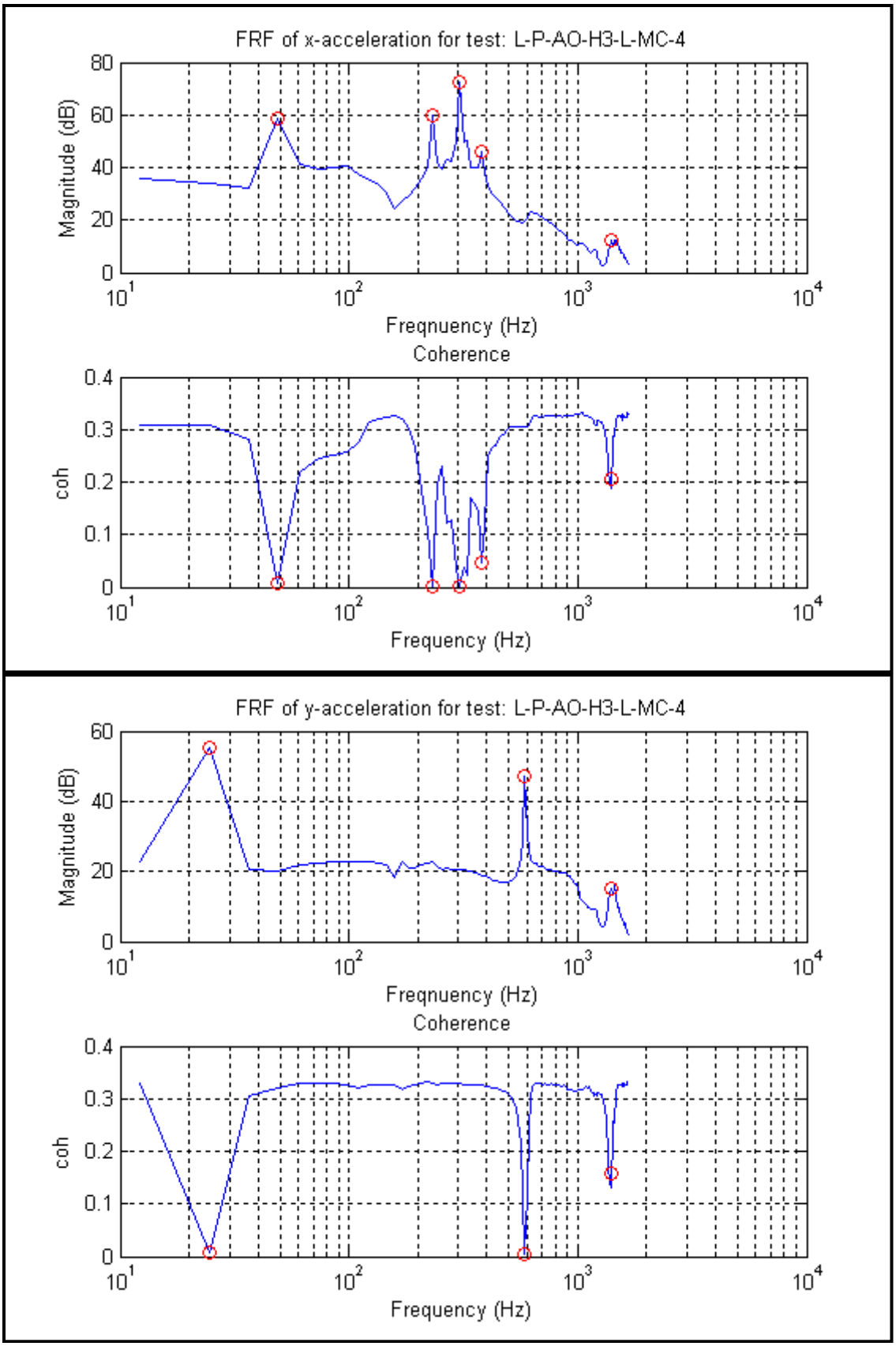
FRF of x-acceleration for test: L-P-AO-H3-L-MC-4
Magnitude (dB)
Freqnuency (Hz)
Coherence
coh
Frequency (Hz)
FRF of y-acceleration for test: L-P-AO-H3-L-MC-4
Magnitude (dB)
Freqnuency (Hz)
Coherence
coh
Frequency (Hz)

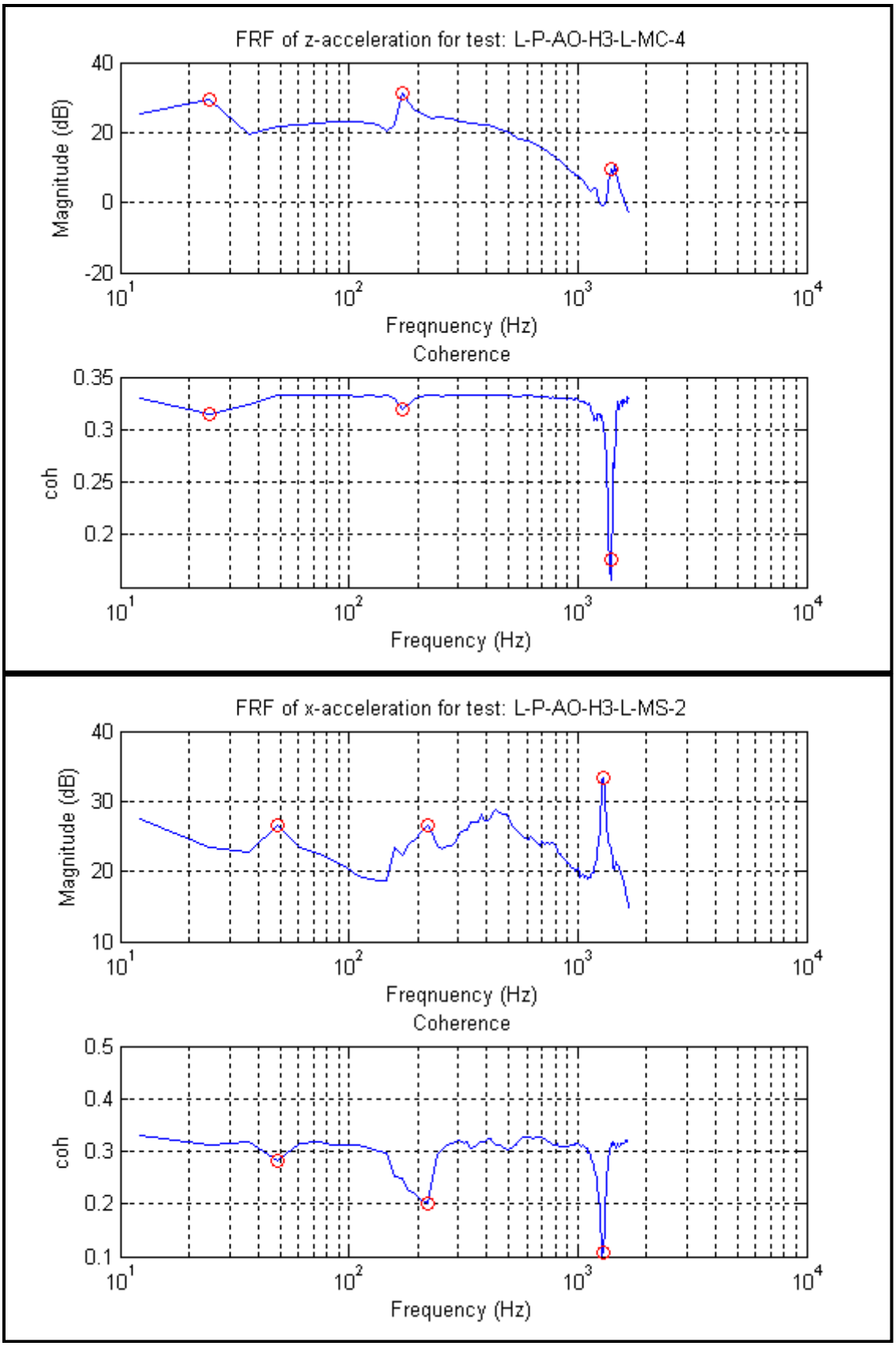
FRF of z-acceleration for test: L-P-AO-H3-L-MC-4
Magnitude (dB)
40
20
0
-20
10^1
10^2
10^3
10^4
Freqnuency (Hz)
Coherence
coh
0.35
0.3
0.25
0.2
Frequency (Hz)
FRF of x-acceleration for test: L-P-AO-H3-L-MS-2
Magnitude (dB)
40
30
20
10
Freqnuency (Hz)
Coherence
coh
0.5
0.4
0.3
0.2
0.1
Frequency (Hz)

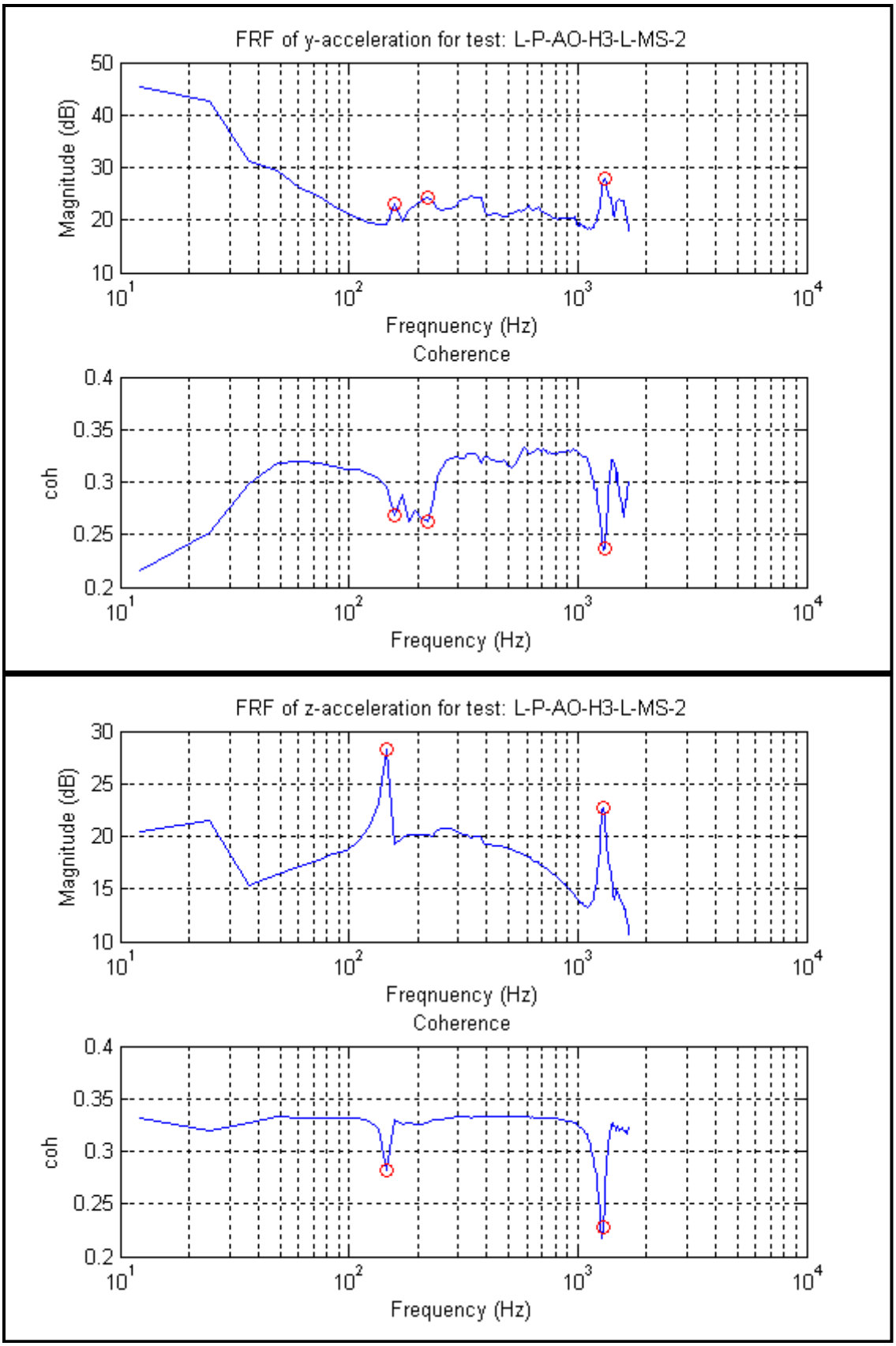
FRF of y-acceleration for test: L-P-AO-H3-L-MS-2
Magnitude (dB)
Freqnuency (Hz)
Coherence
coh
Frequency (Hz)
FRF of z-acceleration for test: L-P-AO-H3-L-MS-2
Magnitude (dB)
Freqnuency (Hz)
Coherence
coh
Frequency (Hz)

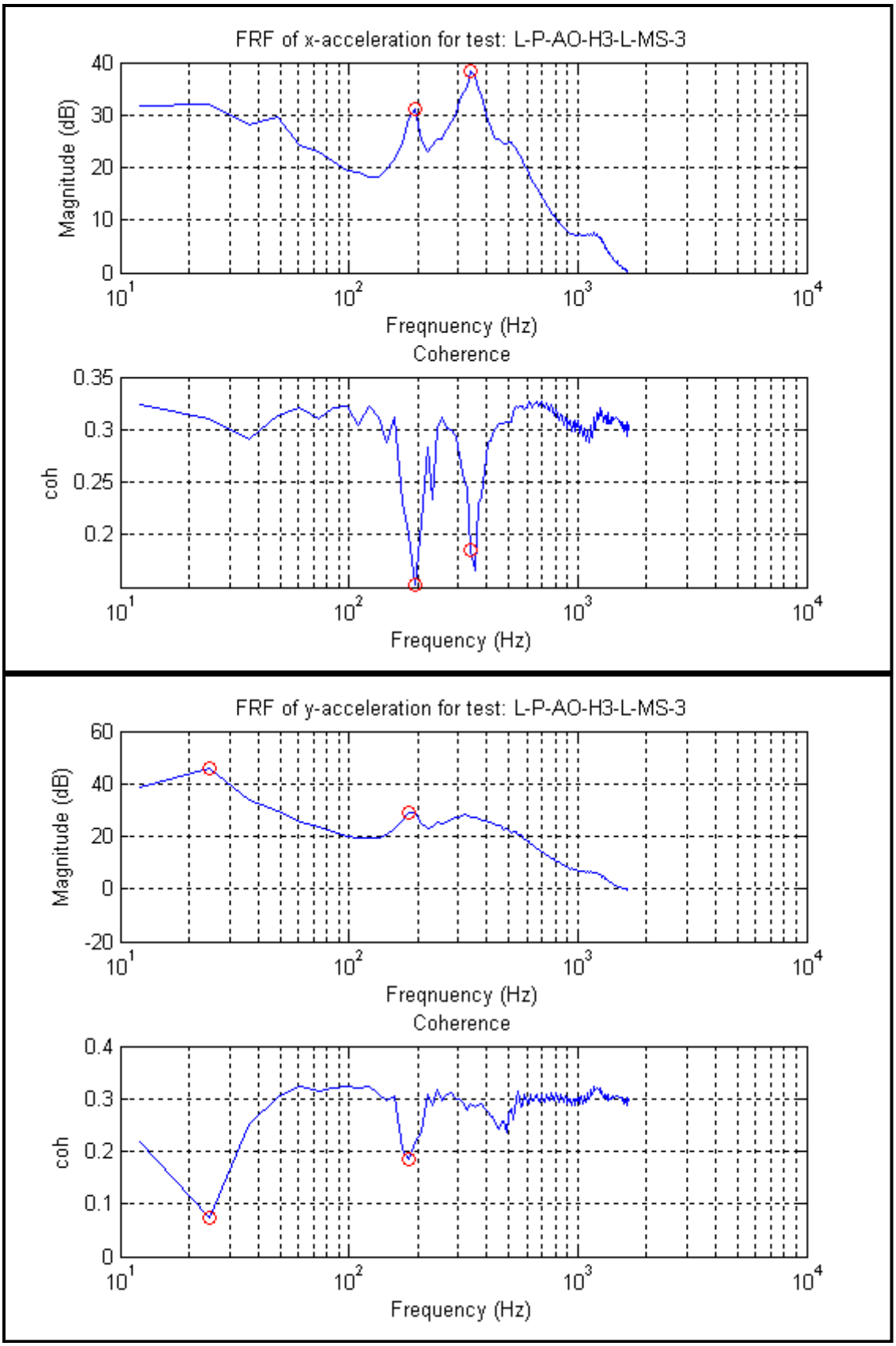
FRF of x-acceleration for test: L-P-AO-H3-L-MS-3
Magnitude (dB)
Freqnuency (Hz)
Coherence
coh
Frequency (Hz)
FRF of y-acceleration for test: L-P-AO-H3-L-MS-3
Magnitude (dB)
Freqnuency (Hz)
Coherence
coh
Frequency (Hz)

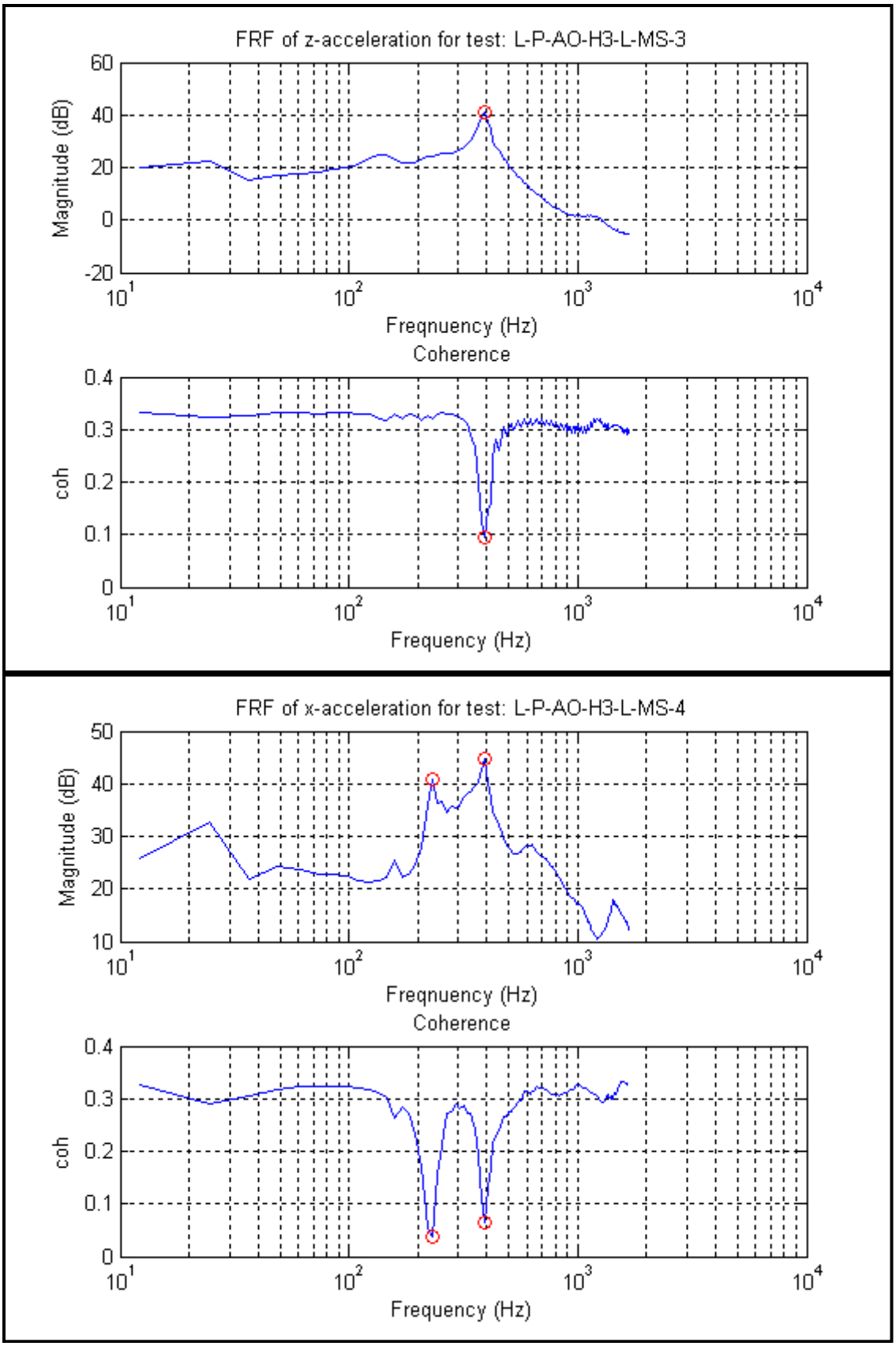
FRF of z-acceleration for test: L-P-AO-H3-L-MS-3
Magnitude (dB)
Freqnuency (Hz)
Coherence
coh
Frequency (Hz)
FRF of x-acceleration for test: L-P-AO-H3-L-MS-4
Magnitude (dB)
Freqnuency (Hz)
Coherence
coh
Frequency (Hz)

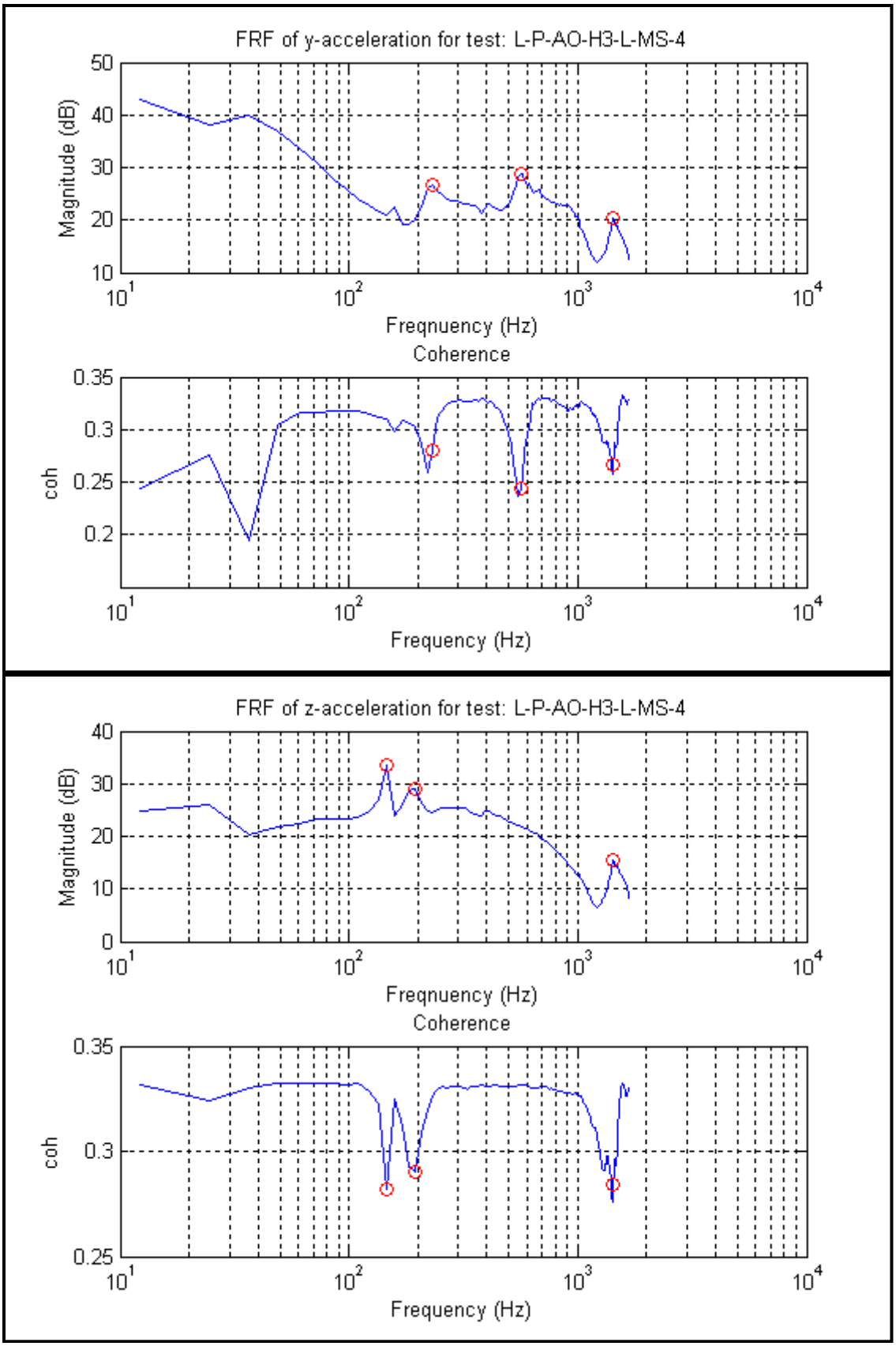
FRF of y-acceleration for test: L-P-AO-H3-L-MS-4
Magnitude (dB)
Freqnuency (Hz)
Coherence
coh
Frequency (Hz)
FRF of z-acceleration for test: L-P-AO-H3-L-MS-4
Magnitude (dB)
Freqnuency (Hz)
Coherence
coh
Frequency (Hz)

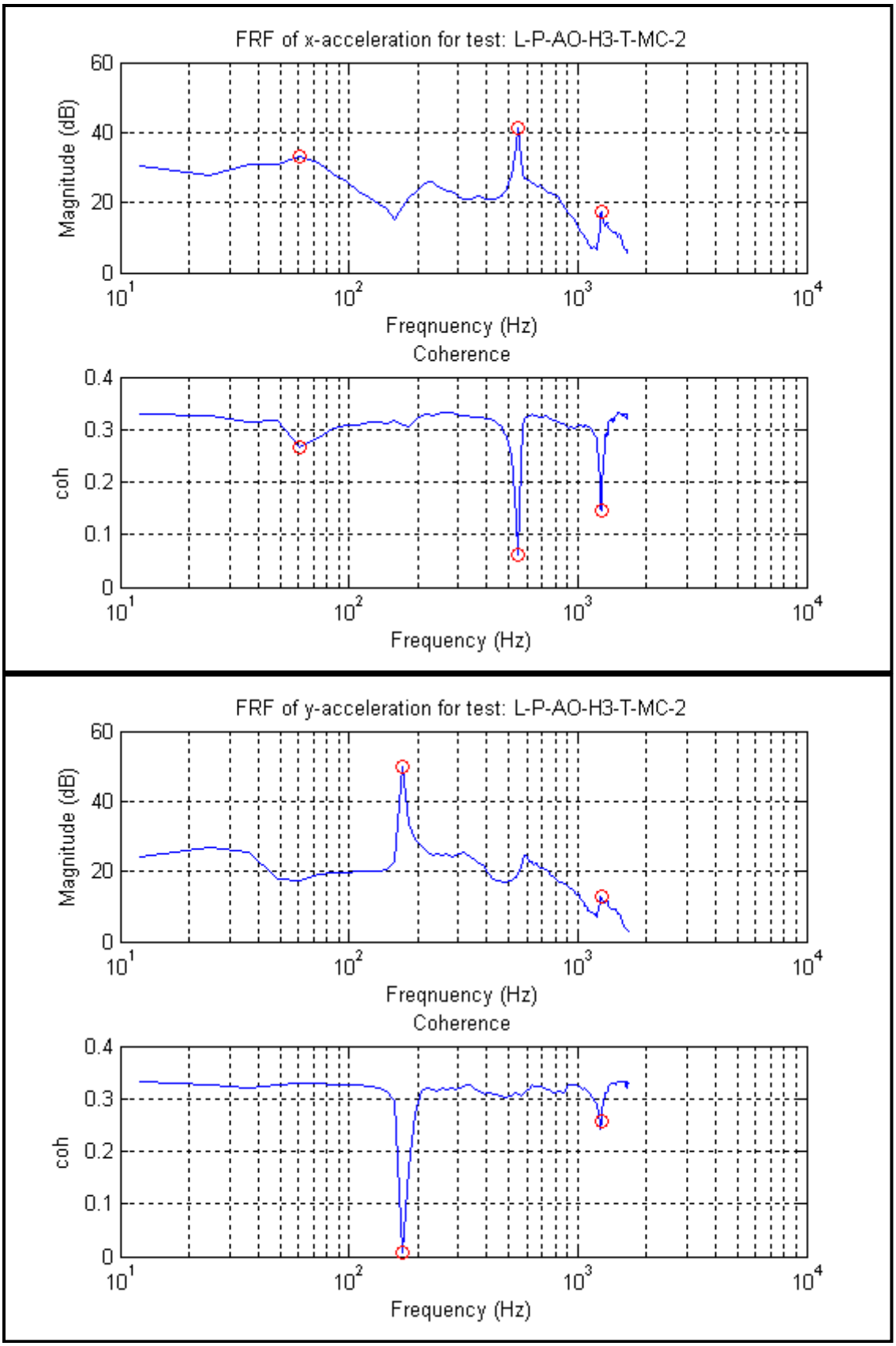
FRF of x-acceleration for test: L-P-AO-H3-T-MC-2
Magnitude (dB)
Freqnuency (Hz)
Coherence
coh
Frequency (Hz)
FRF of y-acceleration for test: L-P-AO-H3-T-MC-2
Magnitude (dB)
Freqnuency (Hz)
Coherence
coh
Frequency (Hz)

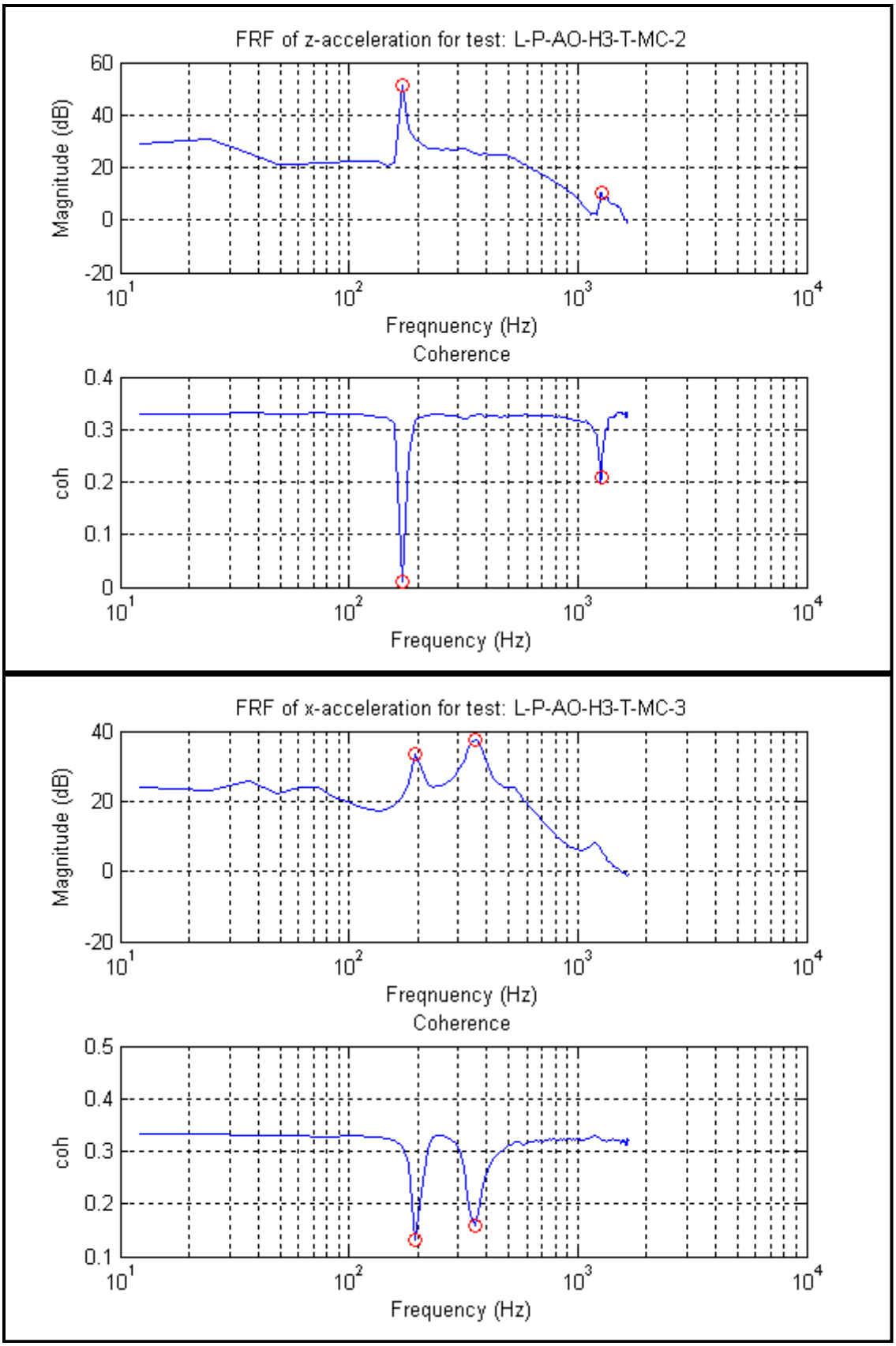
FRF of z-acceleration for test: L-P-AO-H3-T-MC-2
Magnitude (dB)
Freqnuency (Hz)
Coherence
coh
Frequency (Hz)
FRF of x-acceleration for test: L-P-AO-H3-T-MC-3
Magnitude (dB)
Freqnuency (Hz)
Coherence
coh
Frequency (Hz)

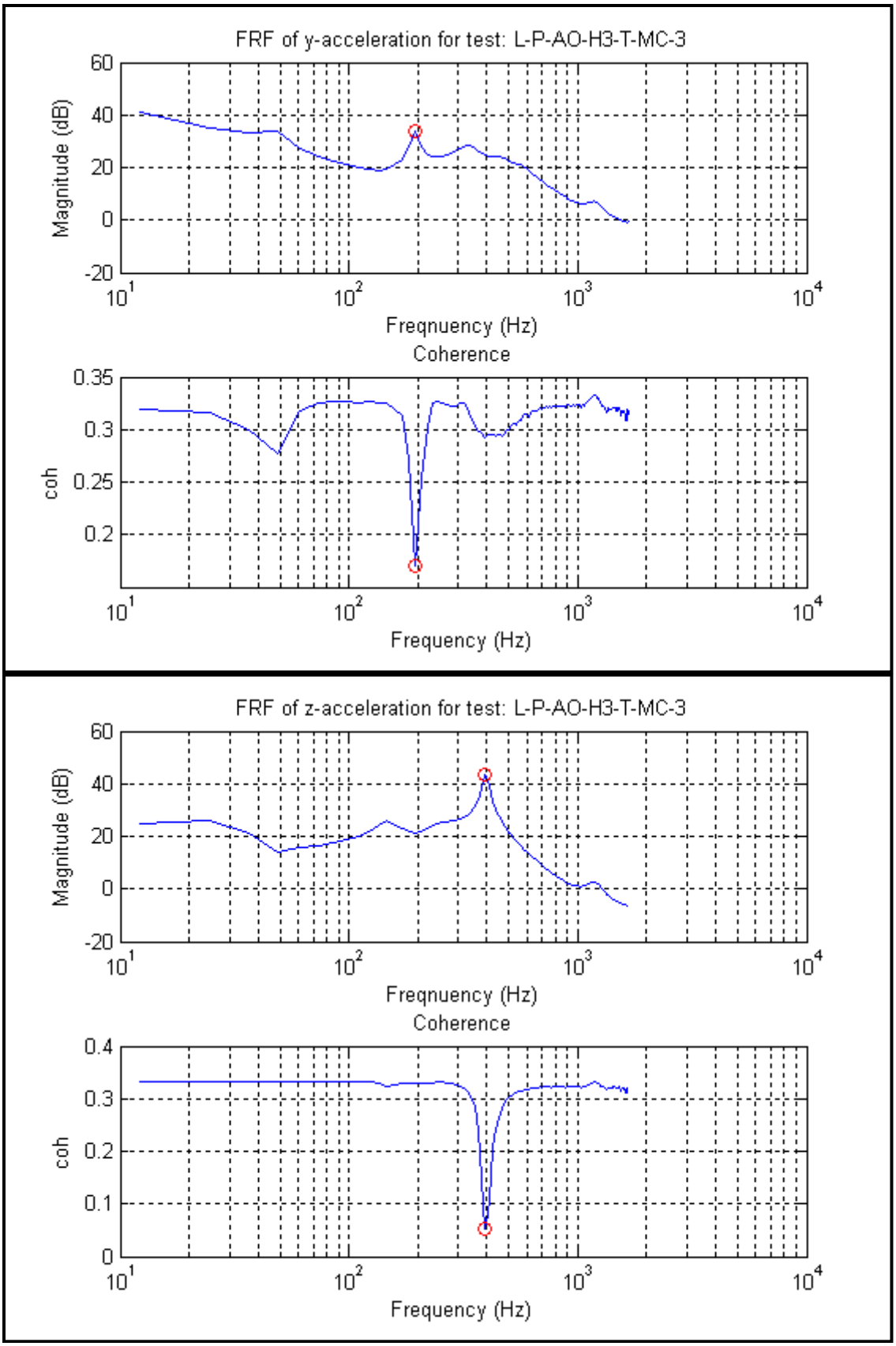
FRF of y-acceleration for test: L-P-AO-H3-T-MC-3
Magnitude (dB)
60
40
20
0
-20
10^1
10^2
10^3
10^4
Freqnuency (Hz)
Coherence
coh
0.35
0.3
0.25
0.2
Frequency (Hz)
FRF of z-acceleration for test: L-P-AO-H3-T-MC-3
Magnitude (dB)
Freqnuency (Hz)
Coherence
coh
0.4
0.3
0.2
0.1
0
Frequency (Hz)

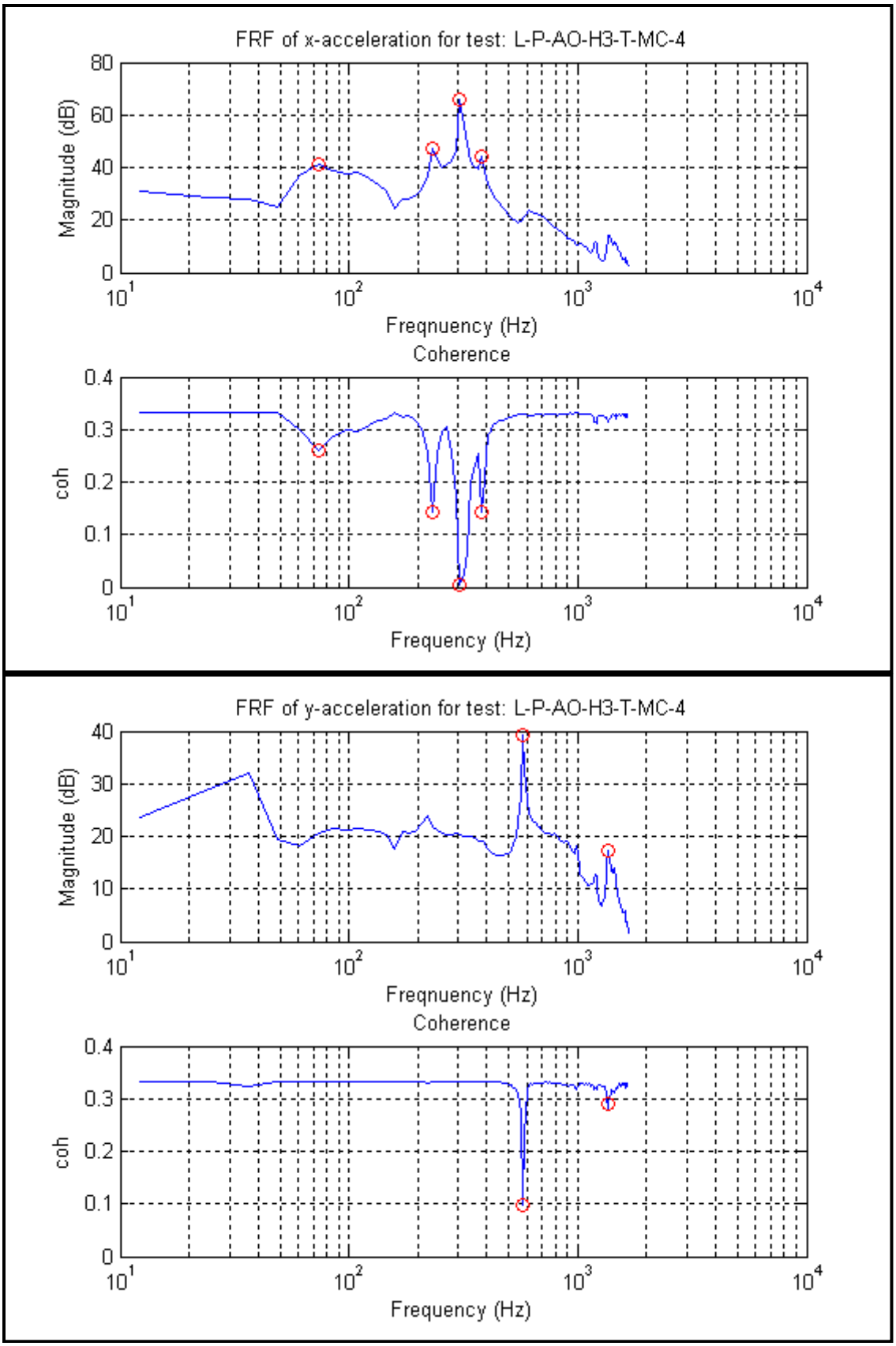
FRF of x-acceleration for test: L-P-AO-H3-T-MC-4
Magnitude (dB)
Freqnuency (Hz)
Coherence
coh
Frequency (Hz)
FRF of y-acceleration for test: L-P-AO-H3-T-MC-4
Magnitude (dB)
Freqnuency (Hz)
Coherence
coh
Frequency (Hz)

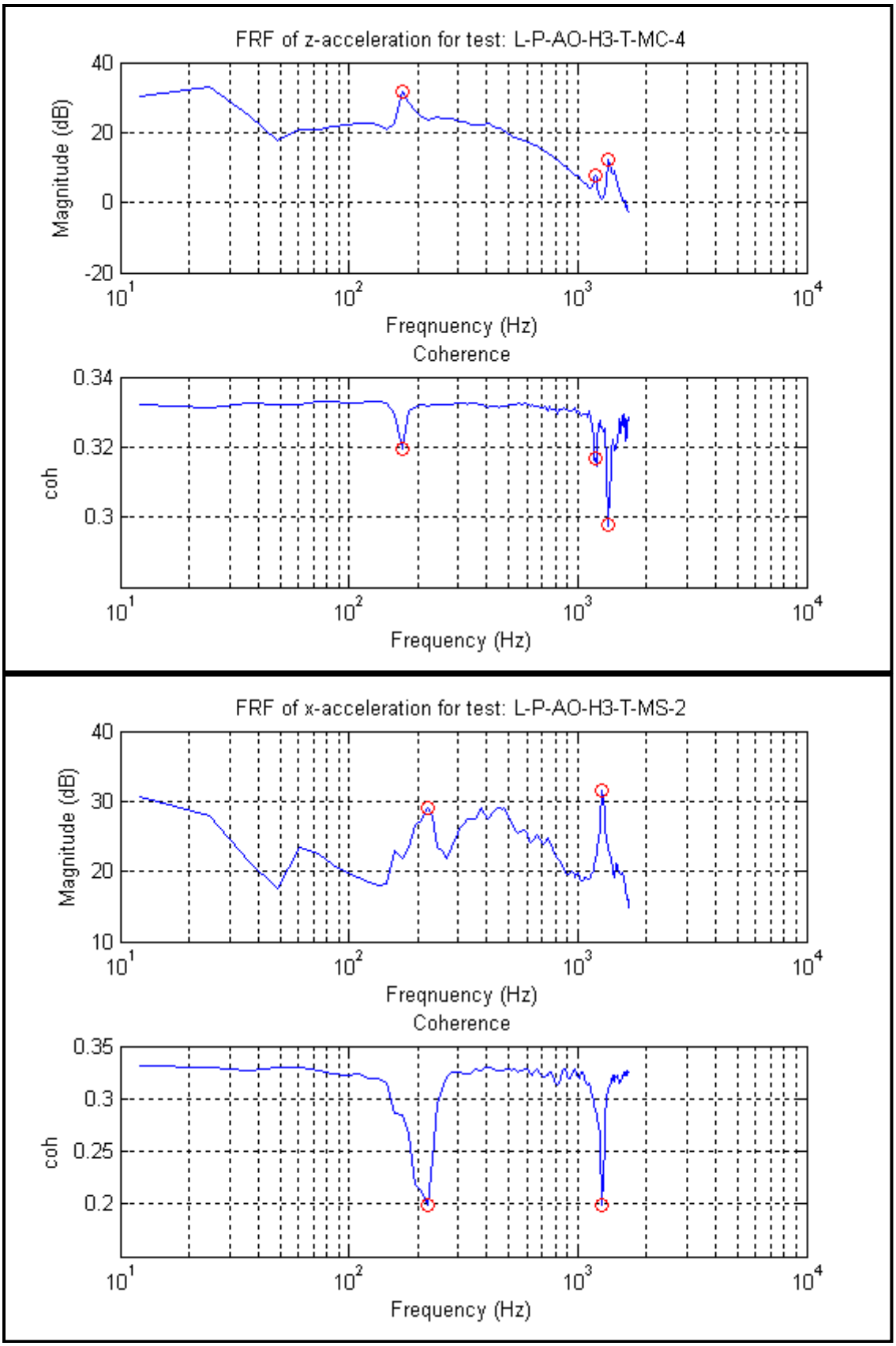
FRF of z-acceleration for test: L-P-AO-H3-T-MC-4
Magnitude (dB)
40
20
0
-20
10^1
10^2
10^3
10^4
Freqnuency (Hz)
Coherence
coh
0.34
0.32
0.3
Frequency (Hz)
FRF of x-acceleration for test: L-P-AO-H3-T-MS-2
Magnitude (dB)
40
30
20
10
Freqnuency (Hz)
Coherence
coh
0.35
0.3
0.25
0.2
Frequency (Hz)

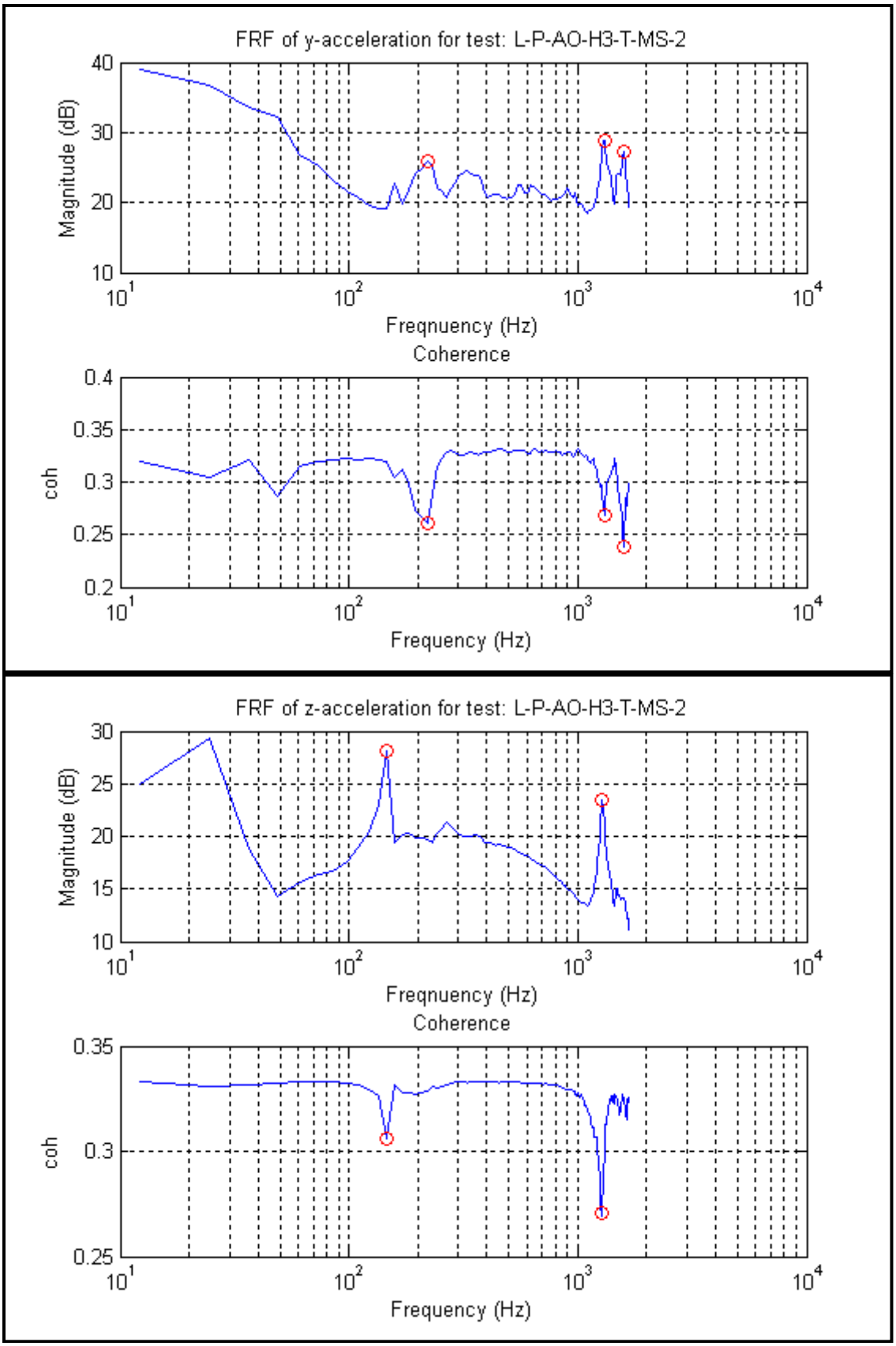
FRF of y-acceleration for test: L-P-AO-H3-T-MS-2
Magnitude (dB)
Freqnuency (Hz)
Coherence
coh
Frequency (Hz)
FRF of z-acceleration for test: L-P-AO-H3-T-MS-2
Magnitude (dB)
Freqnuency (Hz)
Coherence
coh
Frequency (Hz)

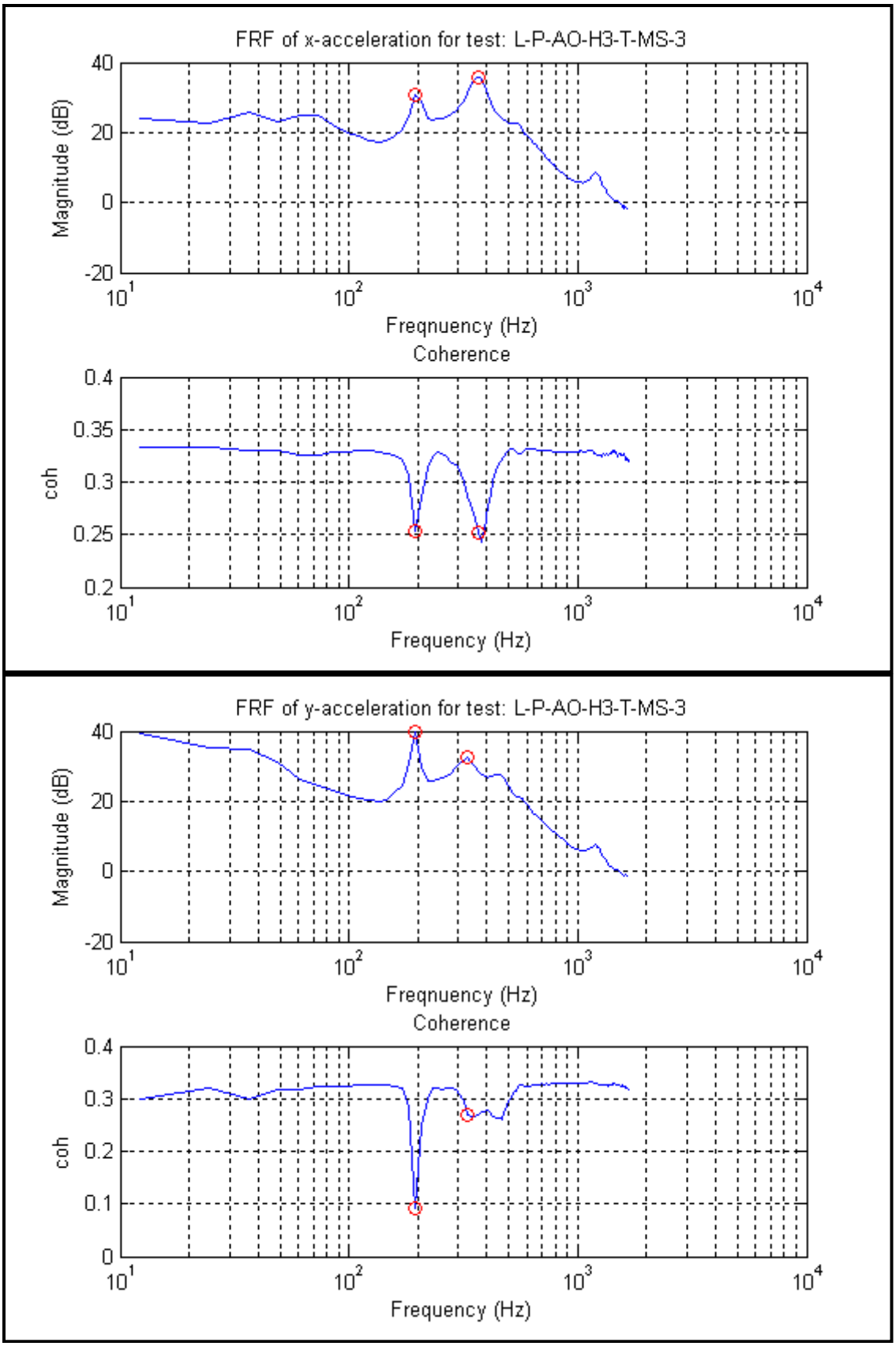
FRF of x-acceleration for test: L-P-AO-H3-T-MS-3
Magnitude (dB)
Freqnuency (Hz)
Coherence
coh
Frequency (Hz)
FRF of y-acceleration for test: L-P-AO-H3-T-MS-3
Magnitude (dB)
Freqnuency (Hz)
Coherence
coh
Frequency (Hz)

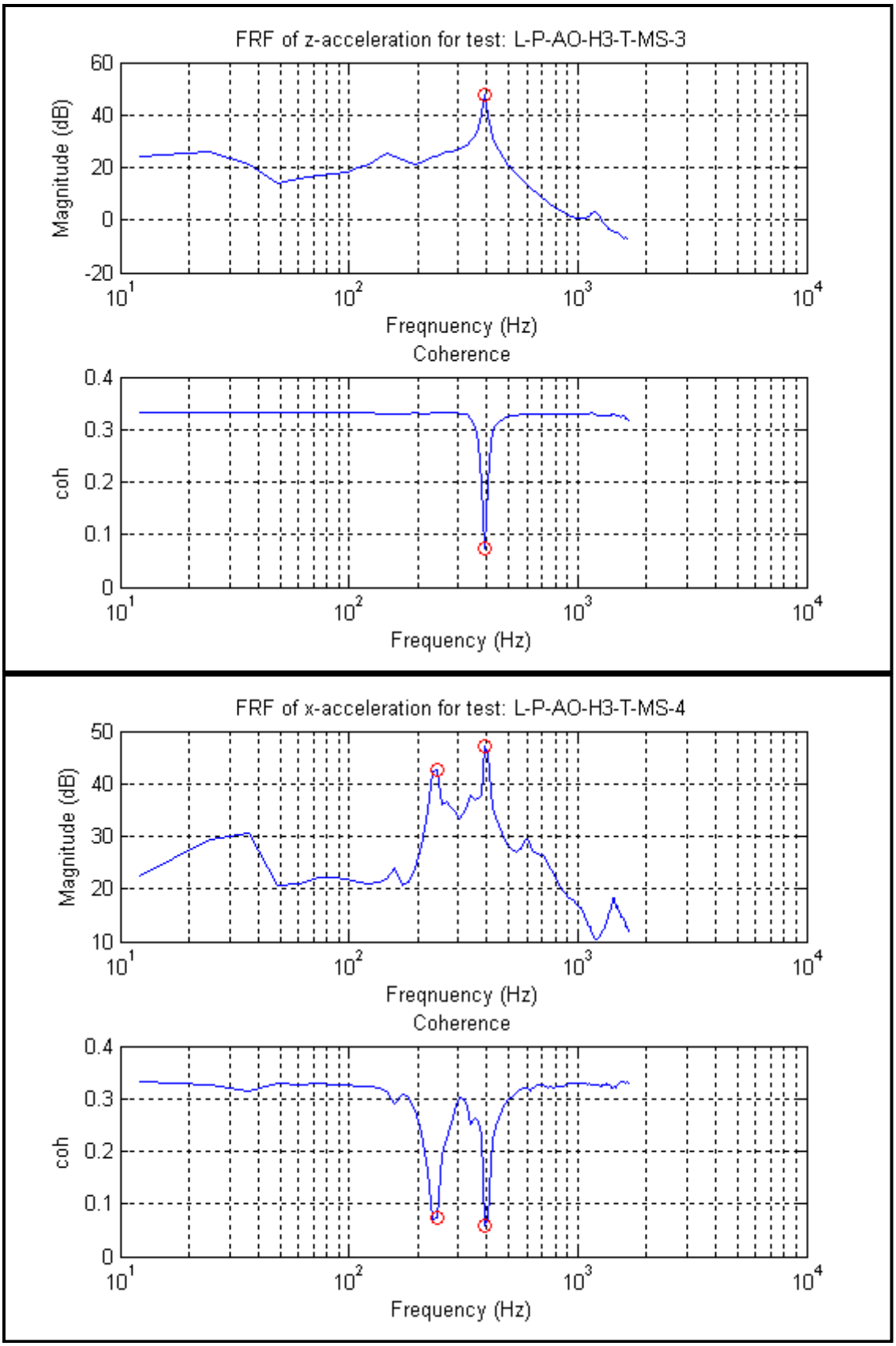
FRF of z-acceleration for test: L-P-AO-H3-T-MS-3
Magnitude (dB)
Freqnuency (Hz)
Coherence
coh
Frequency (Hz)
FRF of x-acceleration for test: L-P-AO-H3-T-MS-4
Magnitude (dB)
Freqnuency (Hz)
Coherence
coh
Frequency (Hz)

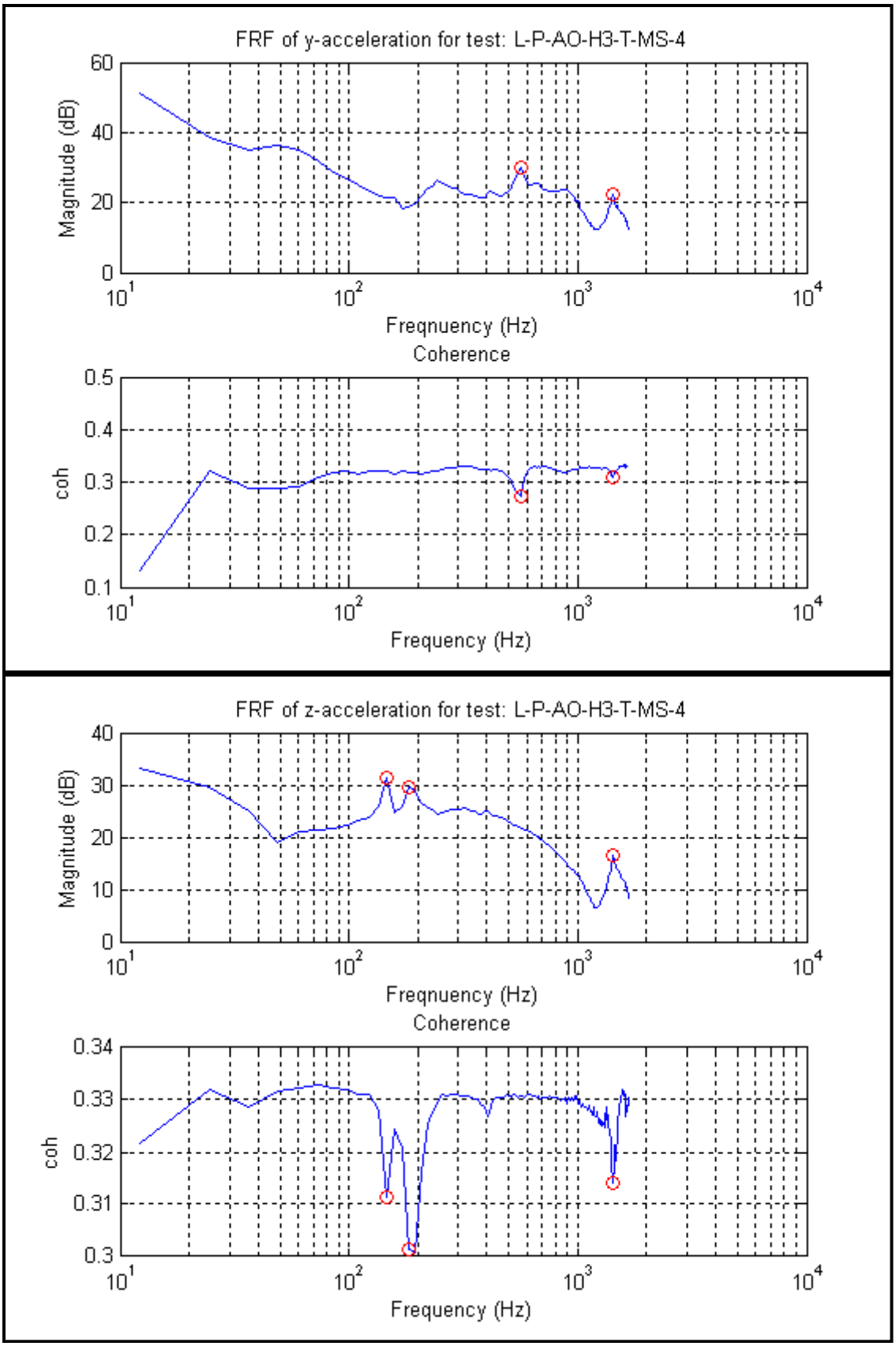
FRF of y-acceleration for test: L-P-AO-H3-T-MS-4
Magnitude (dB)
Freqnuency (Hz)
Coherence
coh
Frequency (Hz)
FRF of z-acceleration for test: L-P-AO-H3-T-MS-4
Magnitude (dB)
Freqnuency (Hz)
Coherence
coh
Frequency (Hz)